

Non-equilibrium Dynamics of DNA Nanotubes

Thesis by
Rizal Fajar Hariadi

In Partial Fulfillment of the Requirements
for the Degree of
Doctor of Philosophy



California Institute of Technology
Pasadena, California

(Submitted March, 2011)

© 2013
Rizal F. Hariadi
All Rights Reserved

in loving memory of my parents

Muhammad Amin & Suhartati
(1940 - 2010) (1944 - 2009)

*whose unconditional love and altruism
kindle inspiration and motivate me in every step of my life*

Acknowledgments

Having arrived at the end of my odyssey, I now take a great pleasure in thanking those who mean a lot to me.

My advisor, Erik Winfree, has shaped my scientific philosophy and influenced my direction more than any others. He is a pioneer whose imagination and creativity lead us to a magical endeavor in the quest of truth and beauty in science. As an advisor, he is incredibly generous in letting me pursue my true passions with my own scientific and artistic flare, while providing constant feedback on my growth as a scientist. He has assembled a rich learning environment filled with brilliant and delightful people from a variety of disciplines. It is a great privilege for me to work with a great man like him. I wish to pay his kindness by keeping the same intellectual standards for me and for my future students.

I am one of the fortunate few who get the opportunity to learn from Bernie Yurke who seems to be an expert in everything, including humility. As his apprentice, I have benefited greatly from his broad expertise. He taught me theoretical physics, introduced me to the power of craftsmanship in experimental physics, and showed me different approaches to data analysis. He is an extraordinary example of a scientist; so much so that my wife and I named our first daughter after him as our gesture of respect. Some of my fondest memories are the hiking trips with him and *in situ* investigation of ocean bubbles on Malibu beach with him and Damien Woods.

I am very grateful to the rest of my thesis advisory committee: Rob Phillips, Scott Fraser, and Michael Elowitz. Rob Phillips always has wonderful comments about my project; and his office is always open for unscheduled conversation about physics, science, life, and surfing in Indonesia. I thank Michael Elowitz for profound comments about the importance of nucleation in my artificial cytoskeleton project and Scott Fraser for pointing out the interesting structural features of DNA nanotubes during my candidacy.

Within the DNA and Natural Algorithms lab, I have gotten to know and learned from a lot of amazing people whom I will always be thankful for their scientific help and sincere friendship. I must thank Paul Rothmund and Nick Papadakis who showed me the ropes early on. Paul Rothmund and Georg Seelig instilled the importance of spending time on my bench where science happens. Peng Yin filled many gaps in my science and exemplified

how to be an excellent mentor for a graduate student. Damien Woods was an ideal collaborator for learning the Origin of Life, always had time to carefully read my manuscripts, and will remain a close collaborator. My first office mate, Rebecca Schulman, taught me about molecular self-replication, the Origin of Life theories, and a bit of computer science. I thank Elisa Franco, my second office mate, who helped me tremendously with communicating my ideas effectively in my writings and presentations. My third office mate, Dave Zhang, shared his expertise in entropy-driven chemical reaction networks for controlling self-assembly of DNA nanotubes. Jongmin Kim pursued a project exploring *in vitro* transcription of the RNA tiles with me. Even though we did not have the opportunity to go far with the project, the experience was critical in the catalytic self-assembly project with Dave. I also thank Jongmin Kim for being a great real-life next-door neighbor. Constantine Evans and Christina Wright analyzed our single molecule AFM movies, an often tedious task, and brought the work over the publication barrier. Sungwook Woo lent his expertise in DNA origami and often filled my role as WHYscope czar when I had to be away. Nadine Dabby taught me about DNA walkers and co-supervised a SURF student with me. Si-Ping Han, Rob Barish, Sungwook Woo, and Ashwin Gopinath have been great people to talk to, fellow DNA-world-ers treading into biology. David Soloveichik, Tosan Omabegho, and Ho-Lin Chen helped me think about my long-term plan. Paul Rothmund, Nick Papadakis, Sung Ha Park, Nadine Dabby, Sungwook Woo, Constantine Evans, Peng Yin, Rob Barish, Shaun Lee, and Joseph Schaeffer were excellent AFM czars and underlings; as were Rebecca Schulman, Constantine Evans, Damien Woods, and Niranjana Srinivas with the UV Spectrophotometer. Most of all, I want to thank all past and current group members for intellectually-engaging discussions and for entertaining Biruni during my frequent “take your child to your lab day”.

Throughout my graduate study, I have been fortunate to have the opportunity to discuss the cytoskeleton with a number of experts: Deborah Kuchnir Fygenson, Igor Kulic, Rob Phillips, Chin Lin Guo, Dyché Mullins, Julie Theriot, and Ethan Garner. John Dabiri, Sandra Troian, and Victor Beck contributed very helpful discussion about hydrodynamics and ocean waves. I sincerely thank my undergraduate advisors, J. Tom Dickinson and Jessica Cassleman, for nurturing my early interest in science and inspiring me to take this path. Recently, Joel Swanson, Nils Walter and Sivaramakrishnan helped me finding an ideal lab for my post-doctoral research.

The chapters in this thesis would not have been possible without the support of my collaborators. It is a pleasure to work with Peng Yin, Sudheer Sahu, Harry Choi, Bethany Walters, Tom LaBean, and John Reif in the characterization of a single-stranded tile con-

struct. The fragmentation and bubble bursting projects were collaborations with Bernard Yurke and Damien Woods. Sung Ha Park, Satoshi Murata and Kenichi Fujibayashi were great collaborators in the Sierpinski belt project. My two SURF students: Christina Wright and Yudistira Virgus, taught me about being a better teacher and person. I also embarked on a project in single molecule AFM and TIRF tracking of DNA walkers with Niles Pierce, Harry Choi, Bill Dempsey, Nadine Dabby, Ruobing Zhang, Paul Selvin, Paul Rothemund, and Erik Winfree. The project did not reach its completion but I gained a lot of knowledge about optics from this interaction, which later proved to be very useful in my artificial cytoskeleton projects.

For technical help in microscopy, Rob Phillips' group has been generous with their advice and equipment. In particular, Heun Jin Lee was instrumental in getting me over the many obstacles that popped up in the design and construction of my microscope. David Wu, Hernan Garcia, and Stephanie Johnson let me use their syringe pump, optical stage, and other optical parts. Zahid Yaqoob and Michael Diehl helped me learn about optics and parenting. Rebecca Schulman and Ann McEvoy pointed my attention to the glass capillary chamber. Jeffrey Kuhn shared his filament snapping and length measurement codes.

Karolyn Yong was a very resourceful lab administrative assistant; and more importantly, a great friend of mine. Esthela Jalabert has been keeping the building clean and tidy. The Applied Physics program, headed by Rob Phillips who was succeeded by Kerry Vahalla and later Sandra Troian, has been a tremendous source of moral and technical support. John P. Van Deusen taught me a lot of craftsmanship and supervised my machine shop time in Jim Hall Design and Prototyping Lab (Mechanical Engineering machine shop). Saurabh Vyawahare and Caltech Microfluidic Foundry assisted in the designing and manufacturing process of the PDMS microfluidic chip. Grant J. Jensen allowed me to use plasma cleaner and to have fun with his cryo-EM with supervision from Bill Tivol and Alasdair McDowall.

I thank the NSF, the NSF Molecular Programming Project (MPP), the NSF Center of Molecular Cybernetics (CMC), Caltech Center for Biological Circuit Design (CBCD), and NASA for funding.

Erik Winfree is an altruistic advisor who genuinely understands the importance of contributing to society; he always gave me permission to participate in outreach activities. I thank Yohanes Surya and Srisetiowati Seiful from Surya Institute for inviting me to speak at the 2008 Asian Science Camp in Bali. I treasure the experience. The science camp helped me decide what I want to pursue after the thesis. Achmad Adhitya, Willy Sakareza, Mahir Yahya Baya'sut, Teuku Reiza Yuanda and others sharpen my organizational skill during the launch of Ikatan Ilmuwan Indonesia Internasional (International Indonesian Scholar

Society) in Jakarta and our subsequent activities. It has also been a pleasure to interact with Johny Setiawan, Yow-Pin Lim, Nelson Tansu, Ken Soesanto, and Pak Ishadi S. K. who share deep passion in advancing education and research in Indonesia. Two days after the passing of my mother, I gave a talk at Universitas Paramadina in Jakarta. After introducing me as a speaker, Pak Ishadi S. K. requested the audience for a moment of silence in remembrance of my mother. My family and I are still touched by the sincere gesture.

Throughout my time at Caltech, I have had the support of good friends at Caltech who share passions in science and more: Akram Sadek, Aamir Ali, Mohamed Aly, Ahmed Elbanna, Hareem Maune, Suvir Venkataraman, Gabriel Kwong, and Imran Malik. Ann Erpino has continued to amaze me with her beautiful art. She is very generous in giving me permission to exhibit her paintings in this thesis.

Our fellow Indonesians in weekly gathering at the Indonesian consulate in Los Angeles have always been a source of warm comfort for my family, in particular Pak Dhe and Bu Dhe. We are really fortunate that in a short amount of time after leaving Pasadena, we are part of a similar community in Ann Arbor.

This thesis is dedicated to my first teachers, my parents: Muhammad Amin and Suhartati. Although neither of them has the chance to see these chapters finished and submitted, they have the soundest perspective on the completion of this thesis. My parents inculcated the attitude that even the largest task can be accomplished if it is done with pure intention, carefully organized, and executed one step at a time toward perfection. My interesting sisters and caring in-laws have been my favorite counselors. This thesis is also dedicated to my wife and daughter. My wife, Nurul Itqiyah Hariadi, has been my companion, heart, mind, and continuous source of inspiration. When she was a pediatric resident at UCLA, she never let her hectic schedule, ridiculously frequent on-calls, and long daily commute preclude her from raising her two “kids” at home: my daughter and me. My daughter, Aliyapadi Biruni Hariadi (who is currently sitting on my lap) always amazes me with her character, curiosity, and creativity. Both of you make my life a blissful one.

Abstract

Can the fundamental processes that underlie molecular biology be understood and recapitulated by DNA nanotechnology? The early development of DNA nanotechnology by Ned Seeman was driven by the desire to find a general solution to the protein crystallization problem. Much of the later development of the field was motivated by envisioned applications in computing and nanofabrication. While the DNA nanotechnology community has assembled a versatile tool kit with which DNA nanostructures of considerable complexity can be assembled, the application of this tool kit to other areas of science and technology is still in its infancy. This dissertation reports on the construction of DNA nanotubes with non-equilibrium dynamics to probe molecular processes in the areas of hydrodynamics and the physics of biopolymers.

As the first example, we used DNA nanotubes as a molecular probe for elongational flows in different micro-scale settings. The hydrodynamic flow in the vicinity of a simple geometrical object, such as a rigid DNA nanotube, is amenable to rigorous theoretical and experimental investigation. We measured the distribution of elongational flows produced in progressively more complex settings, ranging from the vicinity of an orifice in a microfluidic chamber to within a bursting bubble of Pacific ocean water. This information can be used to constrain theories on the origin of life in which replication involves a hydrodynamically-driven fission process, such as the coacervate fission proposed by Oparin.

A second theme of this dissertation is the bottom-up construction of a *de novo* artificial cytoskeleton using DNA nanotubes. The work reported here encompasses structural, locomotive, and control aspects of non-equilibrium cytoskeletal dynamics. We first measured the kinetic parameters of DNA nanotube assembly and tested the accuracy of the existing polymerization models in the literature. Toward recapitulation of non-equilibrium cytoskeletal dynamics, we coupled the polymerization of DNA nanotubes with an irreversible energy consumption reaction, analogous to nucleotide hydrolysis in actin and microtubule polymerization. Our synthetic approach may provide insights concerning natural cytoskeleton dynamics, such as minimal architectural or reaction mechanism requirements for non-equilibrium behaviors including treadmilling and dynamic instability.

Contents

Acknowledgments	iii
Abstract	vii
1. Self-assembly: an introduction	1
1.1. What is self-assembly?	3
1.2. Classes of self-assembly	4
1.3. Non-equilibrium self-assembly to probe biomolecular processes	5
1.4. Artificial cytoskeleton	7
1.5. Tools for studying non-equilibrium self-assembly	9
1.6. Outlook	10
1.7. Organization of the thesis	10
1.8. Publications outside this thesis	11
2. Programming DNA Tube Circumferences	13
2.1. Introduction	14
2.2. Results	15
2.3. Concluding remarks and outlook	21
2.4. Acknowledgements	23
3. Elongational-flow-induced scission of DNA nanotubes	25
3.1. Introduction	26
3.2. Methods	28
3.3. Results and Discussions	31
3.4. Concluding Remarks	39
3.5. Acknowledgments	39
4. Elongational rates in bursting bubbles measured using DNA nanotubes	41
4.1. Introduction	41
4.2. Materials and Methods	43
4.3. Results and Discussions	45
4.4. Conclusion	50

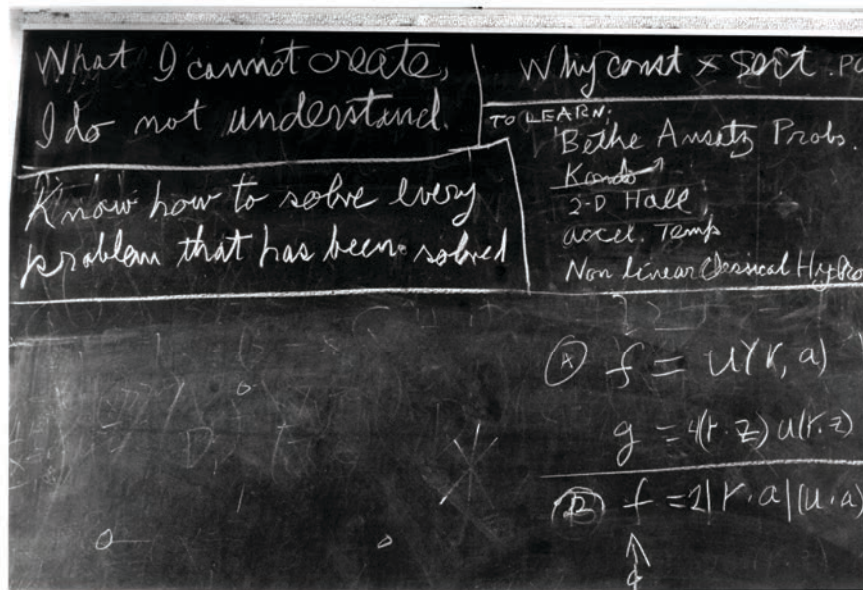
4.5. Acknowledgments	50
5. Could ocean hydrodynamic flows have driven self-replication of the protobiont? 51	
5.1. Introduction	52
5.2. Results	55
5.3. Concluding remarks and outlook	57
5.3.1. What have we learned?	57
5.3.2. Trip to Malibu beach	57
5.4. Acknowledgments	59
6. Single molecule analysis of DNA nanotube polymerization 61	
6.1. Introduction	62
6.2. Materials and Methods	66
6.2.1. Total Internal Reflection Fluorescence microscope	66
6.2.2. DNA tile design	69
6.2.3. Polymerization mix	70
6.2.4. Data acquisition	72
6.2.5. Data analysis	74
6.3. Results	75
6.3.1. Polymerization rate measurements	75
6.3.2. Local and global analysis of combined polymerization data	79
6.4. Discussion	84
6.4.1. Interpretation of the measured k_{on} and k_{off} rate constants	85
6.4.2. Asymmetric polymerization	85
6.4.3. Comparison with previously reported reaction rates of DNA self- assembled structures	93
6.4.4. Comparison with the polymerization rates of actin and microtubules	95
6.5. Concluding remarks and outlook	96
6.6. Acknowledgments	97
7. Toward <i>de novo</i> recapitulation of cytoskeletal dynamics with DNA nanotubes 99	
7.1. Introduction	100
7.2. The biophysics of microtubules	102
7.2.1. The structure of microtubules	102
7.2.2. GTP hydrolysis in microtubule polymerization gives rise to tread- milling and dynamic instability	104

7.3. DNA nanotube implementation of the engineering principles of cytoskeletal assembly	105
7.4. Results	113
7.4.1. The enzymatic activity of EcoRI on dsDNA with nicks	113
7.4.2. Nicking reaction of DNA nanotubes	115
7.4.3. Single molecule movie of DNA nanotube polymerization with nicking reaction	121
7.5. Discussion	122
7.6. Concluding remarks	128
A. Supplementary materials for Chapter 2: Programming DNA Tube Circumferences	131
A.1. DNA sequence design	131
A.2. Sample preparation	131
A.3. AFM imaging.	132
A.4. Fluorescence imaging and length measurements.	132
A.5. Thermal transition profiles.	133
A.6. Curvature analysis	133
A.7. DNA sequences	154
B. Supplementary materials for Chapter 3: Elongational-flow-induced scission of DNA nanotubes	157
B.1. Underlying scission theory	157
B.2. Bayesian inference and stochastic scission simulation	161
B.3. Best L_{crit} fit by Bayesian inference	162
B.4. Best L_{crit} fit by Bayesian inference with truncated Gaussian noise	162
C. Supplementary materials for Chapter 6: Single molecule analysis of DNA nanotube polymerization	167
C.1. Movie of anomalous diffusion and side-to-side joining	168
C.2. Movie of depolymerization experiment	169
C.3. Movie of DNA nanotube growth	170
C.4. Movie of complete depolymerization of DNA nanotubes followed by annealing of newly released free DNA tiles	171
C.5. AFM images of opened DNA nanotubes	173
C.6. UV absorbance of DNA nanotube	175

D. Supplementary materials for Chapter 7: Toward <i>de novo</i> recapitulation of cytoskeleton dynamics with DNA nanotubes	177
D.1. The spacing between neighboring DNA tiles in DNA lattice.	177
Bibliography	183

1

Self-assembly: an introduction



Richard Feynman's blackboard at the time of his death. (Caltech Archive)

I started my graduate study at Caltech in the spring of 2003, just in time to celebrate the 50th anniversary of the discovery of the molecular structure of DNA double helix [WC53]. The specificity of Watson-Crick base pairing rules (A=T and G≡C) provides the molecular foundation of storing genetic information. Aside from its pre-conceived role as the “genetic blueprint of life”, the simple recognition rule of Watson-Crick base pairing, in addition to structural features of the DNA double helix, are being exploited by the emerging field of structural DNA nanotechnology to assemble one-, two-, and three-dimensional nanostructures. Structurally, DNA is an attractive building block for synthesis of nanostructures as the DNA double helix has a defined diameter of 2 nm and 10.5 base pairs in a full DNA turn. An additional desirable physical attribute of DNA is its rigidity. The persistence length of DNA is ~150 base pairs, which implies that up to 50 nm, the DNA molecule behaves as a rigid beam. Therefore, in the context of structural DNA nanotechnology, the end product of molecular programming is the self-assembly of organized DNA helices in specific spatial configurations; whereas in the context of molecular biology, the end product is the transcription of DNA sequence into RNA molecules by cellular machinery.

Structural DNA nanotechnology offers one promising approach to constructing dynamical autonomous nanoscale systems. In this approach, the instructions for how to assemble larger structures are coded in the DNA sequences using the specificity of canonical Watson-Crick hybridization [WLWS98]. Diverse tiling lattices have been constructed [LLRY06], and some of these lattices are reported to form tubes [YPF⁺03, MHM⁺04, LPRL04, RENP⁺04, RSB⁺05, LCH⁺06, KLZY06]. Recently, the DNA “origami” approach of folding viral genomes using hundreds of synthetic oligonucleotides has provided a reliable method for producing pseudo one-, two- and three-dimensional DNA nanostructures of length 100 nm or larger [Rot06, DDL⁺09, ESK⁺10, LZWS10]. Furthermore, algorithmic self-assembly of a small number of DNA tiles can give rise to complex patterns, such as Sierpinski triangles [RPW04, FHP⁺08] and binary counters [BRW05, BSRW09]. Despite the versatile tool kit with which DNA nanostructures of considerable complexity can be assembled, the application of this tool kit to other areas of science and technology is still in its infancy.

This dissertation reports on the construction of non-equilibrium DNA nanotube dynamics to probe molecular processes in the area of hydrodynamics and cytoskeletal behavior. DNA nanotubes have desirable physical features such as (a) long length, (b) long persistence length and (c) inherently simple geometries, which are amenable to rigorous theoretical modelling. Inspired by analogy with the ubiquity of tubular structures in nature and the roles of microtubules and actin filaments in living cells, this thesis reports the

application of DNA nanotubes as a micro-scale fluid flow sensor and for the construction of an artificial cytoskeleton.

Narratives for studying DNA self-assembly

There are various reasons for studying DNA self-assembly. First, humans find beauty in ordered structures. This is seen in the early years of DNA self-assembly after the publication of the seminal paper by Winfree *et al.* in 1998 [WLWS98], when most of the reported constructs were two-dimensional and tubular crystalline structures that were assembled from pre-formed multiple stranded DNA tiles [FS93]. Second, algorithmic self-assembly of a simple set of building blocks can result in complex patterned structures [RPW04, BSRW09]. Third, DNA self-assembly is an efficient bottom-up strategy for synthesizing nanostructures as first proposed in Seeman's classic paper in 1982 [See82]. A striking example of the efficiency of self-assembly is the construction of a 100-nm scaled map of the Americas using a technique called DNA origami [Rot06]. In a one pot reaction, Rothemund produced more maps than human civilizations have ever made.¹ Fourth, a more recent class of DNA self-assembly incorporates non-autonomous [SP04, SS04] and autonomous [LMD⁺10, HL10] DNA robots, thereby enriching our concept of robotics. Fifth, novel properties can be engineered into DNA self-assembly systems, such as self-healing structures [Win06, SCW08] and reconfigurable structures that can sense the existence of molecules in their environment [GHD⁺08]. Sixth, because living systems are non-equilibrium self-assembled system, understanding life requires understanding self-assembly [WG02].

1.1. What is self-assembly?

Before focussing further on DNA self-assembly, it is necessary to examine the definition of self-assembly in general. Within the rich “self-assembly” literature, from the hybridization of the DNA double helix to the formation of galaxies, one can find elastic definitions of “self-assembly” that are typically geared toward the focus of the latest trends. In this thesis, we restrict our definition of self-assembly to the spontaneous formation of organized structures from many pre-existing components that can be controlled by programming the components and reaction conditions, such as temperature and component concentrations. Thus, self-assembly is not synonymous with crystallization or aggregation.

¹adapted from Erik's blurb, www.dna.caltech.edu/DNAresearch_publications.html

In this thesis, we further limit our discussion of self-assembly within the realm of DNA tile-based self-assembly or structural DNA self-assembly, which is a subset of a broader field of DNA nanotechnology. The two main signatures of structural DNA self-assembly are the high order and rigidity of the final assembly. This rigidity can be inherited from the rigid structural core of the building blocks, called DNA tiles, such as in the nanotubes of chapter 6 or can emerge from interactions between floppy building blocks during the nucleation and growth of the end products, such as in the structures of chapters 2–5. Since we stipulate that the end product must be rigid, we strictly exclude all of the dynamic strand-displacement reaction-based systems [YTM⁺00,SSZW06,ZW09,BT07,ZS11,SSW10] from our definition of structural DNA self-assembly

1.2. Classes of self-assembly

Based on the definition of self-assembly above, there are two major classes of self-assembly: equilibrium self-assembly and non-equilibrium self-assembly, which are also often referred as static and dynamic (dissipative) self-assemblies, respectively as in refs. [WG02,FBK⁺06]. The distinction between equilibrium and non-equilibrium self-assemblies is strictly based on the thermodynamic description of the final assemblies and not to the self-assembly processes by which such structures are synthesized, as will be detailed below.

Equilibrium self-assembly

In equilibrium self-assembly, the final structures are at global or local minimum and do not dissipate energy. The formation of the ordered structures often requires non-equilibrium agitation or processing; but once the final structure is formed, it is static and stable. In the context of chemical potential of the building blocks, each component is initially at high chemical potential and as each component is added to the assembly, the chemical potential goes down until reaching its equilibrium chemical potential. Most reported DNA self-assemblies lie in this territory. One of the most celebrated example in structural DNA nanotechnology is Rothemund’s two-dimensional DNA origami [Rot06]. The structures are formed by equilibrium self-assembly, although the synthesis involves a non-equilibrium step. Typically, DNA origami constructs are made by annealing a set of equimolar short DNA strands and a substoichiometric concentration of scaffold strand from 90 °C to room temperature.

Non-equilibrium self-assembly

In the formation of non-equilibrium dynamic structures or patterns, one must drive the self-assembly away from equilibrium by continuous supply of energy, which is an integral part of the local interaction rule set between the components and with the environment. These non-equilibrium self-assembled structures continue to consume and dissipate energy for their survival in the form of irreversible entropy producing processes and die when the flow of energy ceases. The study of non-equilibrium structural DNA self-assembly is still in infancy.

We further define two subclasses of non-equilibrium self-assembly based on the energy source. The first subclass obtains the energy from its environment. Most synthetic non-equilibrium self-assembly systems are in this subclass. As an example, Whitesides *et al.* studied a variety of non-equilibrium assemblies of ferromagnetic disks, floating at the liquid-air interface, under the influence of a rotating external bar magnet [GSW00]. The spinning disks assemble into a variety of stable patterns. The second subclass of non-equilibrium assembly consumes energy that is stored in a reservoir of fuel molecules, which are distinct from the self-assembling components and continuously release waste molecules. My favorite example of the fuel molecule powered assembly is the non-equilibrium polymerization of microtubules. Detailed structural properties and non-equilibrium dynamics of microtubules are presented in section 7.2. The energy is derived from irreversible nucleotide hydrolysis of GTP to GDP, and used to generate physical phenomena that are only possible in non-equilibrium polymers, such as treadmilling and dynamic instability. The main thrust of this thesis is our effort in *de novo* engineering of an artificial cytoskeleton using DNA nanotubes, and which has the potential to exhibit non-equilibrium phenomena.

1.3. Non-equilibrium self-assembly to probe biomolecular processes

From a purely scientific perspective, the most important justification for studying self-assembly is the understanding of life. Although the principles of self-assembly are applicable at all scales, the nanoscale size of the DNA tile is attractive because it lies in the length scale at which gathering, processing, and transmission of information occurs in living systems [Man08]. The construction of non-equilibrium self-assembly systems with features as intricate and complex as their biological counterparts satisfies Feynman's criteria of understanding: "What I cannot create I do not understand". These artificial systems could provide insight to molecular structures, biological process and how dissipation of energy

leads to the emergence of ordered structures from disordered building blocks, which are vital in living system.

From the experimental point of view, engineering artificial systems for understanding biological systems offers three advantages. First, building simple nanoscale systems that are easy to modify provides a platform for rigorous testing, refining, and confirming mathematical models of biomolecular processes. In the case of microtubules, a detailed understanding of the molecular machinery of α,β -tubulin is difficult to attain because the activity of the monomer and polymer are affected by complex systems of exogenous and endogenous cellular factors. Claiming that studying artificial system will help understanding biology is still controversial. Not all insights obtained from artificial systems are guaranteed to have biological relevance, as will be discussed in section 1.5. Second, the similar length scales of the biological molecules and their technological analogs permits engineering of a more advanced artificial system that can alter or even improve the performance of the biological system of interest. Third, for non-equilibrium self-assembly, collective behavior may arise from simple local rules which might yield insights into the principles of self-organized system. This set of principles could be essential for engineering materials that exhibit novel behaviors, such as adaptive assembly [BR09, SY10], self-healing [Win06, SCW08], and self-replication [SW05].

Advances in DNA nanotechnology and clever experimental design have led to successful construction of several artificial systems, such as artificial muscles [LYL05], artificial ribosomes [LS04], artificial listeria [VDR⁺07], and artificial myosins [SP04, SS04, YCCP08, GBT08, LMD⁺10]. Although these artificial constructs were inspired by natural systems, most of them were primarily technologically-driven and made little connection to their biological counterparts. The remainder of this chapter mostly explains our work toward the *de novo* construction of an artificial cytoskeleton with DNA nanotubes. We aim to engineer a DNA nanotube system that satisfies the structural, propulsion, and assembly control aspects found within the biological cytoskeleton, as will be described in the next section.

1.4. Artificial cytoskeleton

In the Wright brothers' conquest of flight², Orville and Wilbur Wright approached the technical challenge as three unique engineering problems³: (1) The structural challenge; How do you engineer a structure that generates lift? (2) The propulsion challenge; How do you power an airplane to move forward? (3) The control challenge; How do you adjust the speed and navigate an airplane?

Inspired by the Wright Brothers' approach, we divided our quest of *de novo* construction of an artificial cytoskeleton into three engineering challenges:

1. Structural challenge: How can non-equilibrium polymers establish polarity for asymmetric polymerizations, such as treadmilling and dynamic instability?

The structural challenge for an artificial cytoskeleton encompasses both (1) equilibrium self-assembly and (2) non-equilibrium self-assembly. First, biological cytoskeleton structures are long-and-rigid polymers composed of non-covalently-bound monomers. DNA nanotubes satisfy these criteria already, as will be described in chapter 6 and appendix C. Second, since asymmetric polymerization requires energy source, we couple an irreversible dissipative reaction with DNA nanotube polymerization (chapter 7). In our design, we inserted the EcoRI restriction sequence at the two opposing sticky ends of a DNA tile, such that docking a DNA tile to a growing polymer will complete the restriction site and will trigger the analog of the nucleotide hydrolysis reaction. Our aim is to investigate minimal architectural or reaction mechanism requirements for asymmetric polymerizations, such as treadmilling and dynamic instability.

Apart from being a candidate material for an artificial cytoskeleton, we also used static DNA nanotubes as a novel micro-scale fluid flow sensor. The simple “structural” features of DNA nanotubes enable us to rigorously calculate a simple fluid-flow-induced tension along an *n*-helix DNA nanotube (appendix B). By Bayesian inference from the nanotube length distribution before and after being subjected to the fluid flow, we measured the strength of elongational flows produced in progressively more complex settings, ranging from the vicinity of an orifice in a microfluidic chamber (chapter 3), to within a bursting bubble of DNA buffer (chapter 4) or of Pacific ocean water (chapter 5).

²On a personal note, I started my graduate study 100 years after the Wright brothers' first controlled, powered and sustained human flight, on December 17th, 1903.

³Paraphrased from Dyche Mullins' lectures on prokaryotic and eukaryotic cytoskeleton at Caltech.

2. The propulsion challenge: What are the mechanisms by which molecular assemblies generate the force required to apply force to other structures?

The non-equilibrium polymerization of rigid polymers has been shown to transduce chemical energy from the concentration gradient into mechanical energy [The00]. This represents another class of molecular motor, called a polymerization motor. Rather than using a general cellular energy currency, such as ATP or GTP, the energy in a polymerization motor is stored in the chemical potential of free monomers μ_s that is either higher or lower than the chemical potential of the monomers at the tip of a polymer μ_p . If $\mu_s > \mu_p$, polymerization is favored, while in the opposite case, $\mu_s < \mu_p$, depolymerization dominates. As an example of a polymerization motor, the polymerizing protein ParM [GCWM07] in prokaryotic cells uses non-equilibrium insertional polymerization to push two chromosomes apart in a dividing cell. Interestingly, Venkataraman *et al.* [VDR⁺07] devised an elegant construct of DNA-based insertional polymers that, in principle, is capable of generating force or transporting nanoscale objects in solution. As another example, depolymerizing microtubules in the mitotic spindle are used by eukaryotic cells to segregate their chromosomes correctly during cell division [DKRLJ05, WWAS⁺06]. In chapter 6 and appendix C, we demonstrated and characterized non-equilibrium polymerization and depolymerization of isolated DNA nanotubes. In this work, similar to the biological polymerization motor, the energy of the assembly is stored in the chemical potential of free DNA tiles.

3. The control challenge: How do alterations in the DNA tile regulate its function? How can chemical reaction networks control when and where the polymerization of DNA nanotubes take place?

Like a flying airplane, active polymers, such as the cytoskeleton, are inherently unstable. The cytoskeletal monomers and cytoskeletal accessory proteins are intelligent molecules that evaluate their environments to assemble and disassemble cytoskeletal polymers at the right time and the right place within cells. In collaboration with Dave Zhang and Harry Choi, I addressed the control challenge by integrating strand displacement circuitry with DNA nanotube polymerization. The interplay between chemical reaction networks and self-assembly described in this thesis is essential toward building non-equilibrium systems that can execute tasks based on the evaluation of molecular information in its environment.

1.5. Tools for studying non-equilibrium self-assembly

Continued progress in the construction of non-equilibrium DNA self-assembly as model systems for molecular biology requires effective light microscopy assays, physical models, computational tools, and equally important, formal criteria for assessing the biological relevance of any insight obtained from an artificial system.

Microscopy

Open a biophysics textbook [PKTG09], you will be presented with many microscopy images of non-equilibrium biochemical reactions that drive the essential processes of life. Light microscopy has been the standard assay for the study of temporal evolution and spatial organization in cells. In contrast, traditional equilibrium self-assembly typically reports the final structures in the form of static AFM images, which provides little information about the dynamics enroute to the end product. Compelling demonstration of non-equilibrium engineered structures or patterns often requires continuous observation of dynamic systems in real time. In chapter 6 and appendix C, we use TIRF microscopy to continuously monitor the non-equilibrium polymerization of self-assembled DNA structures in real time. From a set of polymerization movies at a wide range of tile concentrations and reaction temperatures, we were able to measure both the kinetic and thermodynamic parameters of DNA nanotube assembly and discover the subtle features of polymerization that can be observed with single-molecule microscopy technique.

Theories and principles of non-equilibrium self-assembly

Physical models and computational tools are central in guiding the experimental design of DNA self-assembly as well as understanding the global behavior that emerges in these systems. In chapter 6, we report the experimental verification and refinement of the existing kinetic Tile Assembly Model [Win98]. Measured kinetic and thermodynamic parameters were subsequently used in the stochastic simulation of DNA nanotube polymerization at different circumferences. In a subsequent experiment, we employed both the polymerization model and stochastic simulation in predicting the effect of coupling irreversible chemical reactions, analogous to nucleotide hydrolysis, with DNA nanotube polymerization (chapter 7).

Turing test analog for artificial systems

The engineering approach to studying biomolecular assemblies that is highlighted in this chapter, is still considered controversial because of two reasons: (1) The biological insight that one obtains from artificial systems is inherently indirect. (2) At least in DNA nanotechnology, artificial systems are much simpler than their biological counterparts. Only a small set of primitives and a subset of features used by biomolecules of interest are embedded in an artificial system. Hence, any insight obtained from this approach does not always carry over to meaningful insight about biological system. One way to filter the experimental results from this approach is by subjecting the artificial system to the analog of the Turing test for artificial intelligence. Here, by looking at the behavior of the system that we create, we judge the relevance of our study by our ability to distinguish the artificially constructed system from the biological system [LF09].

1.6. Outlook

The field of DNA nanotechnology can offer opportunities to build artificial systems of biological assemblies. Future developments in non-equilibrium DNA nanotechnology may lead to components for artificial life and materials with novel properties, such as adaptability, self-healing, and self-replication. However, it is unclear whether this herculean effort will lead to an efficient way of advancing biology. We understand biological cells are self-organized chemical systems that acquire material and information, make molecules and decisions, and take actions that regulate their internal functions and their interactions with the environment. Yet we know very little how simple chemical reaction networks obtain the complexity and emergent behaviors found in living cells. We are also still learning how various artificial and natural non-equilibrium systems utilize energy dissipation in the emergence of order from interactions of disordered components. Even modest progress toward solving these scientific mysteries will provide sufficient justification to the study of these artificial systems.

1.7. Organization of the thesis

The author contribution, and publication or work in preparation, associated with each chapter are presented in the first footnote of each chapter. Other than chapter 2, I am the first author or co-first author of the publication or manuscript in preparations in the rest of this thesis.

For the published works, all of the the text and figures in this thesis come directly from the published manuscripts with minor stylistic modification to match the style of the document. The experimental work for all the results presented in the thesis are primarily performed by me and all of the figures were mine, except where explicitly noted, such as all of Ann Erpino's paintings.

The first theme of this thesis describes the elongational flow induced scission of n -helix DNA nanotubes (chapter 2 and appendix A) in progressively more complex settings, ranging from the vicinity of an orifice in a microfluidic chamber (chapter 3 and appendix B) to within a bursting bubble of DNA buffer (chapter 4) and Pacific ocean water (chapter 5). This work was inspired by Rebecca Schulman's project on engineering DNA tile-based artificial life [SW05] and was initiated by a serendipitous observation by Harry M. T. Choi.

The second part of this thesis describes our effort toward *de novo* construction of an artificial cytoskeleton with DNA nanotubes. Chapter 6 and appendix C, indirectly addresses the propulsion challenge of an artificial cytoskeleton. We demonstrated the application of TIRF microscopy to measure the kinetic and thermodynamic parameters of DNA nanotube polymerization. The structural challenge for an artificial cytoskeleton is addressed in chapter 7 and appendix D. Finally, in a paper that is currently in review (see below), we integrated DNA nanotube polymerization and strand displacement circuitry to address the control aspect for an artificial cytoskeleton.

1.8. Publications outside this thesis

During my years as a graduate student, I also embarked on these following projects:

1. Kenichi Fujibayashi, Rizal F. Hariadi, Sung Ha Park, Erik Winfree, and Satoshi Murata, Toward reliable algorithmic self-assembly of DNA tiles: a fixed-width cellular automaton pattern, *Nano Letters*, 2008, Vol. 8, Issue 7, 1791 - 1797.
2. Constantine G. Evans, Rizal F. Hariadi, and Erik Winfree
Direct Atomic Force Microscopy Observation of DNA Tile Crystal Growth at the Single Molecule Level, *Journal of the American Chemical Society*, 2012, vol. 134, Issue 25, 10485-10492.

* Authors contributed equally.

3. Dave Yu Zhang*, Rizal F. Hariadi*, Harry M. T. Choi, and Erik Winfree, Integrating DNA strand displacement circuitry with DNA tile self-assembly, Nature Communications, 2013, Vol. 4, 1965
4. Rizal F. Hariadi, Damien Woods, and Bernard Yurke, Assessing the effectiveness with which breaking waves could have driven protobiont replication, *in preparation*

* Authors contributed equally.

2

Programming DNA Tube Circumferences

Creativity has more to do with the
elimination of the inessential than
with inventing something new.

(Helmut Jahn)

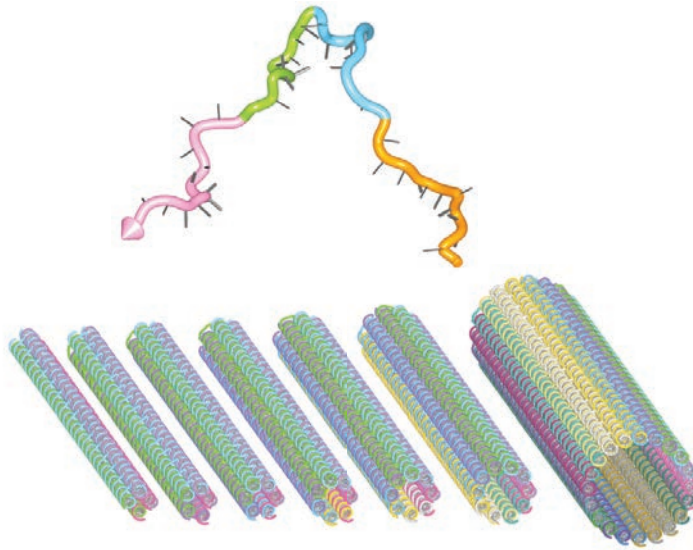


Image courtesy of Peng Yin

Abstract

Synthesizing molecular tubes with monodisperse, programmable circumferences is an important goal shared by nanotechnology, materials science, and supermolecular chemistry. We program molecular tube circumferences by specifying the complementarity relationships between modular domains in a 42-base single-stranded DNA motif. Single-step annealing results in the self-assembly of long tubes displaying monodisperse circumferences of 4, 5, 6, 7, 8, 10, or 20 DNA helices.

2.1. Introduction

DNA, life's information carrier, has recently emerged as a versatile material for constructing self-assembled synthetic molecular structures and devices [See03, FN06, BT07, See07]. The construction of extended DNA arrays has motivated the search for rigid molecular building blocks, as component rigidity is commonly considered necessary for the formation of well-ordered DNA crystals rather than ill-defined aggregates [SWY⁺98]. A typical building block, or tile, has a rigid structural core, and displays several "sticky ends" that allow for specific binding with other tiles to guide lattice formation [FS93, WLWS98]. Diverse tiling lattices have been constructed [LLRY06], and some of these lattices are reported to form tubes [YPF⁺03, MHM⁺04, LPRL04, RENP⁺04, RSB⁺05, LCH⁺06, KLZY06]. Such DNA nanotubes typically possess varied circumferences.

As the precise control of the structure of matter is a central goal for nanotechnology, materials science, and supermolecular chemistry, controlling DNA tube circumferences has attracted intense research interest. One strategy is to encode the circumferential tube geometry directly in each individual building block [MLK⁺05, PBL⁺05, WM05, SS06, DCS07, KWSS07]: barrel/half-barrel like rigid tiles with designed tubular curvature and circumference are first assembled, and then stacked to produce tubes with prescribed circumferences. Using this strategy, researchers have successfully constructed DNA tubes containing three [PBL⁺05, WM05], six [MLK⁺05, KWSS07, DCS07], and eight circumferential helices [KWSS07], and have proposed designs for tubes of arbitrary circumference [SS06].

This work was published in full as:

Peng Yin, Rizal F. Hariadi, Sudheer Sahu, Harry M. T. Choi, Sung Ha Park,
Thomas H. LaBean, and John H. Reif.
Programming DNA Tube Circumferences.
Science (2008) vol. 321 (5890) pp. 824-826

However, this approach requires the circumference-dependent construction of distinct building blocks that often possess complicated molecular structures. This motivates us to search for alternative strategies that are modular and simpler.

We report the construction of DNA lattices using a flexible, single-stranded DNA motif, which is substantially simpler than the current practice using multi-stranded rigid tiles. During lattice formation, the motif configures itself into a tile-like geometry, and motif-motif interactions result in emergent rigidity along the extended growth direction of the lattice. Importantly, this flexible motif allows us to program the tube circumference also as an emergent property collectively defined by the modular interactions between the motifs. In the resulting framework, simply pairing modular domains in the single motif results in the self-assembly of monodisperse DNA tubes with designed circumferences. Additionally, the motif-based, codified construction permits the description of a tube design in the form of an abstract “molecular program”, further simplifying the design process.

2.2. Results

The 42-nucleotide (nt) single-stranded DNA motif has four concatenated modular domains (Fig. 2.1A): the orange domain 1 and the blue domain 2 together contain 21 nucleotides; the green domain 3 and the pink domain 4 together contain 21 nucleotides. By pairing up complementary domains, the motifs can be arranged to form DNA lattices composed of parallel DNA helices connected by single-stranded linkages (or half-crossovers¹) (Fig. 2.1B).

¹The half-crossover can be viewed as a simplified Holliday-junction analog, which utilizes one strand, rather than the normal two strands, at the crossover exchange point. A similar structure was previously used in constructing DNA nanotubes [LCH⁺06].

Author contributions:

PY invented the SST motif, conceived and initiated the project, organized the team, and supervised the work. The work at Duke (May 2005 - Aug. 2005) was hosted in the lab of JHR and THL, and the work at Caltech (Sep. 2005-Aug. 2008) was hosted in the lab of Erik Winfree. While at Duke, PY designed sequences. PY designed the experiments with input from THL and SHP. PY and SS prepared the samples. PY and SS performed the AFM experiments. SHP performed nanotube metalization experiments (not included). Bethany Walters performed melting experiments (not included). PY and SS analyzed the data with input from THL and SHP. While at Caltech, PY designed the sequences, and prepared all the samples. PY and RFH designed the experiments with input from HMTC and SHP. PY, RFH, SS, HMTC, and SHP performed AFM imaging. RFH acquired the high resolution images of 5-helix ribbon. PY and RFH analyzed the data. PY and RFH run the melt experiments. RFH imaged SST with TIRF and confocal microscopes. SHP metalized SST nanotubes (not included). RFH and Bernard Yurke built the TIRF microscope. The figures and the manuscript were prepared by PY, with discussion and input initially from SHP, THL, and JHR, then primarily from RFH and Erik Winfree.

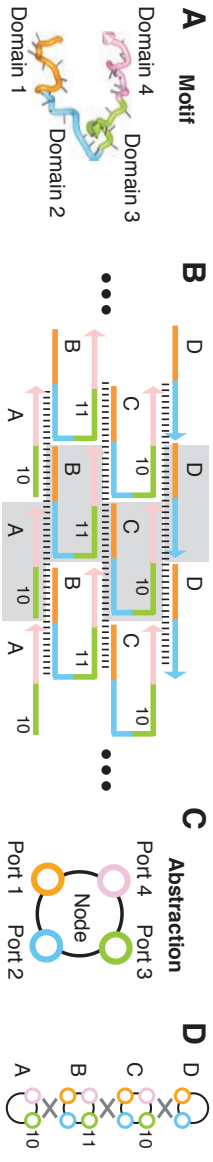


Figure 2.1.: (A) Motif. Colored lines represent modular domains; the arrow head indicates the 3' end. (B) Secondary structure of DNA lattices. Short vertical bars represent base pairing. The shaded area indicates a repeating structural unit. (C) Abstraction of the motif as a node with four ports [YCCP08]. The ports are depicted as colored circles. The color use is consistent with **A**, and the ordering of the ports is specified by their colors: orange → blue → green → pink. (D) Complementarity graph.

As the orange-blue domains and the green-pink domains in a motif each measure 21 nt, the inter-helical linkages are spaced periodically at every two full helical turns (i.e. 21 base pairs). In the lattices, each non-boundary motif is configured into a rectangle-like shape, and is connected to four adjacent neighbors. Thus the motif implements the functionality of a tile, and is termed a single-stranded tile, or SST (see Fig. A.1 for the comparison between a traditional rigid multi-stranded tile and SST). In Fig. 2.1B, the number k associated with a green domain indicates the number of nucleotides contained in the domain, and determines the putative, approximate inter-helix curvature for an un-strained lattice (e.g. not closed into tubes) through a simple formula, $k \times 34.3^\circ - 330^\circ$ [see Appendix A.6 for details].

The modularity and standardization of the SST motif allows us to codify the lattice design procedure: first “wire” together complementary domains and then assign the dimensions of the green domains². The codification further permits us to ignore molecular structure details and express the lattice design in a simple abstract form. Adapting a previous notation system [YCCP08], we abstract our motif as a node with four ports, where each port represents a modular domain (Fig. 2.1C). The lattice design is expressed as a complementarity graph (Fig. 2.1D), where two complementary ports are connected by a grey line, and the dimension of each green port is indicated with an associated number.

A complementarity graph represents a “molecular program” to be executed physically by the corresponding DNA molecules. During the execution of the program through one-pot annealing (see Materials and Methods in Appendix A), the specified complementarity relationship between the modular domains of the motif directs the DNA molecules toward a (global or local) thermodynamic minimum on the free energy landscape, where the designed target structure resides. For example, the execution of the molecular program in Fig. 2.1D results in the formation of the 3-helix ribbon lattice depicted in Fig. 2.1B.

The 3-helix ribbon program can be generalized to program the formation of k -helix ribbons (Fig. 2.2A), using $(k-1)$ full SST species (U_1, U_2, \dots, U_{k-1}) and 2 boundary half-SST species (L_1 and L_k). By executing the general program in Fig. 2.2A, we demonstrate the experimental construction of monodisperse ribbons [SW07] with five distinct widths: 3-, 4-, 5-, 6-, and 20-helix ribbons. Fig. 2.2B depicts the secondary structure for the 5-helix ribbon. Direct imaging of the self-assembly product by atomic force microscopy (AFM) reveals the expected linear filament morphology (Fig. 2.2C). AFM further confirms the

²Due to the modularity and standardization of the motif, assigning the dimensions of all the green domains in the lattice also uniquely determines the dimensions of all the other domains.

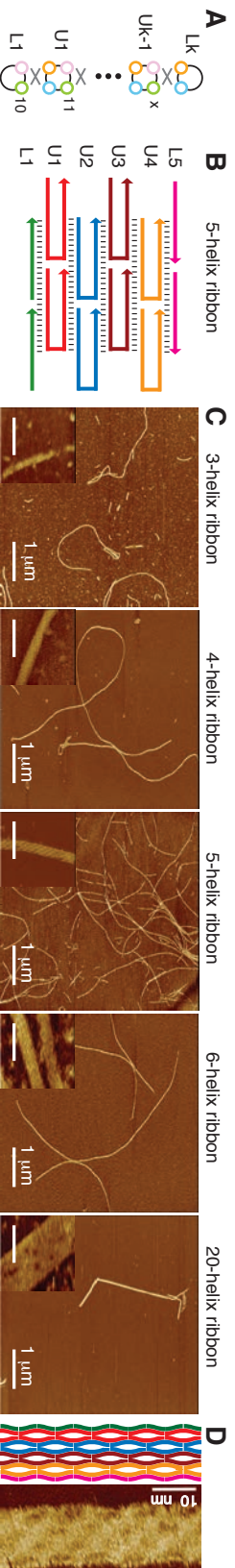


Figure 2.2.: Monodisperse DNA ribbons with programmed widths. (A) The molecular program for assembling a k -helix ribbon. (B) Secondary structure for the 5-helix ribbon. See figs. S3 and S4 for more structures and details. (C) AFM images of 3-, 4-, 5-, 6-, and 20-helix ribbons. See Fig. A.5 for larger AFM images. Insets, scale bar, 50 nm. Measured ribbon widths: 9.3 ± 0.7 nm (3-helix ribbon), 12.5 ± 0.5 nm (4-helix), 14.9 ± 0.7 nm (5-helix), 18.0 ± 0.8 nm (6-helix), and 59.0 ± 1.1 nm (20-helix). See Fig. A.6 for ribbon width measurements. (D) High resolution AFM image of the 5-helix ribbon. Left, depiction of the expected DNA structure, emphasizing banded helices and inter-helix gaps. The color use is consistent with B. Right, AFM image revealing an alternating pattern of four columns of inter-helix gaps, in agreement with the depiction on the left. See Fig. A.7 for details.

designed dimensions of the ribbons: a k -helix ribbon has a measured width of $\sim 3 \times k$ nm (Fig. 2.2C insets). Further, the morphology details of the 5-helix ribbon are revealed by high resolution AFM (Fig. 2.2D).

A natural strategy for constructing monodisperse k -helix SST tubes is to merge the two boundary half SST species in the k -helix ribbon program into a full SST species (Fig. 2.3A). Fig. 2.3B (left) describes the secondary structure for $k = 6$. The execution of the 6-helix tube program through annealing results in linear filament products (Fig. 2.4A, third panel from left). The mechanical force exerted by repeated AFM scanning opens these filaments, confirming their tubular nature (Fig. A.12). Finally, AFM width measurement of 10 random opened tubes establishes the monodispersity (i.e., no $6 \times m$ -helix tubes identified, for $m > 1$) of their circumferences (Fig. A.13).

This molecular implementation could in theory allow concatenation of multiple repeats of U1-U2-U3-U4-U5-T6 along the tube's circumference, resulting in poly-disperse tubes composed of 1×6 circumferential helices, 2×6 helices, 3×6 helices, etc.. Further, geometric modeling [RENP⁺04] suggests that the SST domain dimensions in Fig. 2.3A would result in an average inter-helix curvature of $\sim 30^\circ$ per helix (Appendix A.6). One would therefore expect 12-helix tubes to be less sterically strained [RENP⁺04] than 6-helix tubes and to thus dominate at thermodynamic equilibrium. The observed monodisperse formation of 6-helix tubes suggests that the tube formation should be understood as a kinetic process [MHM⁺04, KLZY06] and that these tubes are trapped at a local minimum on the free energy landscape (Fig. 2.3B, right). These tubes are stable: AFM images obtained ~ 6 months after sample preparation reveal monodisperse 6-helix tubes.

We next tested the general program (Fig. 2.3A) where k distinct SST species self-assemble into k -helix tubes. By choosing appropriate subsets from a common pool of 15 distinct SST species (Fig. A.9), we have engineered monodisperse tubes of 6 different circumferences: 4-, 5-, 6-, 7-, 8-, and 10-helix tubes. The generality of this strategy is further confirmed by the successful engineering of mono-disperse 20-helix tubes. The secondary structures of these tubes are presented in Fig. A.8. Their 3D illustrations are summarized in Fig. 2.3A (right) and detailed in Fig. A.10. In each case, AFM imaging reveals the formation of long tubes (Fig. 2.4A) and AFM width measurement of randomly selected, opened tubes confirms the expected circumference monodispersity (Fig. 2.4A, insets, AFM images. Fig. 2.4B, summary. See Fig. A.13 for details). The length of SST tubes is investigated using fluorescence microscopy (Fig. 2.4C). For 7-helix tubes, the average length is

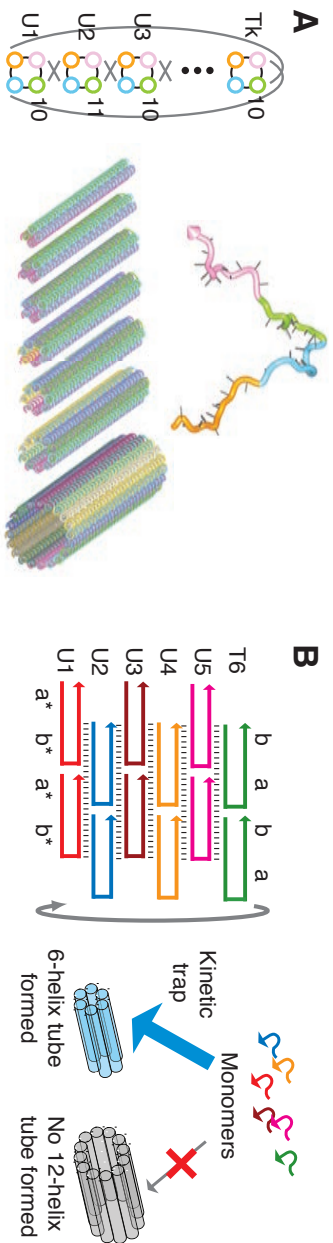


Figure 2.3: Monodisperse DNA tubes with programmed circumferences. **(A)** Molecular program (left) and 3D illustrations (right) for assembling k -helix tubes. **(B)** Secondary structure (left) and putative kinetic trapping (right) for 6-helix tubes. Asterisks denote complementarity.

$\sim 6 \mu\text{m}$, with some tubes reaching $\sim 20 \mu\text{m}$.

Thermal formation and melting profiles of SST tubes (Fig. 2.4D) and SST ribbons (Fig. A.15) reveal hysteresis. Such hysteresis has also been observed in DNA lattices formed from multi-stranded tiles [BRW05, SW07]. It is also worth noting that the annealing/melting curves of SST tubes and ribbons demonstrate only one sharp transition temperature. This is consistent with the expectation that single-stranded DNA oligonucleotides are directly assembled into the growing lattice during annealing and disassembled from the lattice during melting. In contrast, two or more characteristic transition temperatures are commonly observed in multi-stranded rigid tile based lattices [BRW05, SW07]: the lowest temperature corresponds to lattice formation/melting, and the others correspond to tile formation/melting.

We suggest that the structural flexibility of SST may contribute to the success of the putative kinetic trapping of monodisperse tubes. The long sticky ends of SST and the flexible inter-helix single-stranded linkage points in the assembled lattice may facilitate fast cyclization and hence trapping of the tubes with the smallest compatible number of helices. Additionally, it is conceivable that in a nucleation-elongation model [SW07] (see Fig. A.16 for a hypothetical assembly pathway), the nucleation barrier difference between the k -helix tube and the $2k$ -helix tube may help trap the system into monodisperse k -helix tubes. The observed hysteresis (Fig. 2.4D) suggests the existence of a significant kinetic barrier during tube formation and it is conceivable that this kinetic barrier is due to the presence of a nucleation barrier. It would be interesting to experimentally elucidate the kinetic assembly pathways of SST tubes. It would also be interesting to test if a similar kinetic strategy can be applied to programming the circumferences of DNA tubes assembled from multi-stranded rigid DNA tiles [YPF⁺03, MHM⁺04, LPRL04, RENP⁺04, RSB⁺05, LCH⁺06, KLZY06].

2.3. Concluding remarks and outlook

The ribbon/tube systems constructed here are likely to find applications ranging from biophysics, to electronics, and to nanotechnology. In biophysics, the programmable dimensions of the ribbons/tubes and hence their programmable physical properties, e.g. persistence length, make them attractive synthetic model systems. In electronics, metallization of DNA nanotubes [YPF⁺03, LPRL04, PBL⁺05] may result in nanowires with controlled diameters, and hence controlled electronic properties. In nanotechnology, DNA

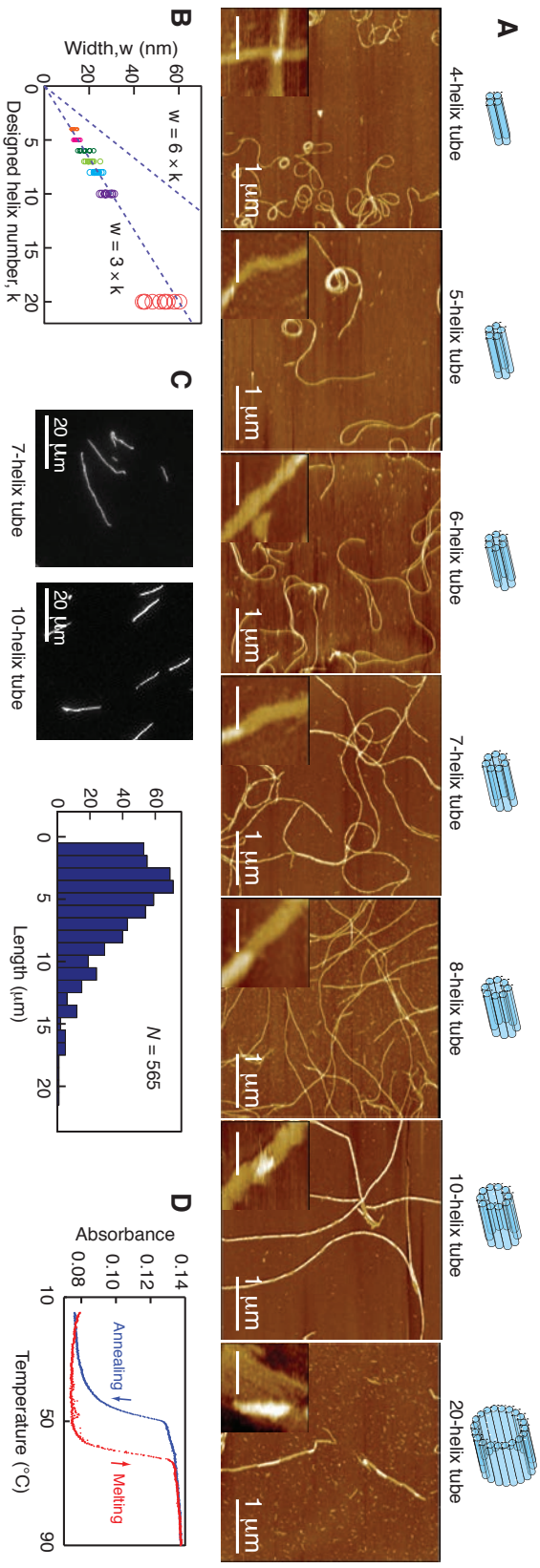


Figure 2.4.: (A) AFM images of 4-, 5-, 6-, 7-, 8-, 10-, and 20-helix tubes. See Fig. A.11 for larger AFM images. (B) Width plot of opened tubes. A k -helix opened tube is expected to have a width $w \approx 3 \times k$ nm, as determined by the width measurement of the k -helix ribbons (Fig. A.6). A $2 \times k$ -helix opened tube, by contrast, is expected to have $w \approx 6 \times k$ nm. Dashed lines corresponding to $w = 3 \times k$ and $w = 6 \times k$ are plotted to facilitate tube circumference monodispersity determination. See Fig. A.13 for a larger picture. (C) Left, fluorescence microscopy images of 7- and 10-helix tubes decorated with Cy3 fluorophores. Right, length profile of 7-helix tubes (sample size $N = 565$). See Fig. 14 for larger images and more profiles. (D) Annealing (blue) and melting (red) curves of 4-helix tubes. Each constituent DNA strand at 100 nM. Cooling/heating rate at 0.15°C per minute. See Fig. A.15 for more thermal profiles.

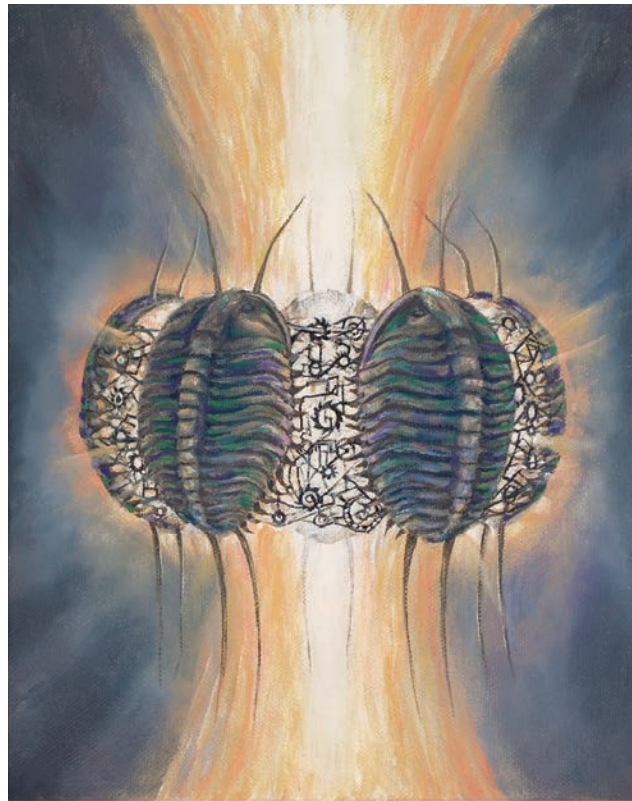
nanotubes with programmable geometrical and mechanical properties can be used as building blocks for more sophisticated architectures and devices (e.g. tracks for molecular motors [PTS⁺06, YCCP08, BT07]) and as templates for organization of functional groups [YPF⁺03, LLRY06].

2.4. Acknowledgements

The authors would like to thank Prof. Erik Winfree at Caltech for generously hosting the majority part of this work in his lab. For inspiring discussions, the authors would like to thank Erik Winfree, Paul W. K. Rothemund, Rebecca Schulman, Victor A. Beck, Jeffrey R. Vieregg, Robert D. Barish, Bernard Yurke, David Y. Zhang, Niles A. Pierce, Shogo Hamada, Marc Bockrath, Hareem Tariq, Y. Huang, Colby R. Calvert, Nadine L. Dabby, and Jongmin Kim. The authors are also grateful to Prof. Niles A. Pierce at Caltech and Prof. Jie Liu at Duke for facility support, to the Pierce group for the use of the unpublished DNA sequence design component and DNA structure illustration component of the NUPACK server (www.nupack.org), and to Bethany Walters for technical assistance. The fluorescence microscope was built by Rizal Hariadi and Bernard Yurke. There is a patent pending on this work. This work is supported by the Center for Biological Circuit Design at Caltech, NSF grants CCF-0523555 and CCF-0432038 to John H. Reif, NSF grant CBET-0508284 to Thomas H. LaBean, NSF grants 0622254 and 0432193 to Erik Winfree, NSF grant 0506468 to Niles A. Pierce.

3

Elongational-flow-induced scission of DNA nanotubes



Compression (Ann Erpino)
www.annerpino.com

Abstract

The length distributions of polymer fragments subjected to an elongational-flow-induced scission are profoundly affected by the fluid flow and the polymer bond strengths. In this paper, laminar elongational flow was used to induce chain scission of a series of circumference-programmed DNA nanotubes. The DNA nanotubes served as a model system for semi-flexible polymers with tunable bond strength and crosssectional geometry. The expected length distribution of fragmented DNA nanotubes was calculated from first principles, by modeling the interplay between continuum hydrodynamic elongational flow and the molecular forces required to overstretch multiple DNA double-helices. Our model has no free parameters; the only inferred parameter is obtained from DNA mechanics literature, namely the critical tension required to break a DNA duplex into two single-stranded DNA strands via the overstretching B-S DNA transition. The nanotube fragments were assayed with fluorescence microscopy at the single-molecule level and their lengths are in agreement with the scission theory.

3.1. Introduction

Elongational-flow-induced scission can break a long polymer into fragments with controlled size and is an important physical technique in genome sequencing and biopolymer science [BZK⁺04]. Elongational-flow-induced scission of genomic DNA into controlled narrow distribution of short fragments, but with random break points, is a critical preparatory technique for producing unbiased DNA libraries in shotgun genome sequencing [OHSC⁺96, THSOD98, Qua03]. The fluid-flow-induced mechanical shearing of prion fibrils is routinely used in prion studies to replicate structural conformation of the determinant nuclei by generating new polymerizing ends [SCK⁺00, CDVW04].

Polymer scission in a strong elongational flow occurs because of the interplay between macro-scale hydrodynamic flows and atomic-scale intramolecular interactions of the poly-

This manuscript is published as:

Rizal F. Hariadi and Bernard Yurke
Extensional-flow-induced scission of DNA nanotubes in laminar flow.
Physical Review E, 2010, 82, 046307

Author contributions:

Bernard Yurke and I conceived the idea and prepared the first draft of the paper. I carried out the experiment, analyzed the data and wrote the first draft of this manuscript.

mer [HM84]. Substantial effort has been made toward understanding polymer scission, including elucidation of the scaling relations between key physical parameters [BD72, Dan78, OK86, NK92, OT94, THSOD98, VCS06, LYZ⁺06] and measurement of the polymer bond strength based on the fragment distributions. Recently, Vanapalli *et al.* reconciled the scaling discrepancies between theory and scission experiments and showed the significance of turbulent flow in polymer scission data [VCS06].

Despite the amenability of laminar flow in the vicinity of a rigid rod to rigorous theoretical investigation, there have been no systematic studies of the scission of rigid polymers in the absence of turbulence. First, because of the weak elongational flow in the laminar regime, only long polymers on the order of a micron in length can accumulate enough tension for polymer scission to occur. Due to this requirement, polymer scission in laminar flow is considered “extraordinarily difficult” to achieve [VCS06]. In our investigation, this long contour length challenge was satisfied by using long DNA nanotubes. This structure self-assembles cooperatively from individual 5–15 nm size components through a nucleation and condensation mechanism [YHS⁺08, SW07, OK62] that yields long tubular structures on the order of 5 μm . The second ramification from the weak induced tension in laminar flow is that for polymer scission to occur, the molecular forces between polymer subunits must be weak enough to be broken apart by the weak flow. In contrast to the polymer samples in previous scission studies, DNA nanotubes are held together by non-covalent interactions between their subunits. These two properties of DNA nanotubes, namely, long contour length and weak non-covalent intramolecular interactions, enable us to rigorously investigate polymer scission in laminar flow.

Here we report the scission of circumference-programmed DNA nanotubes in a purely laminar flow device. Scission is achieved when the tension along a DNA nanotube becomes sufficient to break the non-covalent base-pair interactions holding the structure together. In our DNA nanotube construct, breakage is expected when the tension along individual duplex DNA strands is sufficient to induce a B-S transition from the B form of the double helix to the S form of the DNA overstretched state [SCB96]. In a duplex DNA with two opposite nicks, the overstretching transition disrupts base pairings along the entire length of duplex DNA and allows the two strands to slide past each other until duplex DNA is completely melted into two free single-stranded DNAs. To generate quantifiable fluid flows with sufficient elongation rates, a syringe pump-driven microfluidic device was employed. The DNA nanotube fragment size distribution was quantified using single-molecule fluorescence microscopy. We derived a model without free parameters and validated the model

predictions using the experimental data over nearly a decade of elongational flow rates and for DNA nanotubes having three different tube circumferences and bond strengths.

3.2. Methods

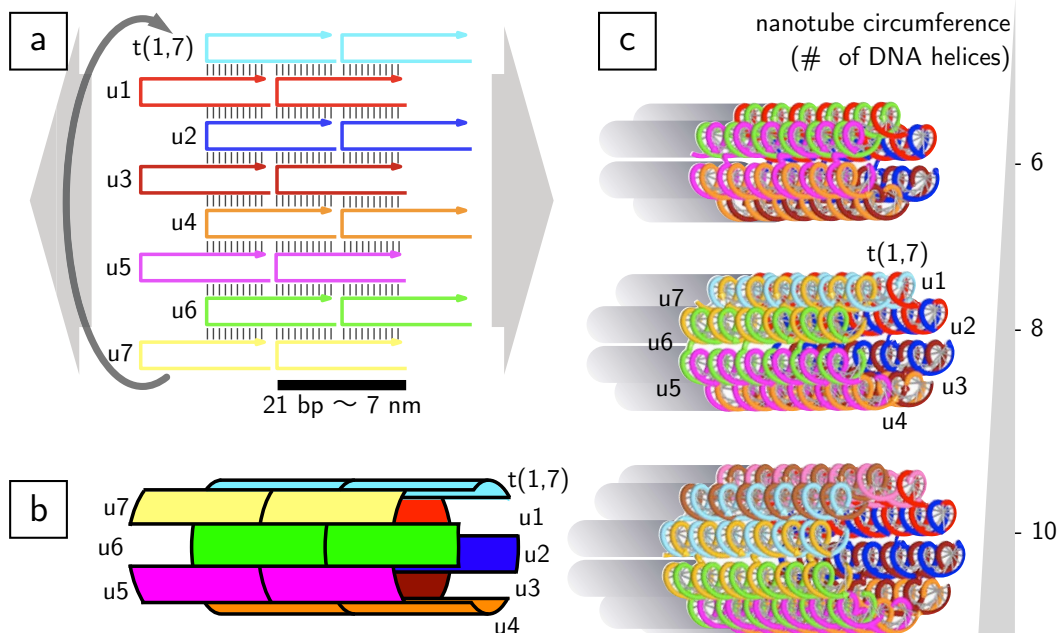


Figure 3.1.: (Color) An 8-helix nanotube is chosen to illustrate the modular construct of the DNA nanotube system used in this experiment adapted from [YHS⁺08]. (a) Complementarity graph of the 8-helix DNA nanotube. Each tile has four binding domains; each domain has a unique complement in its adjacent tile. The interaction between complementary domains drives the assembly into the designed order. (b) Each $t(1,n-1)$ strand concatenates two $u1$ and two $u(n-1)$ strands, and, thus wraps the two-dimensional crystalline structure into an n -helix nanotube. The same strategy has been demonstrated to successfully produce DNA nanotubes up to 20 duplex helices in circumference [YHS⁺08]. (c) Putative structures of 6-, 8-, and 10-helix nanotubes.

The DNA nanotubes used in this experiment are composed of recently devised “single-stranded-tile” structures [YHS⁺08]. These nanotube constructs are self-assembled structures that are rationally designed by encoding information in the sequence of DNA subunits using the techniques of structural DNA nanotechnology [WLWS98, RENP⁺04, RPW04, APS08]. Single-stranded tile-based DNA nanotubes [YHS⁺08] represent a new variant of one-dimensional crystalline DNA nanostructures, as they are homogeneous in their circumferences. Current common model systems for semi-flexible biopolymers, such as micro-

tubules [WC93] and earlier DNA nanotube motifs [RENP⁺04,ENAF04], suffer from a circumference heterogeneity. Single-stranded tile-based DNA nanotubes can potentially serve as a controlled model system for semi-flexible polymer physics, due to their monodispersity and amenable physical properties, namely circumference, bond strength, and persistence length.

In the single-stranded-tile construct, each 42-base DNA subunit binds to four of its neighbors with non-covalent base-pair interactions [Fig. 3.1(a)]. Monodisperse n -helix nanotubes consist of n unique DNA single-stranded subunits that self-assemble according to the complementarity graph shown in Fig. 3.1(a). Remarkably, the collective interaction between flexible single-stranded DNA subunits during lattice formation yields a tubular structure with uniform circumference and long contour length on the order of $5 \mu\text{m}$ [YHS⁺08]. The DNA base sequence, cross-over points [FS93], and location of nicks have translational symmetries along the longitudinal axis with periodicity of 21 base pairs ($\sim 7 \text{ nm}$). The rupture is expected to occur when the drag force is sufficient to break a ring of n -DNA binding domains along the angular axis of the n -helix nanotube.

The persistence lengths of our DNA nanotubes were calculated to be on the order of $10 \mu\text{m}$, based on the model described in references [RENP⁺04,BCTH00]. This considerable rigidity to nanotube bending is likely to arise collectively from the electrostatic repulsion of charges and the steric interaction of chemical groups along a single DNA helix and between multiple parallel DNA helices. The single-stranded tile-based DNA nanotubes have persistence lengths that are three orders of magnitude longer than the persistence length of their single-stranded DNA subunits (that is, less than 5 nm [TPSW97]). More importantly, these persistence lengths are longer than their average nanotube lengths, that is, on the order of $5 \mu\text{m}$. Note also that in a different DNA nanotube construct [RENP⁺04], the mean and variance of nanotube length have been observed to increase over time, due to end-to-end joining [ENAF04]. In hydrodynamic flow analysis, the substantial persistence length allows the treatment of the DNA nanotubes as rigid rods and allows us to neglect polymer vibrations.

The DNA nanotubes were prepared by mixing an equimolar subunit concentration ($\leq 3 \mu\text{M}$) of n -programmed single-stranded DNA subunits (IDT DNA) in $1\times$ TAE [40 mM Tris-acetate and 1 mM EDTA(Ethylenediaminetetraacetic acid)] with 12.5 mM Mg-acetate.4H₂O and then slowly annealing from 90°C to room temperature over the course of a day in a styrofoam box. For fluorescence imaging, a Cy3 fluorophore is covalently linked into the 5' end of the single-stranded DNA subunit $u1$ [see Fig 1(a)], which corresponds to

one fluorophore every ~ 7 nm along the DNA nanotube.

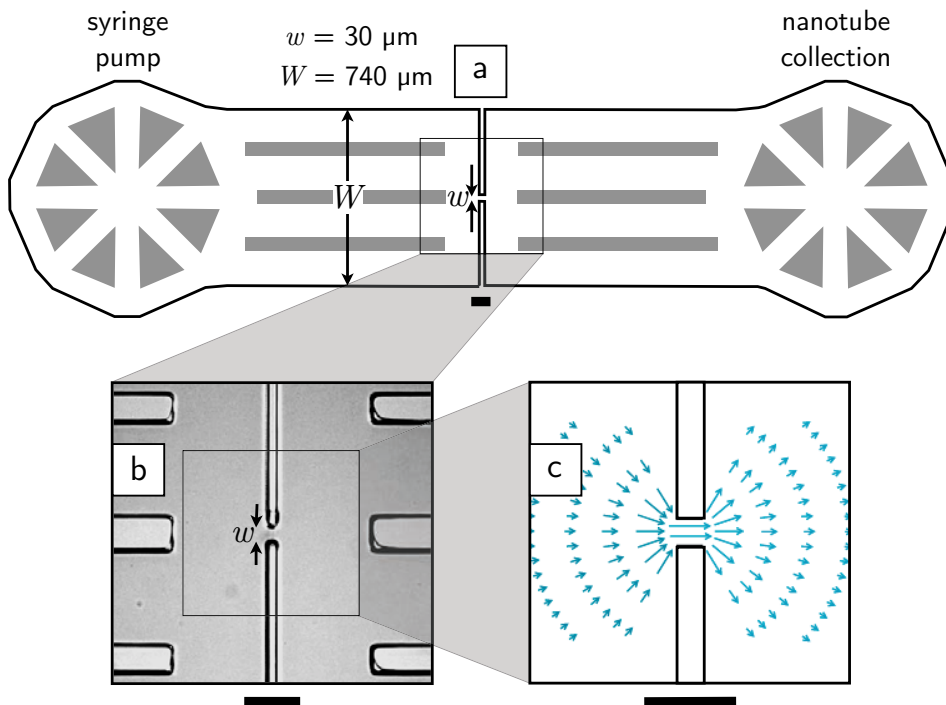


Figure 3.2.: (Color) (a) Schematic of the microfluidic chip used in the scission experiment. The nanotube sample was supplied via a syringe pump and collected in a vial before deposition on a microscope slide. (b) Light microscopy image of the microfluidic chamber used to produce the laminar elongational flow field. (c) Schematic of the putative streak lines of flow around the orifice. All scale bars are $100 \mu\text{m}$.

The Polydimethylsiloxane (PDMS) microfluidic device [DMSW98, UCT⁺00] produces high elongational flow at the transition volume between a wide channel and a small orifice (Fig. 3.2). The width of the wide channel W is $740 \mu\text{m}$ and the orifice has a rectangular cross-section with a width w of $30 \mu\text{m}$. We estimate that the width of the orifice is larger than the length of 84% of the DNA nanotubes in the test tube. The channel height h is $20 \mu\text{m}$ throughout the microfluidic chip.

Near the orifice, the flow is a laminar elongational flow [Fig. 3.2(c)]. At the microfluidic device entrance [labeled “syringe pump” in Fig. 2(a)], a capillary tube feeds the DNA nanotubes into the flow channel. In this region, the nanotubes are subjected to a much weaker elongational flow than in the area close to the orifice. This weak elongational flow is useful for pre-conditioning DNA nanotubes into a stretched conformation before entering the zone with high elongational flow. A control experiment involving a microfluidic chip without an

orifice shows no detectable difference between the length distributions before (in the test tube) and after being subjected to the control microfluidic device. The large rectangular and triangular posts [gray-shaded regions in Fig. 3.2(a)], were required to prevent chamber deformation due to the elastomeric nature of PDMS and the relatively high pressures used in the scission experiments. Based on the comparison between dimensions of our device and the initial distribution of the DNA nanotubes, we claim that the presence of the posts does not perturb the flow pattern in the vicinity of the orifice where the scission occurs.

The upper bound on the range of flow rates investigated is given by the maximum rate at which the syringe pump can inject fluid into the microfluidic device without resulting in noticeable deformation and mechanical failure of the device. The minimum flow rate required to break a substantial fraction of the DNA nanotubes sets the lower limit on the range of flow rates used in the reported experiments.

3.3. Results and Discussions

In a scission experiment, a dilute DNA nanotube solution at ~ 1 nM initial tile concentration was injected into the microfluidic device at rates in the range 0.500–4.00 *mL/hr* using an automatic syringe pump. We found that the syringe pump is a better injection method than pressurized gas because of the absence of initial dead volume that slows down the initial volumetric flow rate. Each nanotube was passed into the microfluidic chamber only once. The first 50 μL sample was discarded to avoid any contamination from the previous run and to make sure that the volumetric rate was constant during the scission of the collected sample. Without stopping the syringe pump, the next 20 μL sample of fragmented DNA nanotubes was collected at the outlet port in a 500 μL vial. A 5 μL drop of this DNA solution was deposited between an RCA cleaned [BHKQ03] microscope slide and a coverslip and placed on the microscope sample stage. The presence of divalent cations in the buffer facilitates the formation of salt bridges between the two negatively charged species, namely the DNA fragments and the glass surface. Once the DNA nanotubes were immobilized on the glass coverslip, any further reaction, such as end-to-end joining, spontaneous scission [ENAF04, RENP⁺04], and polymerization, are quenched. Thus, the images are the record of the fragment distribution immediately after being subjected to the elongational flow.

The nanotube fragment distribution was imaged with a home-built Total Internal Reflection Fluorescence (TIRF) microscope as previously described in [YHS⁺08] and quantified at the single-molecule level with ImageJ (available at <http://rsbweb.nih.gov/ij/>). The

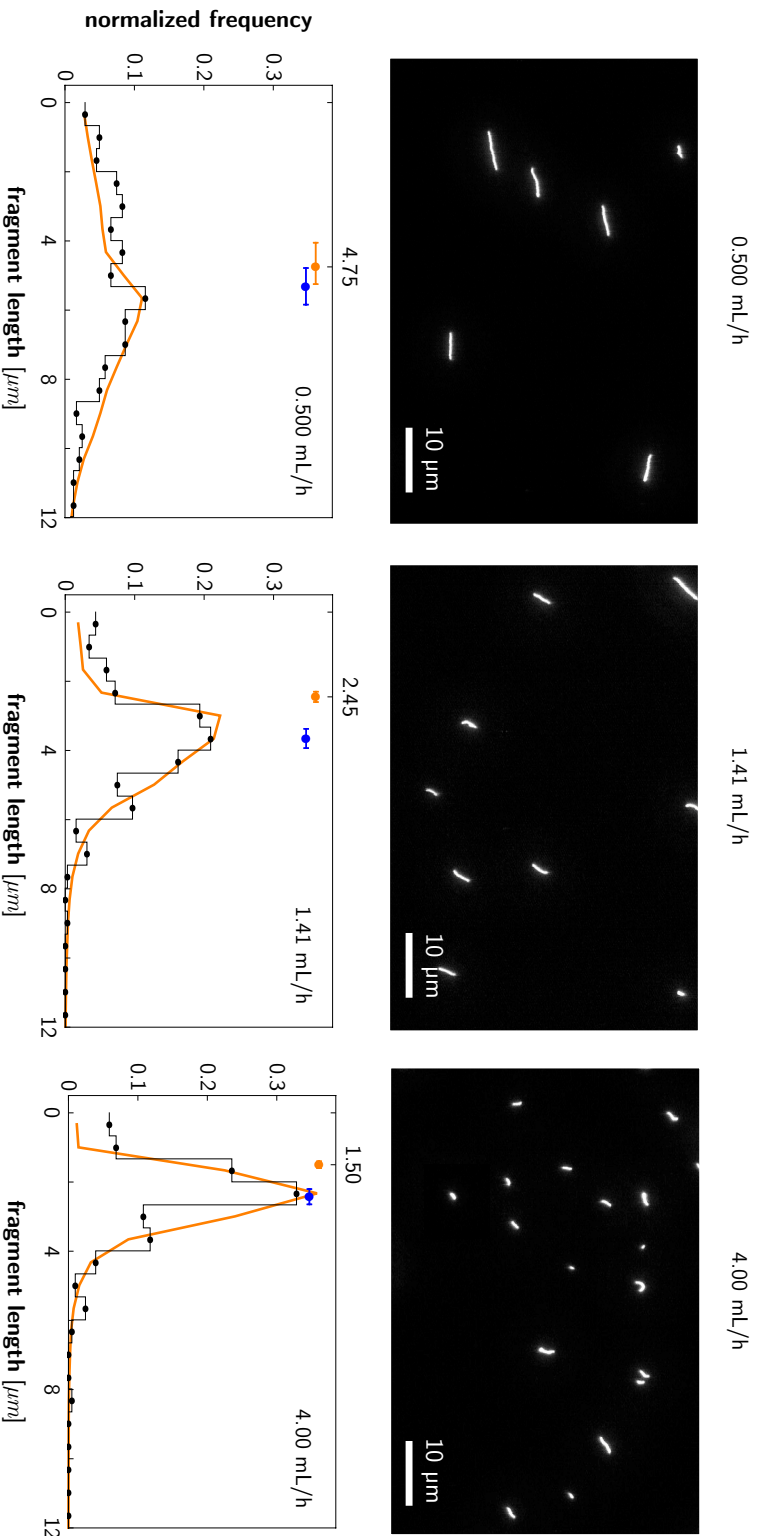


Figure 3.3.: (Color) Light microscopy images and fragment length histogram of 8-helix nanotubes after being subjected to volumetric flow rates at 0.500 mL/hr, 1.41 mL/hr, and 4.00 mL/hr. The mean fragment length and Bayesian fit results are summarized in Table I. The orange solid line is the best Bayesian fit of the experimental data. The blue and orange dots with error bars are the average fragment length and most probable inferred L_{crit} , respectively.

number of photons emitted by a DNA nanotube was used as a proxy for nanotube length. In each frame, the longest nanotube whose length could be easily measured provided a calibration for this proxy. This technique is insensitive to the curvature of DNA tubes and how focused each fragment image is. Moreover, the photon-counting method allows for the determination of nanotube lengths even for fragments that are not optically resolved. The single-molecule assay enables us to exclude experimental artifacts resulting from the rare occurrence of high mass nanotube aggregates which were visually identified and not counted. Nanotube aggregation is expected to behave differently in elongational flow, leading to different fragment size distributions than for pristine DNA nanotubes. All features whose maximum pixel intensities were above the saturation level of the camera were excluded from the length measurement.

In Fig. 3.3 (top row), we show snapshots of 8-helix nanotube fragments imaged immediately after a scission experiment at 0.500 mL/hr, 1.41 mL/hr, and 4.00 mL/hr volumetric flow rates \dot{V} . The Reynold's number Re for the fluid flow within the orifice, at the fastest volumetric flow rates used, was calculated to be 25, which is safely within the laminar regime ($Re < 2000$). Elsewhere in the system, the fluid velocities and the corresponding Re are smaller. The light microscopy images and the corresponding length histograms show the dependence of fragment size on volumetric flow rate. Faster flow rates generate higher elongational rates and shorter fragment size (Fig 3.3). The same experiment was repeated with DNA nanotubes having different circumferences and corresponding bond strengths, namely the 6- and 10-helix nanotubes, and the same trend was consistently observed in all nanotubes (see Table I, Figs 3.4, B.2, and B.3).

Elongational flow induces the alignment of DNA nanotubes along the flow gradient. According to the scission theory presented in Appendix A, the drag force experienced by the nanotubes induces tension along the axis of the DNA nanotubes. This tension is greatest at the midpoint of DNA nanotubes [LPSC97], and when it exceeds the tensile strength of the nanotube, the tube fragments into two shorter tubes of approximately equal length. In our microfluidic device, the elongational rate is proportional to the reciprocal of the square of the distance to the orifice $1/\rho^2$ (Eq. B.13). Hence, after encountering an elongation flow regime sufficient to break the nanotube in two, the fragments may encounter a flow regime which is sufficient to break each newly generated fragment again into two shorter fragments of approximately equal length. This process of scission will continue until the length of the individual fragment is such that the tensions exerted in the region of highest elongational flow is insufficient to result in chain scission. In our model,

volumetric flow rate (mL/hr)	6-helix nanotube		8-helix nanotube		10-helix nanotube				
	L_{crit} (μm)	Mean (μm)	L_{crit} (μm)	Mean (μm)	L_{crit} (μm)	Mean (μm)			
$\sqrt{2}^{-2} = 0.500$	3.95	[3.65, 4.50]	4.40 \pm 0.22	4.75	[4.05, 5.25]	5.31 \pm 0.48	4.85	[4.25, 5.25]	5.87 \pm 0.22
$\sqrt{2}^{-1} \approx 0.707$	3.00	[2.80, 3.25]	4.19 \pm 0.43	3.95	[3.60, 4.15]	5.35 \pm 0.53	4.20	[3.90, 4.95]	5.47 \pm 0.51
$\sqrt{2}^0 = 1.00$	2.70	[2.45, 2.85]	3.91 \pm 0.38	2.80	[2.65, 2.95]	4.10 \pm 0.48	3.70	[3.45, 3.95]	5.10 \pm 0.46
$\sqrt{2}^1 \approx 1.41$	2.10	[1.95, 2.20]	3.13 \pm 0.34	2.45	[2.30, 2.60]	3.65 \pm 0.37	2.70	[2.50, 2.85]	4.04 \pm 0.43
$\sqrt{2}^2 = 2.00$	1.80	[1.70, 2.05]	3.06 \pm 0.28	2.15	[1.90, 2.25]	3.18 \pm 0.28	2.20	[2.05, 2.30]	3.58 \pm 0.34
$\sqrt{2}^3 \approx 2.83$	1.50	[1.40, 1.60]	2.51 \pm 0.27	1.80	[1.65, 1.95]	2.90 \pm 0.28	1.75	[1.65, 1.90]	2.95 \pm 0.30
$\sqrt{2}^4 = 4.00$	1.35	[1.25, 1.45]	2.29 \pm 0.22	1.50	[1.40, 1.60]	2.43 \pm 0.26	1.65	[1.55, 1.75]	2.71 \pm 0.25
control (device without the orifice)	—	—	5.70 \pm 0.45	—	—	6.32 \pm 0.31	—	—	6.03 \pm 0.29

Table 3.1.: The most probable L_{crit} and mean fragment length for 6-, 8-, and 10-helix nanotubes after scission at flow rate chosen to be powers of $\sqrt{2}$ in mL/hr . For L_{crit} , the first number is the most probable value, the second and third entries are the lower and upper bounds of the 90% confidence interval. The mean is the mean fragment length of the sample. The uncertainty of the mean length is the standard deviation as determined by a bootstrapping technique.

$2L_{crit}$ is defined as the length of the shortest DNA nanotube that can be broken in two in the region of the highest elongational flow $\dot{\epsilon}_{max}$. Therefore, L_{crit} is the length of the shortest DNA nanotube that can be produced by each elongational-flow-induced scission in our device at a particular volumetric flow rate. For a tube i of length L_i , the number of scission rounds is given by $m_i = \lfloor \ln(L_i/L_{crit_i}) / \ln(2) \rfloor$, where the brackets denote rounding down to the nearest integer (Appendix B.2). In our model, an initial tube i of length L_i yields 2^{m_i} output fragments that have identical length of $L_i/(2^{m_i})$.

We employed stochastic scissions simulation and Bayesian inference (Appendix B.2) to extract L_{crit} from each fragment histogram data \mathcal{H} . The mean fragment length is not a valid estimate for L_{crit} because the mean of the fragment length distribution is affected by the DNA nanotube distribution before being subjected to the elongational flow. The Bayesian inference has to include the stochasticity of the scission events in our device. The elongational flow in the device and the flux of the DNA nanotube are not uniform, but are functions of position (x_i, y_i) of DNA nanotube i within the channel. In particular, they will be zero at the channel walls and maximum at the center of the channel. Hence, even if we start with a population of DNA nanotubes that is monodisperse in size, the length of the DNA nanotube fragments produced will be different at different points within the orifice.

The results of the Bayesian inference of L_{crit} are presented in Figs. 3.3–3.4, Table I, and Appendix B.3. Table I lists the most probable L_{crit} , its 90% probability interval, and the mean DNA nanotube length for 6-, 8-, and 10-helix nanotubes for various fluid flow rates. In Fig. 3.3 and also in Fig. B.2 of Appendix B.3, the orange circle represents the most probable L_{crit} and the orange error bar is the range where the *a posteriori* probability is over 90%. For comparison, the mean fragment lengths and their uncertainties are indicated in blue. As expected, the difference between fragment mean and L_{crit} is less significant when L_{crit} approaches the initial fragment mean [Fig 3.3 (left panel)], because in that regime the elongational flow breaks only an insignificant portion of the initial nanotubes. The Bayesian inference performs poorly when L_{crit} approaches the mean of control nanotube distribution, as illustrated by the wider 90% confidence bands in Table I and longer error bar in Fig. 3.3 (and also in Fig. B.2 of Appendix B.3) for the slowest volumetric flow rate. The Bayesian inferred L_{crit} of the slowest volumetric flow rate experiment might be still very good, but the data does not warrant strong conclusion.

The most probable inferred L_{crit} is plotted against the volumetric flow rate in Fig. 3.4. For comparison, the no-free-parameter theoretical prediction of Eq. (B.15) using $f_c = 65$

pN is shown as a dashed line in the figures, where f_c is the critical tension required to overstretch a single DNA double helix [SCB96, MKB⁺07]. The theoretical line has a slope of -0.5 in these double logarithmic plots, indicating that L_{crit} scales as the square root of the flow rate. Linear fitting of the Bayesian inferred L_{crit} with respect to volumetric flow rate yields the slope to be -0.52 ± 0.06 , -0.55 ± 0.07 , and -0.57 ± 0.07 for 6-, 8-, and 10-helix nanotubes, respectively. In all measured nanotubes, the theoretical exponent is within the 90% confidence interval of our linear fit, giving us confidence in the -0.5 theoretical scaling of L_{crit} with the volumetric flow rate or with the elongational rate. The $L_{crit}/2R$ term in Eq. (B.15) is on the order of 10^2 and its natural log was treated as constant and absorbed by the fitted slope in the linear fit for each DNA nanotube circumference.

Having established confidence in the scaling based scission theory, we use Eq. (B.15) in a separate Bayesian inference to obtain an experimental value of the tension required to simultaneously break n parallel DNA helices $T_{crit} = n \times f_c$ (Eq. B.11). In this Bayesian inference, the fit takes into account the probability $Pr(L_{crit}|\mathcal{H})$ at various volumetric flow rates. Separate inference analysis of each nanotube yields 330 pN, 488 pN, and 590 pN as the most probable bond strength of 6-, 8-, and 10-helix nanotubes. The 90% confidence bands span across 282 pN to 468 pN, 376 pN to 544 pN, 500 pN to 740 pN, for 6-, 8-, and 10-helix nanotubes, respectively. In Fig. 3.5, the linear trend of the inferred T_{crit} as a function of the number of DNA double helices in the tube circumference is in agreement with Eq. B.11.

Finally, to extract an experimental f_c , we perform a Bayesian inference on all the data, imposing the -0.5 scaling relation between L_{crit} and flow rate and the linear scaling of T_{crit} with n . The most probable f_c was inferred to be 58 pN, with a 90% confidence band spanning across 47 pN to 76 pN. Our measurement is consistent with the reported 45 - 65 pN as the applied tension when overstretch transition occurs in various experimental conditions, namely ionic concentration and temperature [SCB96, MKB⁺07]. All of our scission experiments were performed at room temperature. The striking agreement further validates our scission model and its assumption that all the DNA helices contribute to the total bond strength cooperatively as assumed in our model. The measured critical tension is consistent with the notion that the elongational-flow-induced tension breaks the non-covalent interactions, and the DNA nanotube scission occurs via a collective B-S transition from the B-form of double helices to the S-form of the overstretched state of DNAs at the breaking point. We note that the bond strength value for breaking a covalent phosphodiester bond in the DNA backbone was measured and calculated to be of the order

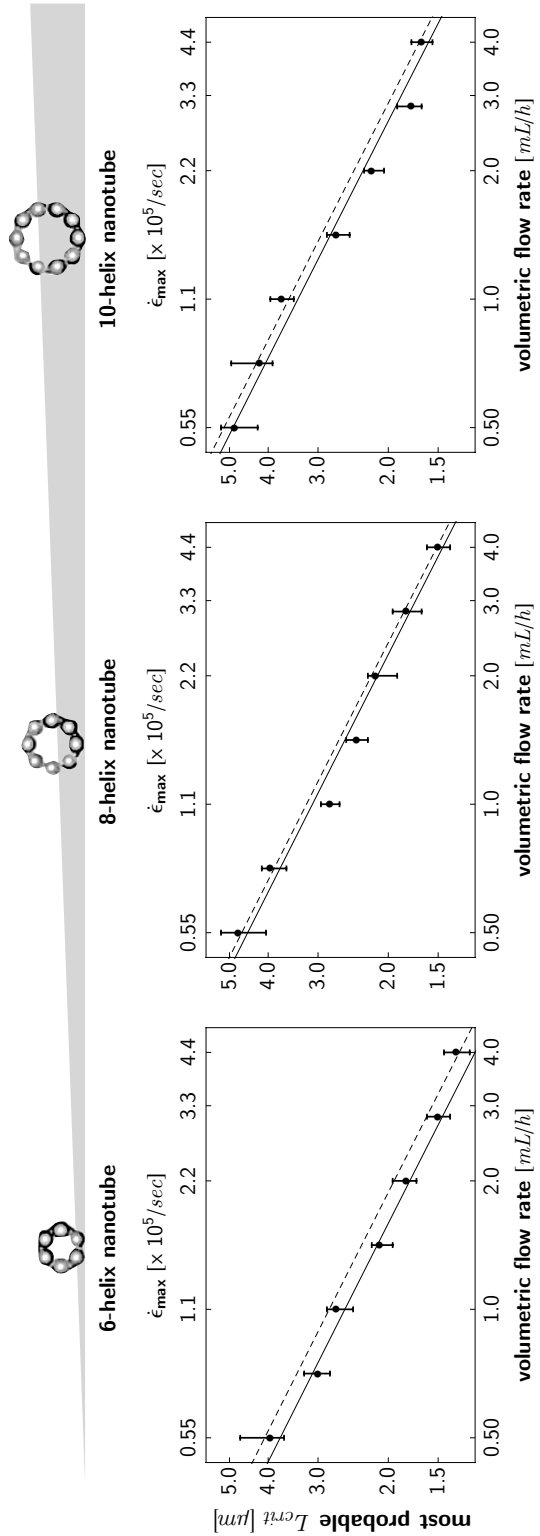


Figure 3.4.: Fragment length as a function of volumetric flow rate of 6-, 8-, and 10-helix nanotubes. The solid line corresponds to the most probable of L_{crit} from all data based on our theoretical model by Bayesian *a priori* probability. The dashed line is the theoretical curve with $f_c = 65$ pN [SCB96]. Note that for the same volumetric flow rate, the most probable L_{crit} (solid black circle) increases with larger nanotube circumference.

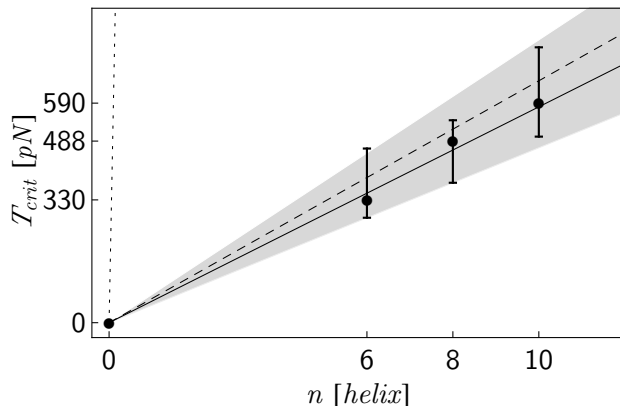


Figure 3.5.: Inferred T_{crit} as a function of nanotube circumference. The solid and dashed lines correspond to the most probable ($f_c = 58$ pN) and the literature value of the critical tension required B-S DNA overstretching transition ($f_c = 65$ pN) [SCB96], respectively. The linear fit was constrained to intersect the point of origin (0,0). The grey region represents the 90% confidence area for the linear fit that passes through the point of origin. The steep dotted line illustrates the critical strength of breaking covalent bonds in DNA backbones ($f_c = 2n \times 5860$ pN) [BSLS00, VCS06, LYZ⁺06], which has a much steeper slope than our experimental data.

of 5×10^3 pN [BSLS00, VCS06, LYZ⁺06], which is approximately two orders of magnitude larger than the measured f_c in this work (see Fig. 5).

That f_c should be the force required to overstretch DNA is based on the notion that passage through the region of high elongational flow is fast compared to the time scale which would allow the DNA tubes to break apart by slower, less energetic, relaxation mechanisms, such as those involving thermal fluctuations and base-pair breathing. In particular, the transit time of the DNA through the region of high elongational flow in our microfluidic device ranges from $7 \mu s$ to $60 \mu s$ for the fastest and slowest flow rates used in this experiment, respectively. These times are comparable to the $10 \mu s$ that it takes for a branch point to move by one base position in three-strand branch migration [RBHW77, PH94]. We note that the time scale involving rearrangement of a few bases is already comparable to the transit times of the high flow region.

It is conceivable that each midpoint scission event will produce two fragments that are not exactly equal in length. Based on our theory in Appendix A (Eq. B.10), the distribution of tension along the nanotube is approximately parabolic, being maximum at the midpoint and symmetrically dropping to zero at both ends. Thus, the applied tension reaches a plateau at the center of the fragment in which the scission could occur anywhere due to unmodeled physical sources of randomness, while still maintaining its midpoint as the most

probable location for scission.

In order to evaluate the effect of randomness in our experiment, we incorporated tunable truncated Gaussian noise into the previously presented Bayesian inference to account for other plausible sources of randomness that are unmodeled in our theory (see Appendix B.4). The tunable parameters in this new Bayesian fit are L_{crit} and the standard deviation of the truncated Gaussian noise σ_i relative to the nanotube length L_i . Excluding the slowest volumetric flow rate result, the most probable L_{crit} from Bayesian inference by *a posteriori* probability from the same model with various Gaussian noise added agrees with the most probable L_{crit} from inference with our simple scission theory within 5%. This insight leads us to conclude that the noise has to be implausibly large to make a noticeable difference in our inference and that the assumption of the absence of other plausible physical factors which could contribute to noise in the theoretical model and Bayesian inference is justified.

3.4. Concluding Remarks

In this paper, we presented the results of systematic experiments on the scission of DNA nanotubes with well-defined circumferences in a microfluidic device with a well-defined region of laminar elongational flow. This allowed us to rigorously test the scission theory involving no adjustable parameter, presented in Appendix B. We find that the theory accurately predicts DNA nanotube fragment size as a function of elongational rate and the number of circumferential helices of the tube. Since fragment size is a predictor of the maximum elongation rate encountered by a DNA nanotube, we suggest that DNA nanotubes can be used as microscopic probes to measure the maximum elongation rates encountered in fast, small-scale, or complex hydrodynamic flow fields (chapter ??).

3.5. Acknowledgments

We are indebted to Erik Winfree for his generous support throughout the period of the research. The authors would like to thank Erik Winfree, Rebecca Schulman, Peng Yin, Damien Woods, Victor A. Beck, Elisa Franco, Zahid Yaqoob, Karthik Sarma, Saurabh Vyawahare, Nadine Dabby, Tosan Omabegho, Jongmin Kim, Imran Malik, and Michael Solomon for valuable discussions. It is our great pleasure to acknowledge the support of the NASA Astrobiology NNG06GAOG, NSF DMS-0506468, NSF EMT-0622254, NSF NIRT-0608889, and the Caltech Center of Biological Circuit Design grants. This work was initiated by a serendipitous observation by Harry M. T. Choi and was inspired by

Rebecca Schulman's project on engineering DNA tile-based artificial life [SW05]. The DNA nanotubes used in this experiment and their three-dimensional illustrations were generous gifts from Peng Yin. The design and manufacturing process of the PDMS microfluidic chip were assisted by the Caltech Microfluidic Foundry.

4

Elongational rates in bursting bubbles measured using DNA nanotubes

■ Abstract

Flow induced scission of DNA nanotubes can be used to measure elongational rates in aqueous fluid flows [HY10]. Here we report the measurement of elongational rates generated in bursting films within aqueous bubble foams with this technique. Elongational rates as large as $\dot{\epsilon} = 3.2 \times 10^7 \text{ sec}^{-1}$ are generated by the bursting of bubbles with a 9.26 mm^3 volume.

4.1. Introduction

Bursting bubbles and films exhibit a rich variety of phenomena [BdRCS10, NN09, KNT⁺08, DdGBW98, MIKS07, SCM00, ESF97, LCC96, DMBW95] that often provide keys to understanding processes that occur in environmental, industrial, and laboratory settings.

This manuscript is submitted to a journal as:

Rizal F. Hariadi, Bernard Yurke, and Erik Winfree
Elongational rates in bursting bubbles measured using DNA nanotubes.
submitted

Author contributions:

Bernard Yurke conceived the idea. Bernard Yurke and I carried out the experiment, analyzed the data, and revised the manuscript. I assayed measured the fragment length distribution from TIRF microscopy images.

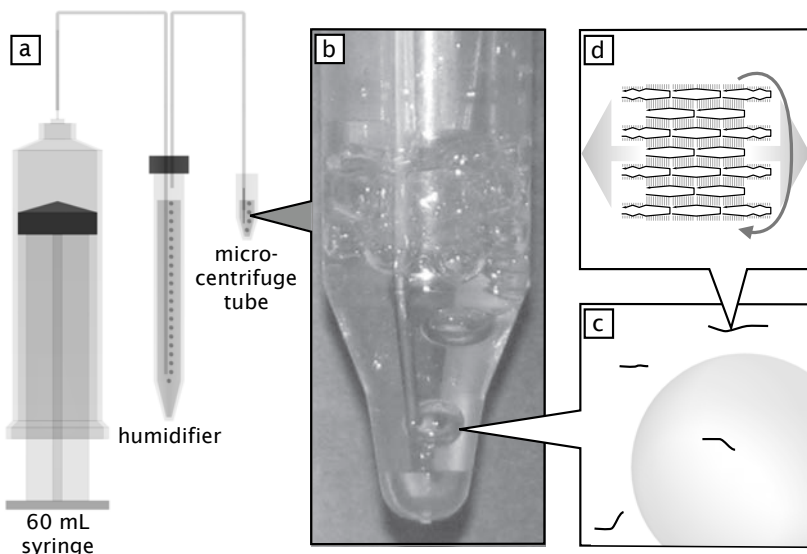


Figure 4.1.: (a) Schematic of apparatus. (b) Sample, housed in a microcentrifuge tube, to which air is being delivered. For scale, the outer diameter of the upper section of the microcentrifuge tube is 1.1 cm. (c) Bubbles and 7-helix nanotubes (not in scale) are in the solution. (d) Schematic of the 7-helix nanotube used in this experiment [YHS⁺08].

Bursting ocean bubbles, through production of sea spray and marine aerosol, significantly influence climate [RHF⁺10, Wu81]. Bursting bubbles also provide a means by which microorganisms become airborne [BPB77, BS70]. Many industrial and laboratory processes involve the flow of gas bubbles through liquid columns where bubble bursting can affect the process. For example, detrimental effects on cell lines by the gas bubbling of bioreactors have been attributed to hydrodynamically induced death of cells caught within the films of bursting bubbles [CH92]. Lastly, building on a suggestion by Oparin [Opa52], ocean bubble bursting may have played a role in abiogenesis by providing fluid flows of requisite strength to drive the fissioning of organic aggregates.

In previous work [HY10], we determined the relationship between the elongational rate of the fluid flow encountered by DNA nanotubes and the length of the fragments produced. This relationship allows the determination of elongational rates by measurement of tube fragment length. This novel probe of fluid flow is particularly well-suited for the study of small-scale flows of short duration and for situations where following tracer particles by high-speed photography is impractical.

Here we report the use of the 7-helix DNA nanotubes [YHS⁺08] to measure elongational flow rates within bursting bubbles in a bubble foam at the surface of an aqueous

buffer solution. DNA strands self-assemble into DNA nanotubes of well-defined diameter of ~ 7 nm and tube lengths that can exceed $20 \mu\text{m}$ in length. The tubes have a theoretical persistence length of $16 \mu\text{m}$ and, for the experiments reported here, can be regarded as rigid rods. The design and characterization of these nanotubes has been discussed by Yin *et al.* [YHS⁺08] and, apart from the oligomer T7, we have employed their published DNA sequences. The modified T7 strand (5'-GGAGGTGCAT-CATTCAAAGCT-TGGCTTAGCGT-CCTAATCGCC-3') was designed to reduce the twist energy in the 7-helix nanotube. Cy3 fluorophores were attached to the tubes for fluorescent imaging, as described in [YHS⁺08].

4.2. Materials and Methods

A stock solution of DNA nanotubes was prepared by mixing 7 DNA strands (ordered from Integrated DNA Technologies, Inc.) at equimolar concentration of $3.50 \mu\text{M}$ in a buffer consisting of $1\times$ TAE [40 mM Tris-acetate and 1 mM EDTA (Ethylenediaminetetraacetic acid)], pH 8.3 with 12.5 mM Mg-acetate and then slowly annealing from 90°C to room temperature over the course of a day in a styrofoam box. The nanotube stock solution was then diluted by a factor of 20 for the experiments.

A schematic of the apparatus used to flow air through the buffer solution containing DNA nanotubes is shown in Fig. 4.1(a). Air was supplied via a motorized syringe pump equipped with a 60 mL syringe. The air was delivered via polyethylene tubing, 0.58 mm ID (Inner Diameter), to a humidifier consisting of a 15 mL centrifuge tube filled to 13.5 mL with the buffer solution. Two stainless steel capillaries, passing through the cap and cemented with silicon aquarium sealant served as feedthroughs for air to and from the airtight humidifier chamber. To minimize sample evaporation, the air was bubbled through a 45 mL 9 cm column of buffer and delivered via the polyethylene tubing to the sample chamber. The bubbles were generated at the end of a stainless steel capillary, 0.635 mm OD (Outer Diameter) and 0.432 mm ID, connected to the end of the polyethylene tubing that was pointed downward into the sample fluid, Fig. 4.1 (b). To minimize the amount synthetic DNA used, the sample, typically consisting of $100 \mu\text{L}$ of fluid, was housed in a 2.0 mL microcentrifuge tube (Sorenson BioScience, Inc., West Salt Lake, Utah). The nose of the tube has a 4 mm ID and a depth of 6 mm. The tapered region flares out to a 1 cm ID.

Two air flow rates, 1.8 mL/min and 18 mL/min, were employed in the experiments. The ratio of the size of the bubbles produced at the faster flow rate to that of the slower flow rate was measured to be 1.74 via photographs taken of bubbles produced at the end of the

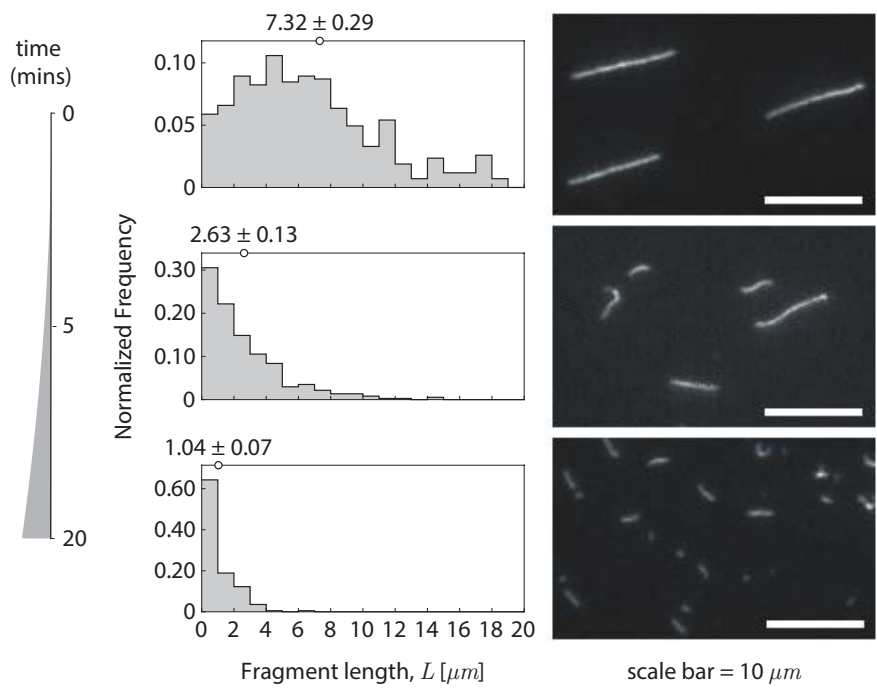


Figure 4.2.: (Right) Representative TIRF microscopy images of DNA nanotubes withdrawn from a sample with an initial volume of $100 \mu\text{L}$ after 0, 60, and 360 mL of air had passed through the sample at a flow rate of 18 mL/sec. (Left) The corresponding normalized fragment length L histograms constructed from measuring the tube lengths from such images. The mean tube length \bar{L} for each distribution is given at the top of each histogram in μm .

capillary when immersed in buffer in a flask with flat side walls. The height and width of the bubbles were measured and the volumes were computed under the assumption that the bubbles are oblate spheroids. By counting the number of bubbles produced from a known air volume, the volume of the bubbles produced at the slower flow rate (1.8 mL/min) was determined to be $V_b = 5.32 \text{ mm}^3$. From the ratio of the bubble volumes, the bubble volume at the faster flow rate (18 mL/min) is $V_b = 9.26 \text{ mm}^3$.

Following a procedure previously reported for the microscopy assay [YHS⁺08, HY10], a $1 \mu\text{L}$ volume of fluid was withdrawn and immediately diluted by a factor of 40 in buffer. A $5 \mu\text{L}$ volume of this diluted sample was then deposited between a cleaned [BHKQ03] microscope slide and coverslip and then imaged with a Total Internal Reflection Fluorescence (TIRF) microscope [YHS⁺08], and quantified as described in [HY10].

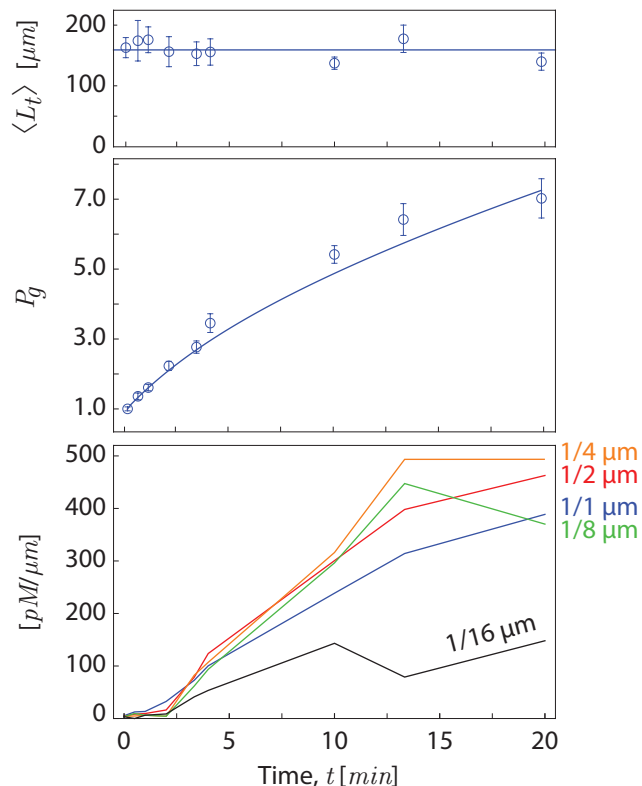


Figure 4.3.: DNA-nanotube fragmentation data plotted as a function of time at a flow rate of 18 mL/min. (top) Total tube length per microscope field of view. The horizontal line represents a constant total tube length of 159 μm per image. (middle) Plot of the population ratio P_g . (bottom) Plot of the number of tubes in the length range $0 < L < \Delta_{bin}$ for $\Delta_{bin} = 1, 1/2, 1/4, 1/8,$ and $1/16 \mu\text{m}$.

4.3. Results and Discussions

To follow the fragmentation of the DNA nanotubes by bubbling, an experiment, consisting of two runs, was performed in which air at a flow rate of 18 mL/min was bubbled through a 100 μL sample. In the first run, 1 μL volumes were drawn at time points when 0, 16, and 240 mL of air had passed through the sample V_a . In the second run, the data was acquired at $V_a = 0, 9, 18, 36, 72, 180,$ and 360 mL. Representative TIRF microscopy images taken from the second run samples and the corresponding length histograms are shown in Fig. 4.2. The data of both runs were treated as a homogenous set.

Under shearing, the sum of tube lengths L_t should remain conserved. This was tested by measuring the total tube length per image for the samples extracted during the run

at different time points. Fig. 4.3(top) shows that L_t remains constant as a function of the air volume that has passed through the sample V_a . Since $L_t = N\bar{L}$ where N is the total number of nanotubes and \bar{L} is the mean tube length, the constancy of L_t allows one to infer the population ratio $P_g = N/N_0$, where N_0 is the initial number of nanotubes, via $P_g = \bar{L}_0/\bar{L}$ where \bar{L}_0 is the initial mean tube length. P_g , inferred by this method, is plotted as a function of V_a in Fig. 4.3(middle). There is a sevenfold increase in the number of nanotubes by the time an air volume of 360 mL has passed through the sample. The smooth curve is a fit to the function $P_g = 1 + P_i(1 - e^{-V_a/V_g})$ with the fitting parameters given by $P_i = 7.13 \pm 0.29$ and $V_g = 182 \pm 13$ mL.

To determine the smallest tube fragments that were produced, the number of tubes N_{bin} in the length range $0 < L < \Delta_{bin}$ for $\Delta_{bin} = 1, 1/2, 1/4, 1/8,$ and $1/16 \mu\text{m}$ was tabulated at different V_a . As was done in [HY10], nanotube lengths were inferred from photon counts that were calibrated to the longest nanotube in the image; this method allowed us to infer lengths below the diffraction limit of optical microscopy, so long as the photon counts were sufficiently above background. In Fig. 4.3(c), we plotted $N_{bin}/N_{total}\Delta_{bin}$ which is the normalized observed tubes at the smallest bin of size Δ_{bin} where N_{total} is the total number of tubes at V_a . For $\Delta_{bin} \geq 1/8 \mu\text{m}$ this quantity grows while $\Delta_{bin} = 1/16 \mu\text{m}$ data remains relatively fixed, indicating that fragments as short as $1/8 \mu\text{m}$ are produced.

In previously reported experiments [HY10] we have shown that the suddenly applied fluid elongational rate $\dot{\epsilon}$ required for mid-point scission of an n -helix single-stranded tile DNA nanotube of length $2L$ in half is given by

$$\dot{\epsilon} = \frac{T \ln(L/R)}{\pi \mu L^2} \quad (4.1)$$

where R is the tube radius, μ is the viscosity of the fluid, and the tension T required to break the tube is given by $T = n f_c$ where n is the number of duplex DNA strands along the circumference of the tube and $f_c = 65$ pN is the critical force to overstretch a DNA helix. Here $n = 7$ and $R \approx 4$ nm. The observation of $1/8 \mu\text{m}$ tube fragments implies that tubes as short as $0.25 \mu\text{m}$ are broken in two via the hydrodynamic flows generated within the bubbles of the experiment of Fig. 4.2. Taking $\mu = 1.0 \times 10^{-3}$ Pa·sec, Eq. (4.1) indicates that elongation flow rates as large as $\dot{\epsilon} = 3.2 \times 10^7 \text{ sec}^{-1}$ are generated during bubble rupture.

An estimate for the $V_f(L)$ parameter can be obtained from a model of film hole dynamics.

The fragmentation volume $V_f(L)$ is defined as the fluid volume in which all tubes of length L or greater are broken on the passage of one air bubble through the sample. For a film of uniform thickness, considered by Strutt and Rayleigh [Str99, Str02] and later by Culick [Cul60] and Taylor [Tay59] in which the rupture is modeled as a circular hole that propagates outward with the film fluid accumulating in a toroid at the hole perimeter. From momentum balance, the hole propagates outward with a speed given by $v = \sqrt{2\sigma/\rho\delta}$ where σ is the surface tension of the film, ρ is the fluid density, and δ is the film thickness. The elongation rate of the circumference is given by $\dot{\epsilon} = v/r$ where r is the hole radius. The volume of fluid swept up by the hole before the elongation rate falls below a particular value $\dot{\epsilon}$ is then given by $V_f = \pi\delta r^2 = 2\pi\sigma/(\rho\dot{\epsilon}^2)$. Using Eq. (4.1), one obtains $V_f = 1.37 \times 10^{-3} \text{m}^{-1} \times L^4/\ln^2(L/R)$ where we have used $\rho = 1 \text{ g/cm}^3$ and $\sigma = 73 \text{ dyn/cm}$ for the density and surface tension of water. Within this model, energy conservation requires that half of the surface tension potential energy released must be dissipated within the toroid, which implies that the micro-scale fluid flows within the toroid must be taken into account in order to accurately determine V_f . In addition, an accurate calculation would require taking into account the geometry of a bubble contacting a water surface [BSB93], which differs from that of a planar film of uniform thickness.

We repeated the experiment at an order of magnitude slower flow rate at 1.8 mL/min to assess the extent to which fluid flow associated with bubble inflation was responsible for the tube fragmentation. The mean tube length when 60 mL of air had passed through the sample was $2.32 \pm 0.13 \mu\text{m}$ (Fig. ??) which is close to the $2.63 \pm 0.13 \mu\text{m}$ value observed at flow rate of 18 mL/min (Fig. 4.2) for the same volume of air. However, because the slower flow rate results in smaller bubbles (5.32 mm^3 vs 9.26 mm^3), we expect that the experiment at the slower flow rate would produce more bubbles; 60 mL of air at the slower flow rate is expected to produce a comparable number of bubbles as 104 mL of air at the faster flow rate. According to the theoretical analysis of the preceding paragraph, fragmentation volumes should depend predominantly on the number of bubbles, since larger bubbles will additionally contribute only weaker flows that are incapable of breaking shorter nanotubes. Using the phenomenological fitting equation for P_g and $\bar{L} = \bar{L}_0/P_g$, we estimate that at the faster flow rate, 104 mL of air would result in nanotubes with mean length $\bar{L} = 1.78 \mu\text{m}$. Thus, the fragmentation per bubble at the slower flow rate is slightly less than that for the faster flow rate, but still consistent with the notion that bubble bursting is the predominant driver of fragmentation.

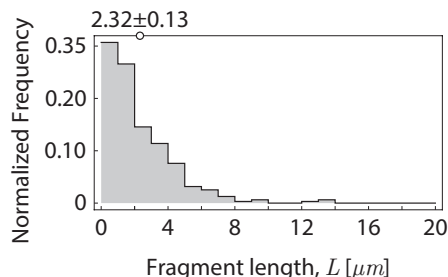


Figure 4.4.: The normalized nanotube length L histogram of the fragment lengths after bubble bursting experiment at 1.8 mL/min for 33.3 minutes, i.e. 60 mL of air.

That fluid flows associated with bubble bursting are primarily responsible for tube breakage was demonstrated by the suppression of tube fragmentation through the addition of 100 μL of heptane to the sample vial to form a fluid layer on top of the solution. Air bubbles rising through this layer would leave the hydrophilic DNA in the aqueous phase. The aqueous fluid flows associated with this process are also reduced because of viscous coupling of the buffer with the heptane at the interface [RQ06, MBBW94]. The mean tube length when 60 mL of air was bubbled through the sample was $6.03 \pm 0.50 \mu\text{m}$ which is comparable to the initial mean tube length $7.32 \pm 0.29 \mu\text{m}$ and large compared to the mean tube length 2.63 ± 0.13 measured at $V_a = 60 \text{ mL}$ for the experiment of Fig. 4.2.

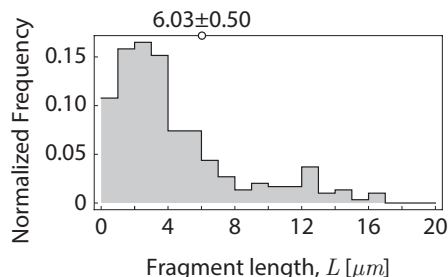


Figure 4.5.: The fragment length histogram after subjecting DNA nanotubes to air bubbles at 18 mL/min for 3.3 minutes in DNA buffer covered with a layer of heptane.

Finally, we demonstrated that fluid flows associated with bubble bursting are primarily responsible for tube breakage by reducing the suppression of tube fragmentation through the addition of 2 mM of the surfactant Sodium Dodecyl Sulfate (SDS) to the buffer. The surfactant reduces the surface tension, increases surface viscosity effects [BS95], and in-

creases the bubble lifetime. These effects reduce nanotube breakage by reducing surface-tension driven flow velocities and by reducing the film fluid volume through film drainage. The foam produced during this experiment necessitated using a $300 \mu\text{L}$ sample volume. Even then it was necessary to periodically stop the air flow to allow the foam to subside. Because of the $3\times$ greater volume, the mean tube length $\bar{L} = 6.23 \pm 0.5 \mu\text{m}$ at $V_a = 180 \text{ mL}$ for this experiment should be compared with the $\bar{L} = 2.63 \pm 0.13 \mu\text{m}$ at $V_a = 60 \text{ mL}$ for the experiment of Fig. 4.2. One sees that reducing the surface tension suppresses the breakage of the nanotubes. In accord with the experience of other laboratories [DCS07, GCL⁺10], we verified that DNA nanotubes are stable in SDS buffer by constructing a length histogram of a sample that was incubated in SDS buffer for 30 min without air flow. The final mean tube length $7.45 \pm 0.54 \mu\text{m}$ was found to be essentially the same as the initial mean tube length $7.65 \pm 0.58 \mu\text{m}$, indicating the stability of DNA nanotubes in SDS containing buffer.

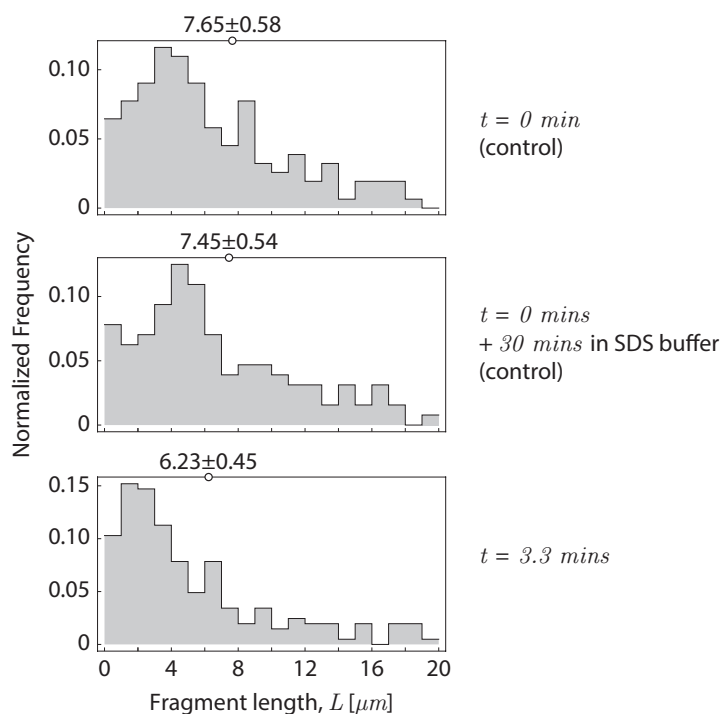


Figure 4.6.: The normalized nanotube length L histogram of the fragment lengths after bubble bursting experiment in SDS buffer at 18 mL/min for 0 and 3.3 minutes.

4.4. Conclusion

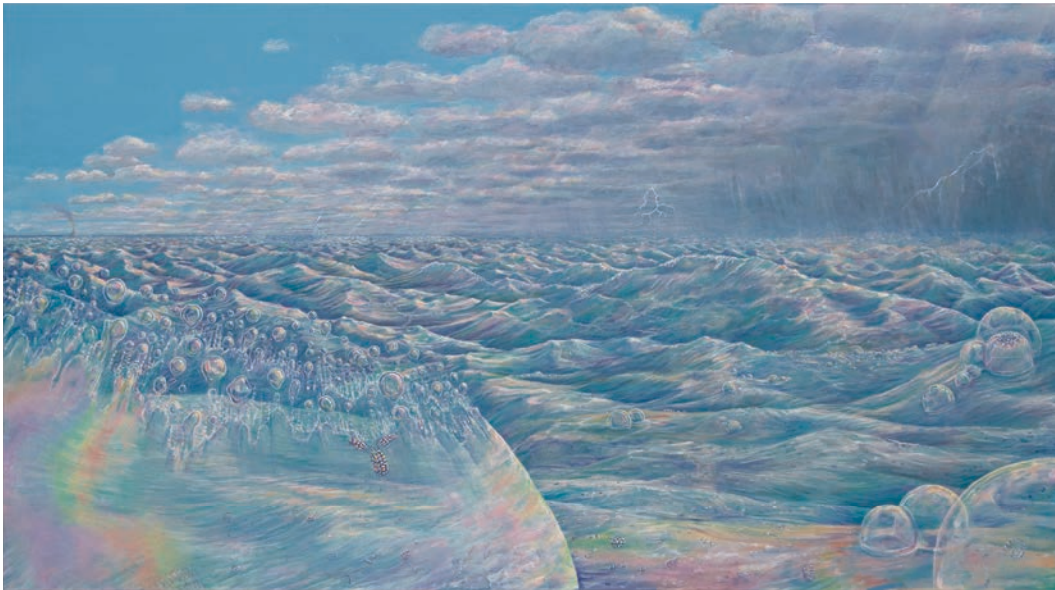
Our experiments show that DNA nanotube fragmentation can serve as a probe of elongational flows generated at small scales, and in complex fluid flows where imaging tracer particles would be impractical.

4.5. Acknowledgments

The authors gratefully acknowledge Erik Winfree, Damien Woods, Rebecca Schulman, John O. Dabiri, and Sandra Troian for helpful discussions. This work was supported by NSF through the grants EMT-0622254, NIRT-0608889, CCF-0832824 (The Molecular Programming Project), and CCF-0855212.

5

**Could ocean hydrodynamic flows
have driven self-replication of the
protobiont?**



An Inevitable Miracle (Ann Erpino)
www.annerpino.com

Abstract

That mechanical forces produced by ocean fluid flow could have been instrumental in the origin of life by driving a primitive form of self-replication through fragmentation was first suggested by [Opa52]. However, little work has been done to characterize the strength of the ocean fluid flow. Using DNA nanotubes as a novel fluid flow sensor, we investigated the effectiveness with which bursting bubbles can induce tension within particle aggregates on the ocean water surface. This measurement is essential in assessing the effectiveness with which ocean fluid motion could have driven self-replication of organic aggregates.

5.1. Introduction

Reproduction is a key feature of biological organisms that is carried out by elaborate molecular machinery [YO10, Alb03] that consumes chemical energy, even for single-celled organisms undergoing vegetative reproduction through cell division. The earliest ancestors of biological organisms would have had simpler reproductive machinery that would nevertheless have required energy consumption, whether the self-replication process involved the fissioning of a loose aggregate of molecules or the separation of the template from the product for a template replicating molecule. Although prions are infectious agents operating in the complex biochemical environment of highly-evolved biological organisms, they are suggestive of what the first replicators may have been like. Two key components of prion replication [SCK⁺00, CDVW04] are (1) the linear growth of protein fibrils through catalytic misfolding followed by the addition of protein molecules to the fibril ends and (2) the fragmentation of these fibrils. This linear growth of both fibril ends and fragmentation gives rise to exponential growth. Although, *in vivo*, enzymes [SL06] are instrumental in the fragmentation of prion fibrils; *in vitro*, prions can be propagated through fluid flow induced mechanical shearing [SCK⁺00, CDVW04]. Growth of an organic complex through the aggregation of molecules followed by fragmentation, where the energy needed for frag-

The version presented in this chapter is not a final manuscript. This work is in preparation for submission as:

Rizal F. Hariadi and Bernard Yurke
Could ocean hydrodynamic flows have driven self-replication of the protobiont?
in preparation

Author contributions

BY conceived and designed the experiments. RFH and BY built the microscope. RFH and BY performed the experiments, analyzed the data, and revised the manuscript. RFH measured the DNA nanotube fragment length.

mentation is supplied by mechanical rather than chemical means, provides an appealing model for the first replicators may have been like. To this end, the prions can exhibit a non-nucleic acid based form of inheritance in which the same protein can give birth to several distinct prion strains due to its capacity to mis-fold and arranged in several distinct fibril forming configurations [CC07, AKN⁺10]. Natural selection pressure can act on these distinct strains to favor one strain over the others.

The notion that self-replication through fragmentation via mechanical forces could have played in an important role in the origin of life by providing a primitive mechanism for self-replication was proposed by A. I. Oparin in his theory of abiogenesis [Opa52]. An important step in his theory was the formation of coacervates (organic aggregates in aqueous solution) in the primordial ocean. Fragmentation by fluid agitation was envisioned as a primitive form of replication allowing natural selection to act on the coacervates. Among the origin of life theories, mechanical fragmentation has also featured as a replication mechanism for inorganic crystals in proposals by Cairns-Smith [CS66, CS08] and as a mechanism for vesicle fissioning in proposals by Szostak [SBL01, ZS09, BS10]. Inspired by Cairns-Smith's proposal, Schulman and Winfree [SW05, Sch07] has devised a DNA-based tile system that grows long ribbons in which tiles are added to the ends in a zig-zag growth pattern. The composition of tile types in a given row of the growth front is a copy of the the composition of tile types in the previous row. This endows the system with the capability of propagating inheritance information to daughters produced by ribbon fragmentation in a manner similar to that of *in vitro* prion replication. It has been shown that in principle, this system is capable of open ended evolution in which suitable selection forces could drive a population of these ribbons to evolve ever more complex tile patterns [SW11].

Although sources of mechanical energy to drive replication have been featured in a number of proposals on abiogenesis, there seems to have been little work done to characterize the strength, availability, and suitability of these sources. The shearing of small particles by fluid flow requires large gradients in flow velocity in the vicinity of the particle. Although mechanical energy in the form of gravity driven or wind driven fluid flow is ubiquitous much of this flow does not result in the large velocity gradients needed for small particle fragmentation. It is also important to consider the nature of the environment in which these forces act. In particular, the environment should allow for long residence time and for the processing of the replicator through multiple rounds of replication. Erosional environments such as sea shores and rivers are unattractive, in this regard, in that primitive replicators incapable of their own motility would have a tendency to be swept away. It should be noted, however, that small replicators resistant to desiccation could, in principle,

be wind dispersed against the prevailing direction of water flow and may provide a means of survival of nonmotile replicators in an erosional environment. Similarly, depositional environments such as the ocean or lake floors are unattractive in that replicators incapable of their own motility would become buried.

The ocean surface has a number of features that make it worth considering as the place of origin of the first replicator. This surface could provide an accumulation site for organic molecules more buoyant than the water, especially amphiphilic and hydrophobic molecules that would tend to form buoyant aggregates. The concentration of organics at the ocean surface would depend on the rate of their production in the prebiotic environment and on the rate of their destruction, for example, by UV light, and on their rate of removal by sedimentation through binding to silt or mineral precipitates to form aggregates less buoyant than water. This last process would be most active in near shore environments where fresh sediment is being supplied by river transport or beach erosion. The presence of stable prebiotic ocean environments in which organic aggregates could concentrate and in which self-replicators could have had long residence time is suggested by the existence of stable Gyres in modern oceans in which plastic debris accumulates [LMFM⁺10]. Of particular significance for mechanically driven self-replication, the ocean surface serves as an abundant source of mechanical energy resulting from wind driven wave action. Wave motion can generate regions of fluid flow with high velocity gradients. For the case of spilling breakers where the crest spills over to form a toe on the slopes of the wave, high velocity gradients can be expected to occur at the edge of the toe [LR95]. For the case of plunging breakers in which the wave crest topples over to form a sheet of plunging water, high velocity gradients can be expected to be found where the sheet of water plunges into the ocean surface below [SS76, KNYO90, Bow92, BJ93, BC98, Ogu98, SB99, HAD02, BBS02, CAH04]. This process results in the copious generation of bubbles which rise within the wave to form whitecaps. The bubbles themselves can be expected to produce flow fields with high velocity gradients when they burst upon rising to the ocean surface. These velocity gradients would reside within the bubble films and would come about as a result of the high velocities that can be produced by surface tension at the edge of the hole of a bursting bubble due to the bubble film's low mass and water's low viscosity. Elongational flows within the bursting bubble will exert tensile stresses within a particle suspended in the film. Fragmentation results if these stresses exceed the tensile strength of the particle.

Here we report on experiments using DNA nanotubes to measure the elongational rates produced in bursting bubble films in a natural sea water sample obtained from a beach near Ventura California.

5.2. Results

In this chapter, 7-helix DNA nanotubes were employed as scientific tools for measuring the elongational flow rates in bursting bubbles of Pacific ocean buffer. The experimental methods employed in these experiments are the same as those of reference [HY] and Chapter 4 except that sea water is used instead of TAE-based DNA buffer. Hence, only a brief summary of the experimental procedure is given here.

A stock solution of DNA nanotubes was prepared as before [HY] by mixing 7 DNA in 1x TAE/Mg⁺⁺ buffer consisting. Then, the nanotube stock solution was diluted by a factor of 20 in filtered sea water for the experiments. The sea water was collected from a rock breakwater in San Buenaventura State Beach in Ventura, California. For use in the experiments a 1 mL sample of sea water was filtered through a MILLEX GP Filter Unit, 0.22 μm (MILLIPORE) using a syringe. A detailed description of the bubble bursting apparatus is given in [HY] and Chapter 4.

For the experiment, two samples were prepared. (1) A control sample was left undisturbed and served as a check on the stability of the DNA nanotubes in salt water [Fig. 5.1(a-b)]. (2) Air was bubbled through the second and samples were withdrawn when 0, 60, 120, and 360 mL of air had passed through the sample [Fig. 5.1(c-e)]. In the beginning of the run, the mean fragment length of the control sample was determined to be $7.01 \pm 0.41 \mu\text{L}$. After one hour of incubation, the mean fragment length in the undisturbed sample was measured to be $6.88 \pm 0.41 \mu\text{L}$, which is not significantly different from the initial value. Therefore, DNA nanotubes are stable in sea water. In contrast, after only 20 min when 360 mL of air had been bubbled through the second sample, the mean fragment length was measured to be $1.02 \pm 0.10 \mu\text{L}$. This indicated that a substantial amount of tube fragmentation had occurred.

To show that fragmentation in sea water is similar to fragmentation in 1x TAE/Mg⁺⁺ buffer, we compare the population ratio P_g as a function of time for both experiments. As before (Chapter 4), P_g is defined as $P_g = N/N_0$ where N_0 is the initial number of nanotubes, and N is the number of nanotubes at time t . P_g can be calculated, as before (Chapter 4), from the average lengths of nanotubes, and the data can be plotted and fit with the phenomenological fitting function $P_g = 1 + P_i(1 - e^{-V_a/V_g})$, where $P_i = 7.1 \pm 1.3$ and $V_g = 203 \pm 73 \text{ mL}$. For comparison, the corresponding results in 1x TAE/Mg⁺⁺ buffer [HY] is plotted as open circles and a dashed curve (Fig. 5.2). Bubble-bursting-induced DNA fragmentation of the DNA nanotubes is very similar for sea water and 1x TAE/Mg⁺⁺

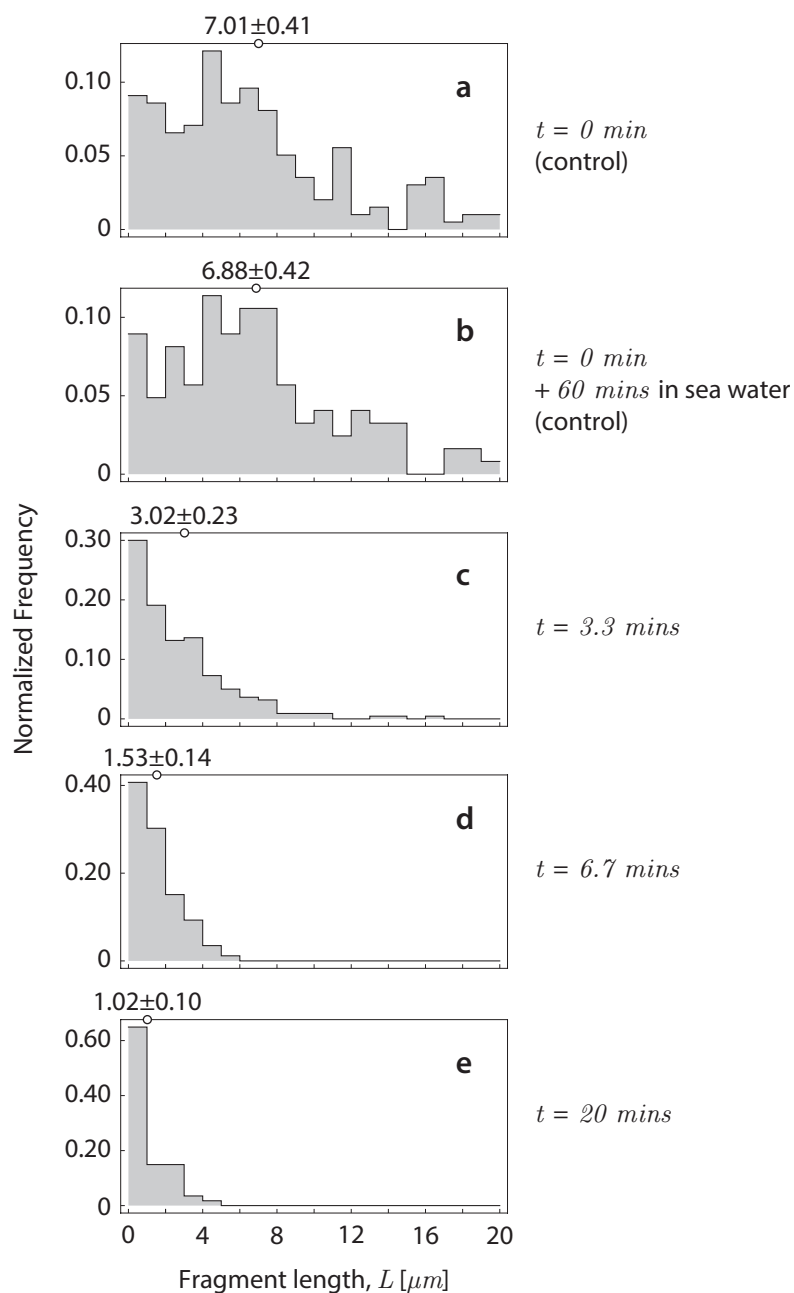


Figure 5.1.: Fragment length histogram of DNA nanotubes in sea water at indicated time points during bubbling. The mean \pm standard error of each distribution is presented on the horizontal axis of the plot. (a,b) One hour incubation in sea water does not significantly change the length distribution. (c-d) Systematic exposure to bubbles decreases the nanotube length.

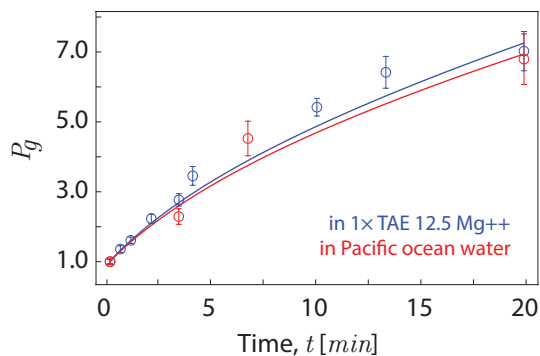


Figure 5.2.: DNA nanotube population ratio P_g plotted as a function of the air volume V_a passed through the sample. The red circles are the sea water data. The red curve is a fit to the sea water data. For comparison, previous results in $1 \times \text{TAE}/\text{Mg}^{++}$ buffer instead of sea water are indicated by the blue circles and the blue line.

buffer.

To obtain information on how the tube length distribution evolves with time tube length histograms were created with $1 \mu\text{m}$ bin size. The histograms are shown in Fig. 5.3 and compared with results we had previously obtained [HY] for $1 \times \text{TAE}/\text{Mg}^{++}$ buffer. The two sets of histograms indicates that bubble-bursting driven DNA nanotube fragmentation proceeds in a similar manner in the two fluids.

5.3. Concluding remarks and outlook

5.3.1. What have we learned?

Our experiments show that bursting bubbles in ocean water can produce sufficient elongational flow to break DNA nanotubes, which is a model system for organic aggregates. We also discovered that DNA nanotubes are as stable in filtered Pacific ocean water as in the standard DNA buffer in $1 \times \text{TAE}/\text{Mg}^{++}$ buffer.

5.3.2. Trip to Malibu beach

As I write this chapter, Bernard Yurke and I are preparing the second half of the manuscript. Bernard Yurke, Erik Winfree, Damien Woods and I had been curious for sometime about the abundance of significant elongational flow in the open ocean. The calculation relies on the measured characteristic fragmentation volume V_f of air bubbles on the ocean water surface. The analysis also requires measurement of size distribution and the number

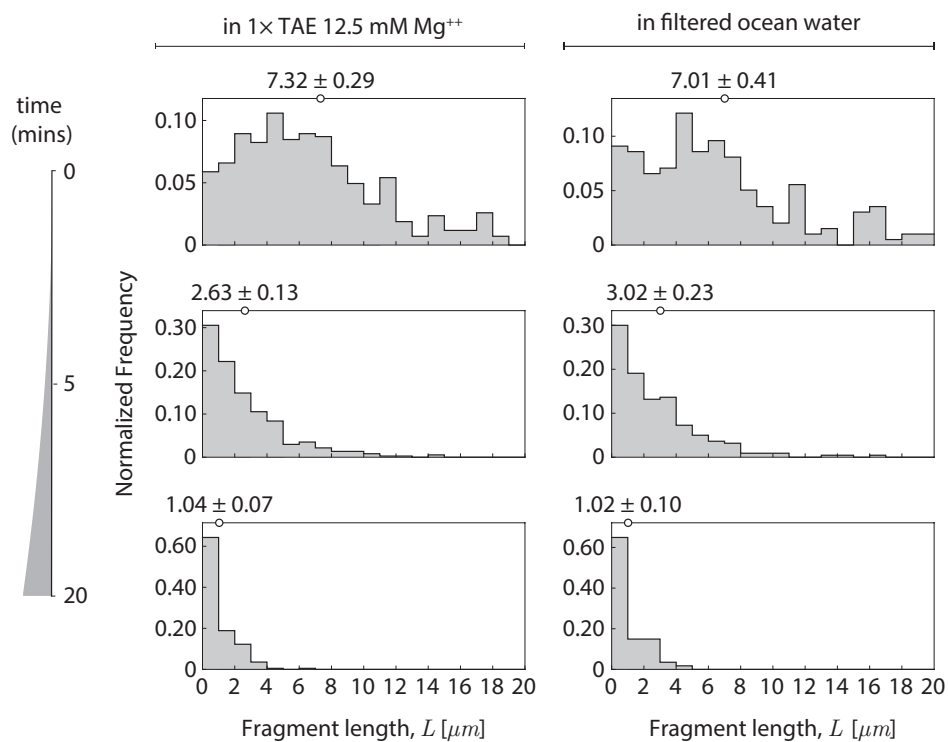


Figure 5.3.: Normalized DNA nanotube fragment length distributions in 1x TAE/Mg⁺⁺ (left column) and sea water (right column) after 0 mL, 60 mL, and 360 mL of air had bubbled through the sample. The mean fragment length of each histogram is indicated as solid circle on top the horizontal axis of the histogram. Note that the range of the normalized frequency (y -axis) increases as the bubbling experiments progress.

of bubbles produced by breaking waves to estimate for the frequency with which hydrodynamic flows of a given elongation rate are encountered in the ocean. Initially, in his backyard in Boise, Bernard Yurke did a clever experiment to measure the bubble size distribution and the rate of air entrainment in plunging water jets. However, to arrive to a valid conclusion, we realize that this essential measurement had to be done correctly. To provide the proper data for the analysis, Bernard Yurke, Damien Woods, and I went to Malibu beach to measure the bubble size distribution and bubble production rate within the surf zone of the beach. The results of these experiments are being used to assess the effectiveness with which ocean fluid motion could have driven self-replication of organic aggregates. Our preliminary analysis indicates that that in order to undergo replication cycles on a sub-annual time the organic aggregate must have a propensity for sticking to the ocean surface or must be sufficiently buoyant to remain in the active layer of the ocean.¹ Organic aggregates on the order of 10 μm in size could achieve the requisite buoyancy.

5.4. Acknowledgments

The authors gratefully acknowledge Erik Winfree, Damien Woods, Rebecca Schulman, John O. Dabiri and Sandra Troian for helpful discussions. This work was supported by NSF through the grants EMT-0622254, NIRT-0608889, CCF-0832824 (The Molecular Programming Project), and CCF-0855212.

¹The result and analysis of the experiment is still in preliminary stage and is not included in this thesis.

6

Single molecule analysis of DNA nanotube polymerization



Joining / Scission (Ann Erpino)
www.annerpino.com

Abstract

DNA nanotubes are amenable materials for molecular self-assembly and can serve as model systems for one-dimensional biomolecular assemblies. While a variety of DNA nanotubes have been synthesized and employed as models for natural biopolymer, an extensive investigation of DNA nanotube kinetics and thermodynamic has been lacking. Using total internal reflection microscopy, DNA nanotube polymerization was monitored in real time at the single molecule level over a wide range of free monomer concentrations and temperatures. The measured polymerization rates were subjected to a global nonlinear fit based on the polymerization theory in order to simultaneously extract kinetic and thermodynamic parameters. For the DNA nanotubes used in this study, the association rate constant is $(5.99 \pm 0.15) \times 10^5$ /M/sec, the enthalpy is 87.8 ± 2.0 kcal/mol, and the entropy is 0.251 ± 0.006 kcal/mol/K. The qualitative and quantitative similarities between the kinetics of DNA nanotubes and microtubules polymerization highlight the prospect of building building complex dynamic systems from DNA molecules inspired by biological architecture.

6.1. Introduction

The design and construction of collective dynamics out of rigorously-characterized molecular components that rival complex cellular systems is a technical challenge at the interface of biology, chemistry, physics, and computer science. The proof of principle demonstrations of self-organization of matter with chemistry is ubiquitous in molecular biology [CW10]. As an example, the cytoskeleton is a system of intracellular biopolymers that evaluates its environments to assemble and disassemble at the right time and the right place within cells. Interactions between the cytoskeleton, molecular motors, and signaling proteins give rise to self-organized intracellular structure [LG08] and motility [ML08], direct the growth of tissues [LC04], and guide the movement of organisms [SW03, SS02].

The version presented in this chapter is not a final manuscript. This work is in preparation for submission as:

Rizal F. Hariadi, Bernard Yurke, and Erik Winfree,
Single molecule analysis of DNA nanotube polymerization,
in preparation

Author contributions

RFH, BY, and EW conceived and designed the experiments. RFH and BY built the microscope. RFH performed the experiments and run stochastic simulations. RFH, BY, and EW analyzed the data. RFH and EW prepared the manuscript.

DNA nanotubes have been proposed as a promising candidate material for constructing an artificial cytoskeleton [RENP⁺04, ENAF04]. A successful demonstration of an artificial cytoskeleton will recapitulate structural, dynamic, force generation, and assembly control aspects of the biological cytoskeleton. Toward that goal, we must understand the design principles of dynamic tubular architectures and develop an accurate physical model of how monomers can assemble and disassemble tubular structures as they respond to information in the environment.

In structural DNA nanotechnology, synthetic oligonucleotides can be engineered to form a small DNA complex, called a DNA tile, that can polymerize to form larger structures using the specificity of Watson-Crick hybridization [See82, WLWS98, Rot06, RENP⁺04, YHS⁺08, SW07, LZWS10, ZBC⁺09]. DNA nanotubes provide a simple example of how a long one-dimensional crystalline structure can arise from the interaction between DNA tiles. Fig. 6.1 shows a DNA tile that possesses 4 short single-stranded regions, known as sticky ends, that serve as binding domains. The sticky end arrangement, in addition to the constraint provided by the biophysical properties of the DNA double helix, directs the interaction of DNA tiles to form tubular DNA structures with a range of circumferences whose distribution is determined by the thermodynamics and the kinetics of the DNA nanotube assembly process.

The first challenge toward *de novo* engineering of an artificial cytoskeleton is constructing a long and rigid polymer out of artificial non-covalently-bound subunits. DNA nanotubes satisfy the length and rigidity criteria. Structurally, the DNA nanotubes used in this work are cooperative polymers that are multiple monomers wide. The cooperativity has two important consequences. First, the tubular organization of DNA tiles along the longitudinal axis of a DNA nanotube gives rise to a long persistence length, $\xi_p^{tube} \sim 20 \mu\text{m}$ [RENP⁺04, ORKF06], which is comparable to the measured persistence length of actin filaments, $\xi_p^{actin} = 17.7 \mu\text{m}$ [GMNH93]. Second, formation of cooperative polymers at reaction conditions where spontaneous nucleation is rare, gives rise to long polymers. The mean length of the DNA nanotubes used in this study is on the order of $5 \mu\text{m}$ for standard assembly conditions. Each DNA tile added to the tip of a growing nanotube interacts with two neighbors, whereas most of the collisions between DNA tiles in solution result in contact with only one neighbor. As a result, there is a high kinetic barrier associated with nucleation whereas elongation proceeds without significant barrier. Therefore, a relatively small number of nuclei grow to form long nanotubes.

Engineering a dynamic DNA nanotube analog of the cytoskeleton requires an accurate

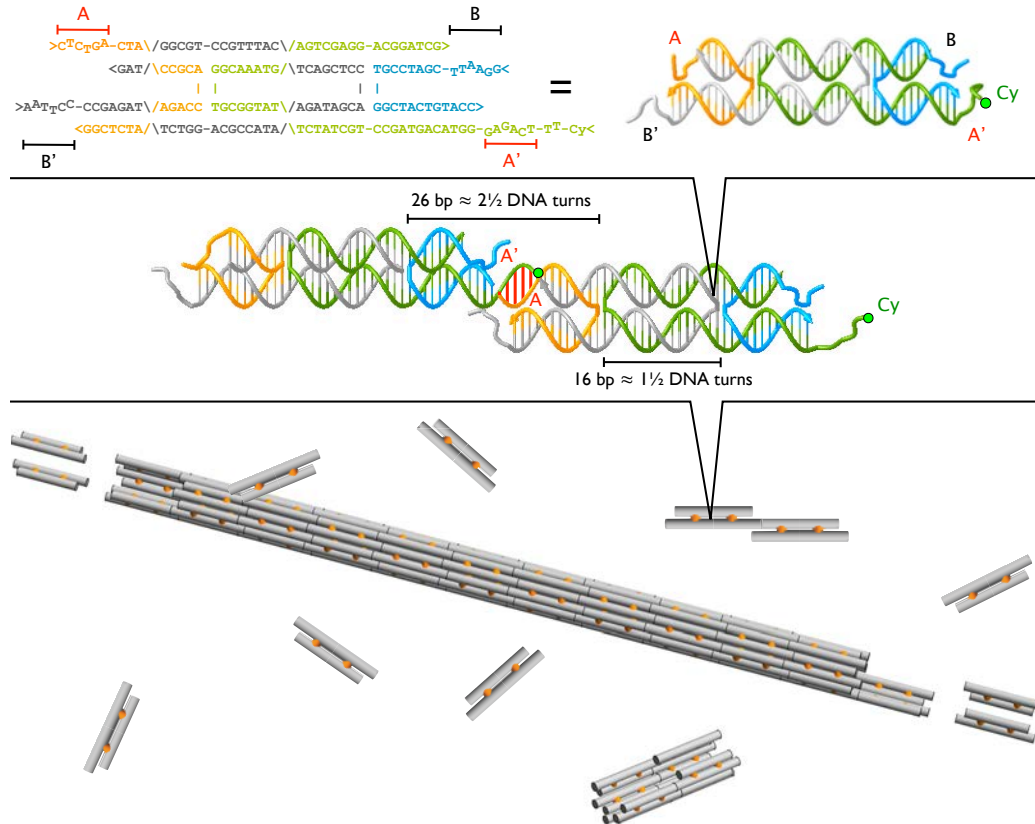


Figure 6.1.: Identical DNA tiles (top) self-assemble into DNA nanotubes (bottom). The four DNA strands form two DNA helices that are joined by two cross-over points, depicted as orange connectors in the cartoon (bottom). The tiles are rigid because of the crossover points. Each tile has four single stranded DNA sticky ends (A, A', B, and B'). The four sticky ends are designed such that A is complementary to A' (red sticky end pairs) and B is complementary to B' (black sticky end pairs). In the dimer picture, the left monomer appears thinner due to 36 ° rotation along the horizontal axis to match the minor and major groove between the ends of two monomers at the sticky end region. For fluorescence imaging, we labeled one of the DNA strands with Cy3 or Cy5 fluorophore (green circles).

polymerization model for DNA nanotubes. In the literature, there are two classes of models that are relevant to the polymerization of DNA nanotubes, namely the kinetic Tile Assembly Model (kTAM) developed for DNA tile assembly and the polymerization theory developed for biopolymers. In the DNA self-assembly literature, the kTAM considers growth by tile self-assembly to be a second order chemical reaction between crystals and monomers, which will be described in more detail in section 6.4.1. The kTAM has been used to guide the design and provide a deeper understanding of algorithmic self-assemblies of DNA tile sets with various levels of complexity [FM09,RPW04,SW07,FHP⁺08,BSRW09,CSGW07]. In the biophysics literature, there is a different class of polymerization models for active one-dimensional polymers that couple their polymerization with fuel consumption reactions in the form of nucleotide hydrolysis [FHL94,FHL96]. Since DNA nanotubes are essentially passive one-dimensional polymers that comprise a single monomer type, these two classes of models are identical when applied to existing DNA nanotubes if one ignores the active aspects of the biophysics model.

Despite the success of the kTAM for guiding the design of complex DNA self-assembly systems, the theoretical framework and its assumptions have not been tested experimentally in detail. The rigorous testing of DNA nanotube polymerization theory requires assays that can determine not only the concentration of free DNA tile monomers, but also the number of nanotubes at any given time, and the direction of growth, without experimentally confounding effects, such as excessive spontaneous nucleation or the presence of tube bundles. Early studies of DNA ribbons [SW07] used bulk UV absorbance data, in combination with static atomic force microscopy (AFM) assays, to measure the concentration of DNA tiles free in solution, and thereby to infer the kinetics of incorporation into ribbon assemblies. Interpreting bulk data is complicated, because polymer growth kinetics depend not only on free monomer concentration, but also on the size distribution of supramolecular assemblies and on the number of such assemblies. This information cannot be accurately measured in bulk UV absorbance assays and must be inferred indirectly, thus, introducing large uncertainties into the analysis. Recently, Evans *et al.* used a single-molecule AFM movie to validate some of the kTAM assumptions for polymerization on mica surface [EHW12]. Despite their rigorous analysis, the interaction between DNA tiles and mica surfaces complicated their measurements and limited their ability to determine quantitative measurements of the rate constants and free monomer concentrations.

In this work, we adopted the standard assay in biopolymer research, namely time lapse light microscopy [TW78,TW80,HH86]. The power of single-molecule cinematography has enabled the continuous observation of non-equilibrium polymers. To minimize background

fluorescence from the sea of unlabeled monomers in solution, fluorescent polymers must be excited either with an evanescent wave by total internal reflection fluorescence (TIRF) microscopy [AP01, KP05, FTT⁺02] or by confocal illumination [IGC02].

Here, we report the application of TIRF microscopy to the study of the polymerization of self-assembled DNA structures. From a set of polymerization movies at a wide range of tile concentrations and reaction temperatures, we were able to measure both the kinetic and thermodynamic parameters of DNA nanotube assembly. The experimental results are consistent with the kinetic Tile Assembly Model for DNA nanotubes and are in agreement with previous kinetic and thermodynamic measurements of DNA hybridization systems.

6.2. Materials and Methods

6.2.1. Total Internal Reflection Fluorescence microscope

Optics

The polymerization movies were acquired with a home-made prism-based total internal reflection fluorescence (TIRF) upright microscope (Fig. 6.2). A solid-state green laser (GCL-025, 25 mW, CrystaLaser) equipped with an adjustable power supply (CL2005, CrystaLaser) provides the 532 nm excitation light. The beam was filtered with a Z532/10× laser filter (Chroma). The filtered excitation beam passed through a quarter-wave plate (Thorlabs) to produce a circularly polarized beam, which effectively has uniform polarization to counter the orientation-dependent fluorescence of Cy3. Two mirrors (Thorlabs, not pictured in the drawing) were used to guide the illumination beam to the field of view below the objective. Another mirror (Thorlabs) and a 15 cm focusing lens (CVI Melles Griot) steered the excitation beam onto a Suprasil 1 right-angle prism (CVI Melles Griot) at approximately 0° from the horizon to produce a weakly focused illumination spot. We calculated that the incident angle between the incoming laser and the normal vector of the microscope slide is sufficiently larger than the critical angle for evanescent wave to occur at the interface between glass and liquid, where the sample and focal plane of the objective are located.

In our experiment, DNA tiles and DNA nanotubes resided inside a glass capillary tube that was optically coupled with the prism by a thin layer of immersion oil. The emitted photons were captured by a 60× 1.2 NA water immersion objective (Nikon) and focused to the electron multiplier CCD camera (C9100-02, Hamamatsu) by a 20 cm tube lens (double achromat, CVI Melles Griot). The combination of bright samples, low background, and

efficient light collection produces images with high signal to noise ratio. We kept the laser power at below 10 mW to minimize photobleaching during imaging.

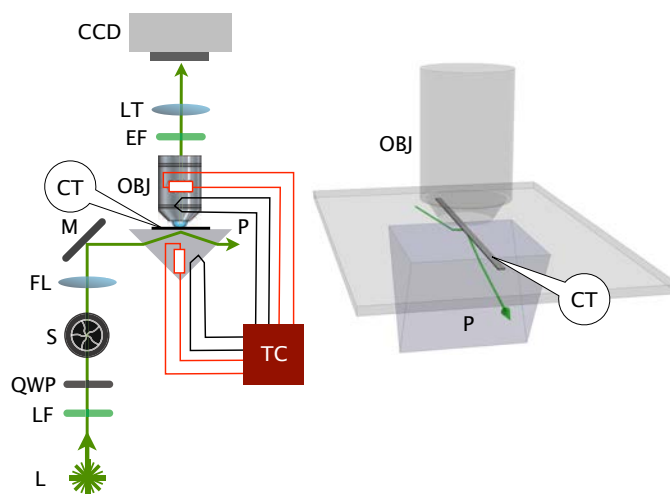


Figure 6.2.: (Left) The schematic drawing of the prism based TIRF microscope. L = 532 nm 25 mW laser; LF = laser filter; QWP = quarter wave plate; S = mechanical shutter; FL = 15 cm focusing lens; M = mirror; P = temperature controlled right angle prism; OBJ = temperature controlled 1.2 NA water immersion objective; EF = emission filter; LT = 20 cm tube lens; CCD = electron multiplier Charged Coupled Device; TC = temperature control. (Right) Capillary flow chamber (CT) for the polymerization assay. In our upright microscope setup, the flow chamber is sandwiched between the prism and the objective. We use immersion oil to optically couple and mount the bottom surface of the 1 mm thick microscope slide with the glass prism. A thin layer of epoxy was used to optically couple the glass capillary chamber to a microscope slide.

Autofocus

The autofocus and temperature control features of our microscope were central in automating the data acquisition. A rotary motor (Z-drive, ASI) was mechanically coupled to the translation stage of the objective turret to control the vertical position of the objective via computer. We used an autofocus module in the μ Manager software (available at <http://micro-manager.org/>) to find and maintain the best-focus-position of the objective based on the image sharpness. A focused image has a higher sharpness than an out-of-focus image. The DNA nanotube images were sufficient for finding the best-focus position without the need for fiduciary beads. The autofocus method was robust for long time-lapse imaging. The μ Manager plugin used the image sharpness function as feedback

to the autofocus routine. We set the μ Manager to run the autofocus step either every 30 or 60 seconds to minimize photobleaching.

Temperature control

In our setup, we used two separate electronic circuits to control the temperature of the prism and the objective. Each setup was composed of a heating tape (Omega), a thermocouple (CHAL-005, Omega), and a temperature controller (Omega). We relied on the heat transfer from the heated objective and prism to achieve the desired temperature in the sample. This method produced highly reproducible sample temperatures. Consequently, in most experiments, we only measured the temperature of the prism and the objective. Two calibrated thermocouples (CHAL-005, Omega) were placed close to the field of view to calibrate the sample temperature as a function of both the prism and the objective. In this paper, we report the sample temperature based on our calibration table.

Flow chamber

A pre-cleaned glass capillary tube (Vitrotubes 5010, VitroCom) with inner dimensions of $100\ \mu\text{m} \times 1\ \text{mm} \times 5\ \text{cm}$ was mounted on a $75\ \text{mm} \times 50\ \mu\text{m} \times 1\ \mu\text{m}$ RCA-cleaned [BHKQ03] plain microscope slide (Corning, 2947-75X25) by applying a thin layer of 5-minute epoxy (Devcon) in between the two glass surfaces. The epoxy was left to cure at least overnight prior to imaging. The mounted capillary chambers were stored in ambient environmental conditions inside a microscope slide storage box and were used within a week. We believe that the small openings of the capillary chamber hinder contamination and consequently, it was safe to use the chamber as is, without any pre-cleaning step.

We serendipitously discovered epoxy to be a convenient adhesive to mechanically and optically couple capillary tubes and microscope glass. First, the cured epoxy is inert with respect to immersion water; thus, the epoxy does not stain the water-immersion objective. Second, and more importantly, the refractive index of cured epoxy closely matches the refractive index of the microscope slide and the capillary tube. (Any refractive index mismatch increases the background signal due to more reflection.) An adhesive with a much higher refractive index than glass will shift the total internal reflection location to the interface between the adhesive and capillary glass surface. Conversely, an adhesive with a refractive index close to water will result in an evanescent wave at the boundary between the microscope slide surface and the adhesive. In the absence of adhesive, immersion water penetrates the cavity between the two glass surfaces, and the evanescent wave occurs at the

microscope slide-immersion water interface instead of at the inner surface of the capillary tube where the fluorescent sample resides. Thus, cured epoxy between the capillary tube and microscope slide solves this problem.

6.2.2. DNA tile design

The DNA tile used here conforms to the “DAO-O” motif (double-crossover, antiparallel, odd-odd) [FS93], which means that it is a double-crossover molecule. At crossover points, strands bend to become antiparallel to themselves. It has an odd number of DNA half-turns between crossover points in the same tile, and also an odd number of half-turns between neighboring tiles (middle). We used the sequence of the previously published DAO-E tile (double-crossover, antiparallel, odd-even) We used the sequence of the previously published DAO-E tile {Fig. 1(d, top left) of Ref. [WLWS98]} as the starting sequence for our DAO-O tile. In the new tile, we increased the distance between intermolecular crossover points by approximately half a turn of DNA, from 21 base pairs to 26 base pairs, which is equal to 5 half-turns. The new DNA tile has 2 pairs of 6-nucleotide sticky ends, instead of 5-nucleotide sticky ends, with the goal being to bring the nanotube formation temperature near 37 °C as required for the artificial cytoskeleton project in our lab. All of the original core and arm sequences were left unmodified during the sequence optimization. We used our custom MATLAB code to design the sequence for the extension of the arms and new pairs of sticky ends based on spurious binding minimization (available at <http://www.dna.caltech.edu/DNAdesign/>).

Name	Sequence
NB-1	5'-CTCTGA-CTACCGCACCAGAATCTCGG-3'
NB-2	5'-AATTCC-CCGAGATTCTGGACGCCATAAGATAGCACCTCGACTCATTTGCCTGCGGTAG-3'
NB-3	5'-TCAGAG-GGTACAGTAGCCTGCTATCTTATGGCGTGGCAAATGAGTCGAGGACGGATCG-3'
NB-3-Cy3	5'-Cy3-TT-TCAGAG-GGTACAGTAGCCTGCTATCTTATGGCGTGGCAAATGAGTCGAGGACGGATCG-3'
NB-3-Cy5	5'-Cy5-TT-TCAGAG-GGTACAGTAGCCTGCTATCTTATGGCGTGGCAAATGAGTCGAGGACGGATCG-3'
NB-4	5'-GGAATT-CGATCCGTGGCTACTGTACC-3'

Table 6.1.: DNA sequences for a single-monomer-type DNA nanotube. For the fluorophore-labeled strands, we inserted two additional T's between the fluorophore and NB-3 sequence as a spacer to minimize any potential side effect of having the Cy3 or Cy5 fluorophore at the end of a sticky end.

6.2.3. Polymerization mix

Our polymerization mix consists of pre-formed banded nuclei, supersaturated DNA tile solution, crowding agent, and buffer, as explained below.

DNA stock solution

Each DNA strand (synthesized by IDT DNA Technologies, Inc.) was resuspended separately and stored in purified water at a 10 μM stock concentration. To expedite the subsequent sample preparation step, we typically store our tile as an annealed DNA nanotube stock solution in a 4 $^{\circ}\text{C}$ refrigerator, and use it within 1 week after annealing. The stock of DNA nanotube was made by mixing the four DNA strands at a final equimolar concentration of 1.5 μM each in a buffer consisting of 1 \times TAE [40 mM Tris-acetate and 1 mM EDTA (Ethylenediaminetetraacetic acid)] with 12.5 mM Mg-acetate and then annealing from 90 $^{\circ}\text{C}$ to 20 $^{\circ}\text{C}$ at 1 $^{\circ}\text{C}/\text{min}$. In retrospect, we consider this annealing step to be unnecessary because of another annealing step in the preparation of the supersaturated DNA tile solution.

Pre-formed DNA nuclei with fiduciary markers

The simultaneous polymerization measurement of both DNA nanotube ends requires fiduciary markers. To create fiduciary markers, we pre-formed DNA nanotubes with random banding patterns to be used as nuclei. The banding pattern along the DNA nanotubes established fiduciary coordinates that enabled separate kinetic measurement of both ends of each DNA nanotube. The DNA nanotubes with fiduciary markers were prepared, as discussed below, from Cy3- and {Cy3, Cy5}-labeled nanotubes, which were called bright and dim bands, respectively. All of the tiles in the bright nanotubes were labeled with Cy3. For the separately prepared dim nanotubes, only 33% of the tiles were labeled with Cy3 and the remaining 67% were labeled with Cy5. Instead of using an unlabeled tile, we chose Cy5-labeled tiles to decrease the brightness of the fluorescence tube in the Cy3 channel. We hope that the physical similarity between the Cy5-DNA and Cy3-DNA tiles will result in similar perturbation to the DNA tile and DNA nanotubes, e.g., in terms of melting temperatures, kinetics, etc.

The DNA nanotube nuclei were prepared as follows: First, we annealed bright and dim DNA nanotubes separately at a tile concentration of 1.0 μM from 90 $^{\circ}\text{C}$ down to 50 $^{\circ}\text{C}$ at 1 $^{\circ}\text{C}/\text{min}$ and from 50 $^{\circ}\text{C}$ to 20 $^{\circ}\text{C}$ at 0.1 $^{\circ}\text{C}/\text{min}$. This annealing protocol produces DNA nanotubes with mean length on the order of 5 μm . On the same day, equal volumes of 1 μM

bright and dim DNA nanotubes were fragmented into shorter nanotubes by subjecting the DNA nanotube mix to a high elongational fluid flow within a $20\ \mu\text{m} \times 20\ \mu\text{m}$ constriction in a microfluidic chip [HY10] at a $150\ \mu\text{L}/\text{min}$ volumetric flow rate. The elongational flow near the constriction was sufficient to induce significant tension and induce DNA nanotube scission. The fragments had a mean size on the order of $1\ \mu\text{m}$. Subsequently, the stochastic end-to-end joining between fragmented bright and dim DNA nanotubes produced hybrid DNA nanotubes with random banding patterns [RENP⁺04, ENAF04].

The bright and dim segments are visible in the microscopy images (the left panels of Figs. 6.3 and 6.4) and are more obvious in the kymograph (the right top panel of Figs. 6.3 and 6.4). As expected, the position of bright and dim segments did not move relative to each other during the course of data acquisition, which justified the choice of band positions along the DNA nanotubes to act as bonafide fiduciary markers.

Supersaturated DNA tile solution

For the polymerization assay, the supersaturated DNA tile solution was synthesized by annealing $10\ \mu\text{L}$ of DNA mix at $15/s \times$ of the desired DNA tile concentration in $1 \times \text{TAE}/\text{Mg}^{++}$ from $90\ ^\circ\text{C}$ to $50\ ^\circ\text{C}$. The slow annealing was halted at $50\ ^\circ\text{C}$ because for experimental concentrations, DNA nanotube nucleation is not noticeable at temperatures above $40\ ^\circ\text{C}$. At $50\ ^\circ\text{C}$, which is approximately $10\ ^\circ\text{C}$ above the formation temperature, $5\ \mu\text{L}$ of $3 \times 0.3\%$ (w/v) methylcellulose (previously kept at $50\ ^\circ\text{C}$) was added to the $10\ \mu\text{L}$ supersaturated DNA tiles. Note that the formation temperature is concentration and time dependent. By the end of the experiment, we determined that the observed formation temperature range is $35.2\text{--}38.3\ ^\circ\text{C}$, which corresponds to the temperature where spontaneous nucleation was observed in $100\ \text{nM}$ and $500\ \text{nM}$ samples after ~ 5 minutes of imaging time, respectively. Thus, $50\ ^\circ\text{C}$ incubation is above the formation temperature in any free monomer concentration in this work. The sample temperature was then lowered to $45\ ^\circ\text{C}$. $2\ \mu\text{L}$ of pre-formed banded nuclei were added at $45\ ^\circ\text{C}$ and immediately the mix was gently injected into the capillary tube, which was already at the specified reaction temperature between the temperature-controlled prism and the objective. Both ends of the capillary chamber were immediately sealed with Vaseline.

Crowding agent confines the nanotubes

We included 0.3% (w/v) methyl cellulose (viscosity $4,000\ \text{cP}$ at $2\ \%$ in H_2O at $20\ ^\circ\text{C}$, purchased from Sigma-Aldrich M0512) as a crowding agent to confine DNA nanotubes

near the bottom (as well as top and side) of the glass surface where the focal plane and evanescence field were positioned. In a crowded environment, the entropy of the system is maximized when all of the long structures are pushed close to another surface, such as capillary tube walls. This entropic confinement did not hinder the mobility of confined DNA nanotubes within their confinement space (middle columns of Figs. 6.3 and 6.4). This behavior is in accord with previous observations of confined biopolymers in the presence of crowding agents [GCK⁺10, WGA⁺10]. The side effect of this confinement strategy is that the same entropic force also favors confining DNA nanotubes to other surfaces, including the surfaces of other DNA nanotubes. Consequently, at high DNA nanotube densities, DNA nanotubes were observed to exhibit side-to-side joining and lateral aggregation. The increasing intensity of tubes in images corresponds to the lateral “bundling” of multiple DNA nanotubes or side-to-side joining (observed directly in Movies C.1 and C.4).

6.2.4. Data acquisition

Since polymerization is temperature sensitive, we paid close attention to the temperature of our sample and minimized exposure to the room temperature.

Before the injection of DNA monomers, the empty sample chamber was mounted onto the heated prism and under the heated objective and immersion water to bring the sample chamber to the desired steady state temperature. Skipping this step will result in a sample chamber that is initially at room temperature, which would cause DNA nanotubes to nucleate very rapidly. In addition, our autofocus did not work well when the temperature of the sample, prism, and objective changed rapidly, such as in the initial heating step of our method of temperature control. The chamber was left empty at the desired steady state reaction temperature until the polymerization mix was ready.

In contrast to adding a liquid sample to a filled chamber, injecting a sample into an empty capillary chamber results in a known initial sample concentration. Previously, studies that used a similar sample chamber would flush the filled chamber with at least twice the chamber volume to ensure that the reaction conditions held during measurements. Because the fluid flow approaches zero near the channel walls, it is difficult to produce samples with known concentration using that method. The second advantage of starting with an empty chamber is fast injection time. Due to stronger capillary action, injecting the sample into an empty chamber requires less time than infusing a filled chamber with sample. The fast injection may also be important in minimizing thermal contact between the heated liquid of DNA tiles, DNA nanotubes, and the ambient room temperature.

However, an empty chamber also possesses an intrinsic problem; the fast injection flow of DNA nanotubes, especially at high temperatures, induces DNA nanotube scission. We minimized the scission problem by adding the sample gently at the opening of the empty chamber. The injection time was approximately 5 sec for $\lesssim 6 \mu\text{L}$ sample. Quantifying how much scission occurs with our injection protocol is not necessary since the polymerization rate measurements should be independent of the initial amount of fragmentation.

We identified three instances in our protocol in which the polymerization mix was exposed to ambient environment. First, we pipetted $5 \mu\text{L}$ methylcellulose to a supersaturated tile solution with a pipette tip that was at room temperature. Second, after we incubated the solution of supersaturated tiles and methylcellulose at $50 \text{ }^\circ\text{C}$, we took the sample out from the temperature cycler and mixed it for ≈ 5 sec at room temperature. Third, we injected the supersaturated tiles, methylcellulose, and pre-formed DNA nuclei at the opening of the heated glass capillary chamber with a pipette tip that was not heated. To minimize the potential problem, such as the rapid nucleation of DNA nanotubes from supersaturated DNA tiles before the sample was injected to the heated glass capillary chamber, we performed these three steps as rapidly as we could. The typical execution time for these steps was 5 sec and no longer than 10 sec. In almost all cases, the fast sample handling seems to be sufficient to avoid spontaneous nucleation before imaging, with the exception of a polymerization assay at 600 nM and $41.4 \text{ }^\circ\text{C}$. An extrapolation of the polymerization model predicted a net negative polymerization rate at 600 nM and $41.4 \text{ }^\circ\text{C}$ (see the bottom right plot of Fig. 6.5). While the model may be true in an ideal protocol, we consistently observed spontaneous nucleation in our 600 nM and $41.4 \text{ }^\circ\text{C}$ movie. We attribute the observed nuclei as a result of spontaneous nucleation that was triggered by the brief exposure to room temperature during one or more of the steps discussed in this section.

DNA nanotube imaging

Our prism-based TIRF microscope, equipped with temperature control and automated focusing, monitored the dynamics of the DNA nanotubes that were confined close to the glass surface (Figs. 6.3 and 6.4) for more than 2 hours of imaging. The signal to noise ratio was very high, even in the presence of a high concentration of Cy3-labeled free monomers in solution. For all of the nanotubes that were analyzed, we did not encounter any pausing of polymerization in any of our movies, which provides evidence that the untreated glass surface is not too sticky. The majority of DNA tiles were in the free monomer state. The typical total concentration of DNA tiles in pre-formed DNA nuclei was less than

10 nM, which is $10\times$ smaller than the most dilute free monomer concentration in our assay (100 nM). Even after 2 hours of imaging, we typically observed a difference of less than a factor of 2 in contour length for all DNA nanotubes, which corresponded to a small DNA tile concentration change.

In the reaction conditions where spontaneous nucleation was hardly observable, the DNA nanotube polymerization was followed for at least 1 hour and no longer than 2 hours. Much to our surprise, our imaging protocol did not require an oxygen scavenger buffer to achieve and maintain a high signal-to-noise ratio for more than 2 hours of time-lapse imaging. At an acquisition rate of typically 4 frames/min, we usually acquired enough data points in less than 30 minutes. If significant spontaneous nucleation was observed, we terminated the data acquisition after ~ 5 minutes because the newly formed nuclei rapidly obscured the visibility of the pre-formed nuclei. Moreover, the new nuclei can also end-to-end join to a growing DNA nanotube end, which made our polymerization rate measurements unreliable. Thus, spontaneous nucleation limited the range of temperatures and concentrations for which we could obtain accurate rate measurements.

6.2.5. Data analysis

The polymerization rate was measured using two methods: (1) kymographs [KP07] or (2) length measurements taken at two frames with a sufficient time difference. The kymograph allows separate measurement of both nanotube ends at the cost of time to construct a kymograph. Obtaining the polymerization rate from the nanotube length at two data points is fast but can only measure the net polymerization rate of a nanotube end. Any asymmetry in the polymerization rate at the nanotube ends will be lost during the measurement, even in the presence of fiduciary markers.

We applied an ImageJ (available at rsbweb.nih.gov/ij/) plugin developed by Kuhn and Pollard [KP07] to construct kymographs from a series of DNA nanotube images. We used their image analysis routine to convert a rough hand trace of each DNA nanotube to a refined trace of the nanotube by snapping each pixel along the trace to the DNA nanotube axis. The intensity along the refined traces was used to construct equivalent straightened images of the curvilinear DNA nanotubes. The straightened images of the same nanotube at different time points were aligned and stacked into a kymograph. We wrote Mathematica (Wolfram Research) code that shifted the longitudinal offset between straightened DNA nanotubes until the sum of the correlations between straightened images in a kymograph was maximized, i.e., the banding patterns were vertically aligned. The

longitudinal position of both nanotube ends in a kymograph was detected by setting a chosen threshold for both DNA nanotube ends, typically less than the half maximum value of any given straightened images. For each nanotube end, we performed linear fitting to the coordinates in each stacked image to measure the polymerization rates.

In the second technique, we simply calculated the net polymerization rate from the ratio of the length change between two frames and the time interval between the frames. Because the kymograph integrates over multiple frames, its standard error is likely to be smaller.

6.3. Results

6.3.1. Polymerization rate measurements

At the critical monomer concentration for a given temperature $[tile]_{crit} = \frac{k_{off}}{k_{on}}$, i.e., the tile attachment rate $k_{on}[tile]_{crit}$ and the tile detachment rate k_{off} are equal, so each DNA nanotube's length fluctuates around the initial monomer concentration value. At a constant tile concentration away from $[tile]_{crit}$, DNA nanotubes either elongate or shrink at a constant rate. The polymerization rate constants discussed here refer to the elongation or shortening of DNA nanotubes (and thus are measured in layers/M/s) and layers/s as opposed to the association and dissociation of a DNA tile to a binding site as illustrated in Fig. 6.8. (The subtle distinction will be discussed in section 6.4.1). The resolution of the microscopy assay was diffraction limited at ~ 250 nm or $\sim 18\times$ the size of a DNA tile. Our imaging optics produced movies that were sufficient to accurately track both ends of individual DNA nanotubes. However, the optics were insufficient to discriminate the precise tile arrangement at nanotube ends and could not detect individual tile attachment and detachment events.

We measured the polymerization rate from time-lapse images such as those presented in Figs. 6.3 and 6.4 by (1) constructing kymographs and (2) measuring DNA nanotube lengths at two time points. We address the results and merits of both approaches below.

DNA nanotubes depolymerize at a steady rate below the critical monomer concentration

To measure the rate at which monomers dissociated from DNA nanotubes, k_{off} , we diluted 1 μ M of DNA tiles (as pre-formed DNA nanotubes) at room temperature by a dilution factor of 143 in imaging buffer [$1\times$ TAE/Mg⁺⁺ 0.3% (w/v) methylcellulose]. At 25 °C, the free tile concentration in the pre-formed DNA nanotube nuclei stock was estimated to

be well under 25 nM, which is the measured critical monomer concentration of our DNA nanotube at 33.6 °C (see Table 6.3). The 143× dilution brought the free tile concentration close to 0 nM and effectively eliminated the contribution of the forward reaction to the net depolymerization rate.

Fig. 6.3 shows that DNA nanotubes depolymerize at 38.3 °C with zero initial monomer concentration. Since the critical monomer concentration is non-zero, we expected DNA nanotubes to depolymerize at zero monomer concentration. Presumably, the monomer concentration was not constant at 0 nM, but instead increased as more DNA tiles dissociated from the shrinking DNA nanotubes. The initial concentration of all monomers in the pre-formed DNA nanotube nuclei was 7 nM, which sets the upper bound of the free monomer concentration in the experiment with 0 nM initial free tile concentration. In the worst case scenario, a complete depolymerization would increase the free tile concentration by 7 nM, which is relatively small compared to the 100 nM concentration interval in our data set. In practice, the concentration change is less significant than the theoretical upper bound. We did not run the assay long enough for a significant fraction of DNA nanotubes to become significantly shorter.

DNA nanotubes elongate at high free tile concentration

To measure the second-order forward rate constant k_{on} at which DNA tiles associated to DNA nanotube ends, we assayed the DNA nanotube polymerization at multiple DNA tile concentrations with intervals of 100 nM and at multiple temperatures ranging from 28.9 to 41.3 °C. As shown in Fig 6.4, DNA nanotubes elongated at a 400 nM tile concentration and at 38.3 °C. In these experiments, elongation due to association was offset by the previously measured dissociation rate.

In the polymerization experiment here, in which the spontaneous nucleation was very rare, the tile concentration was regarded as approximately constant. In contrast to the concentration increase in the depolymerization assay, the elongation of DNA nanotubes consumed free tiles from solution. The initial concentration of tiles incorporated tile in DNA nuclei was 7 nM. Because of the slow DNA nanotube polymerization rate, we did not assay the process sufficiently long enough to achieve doubling of the average DNA nanotube length. Therefore, at the temperatures and free tile concentration parameters where spontaneous nucleation was very rare, polymerization doubled, at most, the average DNA nanotube lengths by consuming 7 nM of free monomer concentration from the buffer, which was less than one tenth of the smallest non-zero concentration in our experiments.

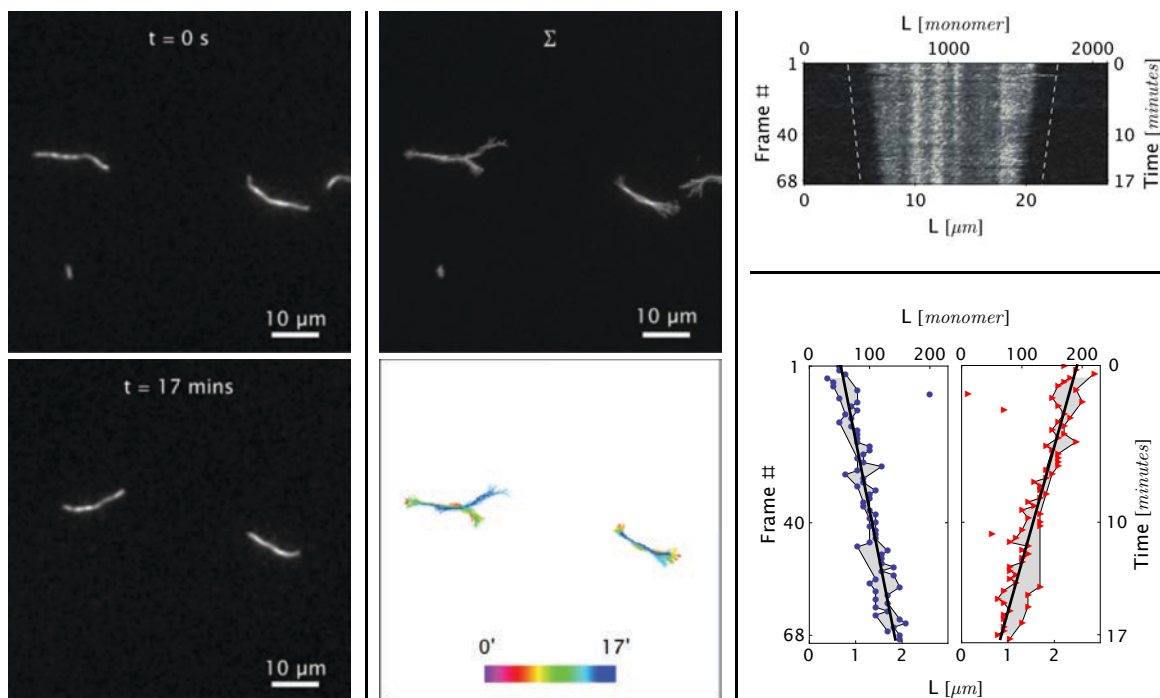


Figure 6.3.: Real-time observation of nanotube depolymerization. (Left) Before and after TIRF images of depolymerizing DNA nanotubes at 38.3°C and 0 initial tile concentration. Here, the original images were at higher resolution and were intentionally blurred over a pixel radius of 4 to ensure image clarity. The higher resolution images are conserved in Movie A.2. (Middle) The superposition of the 69 images shows that the nanotubes were confined close to the glass surface, where the evanescent illumination is maximum and focal plane is positioned. More importantly, the nanotubes were able to diffuse in the confinement space [WGA⁺10, GCK⁺10]. The diffusion was mostly along the longitudinal axis of the nanotube and not sideways. In the middle of the movie, the tube on the left switched between two paths. The bottom middle panel is the superposition of DNA nanotube traces at different time points. The depolymerization is more noticeable when the nanotube curvilinear traces are straightened, aligned, and presented as a kymograph (top right). Only the kymograph of the left tube is shown in this figure. The linear fits of the DNA nanotube end positions show that both ends depolymerized at constant depolymerization rates. The vertices of the gray-shaded regions are the output of the edge detection algorithm. Most of the outputs were included in the linear fitting process and are labeled as blue circles and red triangles for left and right nanotube ends, respectively. The linear fits of both straightened nanotube end positions are also presented as off-set white dashed lines in the top right kymograph. From the linear fit, the polymerization rates for the left and right nanotube ends were measured to be 0.11 ± 0.01 and 0.14 ± 0.01 layers/sec, respectively.

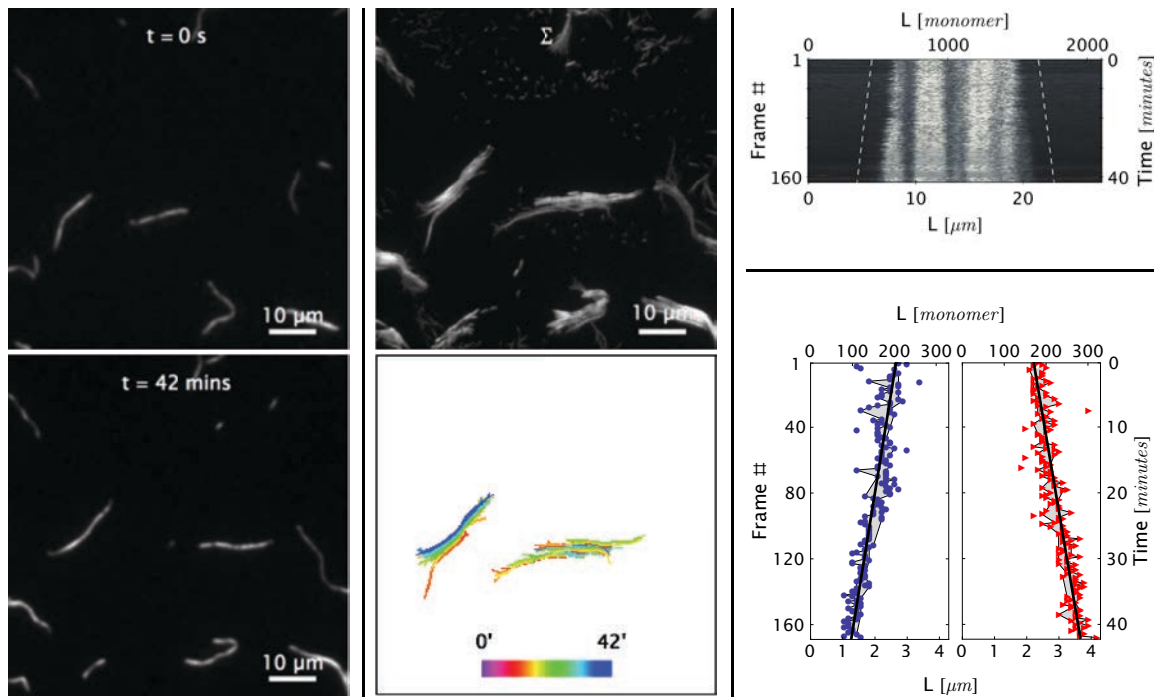


Figure 6.4.: At concentrations above the critical monomer concentration for a given temperature, DNA nanotubes grow at a constant polymerization rate. (Left) Before and after images of DNA nanotubes after 42 minutes of polymerization at $38.3 \text{ }^\circ\text{C}$ and 400 nM initial tile concentration in $1\times\text{TAE}/\text{Mg}^{++}$ and 0.3% (w/v) methylcellulose. The images were blurred over a pixel radius of 4 to reduce its sharpness for clearer presentation. In the original image, DNA nanotubes appear thin and sharp, which is hardly visible in small-sized images. All of the unmodified frames are compiled in Movie C.2. (Middle) DNA nanotubes were mobile during the course of the experiment. The correlated displacement of all DNA nanotubes in the field of view was likely due to the mechanical drift of our sample stage. The drift was very slow ($< 10 \mu\text{m}/40 \text{ min}$), which was much slower than the exposure time and did not affect the data analysis. (Right) The kymograph and linear fits of the right nanotube in the middle bottom panel support our expectation that at high tile concentration, DNA nanotubes grow at a constant polymerization rate. From the linear fit, the growth rate for the left and right nanotube ends were determined to be 0.043 ± 0.003 and 0.040 ± 0.002 layers/sec, respectively.

DNA nanotubes polymerize at steady rates

The linear fits of DNA nanotube end positions in Figs. 6.3 and 6.4 show that both polymerization and depolymerization of DNA nanotubes proceeded at steady rates. From the kymographs, we discovered that asymmetric polymerization rates for the two ends of an individual DNA nanotube were relatively common. A rigorous investigation of the physical source of this asymmetry would have required engineered pre-formed DNA nanotube nuclei, which was beyond the scope of this study.

6.3.2. Local and global analysis of combined polymerization data

To test the polymerization model, we measured the polymerization rates of 347 DNA nanotubes within a 0–500 nM concentration range and a 28.9–41.3 °C temperature range. Having established confidence in the steady polymerization rate, the polymerization rates were measured by comparing the nanotube lengths at two time points determined to be sufficiently far apart. We excluded DNA nanotubes that had undergone spontaneous scission, end-to-end joining, or side-to-side joining from our data set (observed directly in Movies C.1 and C.4). We used the ImageJ plugin by Kuhn and Pollard [KP05] to measure the DNA nanotube length from a refined trace of a curvilinear DNA nanotube image. In contrast to the kymograph method, this technique does not differentiate DNA nanotube ends and only measures the average polymerization rate of a DNA nanotube. This simple measurement method is far quicker than constructing a kymograph for each DNA nanotube. Also, by bypassing the alignment process, we could measure the rates from DNA nanotubes that did not have multiple bands.

The dependence of polymerization rates $\frac{dn}{dt}([tile], T)$ on free monomer concentrations $[tile]$ at different temperatures T (summarized in Fig. 6.5) was determined by non-linear global fit using the equations

$$\frac{dn}{dt}([tile], T) = k_{on}[tile] - k_{off}, \quad (6.1)$$

where

$$k_{off} = k_{on} e^{-(\Delta H^\circ - T\Delta S^\circ)/RT} \times u_0 \quad (6.2)$$

and n is the number of tile layers in a DNA nanotube, t is time, k_{on} is the rate constant associated with polymer growth, k_{off} is the rate constant associated with polymer

shrinking at standard concentration $u_0 = 1$ M, T is the temperature in Kelvin, ΔH° is the standard enthalpy of tile-DNA nanotube dissociation and ΔS° is the standard entropic cost of tile-DNA nanotube dissociation. In this model, we ignored the plausible (but likely small) kinetic and thermodynamic parameter differences between DNA nanotubes of different circumferences.

From the global fitting, the association rate constant k_{on} , was inferred to be $(5.99 \pm 0.15) \times 10^5$ /M/sec. The non-linear fit gave the thermodynamic parameters of the combined polymerization data to be $\Delta H^\circ = 85.9 \pm 0.2$ kcal/mol and $\Delta S^\circ = 0.251 \pm 0.006$ kcal/mol/K.

As a comparison to the global fitting results, the local linear fit results of the plots in Fig. 6.5 are summarized in Table 6.2. In these local fits, the polymerization rates $\frac{dn}{dt}$ at a given temperature T at different [tile] were subjected to linear fitting.

$$\frac{dn}{dt} = k_{on}[tile] - k_{off}, \quad (6.3)$$

The inferred association rate constants, k_{on} and dissociation constant $K_d = \frac{k_{off}}{k_{on}}$ from the local linear fittings were plotted against the reaction temperature in Fig. 6.6. The inferred values from local fits (solid circles) are in agreement with the theoretical model (solid line) using the inferred values of k_{on} , ΔH° , and ΔS° .

T (°C)	N (nanotubes)	[tile] range (nM)	k_{on} ($\times 10^5$ /M/sec)	k_{off} (min^{-1})	K_d (nM)
33.6	16	0–100	5.90 ± 0.61	0.87 ± 0.24	24.8 ± 9.3
35.2	35	0–200	5.06 ± 0.42	1.01 ± 0.31	33.7 ± 12.9
36.7	39	0–300	5.12 ± 0.34	2.87 ± 0.36	93.5 ± 18.1
38.3	48	0–400	6.64 ± 0.32	7.59 ± 0.46	190 ± 21
39.8	68	0–500	6.21 ± 0.30	15.96 ± 0.57	428 ± 36
41.4	62	0–500	5.52 ± 0.50	29.83 ± 0.93	901 ± 110

Table 6.2.: Summary of the inferred reaction rate constants from the local and global fits

To obtain the thermodynamic facet of our analysis, we plotted the same rates in Fig. 6.5 against temperature at different free monomer concentrations in Fig. 6.7. We extended the analysis by obtaining thermodynamic parameters from a local non-linear fitting with Eqs. 6.1 and 6.2. The inferred enthalpy and entropy parameters from the local fits are summarized in Table 6.3. The k_{on} , ΔH° and ΔS° from local fits in the range of were within

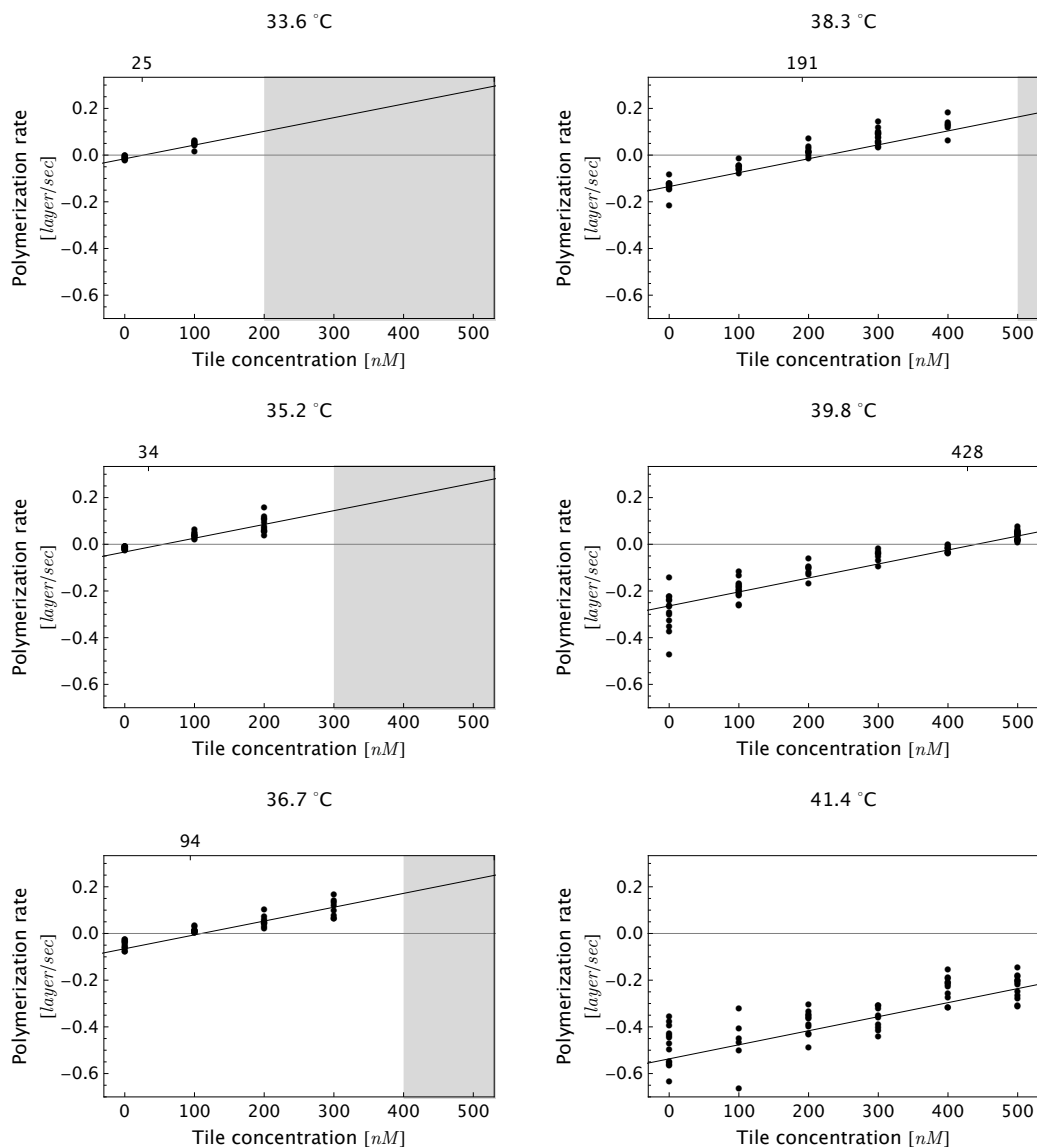


Figure 6.5.: Dependence of DNA nanotube polymerization rates on free tile concentration for several reaction temperatures. As expected, the polymerization rate was faster at lower temperatures and higher free monomer concentrations. The polymerization was assayed at 28.9–41.4 °C and 0–500 nM in $1\times$ TAE/ Mg^{++} 0.3% (w/v) methylcellulose. At each temperature, assays were performed at 0, 100, 200, 300, 400, and 500 nM. The typical tile concentration of the nuclei was 7 nM. The gray-shaded region represents the parameter space where we observed spontaneous nucleation and end-to-end joining, which invalidates measurements due to side-to-side joining between pre-formed nuclei and the newly nucleated nanotubes. Furthermore, the side-to-side joining obscured the time evolution of individual DNA nanotubes. As a consequence, the movies in the shaded parameter space were not analyzed. The fitting line is the global linear fit (Eq. 6.1). The numbers on the top horizontal axis are the inferred critical monomer concentrations, which were calculated by setting Eq. 6.1 to zero at given temperature T . The data at a given temperature and at different monomer concentrations was fitted separately (not shown), and the fitting results are presented in Table 6.2. The critical tile concentration for each temperature is given at the top of each plot in nM.

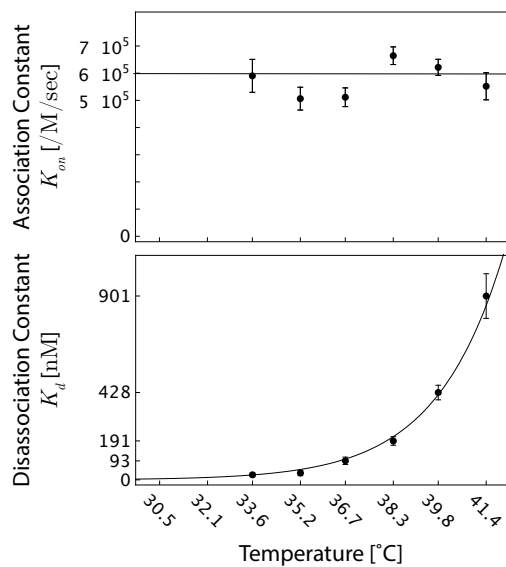


Figure 6.6.: (top) The inferred association rate constant k_{on} is relatively constant at different temperatures T . The solid line represents k_{on} based on global fits. (bottom) The inferred dissociation constant, K_d , for DNA nanotube polymerization grew exponentially (solid line) with the temperatures T . The dissociation constant was calculated by taking the ratio of inferred k_{off} and k_{on} parameters from the local fits. The line was computed by employing the best fitted ΔH° and ΔS° parameters from the global data fit and Eq. 6.2.

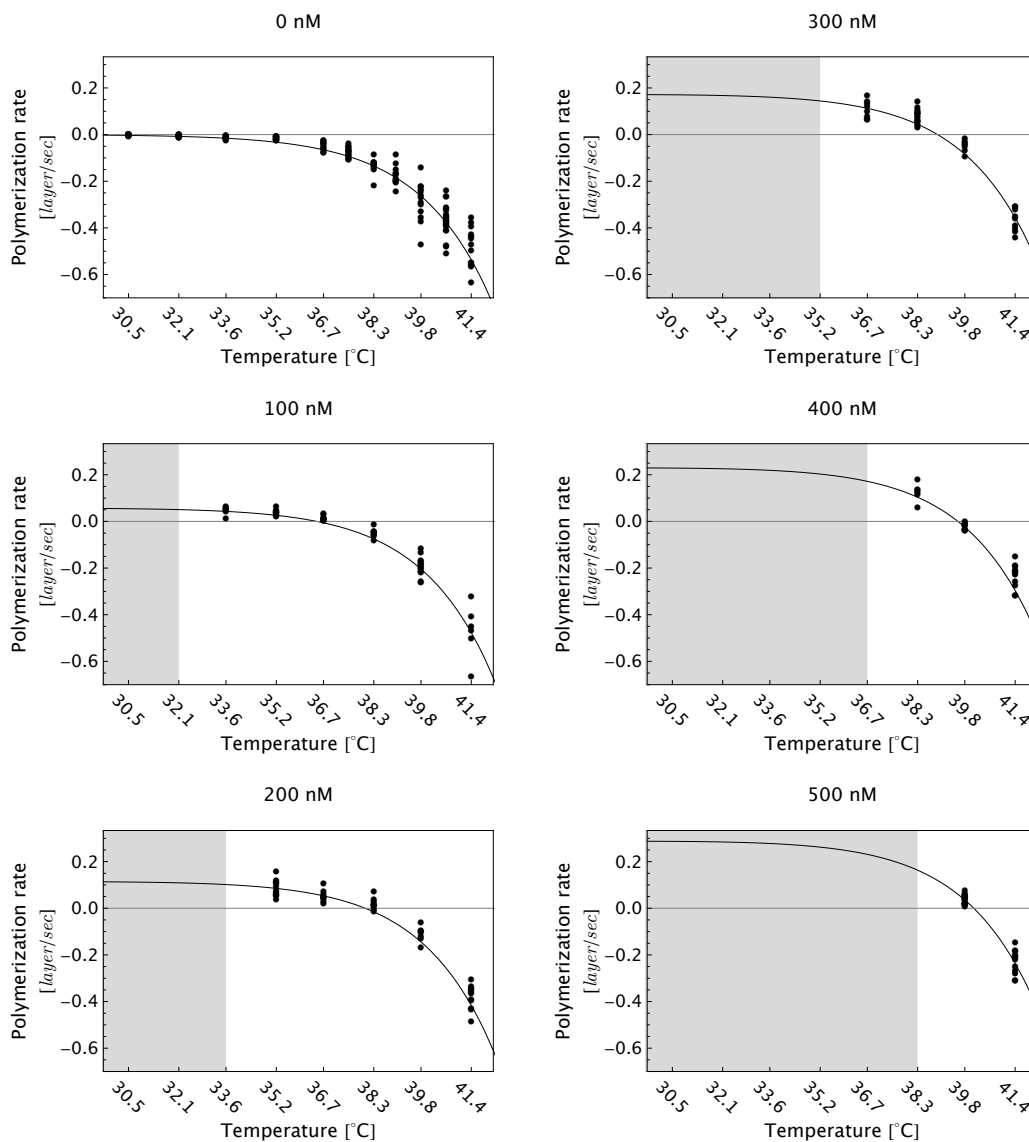


Figure 6.7.: At a given free tile concentration, DNA nanotubes elongate faster at lower temperatures, which reveals that DNA nanotube polymerization is at least partly enthalpy-driven. The gray-shaded region indicates the concentrations where significant spontaneous nucleation was observed for a particular reaction temperature. The solid line is the result of global fitting with Eq. 6.1 and 6.2

a factor of 10 from the global fit output. The local extractions of k_{on} , ΔH° and ΔS° at higher monomer concentrations were less reliable progressively because of the narrower valid temperature range due to rapid nucleation at high free monomer concentrations. Because of the inherent problem in extracting kinetics and thermodynamics parameters from local fitting, we only use the global fitting values of k_{on} , ΔH° and ΔS° in future analysis and discussions.

[<i>tile</i>] (nM)	N (nanotubes)	T range (°C)	k_{on} (10^6 /M/sec)	ΔH° (kcal/mol)	ΔS° (kcal/mol/K)
0	162	30.5–41.4	1.19±0.01	72.6±3.1	0.201±0.010
100	55	33.6–41.4	1.00±2.21	143±46	0.424±0.145
200	47	35.2–41.4	5.25±1.24	118±65	0.346±0.208
300	39	36.7–41.4	5.45±2.10	116±84	0.340±0.266
400	26	38.3–41.4	5.25±3.76	112±126	0.328±0.401
500	30	39.8–41.4	3.21±1.01	138±46	0.413±0.149
global fit	347		0.599±0.015	87.9±2.0	0.252±0.006

Table 6.3.: Summary of the best thermodynamic parameters from the local and global fits.

6.4. Discussion

To summarize our measurements, we developed a TIRF microscopy assay to directly observe the polymerization dynamics of single DNA nanotubes for up to 2 hours of imaging over a wide range of DNA tile monomer concentrations and temperatures. The long duration of time-lapse imaging requires stable temperature control and an autofocus system. The polymerization rates were measured by two methods, which were (1) constructing a kymograph from straightened traces of DNA nanotubes and (2) measurement of the nanotube length difference at two time points. The first method was able to simultaneously obtain the polymerization rates for both filaments and confirmed that each end depolymerizes (Fig. 6.3) or polymerizes (Fig. 6.4) at a steady rate. The second measurement strategy was used to analyze a much larger number of DNA nanotube polymerizations ($N = 347$ nanotubes) for extracting kinetic and thermodynamic parameters via global fitting.

6.4.1. Interpretation of the measured k_{on} and k_{off} rate constants

The polymerization of DNA nanotubes was modeled based on the kinetic Tile Assembly Model (kTAM) developed for theoretical study and simulation of algorithmic DNA tile self-assembly [Win98]. In the kTAM, the association between a tile and a binding site is assumed to be a reaction with forward rate

$$r_f = k_{on}^{site} [tile], \quad (6.4)$$

where k_{on}^{site} is the second-order association rate constant for an individual tile to an individual site. The reverse reaction rate depends on the stability of the binding and is modeled to be

$$r_{r,b} = k_{off,b}^{site} = k_{on}^{site} e^{-b\Delta G_{se}^{\circ}/RT + \alpha} \times u_0, \quad (6.5)$$

where b is the number of sticky end bonds, $\Delta G_{se}^{\circ} > 0$ is the standard free energy for breaking a single sticky end bond at standard concentration $u_0 = 1$ M, and αRT is the initiation energy for dsDNA formation with $\alpha \sim \ln(20)$ [Win98]. The standard free energy ΔG_{se}° can be further expressed as $\Delta G_{se}^{\circ} = \Delta H_{se}^{\circ} - T\Delta S_{se}^{\circ}$. In the kTAM, due to the weak bond strength of one sticky end interaction, a tile that binds with one sticky end will quickly disassociate from the nanotube end, as illustrated by the large arrow in the left panel of Fig. 6.8. In DNA nanotube polymerization, configurations where an incoming tile can bind with 3 or 4 bonds can be neglected because a DNA nanotube end is highly unlikely to contain any tile arrangement allowing for a tile to bind with 3 or 4 sticky ends. For the quantitative analysis, we ignored 1, 3, and 4 sticky end interactions and assigned the inferred ΔG° as the free energy of an interaction with two sticky-ends $\Delta G^{\circ} = 2\Delta G_{se}^{\circ} - \alpha RT$, $\Delta G^{\circ} > 0$ (Fig. 6.8 right panel).

6.4.2. Asymmetric polymerization

One unresolved issue was the surprisingly prevalent observation of asymmetric polymerization of the two nanotube ends. Further, the range in measured polymerization rates in a particular field of view was as large as a factor of 3. Local non-specific interaction between the glass surface and the DNA nanotubes is not likely to explain the difference because the local variation of glass surface is minimal and the measured DNA nanotubes were consistently able to diffuse in the confined space close to the glass surface.

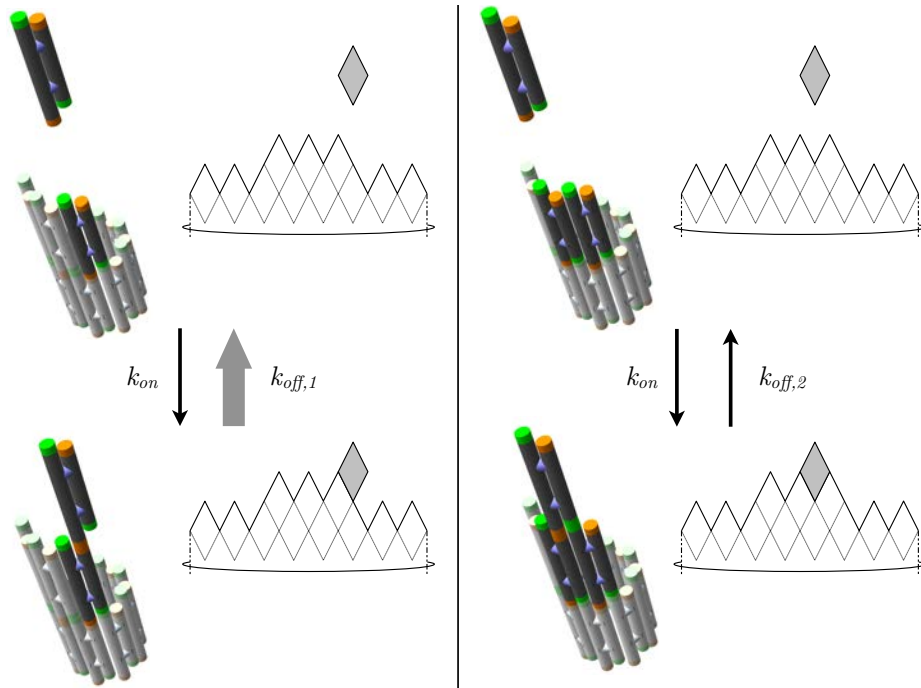


Figure 6.8.: In the kinetic Tile Assembly Model [Win98], the rate of a free tile attachment to an available site in DNA nanotube end k_{on}^{site} is independent of the number of sticky ends in the potential binding site. To satisfy detailed balance, the reverse rates depend on the number of available sticky ends. Hence, a DNA tile that only binds with one sticky end (left panel) will dissociate from a DNA nanotube faster than DNA tile with 2 bonds (right panel). The configuration of DNA nanotube ends and the position of dark tiles are different between left and right panels. Here, the highlighted attachment sites in the left and right panels provide 1 and 2 sticky ends, respectively. The attachment sites are illustrated as darker colored tiles. The sticky ends, illustrated as short green or orange tubes, are complementary when the colors match. The faster rate is indicated by the larger arrow of $k_{off,1}^{site}$ than $k_{off,2}^{site}$.

Hypothesis 1: The location of fluorophores on one end of DNA nanotubes bias the polymerization rate.

One intriguing hypothesis is that the asymmetry may arise from the physical difference between DNA nanotube ends, such as the location of fluorophores with respect to the attachment site. Since we put the fluorophore at one of the four corners of a DNA tile, only the sticky ends on one end of the DNA nanotubes are decorated with fluorophore.

Hypothesis 2: The asymmetric circumference of the pre-formed DNA nanotube ends gives rise to the observed asymmetric polymerization.

In our experiment, the formation of DNA nuclei involves stochastic end-to-end joining of short DNA nanotube nuclei with either Cy3 or Cy5 fluorophores. These short nanotubes has a range of nanotube circumferences. AFM measurements of opened DNA nanotubes on mica have revealed the diameter distribution of our DNA nanotubes (Fig. 6.9). Stochastic end-to-end joining of the heterogenous DNA nanotubes would likely generate DNA nanotubes with asymmetric ends.

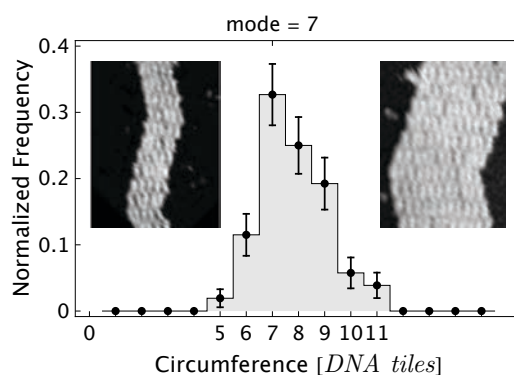


Figure 6.9.: Our annealing protocol produces DNA nanotube nuclei that are 5–11 tiles in circumference, with 7-tiles-wide DNA nanotubes as the most prevalent. Images of individual opened DNA nanotubes for constructing this histogram are presented in the (Fig. C.5). This measurement seems to be relevant to the variation in the polymerization rates observed in this experiment. Heterogeneous diameters were also observed in the *in-vitro* self-assembly of other tubular structures, such as protein microtubule [WCJ90, WC93, CW91]. The error bars are the standard deviation for each bin calculated using a bootstrapping method. (Insets) Representative images of the opened DNA nanotubes with diameter of 5 (left) and 11 (right) DNA tiles.

From a theoretical standpoint, the total ensemble of possible tile configurations along the circumference of DNA nanotubes gives rise to a dependence of the polymerization

rate on the nanotube diameter. Based on kinetic arguments, the only attachment site configurations that contribute to the elongation of nanotubes are the ones that can provide two sticky end bonds, $b = 2$. For multi-monomer-wide nanotubes, there are more binding sites in wider nanotubes than in the thinner nanotubes. However, not all of the binding sites can provide $b = 2$ available sticky ends. As examples, the top half of Fig. 6.8 show a configuration of 8-monomer wide DNA nanotubes ($m = 8$). The configuration provides 7 sites with $b = 2$, which corresponds to $f_{b=2}^{m=8} = 7/8$. The denominator of the calculated f_b^m is the nanotube circumference and accounts for the larger number of maximum $b = 2$ sites observed in wider nanotubes compared to thinner nanotubes.

The average fraction of sites that can provide $b = 2$ sticky ends per m -monomer wide nanotubes $\langle f_{b=2}^m \rangle$ decreases with increasing nanotube circumference m . At the lower limit, $\langle f_{b=2}^{m=1} \rangle$ of a 1-monomer wide nanotube is 1. It is important to realize that a 1-monomer wide nanotube is a chain that behaves differently from nanotubes with $m \geq 2$. The growth of a 1- monomer wide nanotube is isodesmic, which means that the strength of the interactions between monomers in the middle of a 1-monomer wide nanotube is the same as the interaction in the collision between free monomers in solution [dGM08]. It should also be noted that in the analysis of this hypothesis, we are ignoring the diameter-dependent strain energies that are undoubtedly experienced by nanotubes [RENP⁺04,SS06] and which in this case would probably be relieved by breaking stacking bonds at the nicks adjacent to sticky ends.

For nanotube circumference $m \geq 2$, our model assumed that for m monomer wide nanotube, the arrangement at nanotube growth front is a one-dimensional random walk with total number of steps equal to $2 \times m$ (Fig. 6.10). The factor 2 is based on the number of sticky end pairs (A and B) that serve as binding domains for m monomer wide DNA nanotubes. To form a tubular structure, the numbers of A's and B's have be equal to m . In Fig. 6.10, the A and B sticky end interactions are depicted as red (/) and blue (\) lines, respectively. In the language of one-dimensional random walks, a series of A (red /) and B (blue \) lines is equivalent to a sequence of left and right steps of a random walker.

Fig. 6.10 shows ensembles of possible tile configurations for the growing end of 1, 2, and 3 monomer wide nanotubes. Each configuration is unique due to the rotational and translational symmetry. The numbers of on-sites and off-sites were calculated by counting the number of peaks and valleys, respectively. The valleys correspond to the attachment sites (on-sites) with 2 available sticky ends. The peaks are the off-site locations where the tile has to break 2 sticky ends to dissociate from the nanotube. Both valleys and peaks are

found when the random walk switch direction from A to B, and vice versa. Interestingly, because both A and B have to be present in equal number in all configurations, the number of valleys and peaks also have to be equal.

For finite diameters m , the number of red and blue steps must be equal, and therefore there are global constraints on what configurations occur, from which we can see that the probabilities cannot be simply those of an unbiased random walk with independent steps. Nonetheless, we show that if nanotube growth occurs according to kTAM rates with every step involving the addition or removal of a single tile that forms exactly 2 sticky end bonds, then the steady-state distribution of random walk configurations (sequences of an equal number of red and blue steps, m each, treating rotationally symmetric states as distinct) must be uniform. Consider a continuous-time discrete-state Markov process on these states, with transitions according to the kTAM. A configuration i that has n valleys and n peaks, will have n neighbors, j , to which it can transition with rate r_f , and from which it can transition with rate $r_{r,2}$, as well as n neighbors, k , to which it can transition with rate $r_{r,2}$ and from which it can transition with rate r_f . Letting p_i be the steady-state probability of configuration i , the dynamics gives

$$\frac{dp_i}{dt} = \sum_j (p_j r_{r,2} - p_i r_f) + \sum_k (p_k r_f - p_i r_{r,2}).$$

Substituting our ansatz that $p_i = 1/N$ where N is the size of the state space, we see that

$$\frac{dp_i}{dt} = n \left(\frac{1}{N} r_{r,2} - \frac{1}{N} r_f \right) + n \left(\frac{1}{N} r_f - \frac{1}{N} r_{r,2} \right) = 0,$$

which establishes that the uniform distribution is the unique steady state for this connected Markov process.

The steady state behavior of nanotubes with m approaching ∞ is less sensitive to the constraints on the random walk. Consequently, $\langle f_{b=2}^{m \rightarrow \infty} \rangle$ can be estimated from an unconstrained and unbiased one-dimensional random walk. At any position, the probability of finding a valley (on site) or a peak (off site) is $\frac{1}{2}$. Therefore, the limit of $\langle f_{b=2}^{m \rightarrow \infty} \rangle$ is $\frac{1}{2}$.

In summary, $\langle f_{b=2}^m \rangle$ is maximum for 1-monomer nanotubes, decreases with increasing nanotube circumferences, and approaches $\frac{1}{2}$ as the nanotube diameter approaches infinity. Finally, the kinetic rates of m -monomer wide DNA nanotube polymerization, k_{on}^m and k_{off}^m , can be effectively estimated from the kinetic rates of interaction for an incoming tile to

bind to an available site at the end of a DNA nanotube, k_{on}^{site} and k_{off}^{site} , by the simple expressions $k_{on}^m = \langle f_{b=2}^m \rangle k_{on}^{site}$ and $k_{off}^m = \langle f_{b=2}^m \rangle k_{off}^{site}$.

We tested the width-dependent polymerization rate by running stochastic simulations for DNA nanotubes with 1 to 16 monomer circumferences at different free monomer concentrations (Fig. 6.11). The rates at which a monomer arrived to an available site at nanotube end, r_f , and disassociated from a non-empty neighboring site, $r_{r,b}$ were computed based on the kTAM. The simulations (Fig. 6.11) supported the theoretical dependence of the polymerization rate on the DNA nanotube circumference. Quantitatively, $\langle f_{b=2}^m \rangle$ for 1, 2, and 3 monomer nanotubes obtained from the simulations was 1, 0.67, and 0.61, respectively, which is in agreement with the theoretical value based on the Markov chain analysis in Fig. 6.10 (1, $2/3$, and $3/5$, respectively).

Because in the model considered here, we ignore any possible diameter-dependent strain energy, the on-rates, off-rates, and critical monomer concentration do not depend on the nanotube circumference. Thus, we see that there is the variability in overall growth rates k_{on} and k_{off} even when (or if) there is no thermodynamic variability for tile attachment and k_{on}^{site} and k_{off}^{site} both remain constant. That said, for the range of nanotube diameters seen in our experiments (diameters 5 to 11, Fig. 6.9), our simulations show that the polymerization rates should not depend strongly on diameter if there is no diameter-dependent strain energy. In fact, simulated polymerization rates for diameters 5 to 11 were close to the polymerization rate of 2-dimensional DNA lattices (bottom blue dashed line), which was computed to be half the polymerization rate of 1-monomer nanotubes (top blue dashed line).

Assuming that the experimentally observed asymmetric polymerization was due to the heterogeneity in the distribution of the nanotube diameter, the dependence should have arisen from the energetic dependence of m -monomer DNA nanotubes on the nanotube circumference rather than on the logical shape of tile attachment. It is important to note that the kTAM assumes that both ΔH° and ΔS° are independent from nanotube circumference. Based on previous models of DNA nanotubes [REN⁺04] and two-dimensional DNA lattices (Appendix D), the contributions of electrostatic and twist penalty to the overall energetics of DNA nanotubes are expected to depend on nanotube circumference.

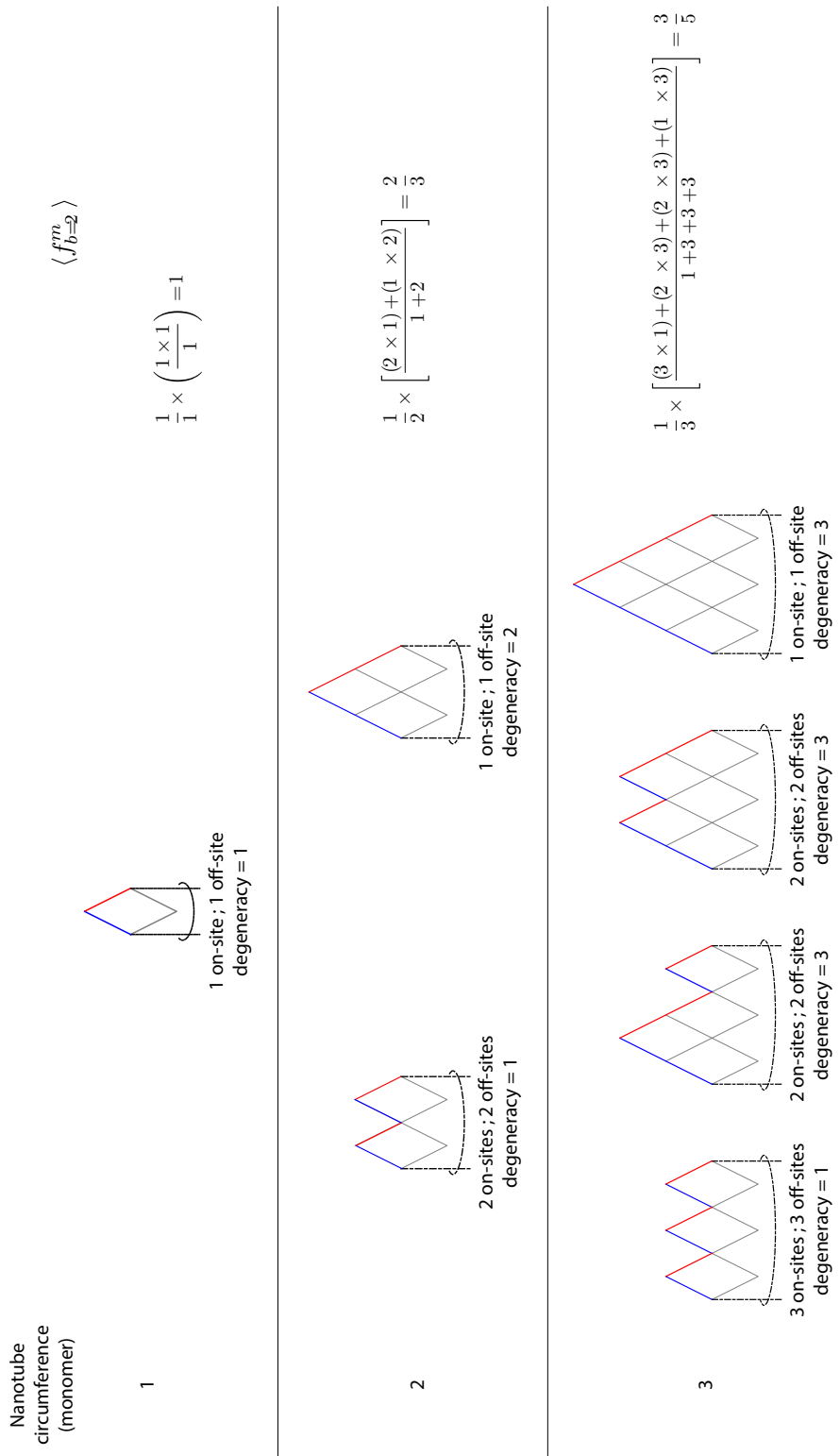


Figure 6.10.: The possible tile configurations along the nanotube end with circumference = 1, 2, and 3 monomers. A tile is represented as a white diamond. Blue and red solid lines denote the sticky end types. Dashed lines indicate connectivity between two longitudinal edges of the two-dimensional representation of a nanotube end. In all configurations, each tile is required to interact with ≥ 2 neighboring tiles. The value of $f_{b=2}^m$ are calculated based on the circumference, numbers of on- and off-sites, and their degeneracies.

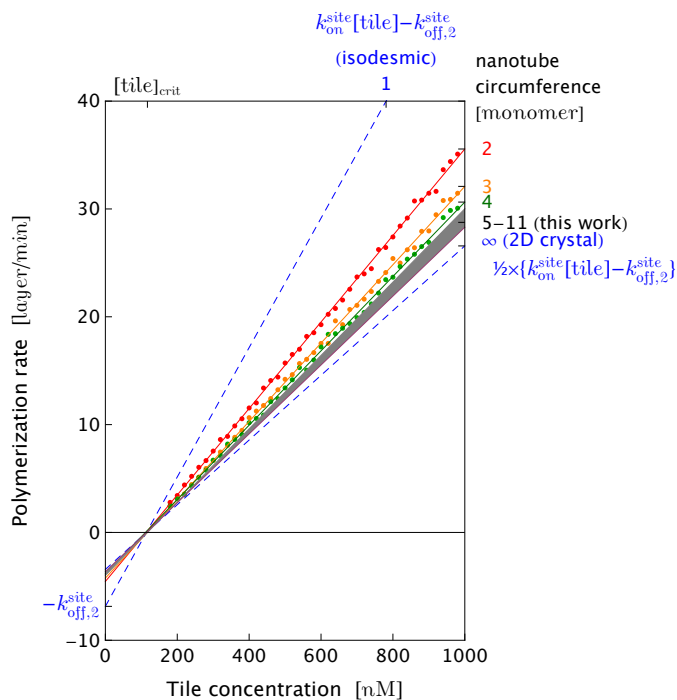


Figure 6.11.: Stochastic simulation reveals the dependence of polymerization rates on DNA nanotube diameter. Nanotubes with larger circumference polymerize slower than thinner nanotubes. In the plot above, the on rate and the standard free energy of a single sticky end was chosen to be $k_{on}^{site} = 10^6$ /M/sec and $\Delta G_{se}^{\circ} = 8 RT$ for all nanotube diameters. In the plot, $k_{off,2}^{site}$ is defined as the disassociation rate of a DNA tile with 2 bonds and is equal to $k_{on}^{site} e^{-2\Delta G_{se}^{\circ} + \alpha RT}$. The polymerization rates for 2-, 3-, and 4-monomer DNA nanotube are denoted as red, orange, and green circles, respectively. Each data set was subjected to linear fit based on Eq. 6.3. The simulation results for 5- to 11-monomer nanotubes, which is the circumference range of the DNA nanotubes in our experiment, reside in the gray shaded region. The upper bound (top blue dashed line) is the polymerization rate for 1-monomer DNA nanotubes = $k_{on}^{site}[tile] - k_{off,2}^{site}$, while the lower bound (bottom blue dashed line) is the expected effective rate for the two-dimensional DNA lattice = $1/2 \times \{k_{on}^{site}[tile] - k_{off,2}^{site}\}$.

6.4.3. Comparison with previously reported reaction rates of DNA self-assembled structures

Inferred association rate constant

In section 6.3.2, we measured k_{on} to be $(5.99 \pm 0.15) \times 10^5$ /M/sec for the polymerization model. In kTAM, the inferred association rate constant for a single DNA tile binding to an available site at the end of a DNA nanotube k_{on}^{site} was expected to be $\approx 2 \times k_{on} = 2 \times (5.99 \pm 0.15) \times 10^5$ /M/sec. The inferred k_{on}^{site} fell within the same order of magnitude as the previously reported forward rate measurements involving DNA hybridization [QW89, GT81, WF91, MS93], and from numerical analysis of tile-based DNA self-assembly [ZW09]. Quartin and Wetmur [QW89] showed that the association reaction of a simple interaction between two short DNA strands is diffusion limited and determined k_{on} to be on the order of 6×10^5 /M/sec. From a series of DNA toehold exchange experiments, Zhang and Winfree obtained the range of forward rate to be $(1-6) \times 10^6$ /M/sec [ZW09].

The most comparable analysis of DNA self-assembly to the DNA nanotube polymerization reported here, is the kinetic Monte Carlo simulation of DNA ribbon growth done by Chen *et al* [CSGW07]. However, their kinetic parameter measurement was indirect. To obtain agreement between their AFM observation of assembly data and their simulations, Chen *et al* chose the forward rate k_{on}^{site} to be 17×10^6 /M/sec, which is $14 \times$ faster than our measurement. Given the sensitivity of their simulation results to the two adjustable parameters, namely k_{on}^{site} and the free energy of sticky-end interaction ΔG° , it is likely that their inference of k_{on}^{site} value had significant uncertainty, which was not explicitly stated in the manuscript. In two separate works with different types of DNA ribbon, Schulman and Winfree [SW07] as well as Fujibayashi and Murata [FM09] used 10^6 /M/sec as the typical association rate constant in their analysis and found the number reasonable.

Thermodynamic parameters

To evaluate the inferred thermodynamic parameters of our measurement, we compared the enthalpy and entropy values to theoretical predictions and to values from previously reported studies of the free energy of DNA hybridization. Both inferred enthalpy and entropy values are very close to the theoretical estimates used in the original presentation of the kTAM paper [Win98]. In that framework, the expected enthalpy of disassembly was calculated to be $\Delta H^\circ = R \times sb \times (4000 \text{ K})$, where s is the number of base pairs in a

sticky end and b is the number of sticky end bonds. For $b=2$, $s=6$, the simple expression yielded the value of $\Delta H^\circ = 95$ kcal/mol, which is within 10% of our measurement of $\Delta H^\circ = 87.9 \pm 2.0$ kcal/mol. For the entropy, using the kTAM, $\alpha = \ln(20)$ [Win98], the theoretical value was predicted to be $\Delta S^\circ = R \times (11sb + \alpha) = 0.268$ kcal/mol/K, which is within 10% of the measured $\Delta S^\circ = 0.251 \pm 0.006$ kcal/mol/K in our experiment. Finally, our inferred values of ΔH° 's and ΔS° 's, we calculated the standard free energy of two sticky end interactions at 37 °C to be $\Delta G_{37^\circ C}^\circ = \Delta H^\circ - T_{37^\circ C} \Delta S^\circ = 12.2$ kcal/mol and 9.5 kcal/mol for the values based on kTAM and our experiment, respectively. The $\Delta G_{37^\circ C}^\circ$ from kTAM is within 30% difference from our measured $\Delta G_{37^\circ C}^\circ$.

To the best of our knowledge, the only published values for thermodynamic parameters of double crossover tile-based DNA structures in solution were obtained from bulk studies of DNA ribbons of designed widths [SW07]. The ribbons of different widths were composed of multiple tiles with 5 bp sticky ends, which is shorter than the 6 bp sticky ends in our tiles. Schulman and Winfree extracted ΔH° and ΔS° from a series of UV absorbance data by employing van't Hoff analysis. They measured $\Delta H^\circ = 102.4$ kcal/mol and $\Delta S^\circ = 0.300$ kcal/mol/K. To account for their shorter sticky ends, we multiplied these values by 6/5, which is the ratio of sticky end lengths of our DNA nanotube and Schulman and Winfree's ribbon, which gives $\Delta H^\circ = 122.9$ kcal/mol and $\Delta S^\circ = 0.360$ kcal/mol/K. Their adjusted values of ΔH° and ΔS° are within 45% and 22% of our measurement, respectively. Using these adjusted ΔH° 's and ΔS° values, we calculated $\Delta G_{37^\circ C}^\circ = 11.3$ kcal/mol, which is within 18% of our measured $\Delta G_{37^\circ C}^\circ$.

The thermodynamic parameters of DNA hybridization depend strongly on the DNA sequences and buffer condition, which could explain the difference of as much as 45% between our measurements and the thermodynamic values obtained by Schulman and Winfree. Moreover, the inter- and intra-monomer strain between DNA ribbons and DNA nanotubes are likely to be different. Their published n -tile-wide ribbons assembled from $2(n-2)$ unique single tile and two double tiles, each have different sticky end sequences compared to the tile used in this work. In addition, their thermodynamic measurements were acquired in the absence of crowding agent and in 12.5 mM concentration of Magnesium, compared to 10 mM in our polymerization buffer.

Furthermore, the measured thermodynamic values are also not incompatible with Nangreave *et al.*'s van't Hoff analysis of their FRET measurement of quadruple-crossover (QX) molecules [NYL09]. The QX molecule, in essence, is a flat sheet of 4 parallel DNA helices. By attaching different 6 bp sticky ends to a QX pair, the thermodynamic properties of dif-

ferent configurations of sticky ends were extensively studied. The relevant subset of their experiments is the measurement of the interaction between 2 pairs of sticky ends that are located adjacent to each other. In the two variants that they constructed, the enthalpy was measured to be 105.1 ± 7.8 kcal/mol and 116.6 ± 19 kcal/mol. For the entropy of the reaction, they determined the values to be 0.301 ± 0.025 kcal/mol/K and 0.334 ± 0.057 kcal/mol/K. These values are within a range that is less than 36% of our measurement.

Another relevant value to compute is the expected melting temperature T_m of DNA nanotubes in Kelvin. From simple thermodynamics, the melting temperature can be calculated as

$$T_m = \frac{\Delta H^\circ}{\Delta S^\circ - R \ln[\text{tile}]} \quad (6.6)$$

Using the theoretical values from kTAM [Win98], the melting temperature for a reaction with 100 nM, 200 nM, 300 nM, 400 nM, and 500 nM free tile concentration is calculated to be 43.5 °C, 44.9 °C, 45.7 °C, 46.4 °C, and 46.9 °C, respectively. The calculated values are less than 8 °C higher than the measured equilibrium temperature in the polymerization rate vs. temperature plots (Fig. 6.7), which is in close agreement with our measurement and predictions based on a simple model. Similarly, the discrepancy in T_m is likely because the kTAM number is derived from a simple model and ignores the sequence dependence of ΔH° and ΔS° . Nonetheless, this close agreement illustrates the usefulness of the simple energetics model in the kTAM for estimating thermodynamic values in DNA self-assembly.

6.4.4. Comparison with the polymerization rates of actin and microtubules

The kinetic Tile Assembly Model possesses the same kinetic and thermodynamic features as the kinetic model for actin polymerization [KP05]. The forward rates of DNA nanotube, actin filament, and microtubule assemblies are modeled as reactions that depend on the free monomer concentration-dependent reaction. Actin filaments and microtubules are asymmetric polymers. The polymer ends have different thermodynamic free energies and kinetic rates. The association rate constant for an ATP bound actin monomer to attach to an actin filament has been measured at the single molecule level to be 0.5×10^6 /M/sec and 7.4×10^6 /M/sec for the pointed and the barbed end, respectively [KP05]. For microtubules, the association rate constant for α, β -tubulin bound GMP-CPP, an unhydrolyzable analog of GTP, to dock to a microtubule at 37 °C has been measured by bulk assay to be 5.4×10^6 /M/sec [HSD⁺92]. The association rate constant k_{on} values of actin and microtubules are comparable to the measured k_{on} in our assay. The monomer dissociation

rate for actin and microtubule polymerization depends on the bond strength. The dissociation rate of fuel-bound monomers, such as ATP-actin and GTP-tubulin, is slower than waste-bound monomers. The qualitative and quantitative similarities between the DNA nanotube and actin provide additional support for the DNA nanotube as an attractive engineering material for *de novo* creation of an artificial cytoskeleton.

Although both polymers have comparable k_{on} values, typical polymerization of actin and microtubules is on the order of 1 layer/sec or faster, compared to the 0.1 layer/sec mean polymerization rate of DNA nanotubes reported here. Faster polymerization rate gives actin and microtubules morphological flexibility. These biopolymers can assemble structures when cell needs them and stabilize them by capping proteins. The faster cytoskeleton polymerization rate is a direct result of the higher free monomer concentration in cellular *milieu*, which is on the order of 1 μM . In our study, the relatively high spontaneous nucleation rate in DNA nanotubes prevented us from performing polymerization assays at comparable concentrations to those of the actin and microtubules. Hyman *et al.* [HSD⁺92] have shown that the coupling between polymerization and stochastic GTP hydrolysis is responsible for the slow spontaneous nucleation rate of protein microtubules. Docking of an α,β -tubulin monomer that is bound to GTP on a growing microtubule, triggers the stochastic GTP hydrolysis reaction, which weakens the tubulin–microtubule binding and increases the dissociation rate significantly. Inspired by this elegant solution, it will be interesting to examine how to incorporate energy consuming reactions into the interaction between DNA tiles and between DNA tiles and DNA nanotubes in order to achieve a higher nucleation barrier than the one observed in the existing passive DNA nanotube system, such as the one used in this work.

6.5. Concluding remarks and outlook

From single-molecule movies, we were able to systematically test a mathematical model of DNA self assembly while extracting both the kinetic and thermodynamic parameters of DNA nanotube polymerization. The polymerization model depends on the tile concentrations and is sensitive to reaction temperature. To the best of our knowledge, this experiment is the most accurate measurement of DNA tile-based self-assembly to date. Our experiment justifies the use of polymerization theory developed for one-dimensional cooperative polymers, such as microtubules and actin, to accurately model DNA nanotube polymerization.

The most basic demonstration of non-equilibrium polymer dynamics is steady elonga-

tion or shortening at a constant monomer concentration that is far from the critical DNA tile concentration. Toward this end, we have engineered a sustainable far-from-equilibrium dynamic of DNA nanotubes. In the future, the coupling between DNA nanotube polymerization and an analog of nucleotide hydrolysis could potentially recapitulate the more complex non-equilibrium cytoskeleton-based dynamics [HH03], such as treadmilling [CLZ82] and dynamic instability [MK84a], where polymerization and depolymerization co-exist at steady state without ever reaching equilibrium. These novel dynamics can only be observed at the single molecule level, as demonstrated with the TIRF assay reported here.

6.6. Acknowledgments

We would like to acknowledge Rebecca Schulman, Damien Woods, Matthew Cook, Tosan Omabegho, Heun Jin Lee, Ethan Garner, Michael Diehl, Zahid Yaqoob, Nadine Dabby, and Paul Rothmund for their helpful discussions. The authors especially thank Rebecca Schulman and Ann McEvoy for pointing our attention to glass capillary chambers, and Matthew Cook for analysis of 2D crystal growth front dynamics. The length measurements were made possible because of Jeffrey Kuhn's generosity in sharing his filament snapping and length measurement codes. This work was supported by NSF through the grants EMT-0622254, NIRT-0608889, CCF-0832824 (The Molecular Programming Project), and CCF-0855212.

7

Toward *de novo* recapitulation of cytoskeletal dynamics with DNA nanotubes



Cytoskeletal Motor (Ann Erpino)
www.annerpino.com

"Ann envisioned a vine crawling across the desert by extending branches in one direction and withering away in the other" as a macroscopic analog of a microtubule treadmilling in a cellular environment." (adapted from *Coagula Art Journal* (85):22, April 2007)

■ Abstract

Cytoskeletal polymers, such as actin filaments and microtubules, harness energy from nucleotide hydrolysis to exhibit asymmetric polymerization, such as treadmilling and dynamic instability. This study describes how a non-equilibrium polymer that can potentially recapitulate cytoskeletal phenomena is created by rationally engineering existing equilibrium DNA nanotubes. We couple a DNA analog of a nucleotide hydrolysis reaction to the polymerization of DNA nanotubes and embed a simple modification into the currently passive DNA nanotube architecture. We inserted the EcoRI restriction sequence into one sticky end pair on a DNA tile, so that docking the tile to a growing polymer will complete the restriction site, shorten the sticky end length, and, thus, weaken the sticky end strength. The recapitulation of non-equilibrium cytoskeletal phenomena with completely synthetic structures may provide an ultimate test of our understanding of the design principles underlying cytoskeletal dynamics, in particular, the minimal architectural or mechanistic requirements for treadmilling and dynamic instability.

7.1. Introduction

Living systems operate away from equilibrium. The cell, a unit of life, relies on active cytoskeletal polymers, such as actin filaments and microtubules, to separate chromosomes during mitosis [DM97], determine cell shape and polarity [LC04, LG08], probe the environment with filopodia [ML08], and direct cellular motility with lamellipodia [ML08]. These active polymers harness the energy from a reservoir of the fuel molecule nucleoside triphosphate (NTP) by coupling their polymerization with an irreversible reaction, called *nucleotide hydrolysis*. The energy derived from nucleotide hydrolysis powers active poly-

The version presented in this chapter is mostly for documentation purposes and is not a final manuscript. This chapter will be revised and made more concise for submission as:

Rizal F. Hariadi and Erik Winfree,
Toward *de novo* recapitulation of cytoskeleton dynamics with DNA.
in preparation

The materials in the appendix D is taken from my class final project in APh 161: The physics of biological structure and function. The class poster can be downloaded from the class web site

<http://www.rpgroup.caltech.edu/courses/aph161/Lecture/Poster%20RH.pdf>

Author contributions

RFH and EW conceived and designed the experiments. RFH performed the experiments and ran stochastic simulations. RFH and EW analyzed the data. RFH and EW revised the thesis chapter.

mers, such as actin filaments and microtubules, with three properties not found in passive polymers. First, nucleotide hydrolysis removes the constraint that the critical concentration of free monomers near the two ends must be the same. Asymmetric critical concentration permits the simultaneous elongation on one end of the polymer and shrinkage on the other end that results in one class of cytoskeletal dynamics called *treadmilling* [HSD⁺92]. Second, active polymers can stochastically switch between elongation and shrinking phases, thus giving rise to cytoskeletal dynamics called *dynamic instability* [MK84b, MK84a]. Third, nucleotide hydrolysis suppresses spontaneous nucleation [HSD⁺92]. As a result, polymerization occurs at concentrations far higher than the critical monomer concentration. These non-equilibrium implications of nucleotide hydrolysis allow actin filaments and microtubules to respond quickly to signals and perform mechanical work to alter cell morphology during cell growth and motility without synthesizing new proteins or degrading existing polymers.

To shed light on how these cytoskeletal polymers convert chemical energy into directional motion, in this study we adopt an engineering approach in which a *de novo* artificial cytoskeleton is constructed using DNA nanotubes. DNA nanotube polymerization and an analog of nucleotide hydrolysis are coupled in order to investigate how the energy consumption step can be converted to alter DNA nanotube polymerization. In particular, we are interested in investigating minimal architectural and mechanistic features required for treadmilling.

DNA nanotubes are promising candidate materials for the construction of an artificial cytoskeleton [ENAF04, RENP⁺04] due to their programmability and their physical similarities to cytoskeletal polymers (Table 7.1). In structural DNA nanotechnology, short synthetic oligonucleotides can be designed to form a small DNA complex, called a DNA tile, that can act as a monomer for the polymerization of larger crystalline structures using the specificity of canonical Watson-Crick hybridization [See82, WLWS98, Rot06, RENP⁺04, YHS⁺08, SW07, LZWS10, ZBC⁺09]. DNA nanotubes present a simple example of how a long one-dimensional crystalline structure can arise from the interactions between many copies of a single DNA tile type. Fig. 6.1 shows a DNA tile that possesses four short single-stranded regions, known as sticky ends, which serve as binding domains. The sticky end arrangement, in addition to the constraint provided by the biophysical properties of the single- and double-stranded-DNA, directs the interaction of DNA tiles to form tubular DNA structures. Despite the advancement of structural DNA nanotechnology, embedding the suitable DNA implementation of cytoskeletal design principles, as described in

section 7.3, into DNA nanostructure has never been demonstrated.

The morphological, thermodynamic, and kinetic properties of DNA nanotubes have been extensively studied. Single molecule assays of DNA nanotube dynamics have shown that at 25–40 °C, the forward reaction rate k_{on} of both DNA nanotubes and microtubules are comparable (see Chapter 6). The dissociation rate of DNA tiles from DNA nanotubes can be fine-tuned to give desirable depolymerization rates by engineering the sticky end length and sequence and by controlling external parameters, such as buffer conditions and reaction temperatures.

In this study, we describe the strategy of incorporating a DNA analog of nucleotide hydrolysis into DNA nanotube self-assembly. The scheme is characterized by gel assays, visualized by single molecule movies, and theoretically probed by stochastic simulation. The coupling of DNA nanotube polymerization with a DNA analog of nucleotide hydrolysis has the potential to recapitulate more complex cytoskeleton-based dynamics, such as treadmilling and dynamic instability, where polymerization and depolymerization co-exist at steady state without ever reaching equilibrium.

7.2. The biophysics of microtubules

We begin this section by introducing cytoskeleton composition, self-assembly, and their roles in living cells. The physical similarities between α,β -tubulin and DNA tiles provide the basis for our artificial cytoskeleton design. For clarity, we limit our discussion to microtubules [H97]. A comparison of microtubule, DNA nanotube, and carbon nanotube assembly is presented in Table 7.1.

7.2.1. The structure of microtubules

The study of microtubules structures and dynamics has a long history [H97]. Cellular and developmental biologist purified microtubule-containing architectures in 1952 [MD52]. In 1960's, scientists discovered the structural properties of the monomer [ST68]. The structure contains two polypeptide chains (α - and β -tubulin) that act as the monomer for microtubule. The α,β -tubulin dimer has a net ≈ 40 negative charges (at cellular pH) and consists of ~ 900 amino acid (~ 100 kDa). Structurally, the α,β -tubulin dimer is approximately an oblate spheroid 8 nm in one direction and 4 nm in the other two dimensions.

In the study of microtubules dynamics, the first landmark study was the development of a reliable protocol for the *in vitro* assembly of microtubules by Weisenberg [Wei72].

	Microtubules	DNA nanotubes (described in chapter 6)	carbon nanotubes [PF08]
Structural properties			
subunit	α - β -tubulin	DNA tile	carbon atom
subunit size	$\sim 4 \times 4 \times 8 \text{ nm}^3$	$\sim 2 \times 4 \times 14 \text{ nm}^3$	0.26^3 nm^3
subunit mass	$\sim 2 \times 50 \text{ kDa}$	$\sim 50 \text{ kDa}$	12 Da
net charges per subunit	$\approx 40 e^-$	$156 e^-$	0
persistence length	$5.2 \times 10^3 \mu\text{m}$ [GMNH93]	$\sim 20 \mu\text{m}$ [RENP ⁺ 04, ORKF06]	$0.50 \mu\text{m}^a - 50 \mu\text{m}^b$
circumference	8-19 monomers [CW91, WCJ90]	5-14 DNA tiles (Figs. 6.9 and C.5)	0.6-2.0 nm [ACP07]
Self-assembly			
synthesis	self-assembly under physiological condition	self-assembly under mild condition	arc discharge, laser ablation, CVP ^c (harsh conditions)
		(Figs. 6.5 and 6.7)	
association rate constant	$5.4 \times 10^6 \text{ M}^{-1} \text{sec}^{-1}$ [HSD ⁺ 92]	$(5.70 \pm 0.15) \times 10^5 \text{ M}^{-1} \text{sec}^{-1}$	
driving force	predominantly entropy driven ^d	predominantly enthalpy driven ^e	enthalpy H driven
subunit interaction	non-covalent	non-covalent	covalent
nucleating structures	γ -tubulin [ZWAM95]	DNA origami ^f	metal catalyst
fuel	GTP	ssDNA (partially demonstrated)	N/A
energy consumption	GTP hydrolysis	nicking reaction (partially demonstrated)	N/A
Accessory molecules			
molecular motor	kinesin, dynein	DNA walkers	N/A
accessory molecules	various MAPs (Microtubule Accessory Protein)s	ssDNA activator ssDNA deprotector [ZHCW13]	N/A
signaling	protein network	DNA circuit [ZHCW13]	N/A
Higher order system			
self-organized architecture	self-organization of microtubules and motors [NSML97], cellular architecture	has not been demonstrated	N/A

Table 7.1.: A comparison of microtubules, DNA nanotubes, and carbon nanotubes.

^aThe persistence length of acid etched carbon nanotubes [SKOS01].

^bThe persistence length of acid pristine single walled nanotube [KDE⁺98].

^cChemical Vapor Deposition

^dThe microtubule polymerization is inhibited by low temperature T and high pressure p [Mar38]. Since the Gibbs free energy is $G = H - TS = E + pV - TS$, the polymerization of microtubules is predominantly driven by entropy S changes. This should not come as a surprise once the role of water molecules is properly considered. In the presence of α, β -tubulin, water molecules are forced to order near hydrophobic patches on the surface of monomers. Binding of two monomers hides these hydrophobic patches and frees the water molecules into the solution.

^eAside from spurious bindings at low temperature, the nucleation and elongation of DNA nanotubes are inhibited by high temperature (Fig. C.6)

^fIt is conceivable to adapt DNA origami structure to a nucleating structure for DNA nanotubes. Previous studies have used DNA origami as a nucleating structures for algorithmic self-assembly of Sierpinski triangle [FHP⁺08] and binary counter [BSRW09].

The polymerization conditions was established at near-neutral pH, mild ionic strength, and more importantly, mM concentration of GTP. Microtubules in polymers are held together by non-covalent interactions [Wei72]. Microtubules, actin, and other filaments of the cytoskeleton are cooperative polymers. Cooperativity has an important consequence: monomers added to the end of a growing filament interact with at least two neighbors, whereas most of the collisions between monomers in solution result in contact with only one monomer. As a result, there is a significant energy barrier associated with the nucleation of a new nanotube that is absent in the elongation of growing nanotubes.

An α,β -tubulin monomer binds one GTP [ST68], an energy-rich molecule analogous to the fuel molecule for the molecular machine. The GTP hydrolysis reduces the length of the fuel molecule and yields a shorter guanosine phosphate chain (GDP), and an inorganic phosphate molecule P_i . Kinetics measurements of microtubule polymerization showed that GTP is consumed during polymerization [Jac75]. Each tubulin interfaces catalyzes GTP hydrolysis and releases the inorganic phosphate P_i to the environment. The release of the inorganic phosphate increases the net entropy of the system. This local interaction rule of coupling an energy consumption step and polymerization, gives rise to non-equilibrium global dynamics in microtubules, such as treadmilling and dynamic instability.

7.2.2. GTP hydrolysis in microtubule polymerization gives rise to treadmilling and dynamic instability

Microtubule polymerization still proceeds in the absence of GTP, such as in a polymerization reaction with a non-hydrolyzable GTP analog [HSD⁺92] and high concentration of GDP. In the absence of GTP hydrolysis, the critical concentration $[tubulin]_{crit}$ would be expected to be identical for both ends of the polymer, as the molecular interactions on both ends are identical [Weg76]. Under steady state monomer concentrations, GTP hydrolysis gives rise to asymmetric critical subunit concentrations between the two ends. In this state, one end elongates while the other depolymerizes (treadmilling) [MW78, CB81, CLZ82].

The discovery of treadmilling was followed by the observation of another class of non-equilibrium microtubule phenomena, namely dynamic instability. In steady state, Mitchison and Kirschner [MK84b, MK84a] demonstrated that microtubules dynamics can exist in two states, one elongates and one shrinks, with infrequent transition between these states. Transitions from the polymerization state to the depolymerization state are named catastrophes, and the opposite transitions are called rescues [WOP⁺88].

7.3. DNA nanotube implementation of the engineering principles of cytoskeletal assembly

The simplified model of how microtubules work (adapted from Howard and Hyman [HH03]) is presented in Fig. 7.1(left). Other active cytoskeletal polymers, such as actin, ParM, and FtsZ, employ the same principles for their non-equilibrium dynamics. Our proposed artificial microtubule [Fig. 7.1(right)] is in essence, a DNA nanotechnology implementation of the design principles in this model. This section presents the molecular features and components of the proposed system and their justifications in the form of key experimental observations in microtubules and DNA nanotubes. The component names of the biological and the proposed artificial microtubules are summarized in Table 7.2.

Microtubules	DNA nanotube Analog of Microtubules (NAoMi)
 α,β -tubulin	 incomplete-tile
 GTP-tubulin	 complete-tile
 GDP-tubulin	 cleaved-tile
 GTP	 fuel
 GDP	 waste
 microtubules	 DNA nanotube

Table 7.2.: Microtubules and DNA nanotube Analog of Microtubule (NAoMi) components.

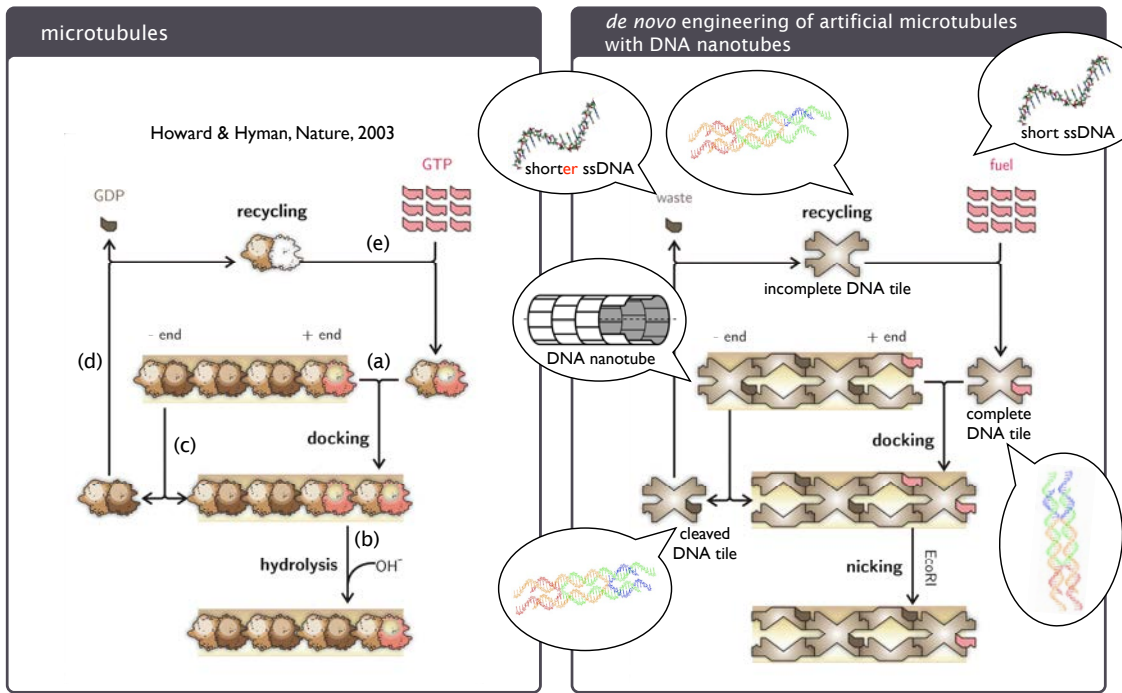


Figure 7.1.: (Right) Inspired by the current understanding of non-equilibrium polymerization of cytoskeleton, we aim to engineer DNA nanotubes as an artificial microtubule. The coupling between DNA nanotube polymerization and an analog of nucleotide hydrolysis could potentially recapitulate the more complex non-equilibrium cytoskeleton-based dynamics, such as treadmilling and dynamic instability. (Left) Model of how microtubules work [HH03]. The red and brown α, β -tubulin denote GTP-tubulin and GDP-tubulin, respectively. (a) Docking of the α, β -tubulin to the microtubule end. (b) Residues from the incoming α, β -tubulin complete the reactive site for triggering the hydrolysis of the GTP bound to the lattice-attached α, β -tubulin (Section. 7.3). (c) In microtubules, GTP-tubulin is more stable than GDP-tubulin; consequently, GDP-tubulin dissociates faster than GTP-tubulin. (d) In the free monomer state, GTP or GDP dissociates slowly from the tubulin. (e) Because the concentration of GTP in living cells is much higher than the concentration of GDP, the newly displaced GTP or GDP will be effectively replaced by GTP (Section 7.3).

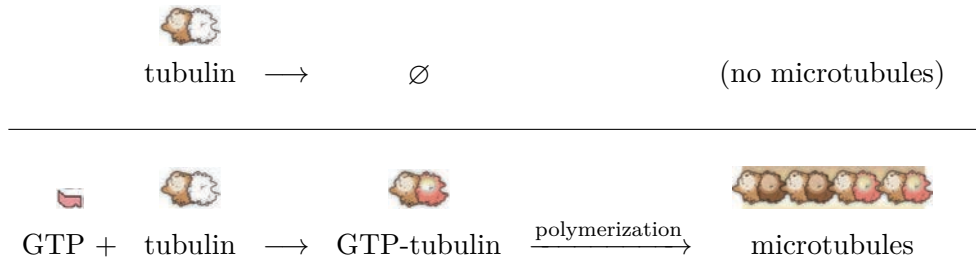
Engineering principle 1:

Cytoskeletal polymers are long, rigid polymers formed from noncovalently-bound monomers

In the cytoskeleton, noncovalently bound monomers give rise to long, rigid polymers. DNA nanotubes satisfy this criteria. Structurally, DNA nanotubes in this work are cooperative polymers that are more than one monomer wide. This cooperativity has important consequences. First, the tubular organization of DNA tiles along the longitudinal axis of a DNA nanotube results in a long persistence length, $\xi_p^{tube} \sim 20 \mu\text{m}$ [RENP⁺04, ORKF06], which is comparable to the persistence length of actin, $\xi_p^{actin} = 17.7 \mu\text{m}$ [GMNH93]. Second, in our lab DNA nanotubes can be prepared to have a relatively mean length on the order of $5 \mu\text{m}$. Spontaneous DNA nanotube polymerization is hampered by the unfavorable nucleation of DNA tile oligomers.

Engineering principle 2:

The addition of fuel molecules to free monomers enables polymerization.



The DNA tile as a monomer for DNA nanotubes

DNA strands can be designed to form a DNA complex, called a DNA tile, that acts as a monomer for different classes of DNA nanotubes [See82, WLWS98, Rot06, RENP⁺04, YHS⁺08, SW07, LZWS10, ZBC⁺09]. Being presented with many constructs of DNA nanotube designs, we first needed to choose which DNA nanotube construct to use. The subunit of microtubule polymerization comprises two components, namely (1) the fuel molecule, GTP, and (2) the monomer, α, β -tubulin. Therefore, to directly implement the design principles of dynamic microtubule assembly, the monomer must consist of at least two molecules.

In our scheme, we chose the double-crossover tile construct [RENP⁺04, WLWS98], because it is the simplest and most characterized DNA tile system that is composed of more

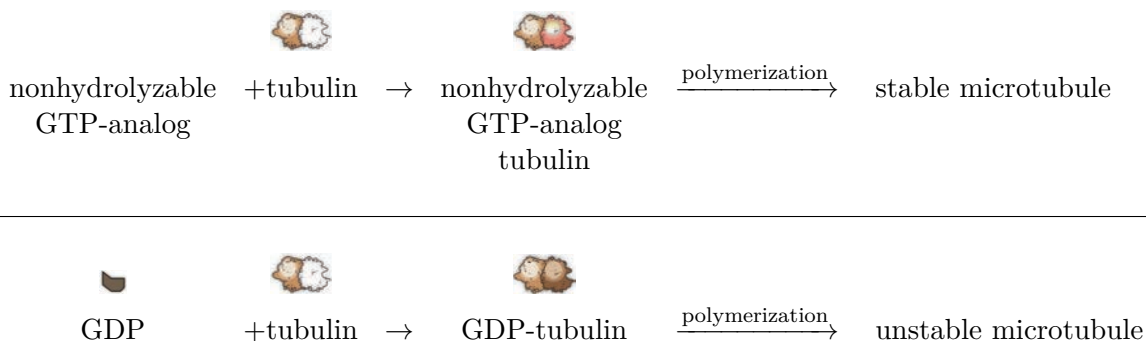
than one DNA strand. Typical double-crossover molecules have four to five strands. One of the strands will be designated as the fuel strand, analogous to GTP, and the rest of the strands collectively act as an incomplete tile, analogous to α,β -tubulin. In our construct, a DNA tile that carries fuel is called a complete tile (Table 7.2).

ssDNA as a fuel molecule

In microtubule polymerization, α,β -tubulins only polymerize in the presence of GTP. Similarly, we have shown that DNA tiles with either covered or missing sticky ends do not form DNA nanotubes [ZHCW13]. These two observations suggest that the sticky end sequence should be part of the fuel molecule.

Engineering principle 3:

Following polymerization, nucleotide hydrolysis destabilizes the polymers.



DNA analog of nucleotide hydrolysis decreases the sticky end strength

A second crucial observation is that GDP-tubulin can only nucleate and elongate into stable microtubules at very high α,β -tubulin monomer concentrations. On the contrary, when GTP is substituted with nonhydrolyzable GTP, a low concentration of α,β -tubulin is sufficient for stable microtubule polymerization [HSD⁺92]. The GTP microtubule depolymerizes at a negligible rate, an order of magnitude slower than the rate of GDP microtubule depolymerization. The difference in binding strength between GDP-tubulin and GTP-tubulin indicates that the free energy of association for GDP-tubulin is weaker than that of GTP-tubulin. In DNA thermodynamics, weaker binding is obtained with shorter sticky ends or, to some extent, lower guanine/cytosine (G/C) content. Therefore, the waste molecule, which is the DNA analog of GDP, is identical to the fuel molecule, but

with shorter sequence length and, consequently, weaker binding. In our design, a DNA monomer that binds to waste molecule is called a cleaved tile.

To convert a complete tile to a cleaved tile, we employ the EcoRI restriction enzyme to shorten the sticky end by n base pairs. In this chapter, n was chosen to be 2. We developed a restriction site situation that tricks EcoRI into nicking the sticky end of a DNA tile (Fig. 7.2) only after it has been incorporated into a DNA nanotube. One of the two cutting positions of an EcoRI recognition site is a pre-existing nick between different strands of neighboring DNA tiles. EcoRI will only cut the opposing cutting position of the pre-existing nick. The product is a nick in the sticky end area, instead of two nicks that occur in the conventional EcoRI-DNA reaction.

On the surface, our choice of using a restriction enzyme to create a nick on the sticky end strand may appear problematic. Why not use a simpler nicking enzyme? Although nicking enzyme might be simpler to design, nicking enzymes also have many intrinsic disadvantages: (1) they are expensive and (2) there is no published atomic structure, nor are there extensive kinetic measurements. For EcoRI, many theoretical studies and experimental work [WJM99,KEW⁺04,HO10,MFZ⁺97,KGL⁺90] have modeled and characterized EcoRI activity, which later proved to be invaluable in our work. The crystal structure of EcoRI has also been solved [KGL⁺90]. The atomic structure of EcoRI and the putative DNA tile and DNA nanotube structures guided the placement of the EcoRI restriction sequences along the DNA nanotubes.

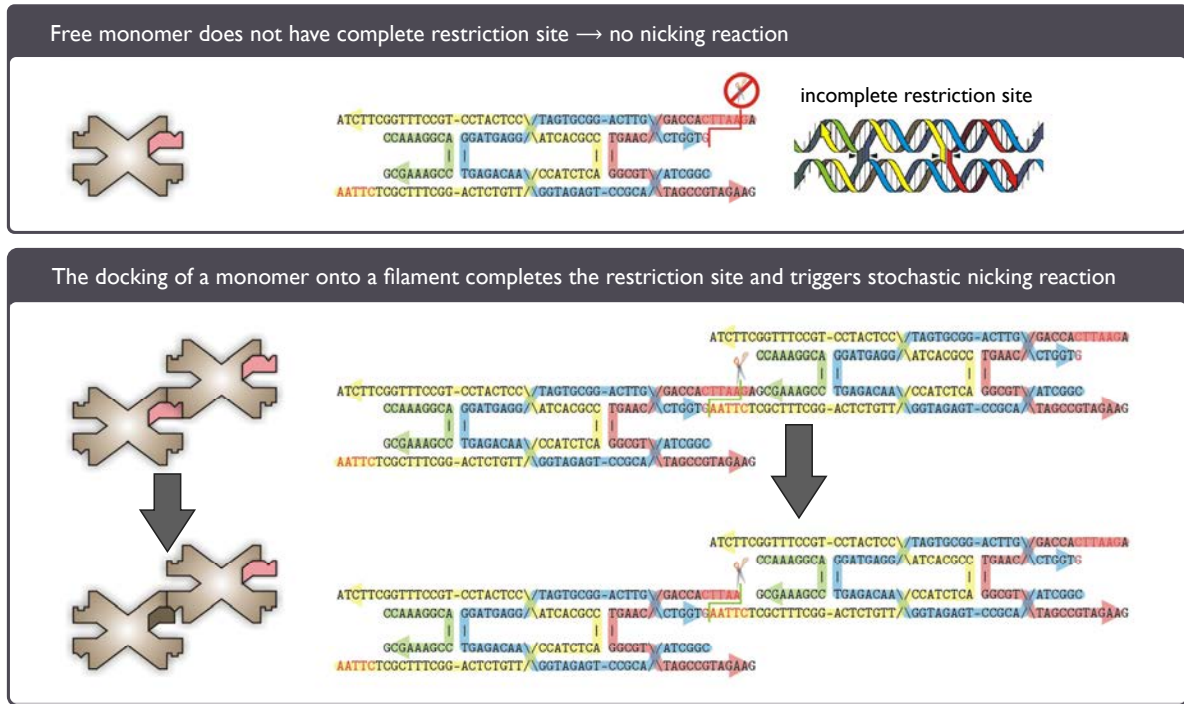
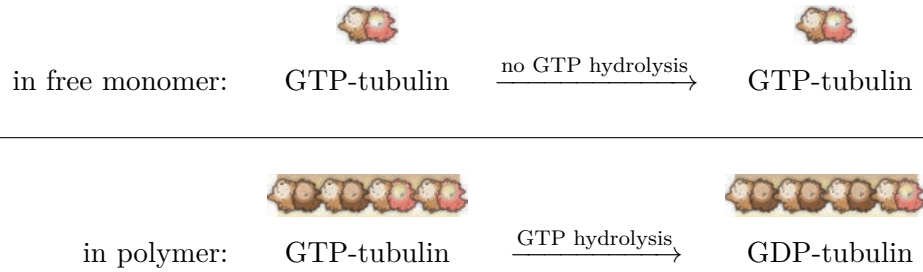


Figure 7.2.: A reaction between EcoRI and a DNA nanotube with strategically positioned restriction sites decreases the sticky end strength by two nearest-neighbor terms and one nicked stacking interaction. (Top) A monomer by itself only contains a partial recognition site for EcoRI. (Bottom) Binding of two identical DNA tiles, either as part of a multimer or a DNA nanotube, completes the restriction site and triggers the nicking reaction. In this construct, EcoRI can only make a nick, because the other cutting site was designed as a pre-existing nick. The 2 nt fragment will dissociate from the complex because of its weak binding and the configurational entropy gain from being unbound from the complex. Since the calculated half-life of a DNA tile dimer is shorter than the half-life of a DNA tile inside a DNA nanotube, within the physical parameter range where DNA dimers are unstable, the nicking reaction is expected to affect only the sticky ends inside the DNA nanotubes.

**Engineering principle 4:
Nucleotide hydrolysis only proceeds in the polymer**



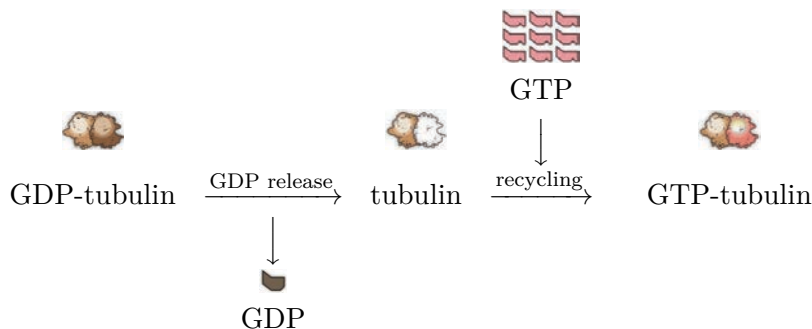
Implementation of engineering principle 4: The recognition site is located at the sticky end region.

The third crucial observation is that in microtubule polymerization, GTP hydrolysis is coupled with polymerization. Hydrolysis does not proceed in a free monomer, because the residues that are responsible for the hydrolysis are split between opposite ends of α,β -tubulin. Although the β -subunit pocket can bind to GTP, it lacks crucial residues required for hydrolysis. These residues are donated by the α -subunit of its α,β -tubulin neighbor, and in this way hydrolysis is triggered. Inspired by the tubulin structure, the coupling of the EcoRI reaction with DNA nanotube polymerization can be achieved in a carefully designed DNA monomer that has the restriction site at one of its sticky end pairs as shown in Fig. 7.2. Analogous to the separation of the hydrolysis residues in the α and β subunits of microtubules, each DNA tile has two halves of the restriction site at the opposite ends of the tile, e.g., at the northeast and southwest positions. The restriction site is only complete when one half of the restriction site meets with another half donated by a different DNA tile, either in the context of a DNA tile oligomer or within a DNA nanotube.

In microtubules, the nucleotide hydrolysis destabilizes GDP-tubulin within a microtubule. Since the stability of each DNA tile monomer is dictated by the sum of sticky end strength, one way to destabilize a DNA tile is by altering its sticky end. Therefore, positioning the restriction site at the sticky end is justified.

Engineering principle 5:

Nucleotide exchange, or fuel recycling, maintains high concentrations of fuel-monomers, well above the critical concentration for the polymers



The destabilization of α,β -tubulin monomers in microtubules plays an important role in microtubule function, such as mechanical force generation during the shrinking phase. However, nucleotide hydrolysis also poses a problem for microtubules, because without waste management, the fast polymerization rate can quickly deplete the pool of GTP-tubulin monomers. The problem is solved by an elegant recycling trick. In the monomer state, GTP and GDP can dissociate from α,β -tubulin. Since the physiological concentration of GTP is much higher than GDP, when a GDP molecule dissociates from α,β -tubulin, it is almost certain that the GDP molecule will be replaced by a GTP molecule. An implementation of this recycling feature is shown in the right panel of Fig. 7.1. Analogous to the recycling trick employed by microtubules, the fuel concentration in our test tube is always significantly higher than the concentration of waste molecules. A recycling process will effectively recharge any free cleaved-tile complex into a free complete-tile complex.

One last crucial piece of information about microtubule structure is that the recycling only affects the free monomer. In microtubule polymers, the position of the GTP or GDP molecule is buried, which in addition to the interaction between α,β -tubulin and GTP or GDP, limits the dissociation of GTP or GDP. It is very difficult to bury any molecule in a DNA nanotube because of the relatively simple molecular structure of the DNA double helix. However, in DNA nanotubes, the waste or fuel strand is being held by an additional 4–6 bp sticky end domain. On the contrary, the sticky end of a free DNA tile is, by default, free. This additional 4–6 bp domain results in decreased dissociation by a factor of 16,000– 2.1×10^6 relative to a free DNA tile. Because the fuel or waste molecule remains bound to two monomers inside DNA nanotubes, the nucleotide hydrolysis-induced modification to DNA nanotubes will

persist over a significantly long period of time.

Initially, we bypassed this recycling pathway by running the polymerization assay at a very slow tile consumption rate with a small number of nuclei in a sea of free monomers. The spontaneous nucleation of DNA nanotubes was suppressed by operating at a temperature and a monomer concentration where nanotube nucleation is very rare. Typically, we started the polymerization assay by introducing less than 10 pM of DNA nanotube nuclei. In our measurement of the passive DNA nanotube polymerization, the fastest forward rate ($k_{on}[tile] - k_{off}$) is no faster than 10 layers/min on each nanotube end. The highest initial tile concentration in the polymerization assay experiments was 600 nM. Based on these numbers, we expect the free monomer concentration to drop by 10 nM after no more than 125 minutes. Hence, for the parameter range in the single molecule polymerization assay, the recycling pathway is not necessary to keep the monomer concentration roughly constant over the course of 60 minutes, which is the typical duration of our polymerization assay in chapter 6. In this case, the consumed monomers are either incorporated into DNA nanotubes or cleaved as tiles.

7.4. Results

7.4.1. The enzymatic activity of EcoRI on dsDNA with nicks

To evaluate the enzymatic activity of EcoRI on our unconventional recognition site structure, we first constructed three different dsDNA targets with different nick positions as shown in Fig. 7.3. The first dsDNA target, named dsDNA-1, was a negative control and did not have nicks near the recognition site. In the second construct (middle), one of the cutting sites started with a nick. The position of the pre-existing nick in our sample was similar to the pre-existing nick in the proposed molecule (Fig. 7.2). In the last construct, EcoRI made two cuts with one of the cuts being 2 nt away from the pre-existing nick.

We ran the restriction enzyme experiment at room temperature and under our lab's standard DNA self-assembly buffer consisting $1\times$ TAE [40 mM Tris-acetate and 1 mM EDTA (Ethylenediaminetetraacetic acid)] with 12.5 mM Mg-acetate. The test tube contained 10% v/v EcoRI, purchased from Roche (Cat. No. 703 737), which is equivalent to 1 U/ μ L. The reaction progress was monitored by a denaturing PAGE gel assay at 65 °C gel running temperature and driven by 100 V and \sim 20 mA current. Surprisingly, increasing the reaction temperature to 37 °C did not accelerate the reaction. Previously, Muir *et al.* has shown that the activity of wild type EcoRI is robust to temperature change in

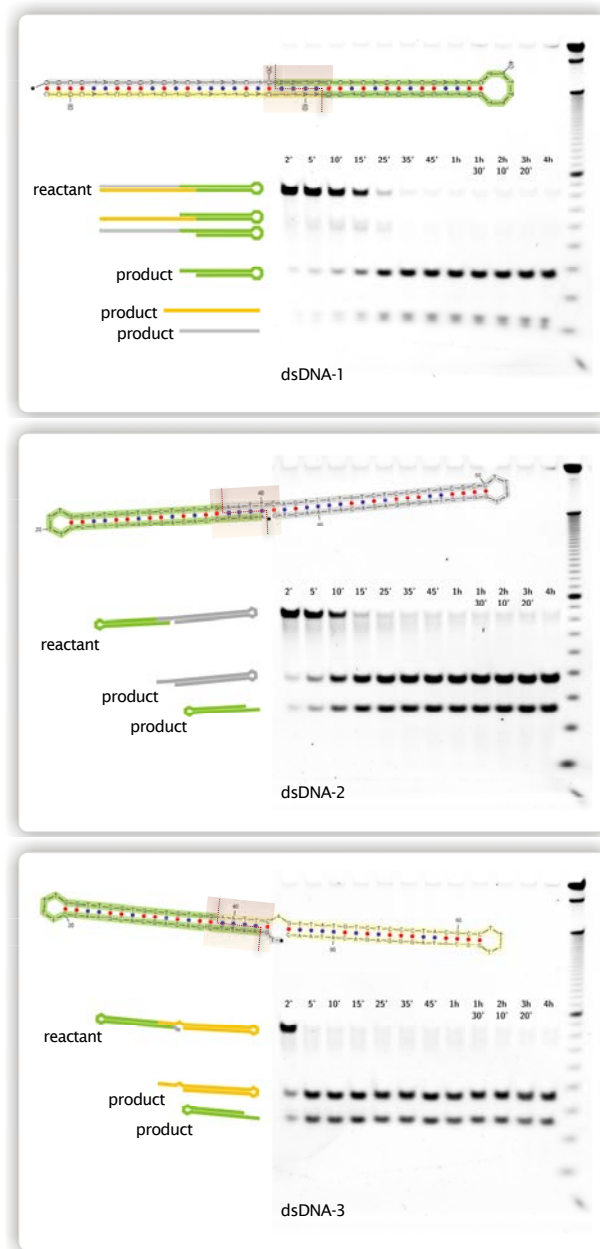


Figure 7.3.: A pre-existing nick does not reduce the activity of EcoRI. We tested the reaction for $2 \mu\text{M}$ dsDNA constructs with 0 nicks (top, dsDNA-1), 1 nick (middle, dsDNA-2), and 1 nick that is located 2 base pairs from the cutting site (bottom, dsDNA-3). The concentration of EcoRI was 10% v/v and the reaction was performed in standard DNA self-assembly buffer consisting of $1\times\text{TAE}$ (40 mM Tris-acetate and 1 mM EDTA [Ethylenediaminetetraacetic acid], pH 8.3) with 12.5 mM Mg-acetate at 37°C . The quantitative analysis of the gels are presented in Fig. 7.5 (top).

target	k [minutes ⁻¹]
dsDNA-1	0.085 ± 0.004
dsDNA-2	0.184 ± 0.014
dsDNA-3	0.490 ± 0.037

Table 7.3.: The inferred nicking reaction rates between 1 U/ μ L of EcoRI and 2 μ M of dsDNA-1, -2, and -3.

the range 34-42 °C [MFZ⁺97]. Similarly, running the experiment in the manufacturer's enzyme buffer for EcoRI did not yield a significant rate difference.

Even more surprising, we discovered that the reactions with cleaved substrates (dsDNA-2 and dsDNA-3) proceeded faster than the control substrate (dsDNA-1). A quantitative analysis of the bands in Fig. 7.3 is shown in the top panel of Fig. 7.5 and summarized in Table 7.3. The normalized intensity $\chi_P(t)$ was subjected to an exponential fit

$$\chi_P(t) = \chi_{P_\infty}(1 - e^{-kt}), \quad (7.1)$$

where χ_{P_∞} and k are fitting parameters that represent the final fraction of completion and first order reaction constant, respectively. The fitting parameter χ_{P_∞} will account for any inaccuracy in the intensity measurement and any incompleteness due to errors in DNA synthesis or other unknown factors.

The faster kinetics of reactions with cleaved substrates should not be unexpected if one properly considers the atomic coordinates of DNA when it interacts with EcoRI before the hydrolysis of phosphodiester bonds. Kim *et al.* [KGL⁺90] have shown that in the crystal structures of the EcoRI recognition site complex, the enzyme bends dsDNA to catalyze the hydrolysis of both dsDNA backbones. DNA bending results in the unstacking of the bases, widening of the minor groove, and compression of the major groove. This results in the phosphodiester linkage being broken closer to the active site of the enzyme, where it can be cleaved. Local deformation of a cleaved dsDNA is expected to incur a lower energy penalty than bending a pristine dsDNA. Lower energy cost implies smaller activation energy and faster reaction rate. The argument presented here exemplifies the power of the atomic structure of EcoRI in understanding our design.

7.4.2. Nicking reaction of DNA nanotubes

With the successful demonstration of EcoRI activity near a nick, we tested the nicking scheme on three different variants of DNA nanotubes (Fig. 7.4). The nicking rate within

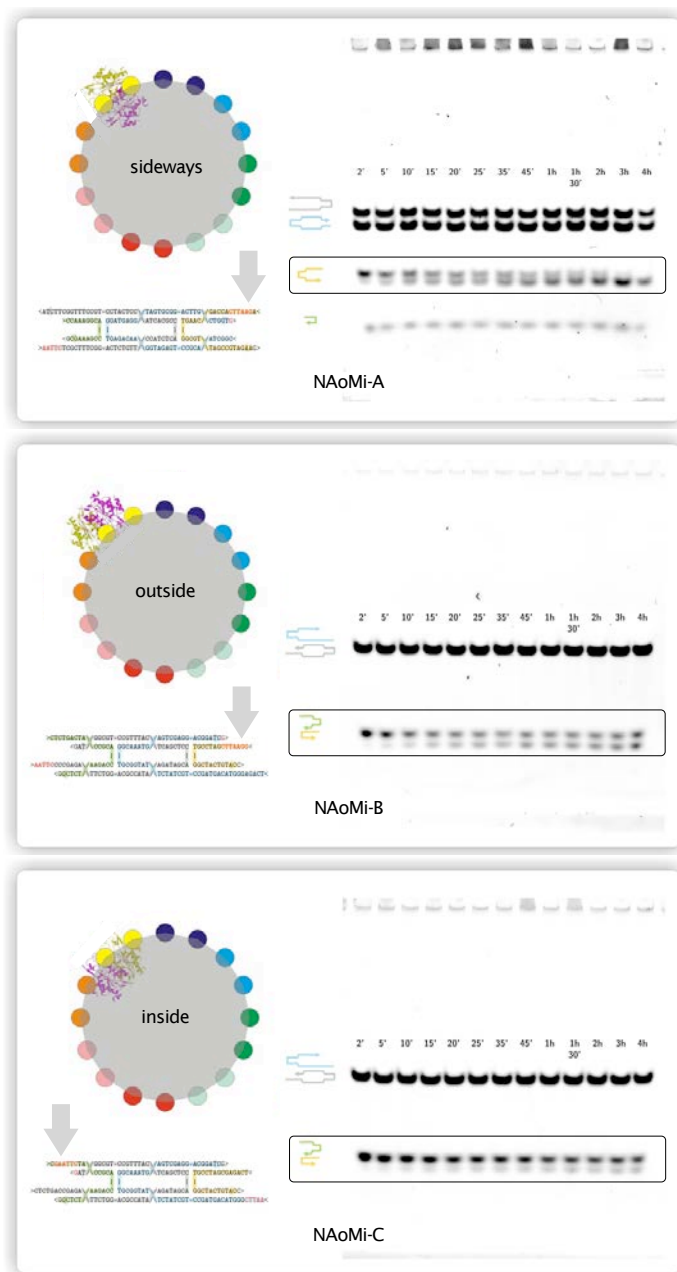


Figure 7.4.: Nicking reaction of DNA nanotubes is sensitive to the orientation of EcoRI at the restriction site. Based on the 3D models of DNA nanotube and EcoRI-dsDNA complex [KGL⁺90], we varied the orientation of EcoRI at the restriction site along the DNA nanotube such that the EcoRI is located between DNA tiles (top, NAOmi-A), outside the DNA nanotube (middle, NAOmi-B), and inside the DNA nanotube cavity (bottom, NAOmi-C). The quantitative analysis of the gels are presented in Fig. 7.5. As expected, the fastest nicking reaction is measured for DNA nanotubes with outside orientation. For scale, the diameter of the DNA helix (colored circles) is 2 nm.

DNA nanotubes was expected to be slower than with dsDNA for two main reasons, namely (1) low accessibility of the restriction site, and (2) obstruction of one-dimensional diffusion [HO10] of EcoRI in the form of periodic crossover points along DNA nanotube surface.

First, a DNA nanotube is a collection of parallel dsDNA with periodic double-crossover points at relatively close proximity (1.5 and 2.5 full DNA turns in the DNA tile used in this experiment). In Appendix D, the DNA lattice was modeled as a collection of isotropic, negatively charged beams that can be deformed with an elastic energy penalty proportional to the persistence length of DNA, ξ_p . The energy minimization of the interplay between the repulsive coulombic interaction between negative charges and the elastic energy penalty of deforming DNA helices gives rise to spacing between DNA tiles. The spacing has been consistently observed in atomic force microscopy (AFM) [HW04, Rot06], electron microscopy [DDL⁺09, DDS09], and cryo-electron microscopy [ADN⁺09].

In our design, we exploited the spacing to provide an access for fuel strand nicking by EcoRI. The recognition site was placed on the flexible arm of each DNA tile, at the most accessible region in the DNA nanotube. To further ameliorate potential accessibility and steric hindrance problems, we resorted to a new DNA tile motif that has longer flexible arms (Fig. 7.2) than any previously published DNA tile design. The flexible arm length of our DNA nanotube was 26 bp \sim 9 nm. For comparison, Rothmund *et al.* designed their DNA nanotube to have 21 bp \sim 7 nm flexible arm length.

Second, how does EcoRI find its target? The current model says that the searching process involves two diffusion steps [HO10, RS10]. Step one is the random three-dimensional diffusion of EcoRI until it finds and weakly binds to a DNA target, regardless of sequence. Step two is either one-dimensional diffusion or hopping along the DNA to locate the restriction sequence. This model has been supported by experiments with target dsDNA of different lengths. The kinetics of the reaction with a longer dsDNA target is faster than shorter dsDNA [WJM99], possibly because long dsDNA speeds up the three-dimensional diffusion step of the reaction. In the DNA nanotube structure, we expect the facilitated one-dimensional diffusion to be periodically suppressed as EcoRI meets the (periodic) crossover points. As a result, we expect a significant decrease in the reaction rate. **It is conceivable that the one-dimensional diffusion of EcoRI along DNA nanotubes will involve frequent hopping.** In this case, the long DNA nanotube can potentially act as an antenna to capture EcoRI, which is analogous to long dsDNA accelerating three-dimensional diffusion of EcoRI and increase the effective reaction rate.

Aided by the putative structure of DNA nanotubes and atomic structures of EcoRI

and the dsDNA complex, we designed three DNA nanotubes that interact differently with EcoRI. We assumed that each tile design does not produce racemic DNA nanotubes, i.e., every DNA nanotube has the same inside and outside surfaces. Fig. 7.4 shows a schematic of the expected interaction between EcoRI and three variants of DNA nanotubes. The diagram represents a cross section of an 8-monomer wide DNA nanotube perpendicular to the longitudinal axis. The pairs of circles are cross sections of dsDNA along the DNA nanotube, and identical color indicates that the DNA helix pair belongs to the same DNA tile. In the three panels, the atomic structure of EcoRI [KGL⁺90,FGM⁺84] was docked to the cross section of the DNA nanotube. The relative scale between EcoRI, dsDNA helix, and tile spacing is based on the three-dimensional structures and the calculation presented in Appendix D. The arrow on top of the tile schematics shows where the designed nicking position is located, based on the EcoRI restriction sequence.

The orientations of EcoRI at the restriction site of the three DNA nanotube variants were determined from the orientation of the major and minor grooves along the DNA nanotubes. The EcoRI orientation can be tuned by sliding the position of the restriction site along the flexible arm of the tile. For NAoMi-A, EcoRI binds the recognition site at a sideways orientation. Due to the steric hindrance and limited space between DNA helices, the sideways orientation is not optimal for nicking reactions. This sub-optimal design was a result of an unintentional mistake when looking at EcoRI crystal structure. In the end, this mistake turned into a valuable data point. The middle and bottom panels are the schematics and gel data of two different DNA nanotubes that have an opposite orientation of the major and minor grooves of the recognition site. Since we have not extensively characterized the inside and outside surfaces of the DNA nanotubes, we designated a DNA nanotube with faster kinetics (middle, NAoMi-B) and slower kinetics (bottom, NAoMi-C) as the one that EcoRI attacks from outside and inside, respectively. In the inside orientation, EcoRI is more likely to diffuse inside DNA nanotubes or between DNA helices before attacking the recognition site with inside orientation.

Similar to the nicking assay of Fig. 1.3, the reaction progress was monitored with a time-lapse denaturing 8% PAGE gel assay (Fig. 7.4). For a nicking gel assay of a tile composed of different strands of unique lengths, such as NAoMi-A, a complete nicking reaction is demonstrated by the total disappearance of the band corresponding to the yellow fuel strand of length n and the emergence of another band of length $n - 2$ with the final total intensity $(n - 2)/n \times$ the initial band intensity of the fuel strand. The intensity ratio is not unity, because the gel intensity depends on the strand length, and the product is shorter than the starting molecule by 2 nuclei.

Contrary to NAOmi-A, the nanotubes in the middle (NAOmi-B) and bottom (NAOmi-C) panels, are symmetric and consist of two pairs of strands with equal lengths. The blue and gray strands have the same length; the yellow strand was initially as long as the green strand. For a nicking gel assay of a symmetric tile, a complete reaction is shown by the decrease of band intensity by a factor of 2, since the other strand of equal length is not cut by the enzyme. The product will appear as a new band at $(n - 2)/2n \times$ the initial band intensity of the fuel strand. In Fig. 7.5(middle), the nicking reaction of NAOmi-B nanotubes proceeded to completion. For unknown reasons, the reaction between NAOmi-C and EcoRI did not go to completion. One plausible explanation is that the incompleteness was caused by nanotube aggregations and/or high concentrations of unpolymerized DNA tiles that are created by poor DNA nanotube synthesis. If these aggregations are stable, accessing the tube and scanning the DNA helices for the restriction site will be difficult and slow. Assuming that our designation of inside orientation of EcoRI is correct, the incompleteness could also be caused by the small orifice size of a fraction of the DNA nanotubes in the test tube. Based on the AFM images, we observed diameter distribution of NAOmi-B nanotubes in the range of 5–11 tile widths (Fig. 6.9), which corresponds to DNA nanotube orifice size distribution of 6–16 nm. If we modeled EcoRI as a sphere with a 5 nm diameter, the opening of thin DNA nanotubes could be too small for an effective nicking reaction from inside the nanotubes.

For all gels, the intensities of the highlighted bands were quantified and plotted in Fig. 7.5. The normalized intensity ratio at different time points were subjected to the nonlinear fitting in Eq. 7.1. The inferred rate constant for nicking reactions is summarized in Table 7.4. NAOmi-B was found to be the DNA nanotube variant that reacted fastest with EcoRI. The reaction kinetics of NAOmi-B and EcoRI were nicely described by the fitting function of Eq. 7.1 in Fig. 7.5. The reaction between NAOmi-A and EcoRI has a more complex kinetics and does not follow the first-order kinetics of Eq. 7.1. The reaction between NAOmi-C and EcoRI did not reach 60% completion. Nonetheless, we fitted the first 30 minutes of data of NAOmi-C to illustrate its poor performance.

These gels show that the DNA nanotube nicking depends on how EcoRI approaches the nicking site and the orientation of EcoRI at the restriction site. Further investigation is needed to provide convincing evidence of the correct designation of inside and outside nanotube variants. Regardless of how correct our orientation assignment is, we now have a DNA nanotube construct that works well for further experiments in the artificial microtubule project.

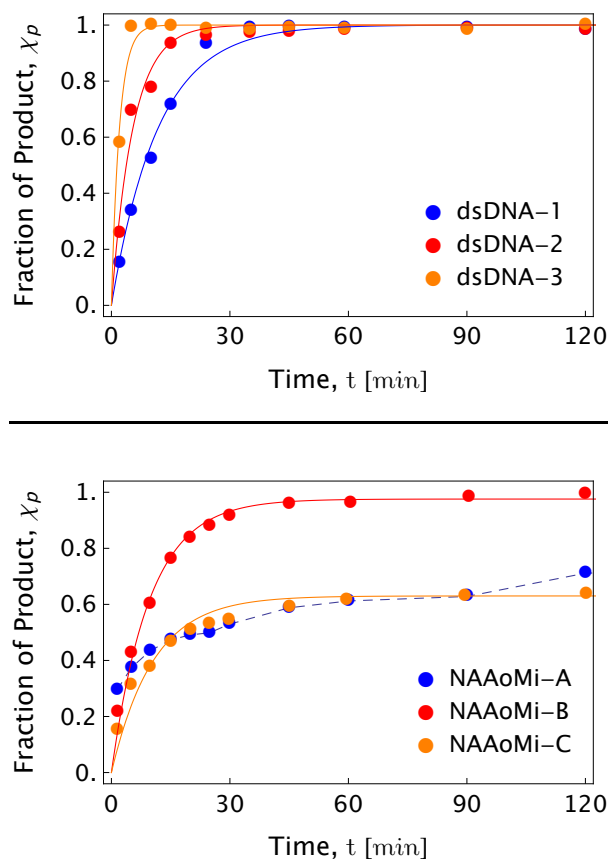


Figure 7.5.: Nicking reaction between EcoRI and 200 nmDNA nanotube with outside orientation (bottom, NAAoMi-B, blue line) is relatively as fast as the nicking reaction of 2 μM dsDNA without the nick (top, dsDNA-1, blue line). The top plot is the quantitative analysis of the interaction between EcoRI and the three different constructs of double-stranded DNA shown in Fig. 7.3. The bottom plot shows the kinetics of the nicking reaction in the context of DNA nanotubes with the three different EcoRI orientations, as shown in Fig. 7.4.

DNA nanotube	k [minutes $^{-1}$]
NAAoMi-A	N/A
NAAoMi-B	0.104 ± 0.006
NAAoMi-C	0.095 ± 0.012

Table 7.4.: Nicking reaction rates of 1 U/ μL of EcoRI and 0.2 μM of NAAoMi-A, -B, and -C.

7.4.3. Single molecule movie of DNA nanotube polymerization with nicking reaction

Finally, we are in a position to experimentally evaluate the implications of the nicking reaction on the stability of DNA nanotubes in real time. The effect of the nicking reaction on DNA nanotube dynamics was assayed by using single molecule TIRF microscopy. Time lapse microscopy enables measurement of nanotube lengths in solution at high data rates. Because of these features, light microscopy has been widely used to study the dynamics of biopolymers, such as microtubules and actin filaments.

Fig. 7.6 shows kymographs of DNA nanotube polymerization at zero tile concentration with and without 5% v/v EcoRI. The imaging buffer contained 0.3% (w/v) methylcellulose (Sigma, 4,000 cP, M0512–100G), which was added to the buffer to confine the nanotubes in the two-dimensional space as described in the polymerization assay section. In this crowded environment, the entropy of the system is maximized when long tubular structures are near a two-dimensional surface, such as the microscope slide surface where the evanescent excitation wave is concentrated, and the focal plane of the imaging optics is positioned. It is important to note that crowding agent-induced confinement is a standard imaging trick in microtubule [BLS⁺07], actin [KP05], ParM [GCM04], and other cytoskeleton studies. The use of crowding agents for confining polymers close to the coverslip surface is yet another example of the lessons that we learn from the more evolved single molecule imaging of cytoskeletal dynamics.

The polymerization assay with EcoRI work is in the early stages; we have only constructed 1 kymograph [Fig. 7.6 (top right)] of the longest initial DNA nanotube length in the data set. Kymographs of long DNA nanotubes tend to be more reliable because of their large number of fiduciary data points for bona fide alignment between the straightened DNA nanotube images. At 35.2 °C, the depolymerization rates with the nicking reaction were measured to be 9.8 ± 0.7 layer/min and 10.8 ± 0.4 layer/min for right and left nanotube ends, respectively. Within our measurement uncertainty, the depolymerization of left and right nanotube ends appeared to be symmetric.

As a control experiment, a kymograph produced from a polymerization assay without EcoRI is presented in the left column of Fig. 7.6. The control kymograph is identical to the data shown in Fig. 6.3. Linear fittings to the position of left and right ends determined the polymerization rates to be 8.1 ± 0.8 layer/min and 6.7 ± 0.4 layer/min, respectively. The control experiment was not ideal because it was performed at 38.3 °C, which was higher than the 35.2 °C for the EcoRI experiment. Based on the kinetic tile assembly model,

the depolymerization rate at lower temperature is calculated to be slower. Even with the “penalized” control shown in Fig. 7.6, the depolymerization rate of EcoRI was still faster than the depolymerization rate in the presented reaction without the nicking reaction. The increased depolymerization in the presence of EcoRI is a clear indication that our scheme works as designed.

A proper control of the EcoRI kymograph is the inferred depolymerization rate k_{off} at 35.2 °C (see Table 6.2). In the previous chapter, the linear fitting of measured polymerization rates of 35 nanotubes at 0–300 nm tile concentration gives k_{off} at 35.2 °C to be 1.01 ± 0.31 layer/min and the global association constant $k_{on} = 6 \times 10^5$ /M/sec. The free energy for dissociation of a tile bound by two full-length sticky end bonds at standard concentration $u_o = 1$ M was calculated by the equation

$$\Delta G_{full}^{\circ} = -RT \ln \left(\frac{k_{off} \times u_0}{k_{on}} \right) = 17.4 \text{ RT}. \quad (7.2)$$

To calculate the expected off rate for tiles with cleaved sticky ends, recall that in the kTAM the free energy for tile dissociation is $(\sum_i s_i \Delta G_{se}^{\circ}) - \alpha RT$, where s_i give the strengths of the bonds attaching the tile to the nanotube. In this case, $\sum_i s_i = 2$, so $\Delta G_{se}^{\circ} = 10.2$ RT is the strength of a single full bond. A cleaved bond is $\frac{2}{3}$ that of a full bond, ignoring stacking at the nicks and dangle energies, so we predict that for tiles attaching by one full bond and one cleaved bond, $\Delta G_{cleaved}^{\circ} = (\frac{2}{3} + 1)\Delta G_{se}^{\circ} - \alpha RT = 14.0$ RT and $k_{off} = 29.9$ layers/min. From experiment, the depolymerization rates were measured to be 9.8 ± 0.7 and 10.8 ± 0.4 layer/min depolymerization rates for the left and right ends of the DNA nanotube in Fig. 7.6 (right). The calculated EcoRI enhanced shrinking rate at zero tile concentration and at 35.2 °C is within a factor of 3 from the measured depolymerization rates. The faster slower depolymerization rate can easily be explained by the uncertainties in the dangle energies at the nicks in our calculation.

7.5. Discussion

The nicking reaction destabilizes interaction between monomer subunits in cleaved DNA nanotubes. Due to the weakened binding, the depolymerization rate k_{off} of the cleaved DNA nanotube is faster than the control DNA nanotubes. The thermodynamics and kinetics of the “instability” is straightforward. In the absence of enzyme, the nanotubes are at zero free tile concentration, which is close to be the critical concentration of control

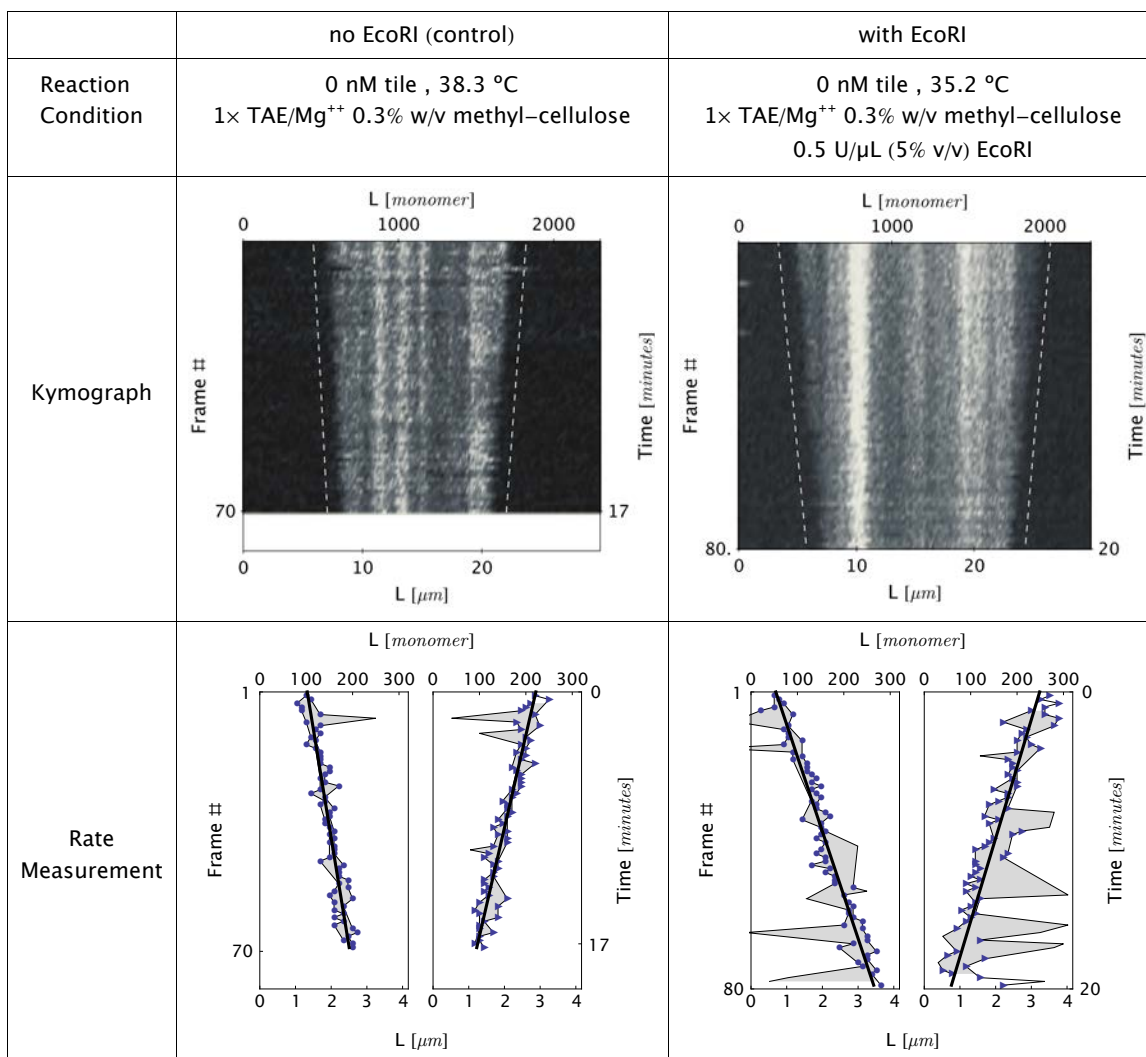


Figure 7.6.: Single molecule assay shows that nicking reaction by EcoRI destabilizes DNA nanotubes, as indicated by the faster dissociation rate k_{off} in the reaction EcoRI (right column) compared to the control experiment (left column). In a kymograph of a DNA nanotube at zero tile concentration, the slopes of the nanotube end coordinates over time are a measure of depolymerization rate. The linear fitting (dashed line) of the nanotube end in the experiment with EcoRI (bottom right) determines the dissociation rates for the right and left ends to be 9.8 ± 0.7 layer/min and 10.8 ± 0.4 layer/min. The dissociation rates of the control experiment (bottom left) were measured to be 8.1 ± 0.8 layer/min and 6.7 ± 0.4 layer/min. Note that the control data was obtained at a higher temperature.

DNA nanotube $[tile]_{crit}^{control}$. After the addition of enzyme, the nicking reaction shortens one of the sticky ends, and the chemical energy is used to destabilize the nanotube, analogous to how GTP hydrolysis destabilizes microtubules [CRS94]. The nicking reaction brings the critical concentration up to $[tile]_{crit}^{cleaved}$. In the EcoRI experiment in Fig. 7.6 and the control (Table 6.3), the calculated $[tile]_{crit}^{control}$ and $[tile]_{crit}^{cleaved}$ are 15 nM and 306 nM, respectively. In the beginning of the reaction, although undetected, the DNA nanotubes are stabilized by a “full tile” cap and depolymerized at a very slow rate. Eventually, the “full tile” cap is lost and the DNA nanotube shrinks to bring the free monomer concentration up to $[tile]_{crit}^{cleaved}$. Since the total tile concentration in the nanotubes was less than 7 nM and much more dilute than $[tile]_{crit}^{cleaved}$, the depolymerization will persist until all of the nanotubes are completely depolymerized.

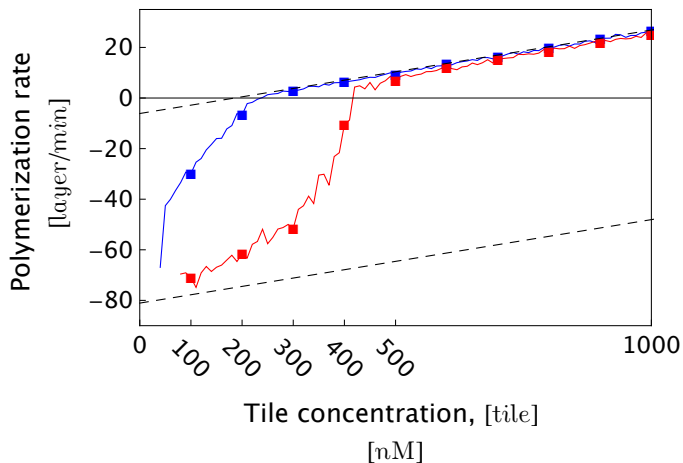


Figure 7.7.: Simulation of DNA nanotube polymerization with nicking rate at different tile concentrations. The lines are colored by the type of nanotube ends in Fig. 7.1 (red – right end, blue – left end). Surprisingly, in our simulation, DNA nanotubes exhibit asymmetric polymerization when the polymerization speed, in the absence of the nicking reaction, is near the rate of the nicking reaction.

While the kinetics of polymerization with nicking at zero tile concentration is straight forward, the kinetics of the reaction at non-zero free tile concentration is not trivial. To provide an insight as to how the nicking reaction might alter DNA polymerization at different tile concentrations, we modified our MATLAB simulation (chapter 6) for the DNA nanotube polymerization assay by adding the nicking reaction at rate $k_{nicking}$. In general, the bond strength of a DNA tile is computed as $\left(\sum_i s_i \Delta G_{se}\right) - \alpha RT$, where

ΔG_{se} is the free energy of one full sticky end and s_i is the strength of sticky end i . For the following discussions, we chose ΔG_{se} to be 7.75 RT and we chose $\alpha = 0$ for convenience. Therefore, the bond strength of a DNA tile with two full sticky end bindings ΔG_{full} is $2 \times \Delta G_{se} = 15.5$ RT. (Experimentally-inferred values for ΔG_{full} and $\Delta G_{cleaved}$ can be found at the end of section 7.4. The energies in this simulation are lower than the calculated energies based on experiments in chapter 6 and Fig. 7.6.) The docking of an incoming monomer to 7-tile-diameter DNA nanotube triggers the nicking reaction with reaction rate $k_{nicking}$. For the purpose of this analysis, we assumed the $k_{nicking}^{site} = 1 \text{ min}^{-1}$. (This is higher than the experimental value in Table 7.4, which requires higher enzyme concentration). In the simulation, the nicking reaction reduced the length of one of the sticky ends, from 6 bp to 4 bp, which is equivalent to a sticky end strength reduction from 1 to $2/3$. Ignoring the energy cost of losing one stacking interaction, the free energy of a DNA tile that is being held by one full sticky end and one cleaved sticky end is estimated to be $\Delta G_{cleaved} = (1 + 2/3) \times 7.75 \text{ RT} = 12.9 \text{ RT}$. We chose the association rate for DNA tile - DNA nanotube k_{on}^{site} to be $10^6 \text{ M}^{-1} \text{ sec}^{-1}$ to match the typical polymerization rate observed in the single molecule polymerization assay. Since we did not embed the recycling pathway in all of our experiments, the recycling was disabled and the recycling rate $k_{recycle}$ was kept at zero. All of the free tiles in the simulation have full sticky ends.

The simulated polymerization rate for a 7-tile-diameter DNA nanotube at 0–1000 nM tile concentration is presented in Fig. 7.7. The blue and red lines are the polymerization rates of the left and the right nanotube ends (Fig. 7.8), respectively. The upper dashed line is the theoretical polymerization model of DNA tile in the absence of nicking reaction, which is computed as $0.55 \times (k_{on}^{site} [tile] - k_{on}^{site} e^{-\Delta G_{full}/RT} \times u_0)$. The factor 0.55 is a fitting parameter that accounts for polymerization rate reduction in n monomer diameter DNA nanotubes due to the different possible edge configurations. The bottom dashed line is the polymerization rate of DNA nanotubes that are composed of DNA tile with one full sticky end pair and one cleaved sticky end pair. Based on our model, we constructed the lower dashed line by the numerical evaluation of $0.55 \times (k_{on}^{site} [tile] - k_{on}^{site} e^{-\Delta G_{cleaved}/RT} \times u_0)$. The nanotube polymerization with nicking reaction at different tile concentrations can be categorized into 4 regimes, which are:

(1) Fast and symmetric depolymerization at $[tile]=0$ nm

The extrapolation of both blue and red curves suggests that at zero tile concentration, both ends depolymerize at the rate of $0.55 \times (k_{on}^{site} e^{-\Delta G_{cleaved}/RT} \times u_0)$. Equally important, the two ends depolymerize symmetrically. Both observations are in agreement with the EcoRI experiment of DNA nanotubes at zero tile concentration presented in Fig. 7.6.

(2) Symmetric elongation at polymerization rate \gg nicking rate

On the other extreme, at high tile concentrations, the nicking reaction lags behind polymerization. Hence, the nicking reaction does not affect DNA nanotube polymerization, and both nanotube ends elongate symmetrically at the rate of $0.55 \times (k_{on}^{site} [tile] - k_{on}^{site} e^{-\Delta G_{full}/RT} \times u_0)$

(3) Asymmetric depolymerization

Interestingly, the simple modification of the local rule gives rise to a profound implication for the case when the polymerization rate is near the nicking rate. Under depolymerization conditions where $[tile] < [tile]_{crit}^{full}$, the nicking reaction increases the depolymerization rate asymmetrically. In the data points highlighted as squares in Fig. 7.7, the asymmetric depolymerization is expected at $[tile] = 100$ nM and 200 nM. Treadmilling, a subclass of the asymmetric polymerization, will be discussed in the section below.

(4) Treadmilling

Remarkably, the simulation predicts that our proposed modification to the DNA nanotubes could exhibit treadmilling at $[tile] > [tile]_{crit}^{full}$ and polymerization rate near $k_{nicking}$. If we run the experiment at $i \times 100$ nM concentration, where i is a positive integer, the simulation predicts that DNA nanotubes will exhibit treadmilling behavior at 300 nM and 400 nM tile concentrations.

How does the asymmetry arise in a seemingly symmetric DNA nanotube construct? The non-existence of asymmetry in the no-free-tile case indicates that the asymmetry should involve an interaction between DNA nanotubes and incoming monomers. Fig. 7.8 shows a particular series of events that produces asymmetric behavior between the nanotube ends. For both nanotube ends, (1) docking of a new monomer triggers the stochastic nicking rate. Initially, the new monomer attaches to the nanotube end with bond strength = 2. If

the polymerization is either slower or near the nicking rate, then the nicking reaction (2) is completed before attachment of another monomer. In this scenario, the monomer at the end of the DNA nanotube binds to the second layer with only $1+2/3$ sticky end, and, as a result, (3) the monomer will quickly dissociate from the nanotube ends. Up to this point, this series of events has not broken the symmetry between the nanotube ends. Because the nicking reaction only cuts one strand of a double-stranded sticky end bond, one of the nanotube ends, which has been designated as the left end, is unaffected by this scenario and always presents a ring of full sticky ends. Meanwhile, one half of the sticky ends in the right end are shortened by the nicking reaction. As a result, with this regime, the left end is predicted to polymerize faster than the right end.

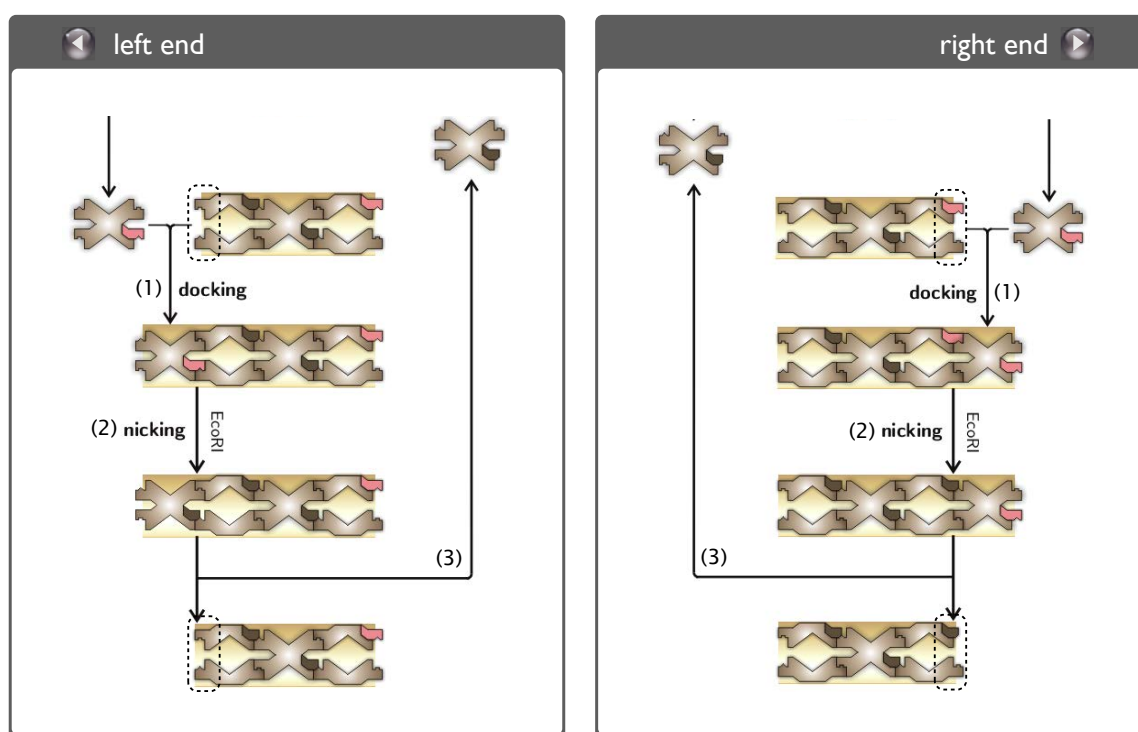


Figure 7.8.: An asymmetry between the left and right nanotube ends can arise after (1) the docking of a free monomer to a DNA nanotube, which is followed by (2) the fast nicking reaction and (3) the dissociation of the newly attached DNA tile from the nanotube. As a result, the nanotube on the left presents two full sticky ends, while the sticky ends exposed at the right end are composed of one cleaved and one full sticky end. Due to the asymmetry in the sticky end strength (highlighted in the dashed boxes), we expect the left end to polymerize faster than the right end.

7.6. Concluding remarks

In this study, we presented a simple modification to an existing DNA nanotube construct to implement a *de novo* artificial cytoskeleton. We used a restriction enzyme to achieve a DNA analog of GTP hydrolysis. The energy source is provided by a polymerization-triggered nicking reaction. A preliminary bulk gel assay, single molecule polymerization movies, and supporting simulation demonstrate the promise of our approach. The demonstration of a treadmilling DNA nanotube is on the horizon and will be pursued upon the completion of this study.

Despite the continuous emphasis of the similar physical properties of DNA nanotubes and microtubules in this current study, the most profound insight may emerge from the structural differences between the structures of the DNA nanotubes and microtubules. Dyche Mullins noticed one missing common microtubule feature in our construct, namely a large conformational change that occurs after a DNA tile attaches to a growing DNA nanotube. The monomer-docking-induced conformational change has been observed on the growing actin filaments [CLS96, LPH93] and microtubules [MMM91, CFK95, MH95], and is thought to be responsible for the different k_{on} 's between the fast and slow polymer ends. In microtubules, the end with faster k_{on} and slower k_{off} polymerizes faster than the end whose k_{on} is slower and k_{off} is faster. Due to the absence of the conformational change in our construct, the k_{on} for both nanotube ends is expected to be identical. It is remarkable that our simulation predicts a polymerization regime in which the nicking reaction gives rise to the polymerization rate asymmetry. This predicted asymmetric behavior shows the promise of DNA nanotube treadmilling.

Richard Feynman once said that “Experiment is the sole judge of scientific truth”. A polymerization assay with nicking reactions over a wide range of tile concentrations will be the ultimate test to evaluate the success of our scheme. A successful demonstration of treadmilling would counter what one might think to be a reasonable assumption about cytoskeletal dynamics, namely that conformational change is required for treadmilling polymers.

The construction of an artificial cytoskeleton can also potentially demonstrate an elegant solution that nature has devised to solve challenges at molecular scale. As an example, eukaryotic cells use the rapid depolymerization of microtubules and microtubule accessory proteins to pull centrosomes apart during mitosis. Nicking-reaction-induced depolymerization, like the one shown in this study, can potentially pull apart another structure that is mechanically coupled to the DNA nanotubes. In the future, incorporation of more biological design principles into DNA nanotube assembly, along with the creation of new

DNA nanotechnology analogs of cytoskeletal accessory proteins, will enable a more complex DNA-based dynamic system that can rival the complexity of cellular behavior.

A

Supplementary materials for Chapter 2: Programming DNA Tube Circumferences

A.1. DNA sequence design

DNA sequences for the chain systems, 3-,4-,5-, and 6-helix ribbon systems, and 4-,5-, and 6-helix tube systems were designed and optimized using the SEQUIN software [See90] and TileSoft software [YGB⁺04] to minimize sequence symmetry. The other systems were designed using an unpublished the design component of the NUPACK server (www.nupack.org) to maximize affinity and specificity for the target structures. Sometimes, manual optimization was further performed on selected regions.

A.2. Sample preparation

DNA strands were synthesized by Integrated DNA Technology, Inc. (www.idtdna.com) and purified by denaturing gel electrophoresis or HPLC. The concentrations of the DNA strands were determined by the measurement of ultraviolet absorption at 260 nm. To assemble the structures, DNA strands were mixed stoichiometrically to a final concentration of $\sim 1\mu\text{M}$ for 20-helix ribbons and 20-helix tubes and $\sim 3\mu\text{M}$ for other structures in $1\times\text{TAE}/\text{Mg}^{++}$ buffer (20 mM Tris, pH 7.6, 2 mM EDTA, 12.5 mM MgCl_2) and annealed in a water bath in a styrofoam box by cooling from 90 °C to 23 °C over a period of 24 to 48 hours. For the samples containing biotinylated strands, streptavidin was added to the aqueous solution

of the assembled structures for 1 hour at room temperature. The final concentration of streptavidin matches the total concentration of the biotinylated strands. The samples were further incubated overnight at 4 °C before AFM imaging.

A.3. AFM imaging.

AFM images were obtained using an SPM Multimode with Digital Instruments Nanoscope IIIa controller (Veeco) equipped with an Analog Q-control to optimize the sensitivity of the tapping mode (Nano Analytics). A 40 μL drop of $1\times\text{TAE}/\text{Mg}^{++}$ followed by a 5 μL drop of annealed sample was applied onto the surface of a freshly cleaved mica and left for approximately 2 minutes. Sometimes, additional dilution of the sample was performed to achieve the desired sample density. On a few occasions, supplemental $1\times\text{TAE}/8\text{mM Ni}^{++}$ was added to increase the strength of DNA-mica binding [HL96]. Before placing the fluid cell on top of the mica puck, an additional 20 μL of $1\times\text{TAE}/\text{Mg}^{++}$ buffer was added to the cavity between the fluid cell and the AFM cantilever chip to avoid bubbles. The AFM tips used were either the short and thin cantilever in the NP-S oxide sharpened silicon nitride cantilever chip (Veeco Probes) or the short cantilever in the BS SiNi tip (Budget Sensor).

A.4. Fluorescence imaging and length measurements.

For fluorescence microscopy imaging, the 5'-ends of U1 and U5 strands were labeled with Cy3 fluorophores. To measure the lengths of the nanotubes, fluorescence light microscopy is preferred over AFM for two reasons: (1) the fast exposure time of the light microscopy, which is on the order of 1 second per frame, as opposed to 200 seconds per frame for AFM; and (2) the larger view field. A 4 μL drop of 10 nM SST sample was deposited onto an untreated coverslip (Gold Seal, 3334). The presence of Mg^{++} and other multi-valent counterions in the buffer creates a net positively charged coverslip surface that immobilizes the nanotubes. The light microscope is a home-built prism-based TIRF. A green wavelength excitation from a solid-state 532-nm laser (CrystaLaser, Reno, NV) was used to excite the immobilized DNA nanotubes through coupling between the prism and the glass coverslip. The Cy3 emission was detected by a 60 \times water immersion objective (Nikon, NA = 1.2), a DualView 2-channel filter cube (Roper Biosciences), and an electron multiplier CCD camera (Hamamatsu, C9100-02). The image was analyzed using the imageJ image processing software (NIH) and MATLAB. A threshold was applied to each image to differentiate the

nanotubes and the glass surface. Each nanotube was then thinned down to a skeleton of 1-pixel thickness with the “skeletonize” command in imageJ. The length was then measured from the skeleton patterns of the nanotubes.

A.5. Thermal transition profiles.

Thermal transition experiments were performed using an AVIV 14DS spectrophotometer (AVIV Biomedical, Lakewood, NJ) equipped with a water bath temperature controller. UV absorbance at 260 nm was measured with a 1 nm bandwidth. The temperature step was set at 0.1 °C, deadband at 0.1 °C with a equilibration time of 0.25 minute. Each data point was smoothed with 10 neighbors to reduce instrument noise.

A.6. Curvature analysis

Adapting previously reported curvature analysis for DNA tubes [RENP⁺04,SS06], we describe below how to analyze the putative, approximate curvature of unstrained SST lattices (e.g. not closed into tubes).

We use a B-DNA model where 21 bases finish exactly two full helical turns. Now consider the three parallel helices depicted in Fig. A.2A. To study the curvature defined by the three axes O_1 , O_2 , and O_3 , we depict the cross-section view in Fig. A.2B. In the cross section view, depict the projected positions of all the bases B_i in helix 2, where $i = 0, \dots, 20$, on a circle. Note that B_i has exactly the same projected position as base $B_{i+21 \times k}$. Further depict the position of base B_{0^*} . Denote the counter clockwise angle from B_{0^*} to B_k as θ_k .

As 21 bases finish two full helical turns, the counterclockwise angle about the helix center between any two consecutive bases B_i and B_{i+1} is $\alpha = 360 \times 2/21 = 34.3^\circ$. The counter clockwise angle from base B_0 to its complementary base B_{0^*} is $\beta = 150^\circ$ [RENP⁺04]. Thus the counter clockwise angle from base B_{0^*} to base B_k is:

$$\theta_k = k \times \alpha - \beta = 34.3^\circ \times k - 150^\circ.$$

In Fig. A.2B, the angle $\theta_{11} = 227.3^\circ$ is depicted.

In unstrained SST lattices, we assume that the two contacting helices H_i and H_{i+1} are approximately tangent to each other. Thus, in the cross-section view, the center O_i of helix H_i , the center O_{i+1} of helix H_{i+1} , and the two contacting bases that define the inter-helix linkage, all lie on the same line. In the case of Fig. A.2B, O_1 , base B_i on Helix 1, base B_{0^*}

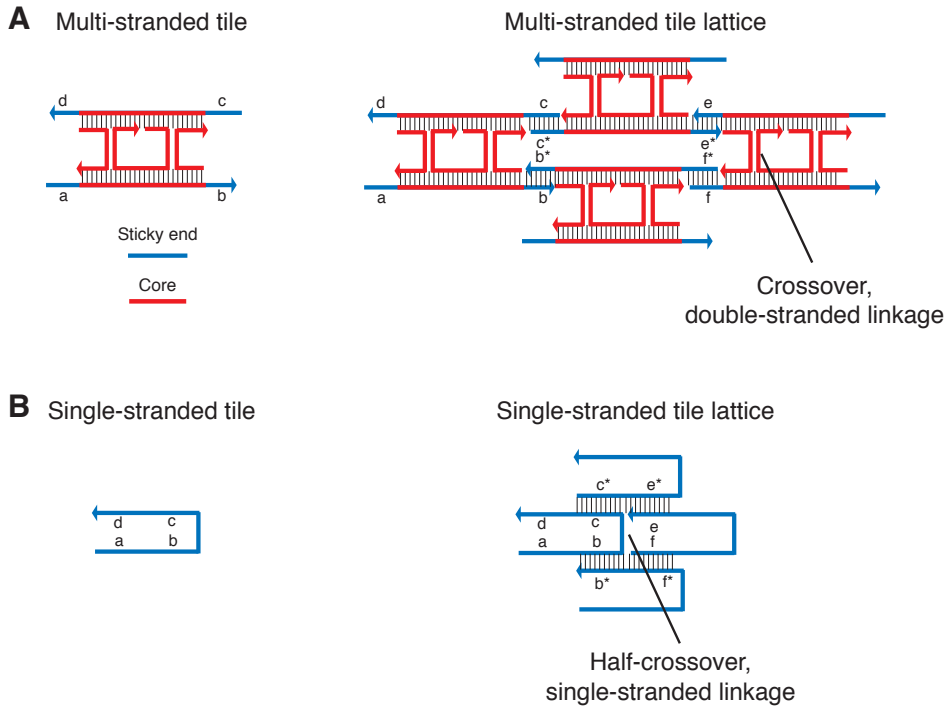


Figure A.1.: Comparison between the multi-stranded tiles and single-stranded tiles. **(A)** Left, a multi-stranded DX tile [FS93, WLWS98] contains a rigid structural core (red) and four flexible sticky ends (blue). Right, sticky end mediated self-assembly of DX tiles. The lattice structure comprises parallel DNA helices connected by double-stranded crossover points. Bold line segments represent the backbone of DNA; short vertical bars represent base pairing; arrow heads indicate 3' ends. Letters marked with * are complementary to the corresponding unmarked letters. **(B)** Left, a single-stranded tile contains only sticky ends (i.e. domains). Right, sticky end mediated self-assembly of SST. The lattice structure comprises parallel DNA helices connected by half-crossover points (i.e. single-stranded linkage).

on Helix 2, and O_2 lie on the same line; O_2 , base B_{11} on Helix 2, base B_j on Helix 3, and O_3 lie on the same line. The angle defined by O_1 , O_2 , and O_3 in Fig. A.2B is determined by the length k of domain a in Fig. A.2A. We immediately have that the angle formed between the three helices O_1 , O_2 , and O_3 is θ_k . In the case of Fig. A.2, $k = 11$, and hence the angle is $\theta_{11} = 227.3^\circ$. For ease of analysis, we further define a *curvature angle*

$$\delta_k = \theta_k - 180^\circ.$$

Now consider the molecular program (Fig. A.2C) that defines the 3-helix ribbon lattice

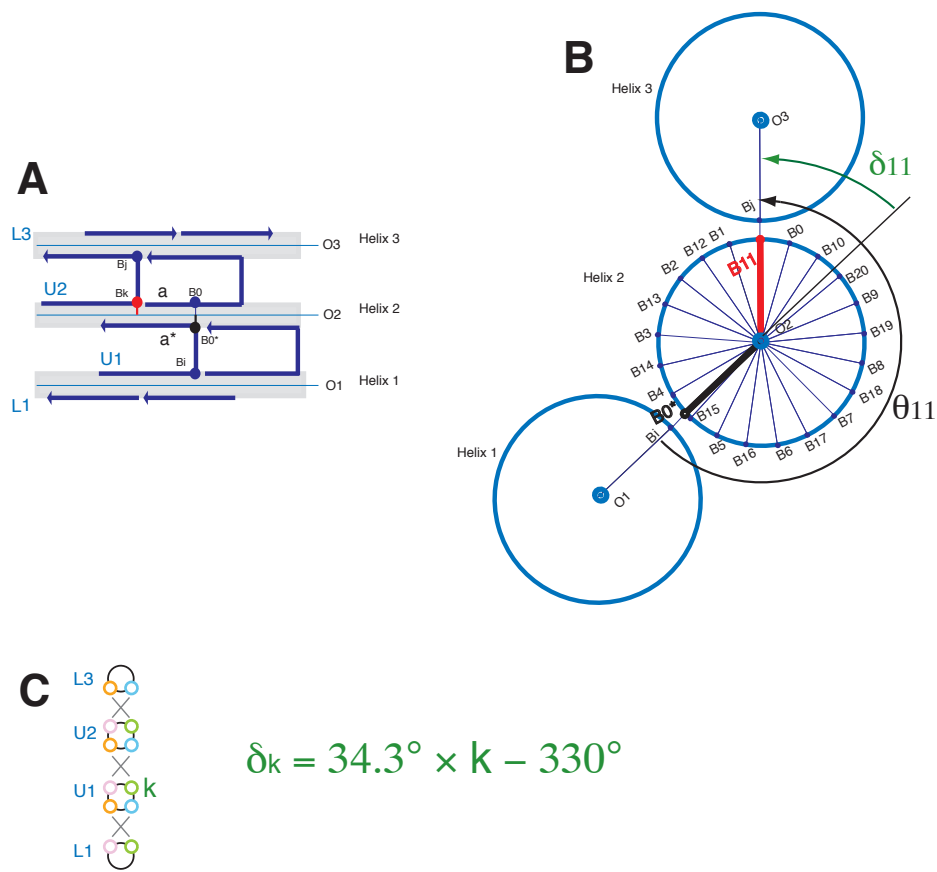


Figure A.2.: Curvature analysis of unstrained SST lattices.

in Fig. A.2A. As the length of domain a in strand U2 in Fig. A.2A equals its complementary domain a^* in strand U1, which in turn equals the value k associated with the green port of U1 in Fig. A.2C, we immediately have the following formula for the curvature angle:

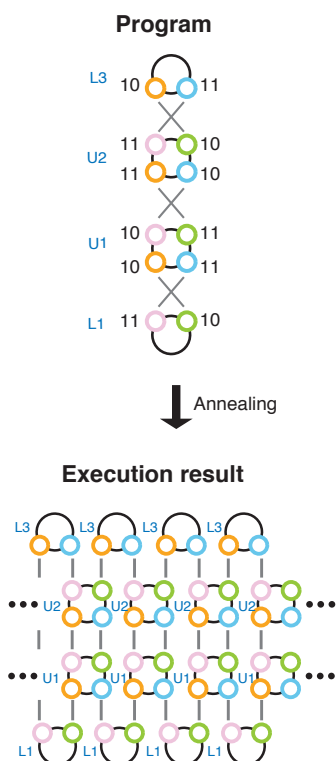
$$\delta_k = 34.3^\circ \times k - 330^\circ.$$

In Fig. A.2B, the angle $\delta_{11} = 47.3^\circ$ is depicted.

Applying the above analysis, we immediately have that for the ribbons in Fig. 2 and the unclosed 4-, 5-, 6-, 7-, 8-, and 10-helix tubes in Fig. 4, which have alternating 10-nt and 11-nt green ports, the curvature angles alternate between $\delta_{10} = 13^\circ$ and $\delta_{11} = 47.3^\circ$, averaging at $(\delta_{10} + \delta_{11})/2 = 30.2^\circ$ per helix; and that for the 20-helix ribbon in Fig. 2 and the unclosed 20-helix tube in Fig. 4, which have only 10-nt green ports, the average curvature per helix is $\delta_{10} = 13^\circ$.

Note that the above analysis is based on the assumption that in unstrained SST lattices, two adjacent helices lie approximately tangent to each other to minimize the putative molecular strain at the linkage points. This assumption, though theoretically plausible, has not been experimentally verified. Also note that the above analysis is intended for unstrained SST lattices and should not be applied to analyze the curvature of closed tubes.

A Nodal abstraction



B Molecular implementation

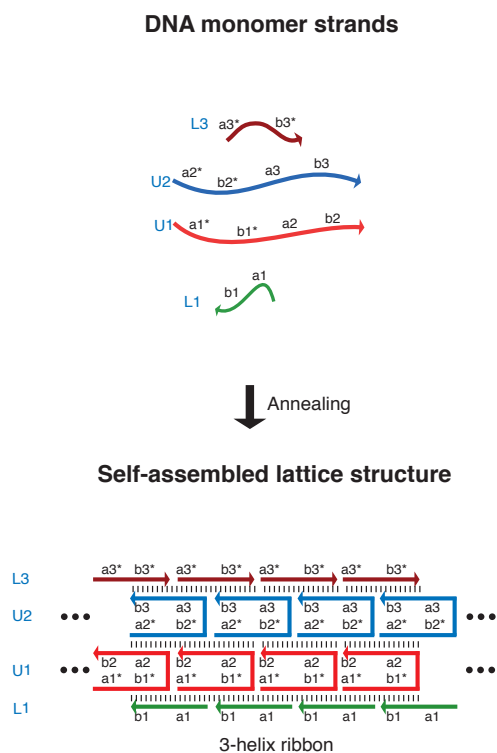


Figure A.3.: Molecular program and secondary structure schematic for the 3-helix ribbon. (A) Top, the molecular program. The number associated with a port indicates the number of nucleotides in the corresponding domain in the SST motif. Grey line segment connects two complementary ports. Bottom, the lattice structure as the output of the program depicted in the top panel. (B) The molecular implementation of the program depicted in A. The domain dimensions correspond to the port dimensions depicted in A: L1, 10 (green port)-11 (pink port) (i.e. $|a_1| = 10$ nt; $|b_1| = 11$ nt); U1, 10-11-11-10; U2, 11-10-10-11; L3, 10-11. See Appendix A.7 for DNA sequences.

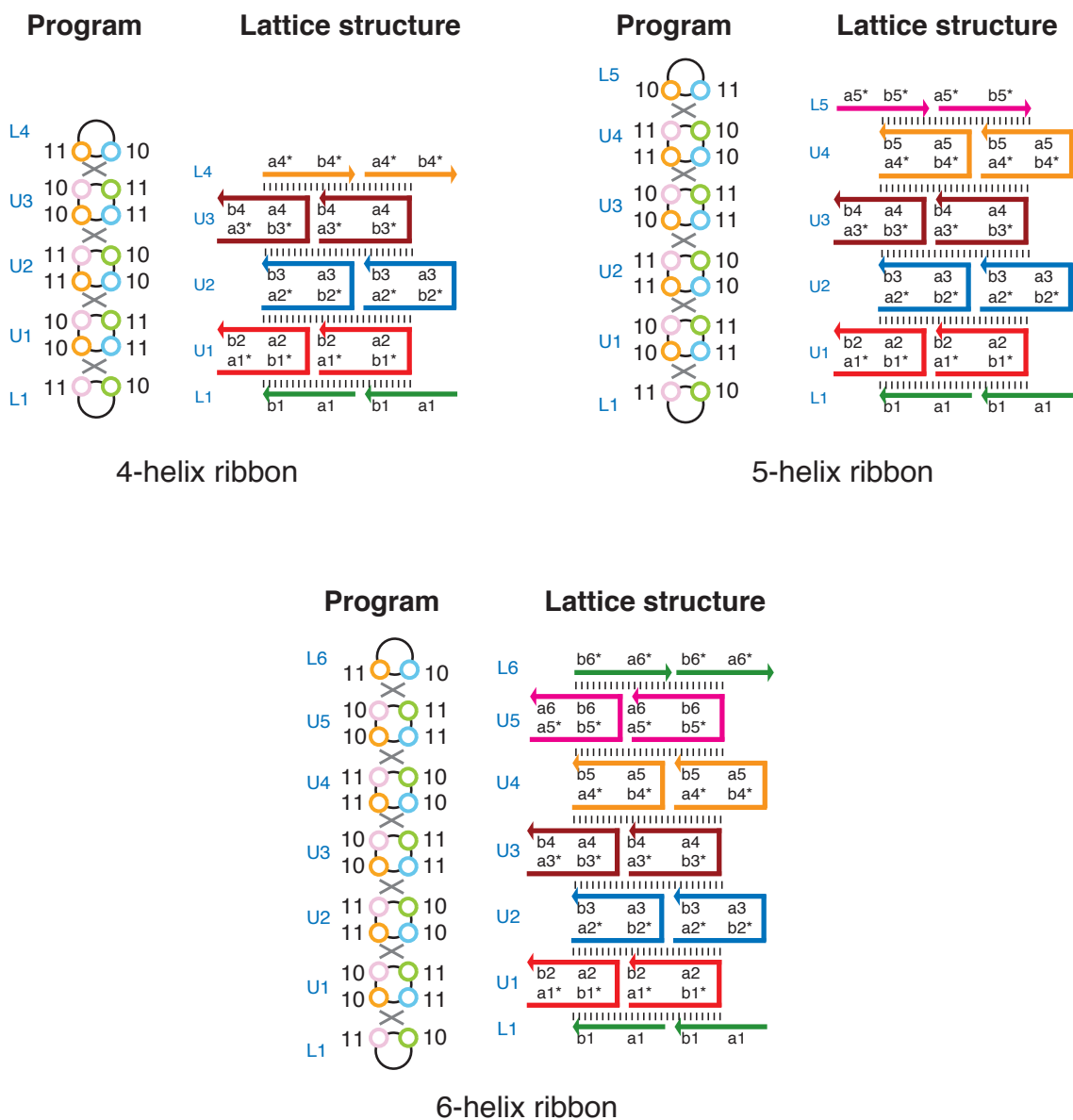


Figure A.4.: Molecular programs and secondary structure schematics for 4-, 5-, and 6-helix ribbons. Left, molecular program. The number associated with a port indicates the number of nucleotides in the corresponding domain in the SST motif. Grey line segment connects two complementary ports. Right, secondary structure schematic. The domain dimensions correspond to the port dimensions depicted in the left panel: L1, 10-11; U1, U3, U5, 10-11-10; U2, U4, 11-10-10-11; L5, 10-11; L4, L6, 11-10. See Appendix A.7 for DNA sequences.

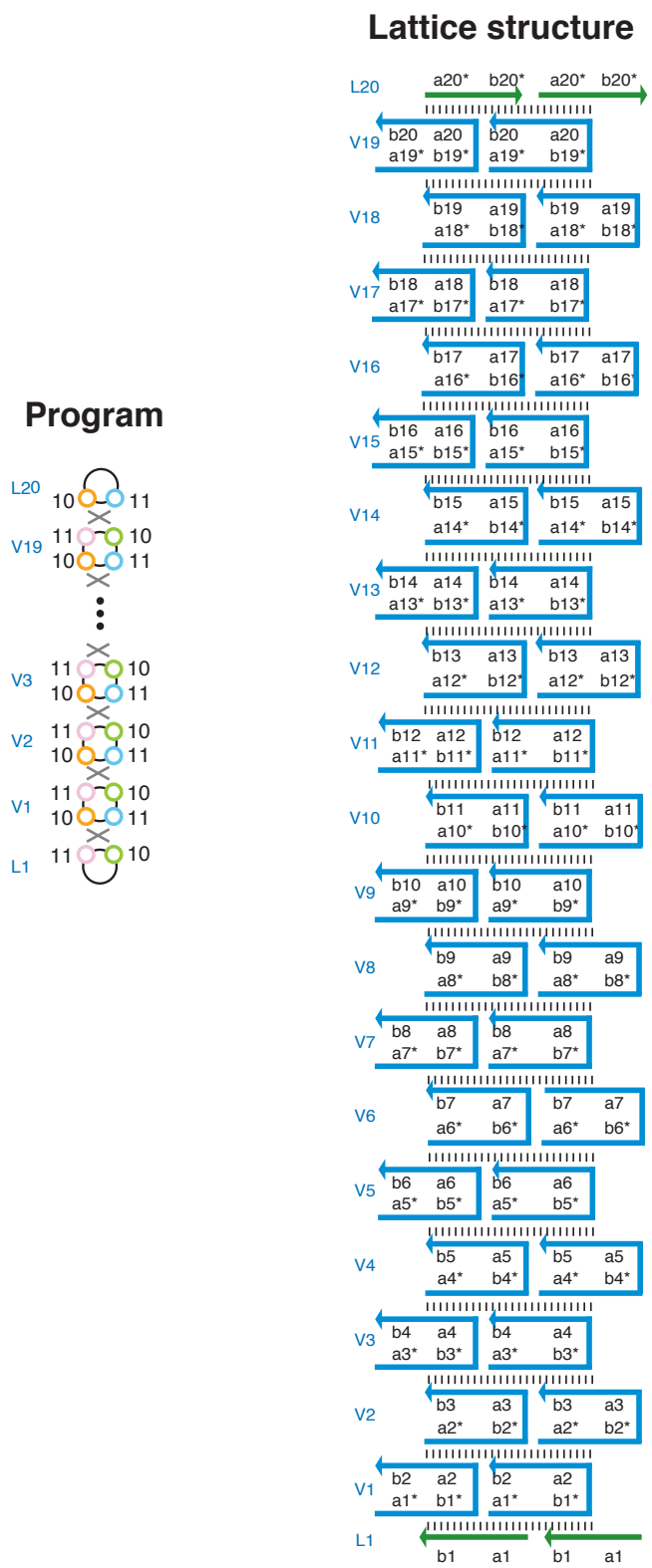


Figure A.4.: Continued. Molecular program and secondary structure schematic for the 20-helix ribbon. The domain dimensions correspond to the port dimensions depicted in the left panel: L1, 10-11; V_k , 10-11-10-11; L20, 10-11. See Section A.7 for DNA sequences.

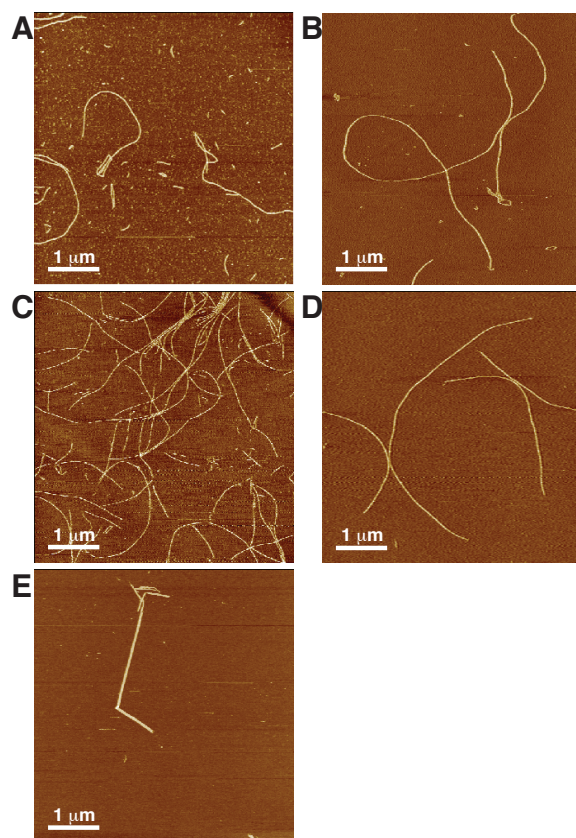


Figure A.5.: AFM images of (A) 3-helix ribbons, (B) 4-helix ribbons, (C) 5-helix ribbons, (D) 6-helix ribbons, and (E) 20-helix ribbons. Some ribbons appear to “branch” in the AFM images. However, zoomed-in images reveal that such “branching” is primarily due to two ribbon segments lying (1) either on top of or (2) tangent to each other. It is likely that the first case results from two separate ribbon segments landing on the mica in a crossing configuration, and that the latter case occurs through electrostatic interactions between the ribbon segments during adsorption onto the mica surface. Though we cannot completely rule out the possibility that such two ribbon segments may share some edge strands, we suggest that such possibility is unlikely for the following reasons. First, in dilute samples, the crossing/tangent co-localization of the ribbons appears to be rare. Second, due to the flexibility of the single-strand motif, an inter-ribbon linkage formed by one or two shared edge strands is likely to be unstable and may be dissolved respectively through three- or four-way branch migration.

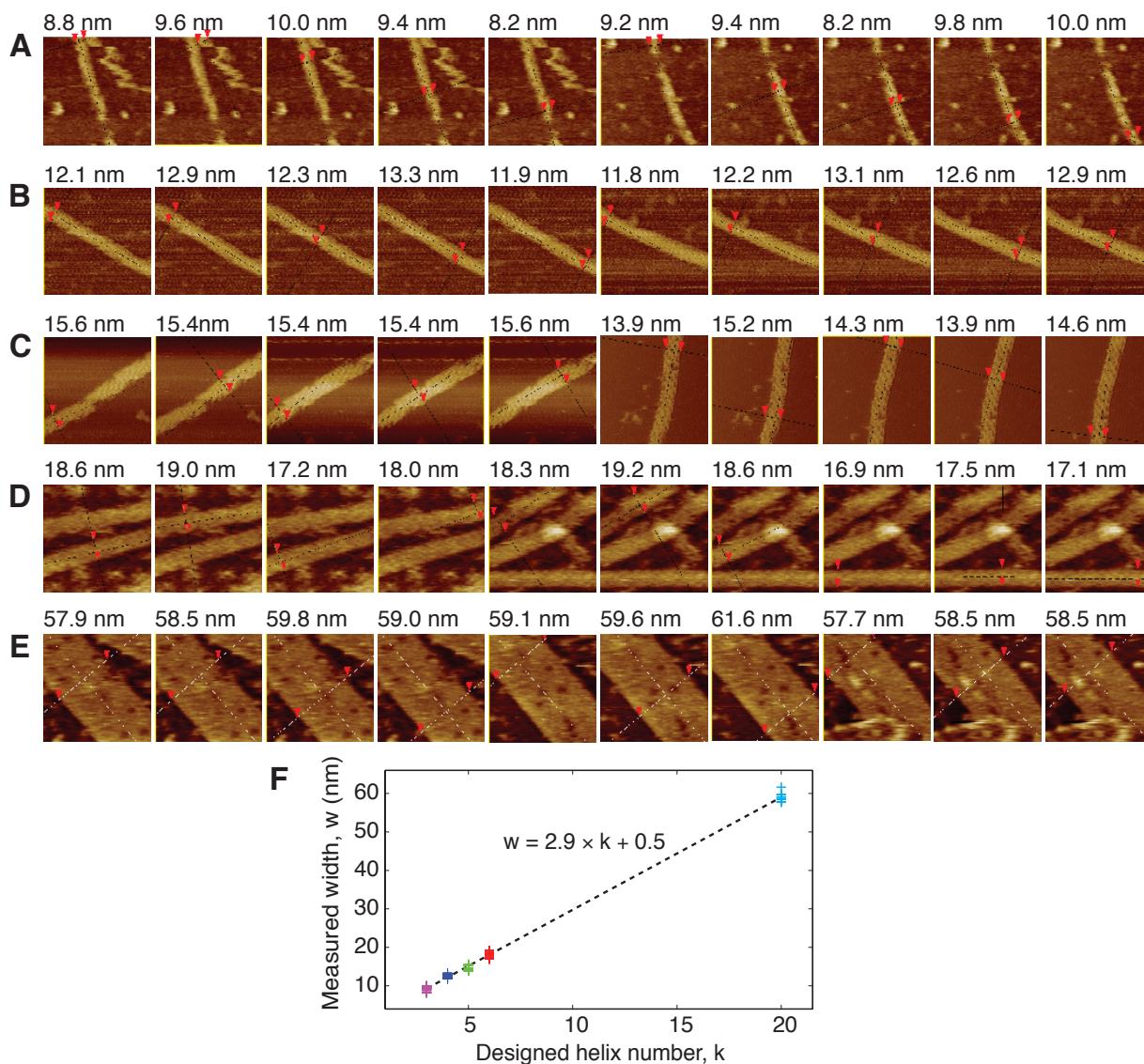


Figure A.6.: SST ribbon width measurement. (A-E) 3-, 4-, 5-, 6-, and 20-helix ribbons. The section file screen shots are presented along with the measured widths of the ribbons. Image size: 100 nm \times 100 nm. (F) Width plot. Linear fit reveals $w = 2.9 \times k + 0.5$, where w is the measured width and k is designed helix number for the ribbon. This linear relationship is approximated by $w \approx 3 \times k$. Note that unlike in Fig. A.13 where 10 random DNA tube structure samples are measured to establish that no $2 \times k$ helix tubes are present, the measurements here are from 10 random points along one to three random ribbon samples for each k -helix ribbon. The measured narrow width distribution thus reflects the uniform width distribution along the ribbons and the narrow distribution of instrument measurement noise. This measured ~ 3 nm per helix width for SST lattice is used later in Fig. A.13 to establish the circumference monodispersity for k -helix tubes.

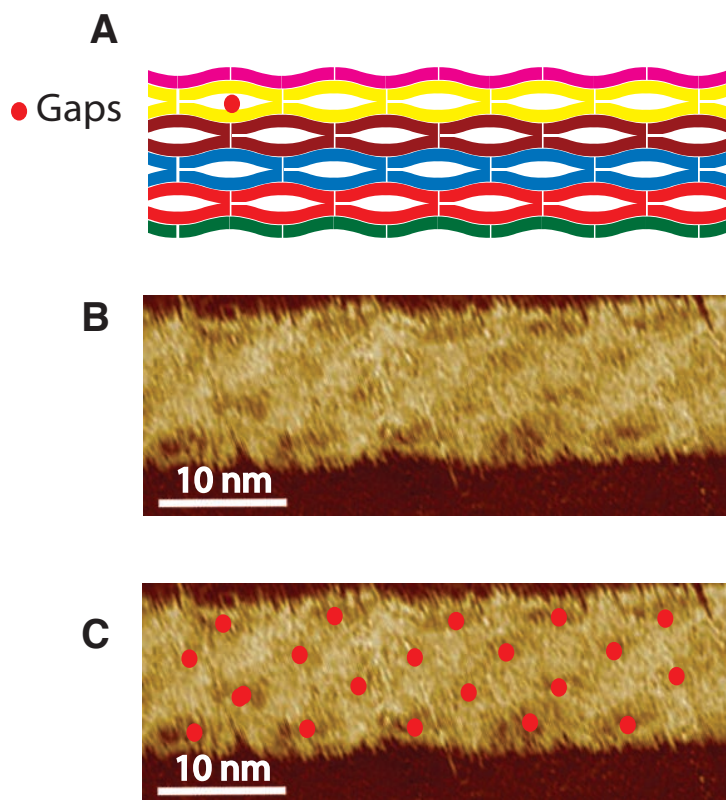


Figure A.7.: High resolution AFM image for the 5-helix ribbon in Fig. 2C. (A) Schematic. (B) High resolution AFM image. (C) AFM image annotated with red dots indicating inter-helix gaps. The ~ 3 nm per helix width measurement for k -helix ribbon structures is greater than the 1.8 nm width of a single DNA helix. The reason for this increased width is revealed in a high resolution image in Fig. A.7, which also presents further unambiguous evidence for the correct formation of the ribbon structures. (A) is a depiction of the expected DNA structure with bended helices and gaps between the helices. The possible mechanism that causes this structure is as follows. The electrostatic force between neighboring negatively charged DNA helices pushes the helices away from each other, resulting in the bending of these helices, which are inter-connected by half-crossovers. The interplay between the electrostatic repulsion force and the bending deformation force is expected to result in a minimum energy lattice structure with alternating holes (indicated by red dots) and an increased width (see Appendix D and [HW04]). The AFM image of the 5-helix ribbon (B) agrees well with the above hypothesis, demonstrating an alternating pattern of four layers of inter-helix gaps (C).

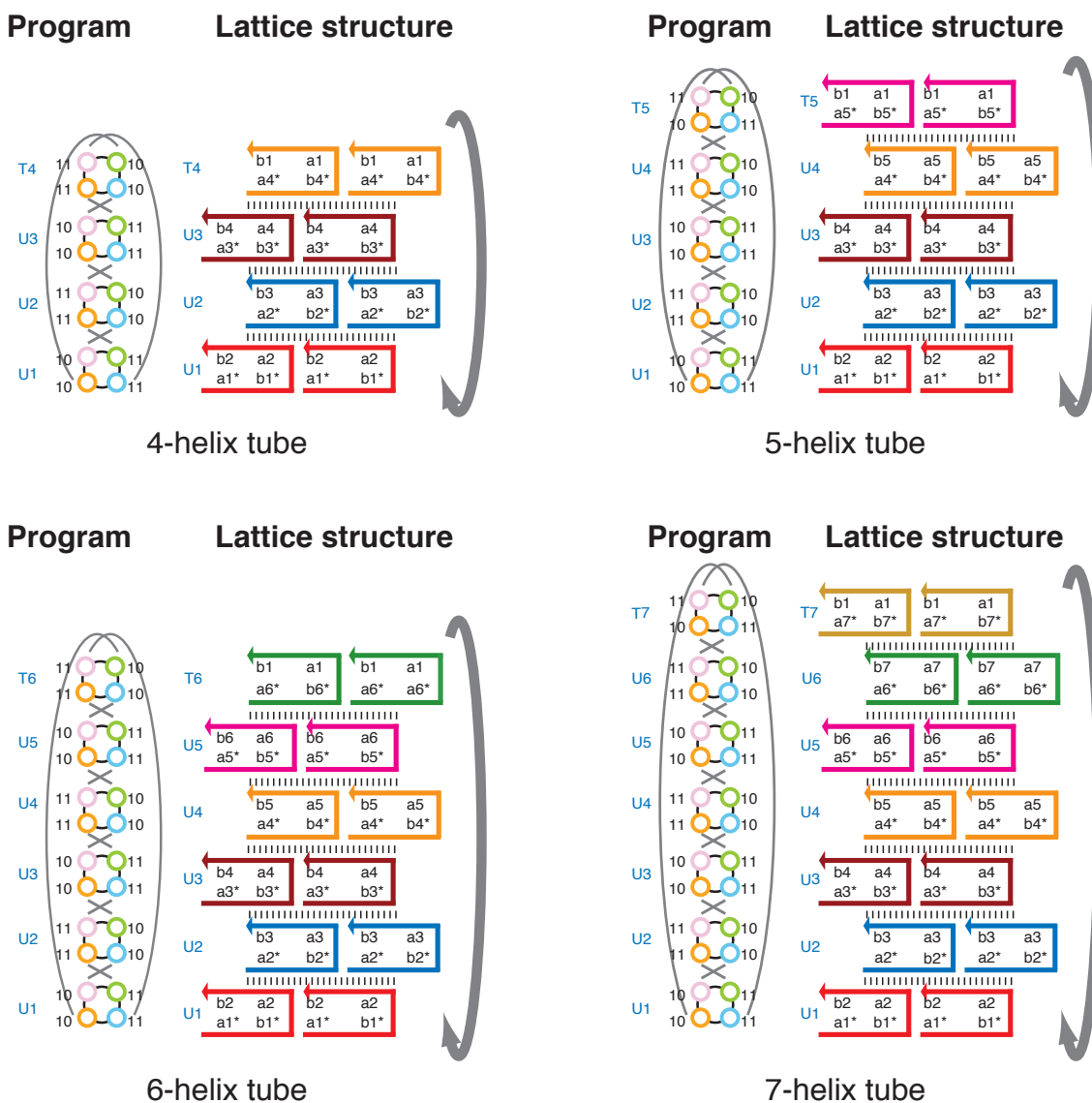


Figure A.8.: The molecular programs and the secondary structures for 4-, 5-, 6-, 7-, 8-, and 10-helix tubes. Left, molecular program. The number associated with a port indicates the number of nucleotides in the corresponding domain in the SST motif. Grey line segment connects two complementary ports. Right, secondary structure schematic. The domain dimensions correspond to the port dimensions depicted in the left panel: U1, U3, U5, U7, and U9 have domain dimensions of 10-11-11-10; U2, U4, T4, U6, T6, U8, T8, and U10 have domain dimensions of 11-10-10-11; T5 and T7 have domain dimensions of 10-11-10-11. See Appendix A.7 for DNA sequences.

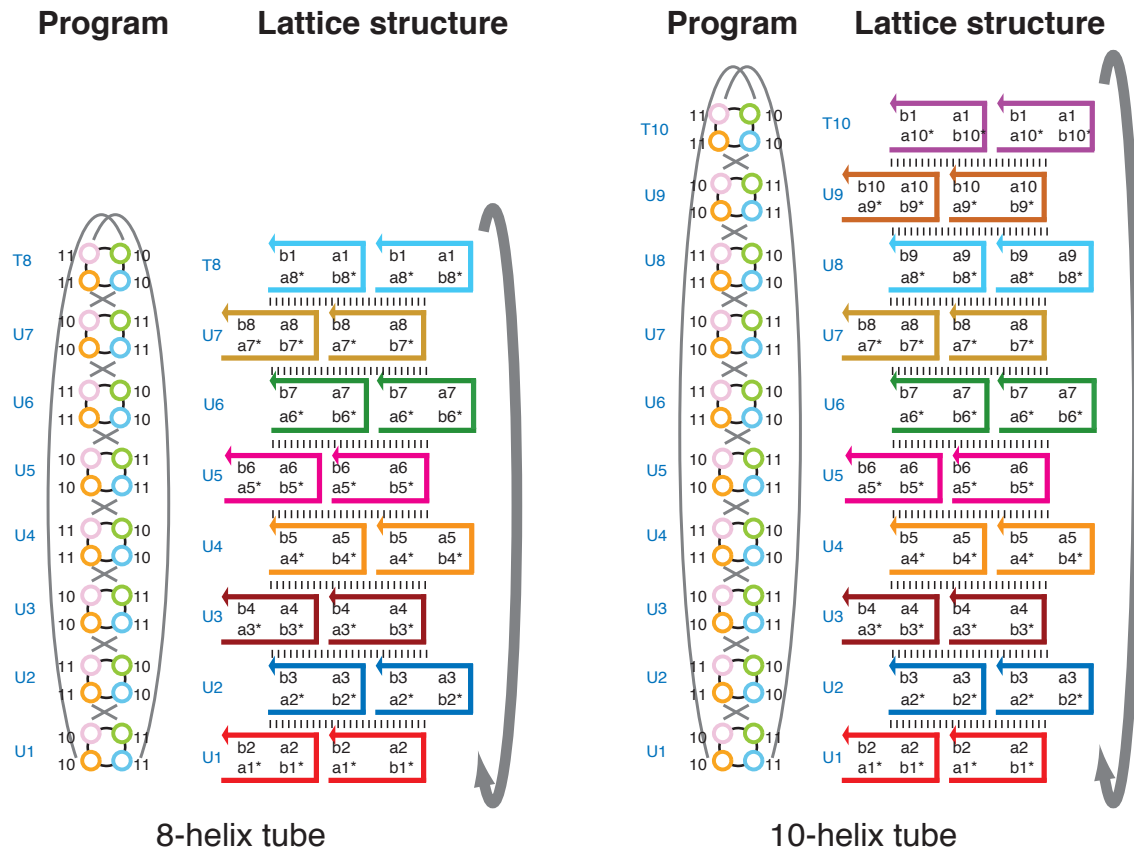


Figure A.8.: Continued.

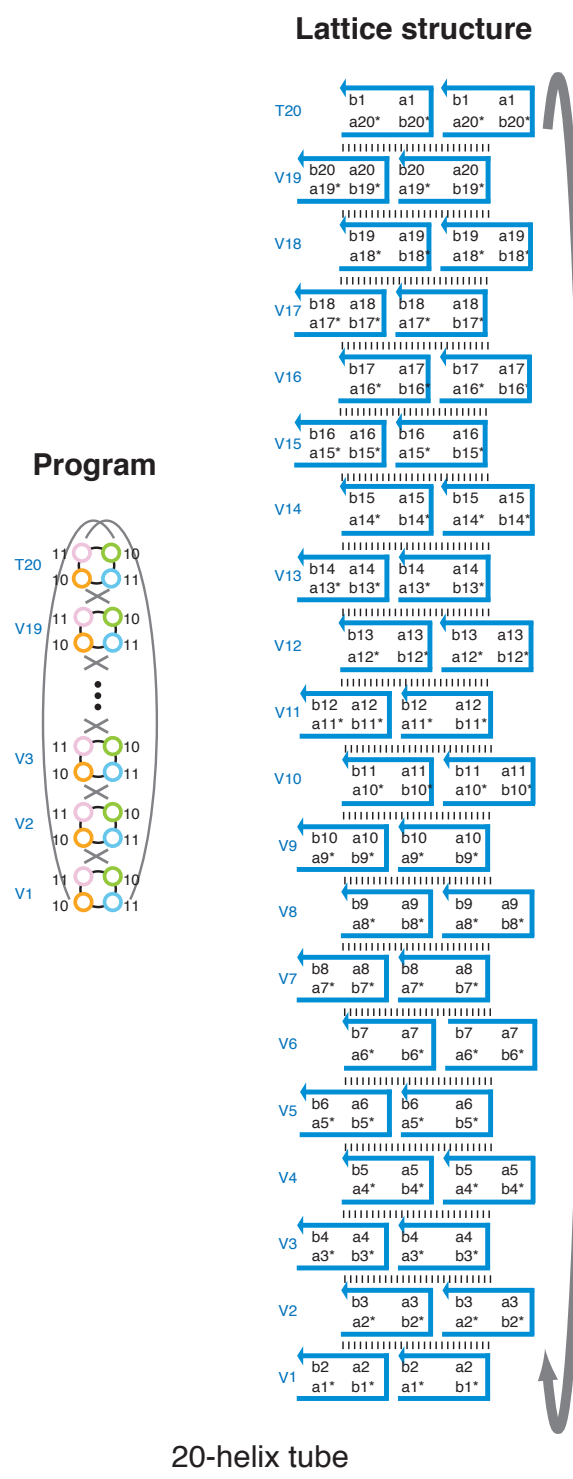


Figure A.8.: Continued. Molecular program and the secondary structure for the 20-helix tube. The domain dimensions correspond to the port dimensions depicted in the left panel: V_k , T20, 10-11-10-11. See Appendix A.7 for DNA sequences.

Tubes \ SST	U1	U2	U3	U4	U5	U6	U7	U8	U9	T4	T5	T6	T7	T8	T10
4-helix tube	x	x	x							x					
5-helix tube	x	x	x	x							x				
6-helix tube	x	x	x	x	x							x			
7-helix tube	x	x	x	x	x	x							x		
8-helix tube	x	x	x	x	x	x	x							x	
10-helix tube	x	x	x	x	x	x	x	x	x						x

Figure A.9.: The component strand table for 4-, 5-, 6-, 7-, 8-, and 10-helix tubes. The strands labeled with the same name are identical in Fig. A.8. Consequently, by selecting appropriate subsets from a common pool of 15 distinct 42-nt SST species (U1-9, T4-8, T10), we can construct monodisperse tubes with 6 distinct circumferences.

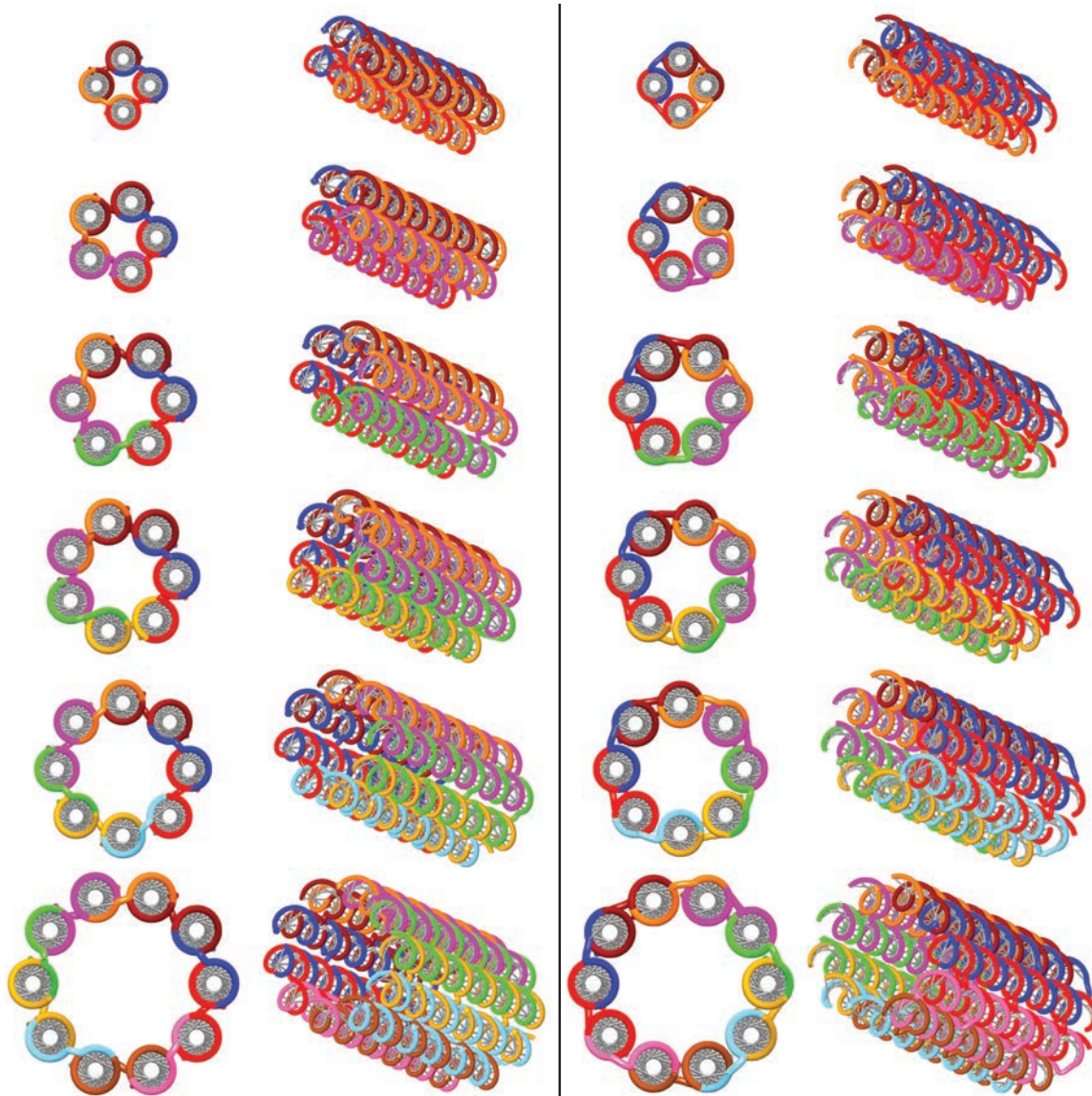


Figure A.10.: 3D illustration of 4-, 5-, 6-, 7-, 8-, 10-, and 20-helix tubes. The figure shows both cross-section views and side views. The left column and the right column describe the tubes that are closed along opposite directions. In other words, a tube on the left is flipped inside out compared to the tube to its right. Based on this geometrical modeling, the configurations on the left appear to be less strained and are likely to dominate the configurations on the left thermodynamically. It is also conceivable the left configurations may dominate the right configurations kinetically, e.g. through faster cyclization. However, we have not performed experiments to characterize the closure directions of the SST tubes. It is also interesting to note the 10-base translational shift along the helix axial direction in the 5-helix tube and the 7-helix tube and the consequent putative mechanical strain that these tubes may have successfully absorbed.

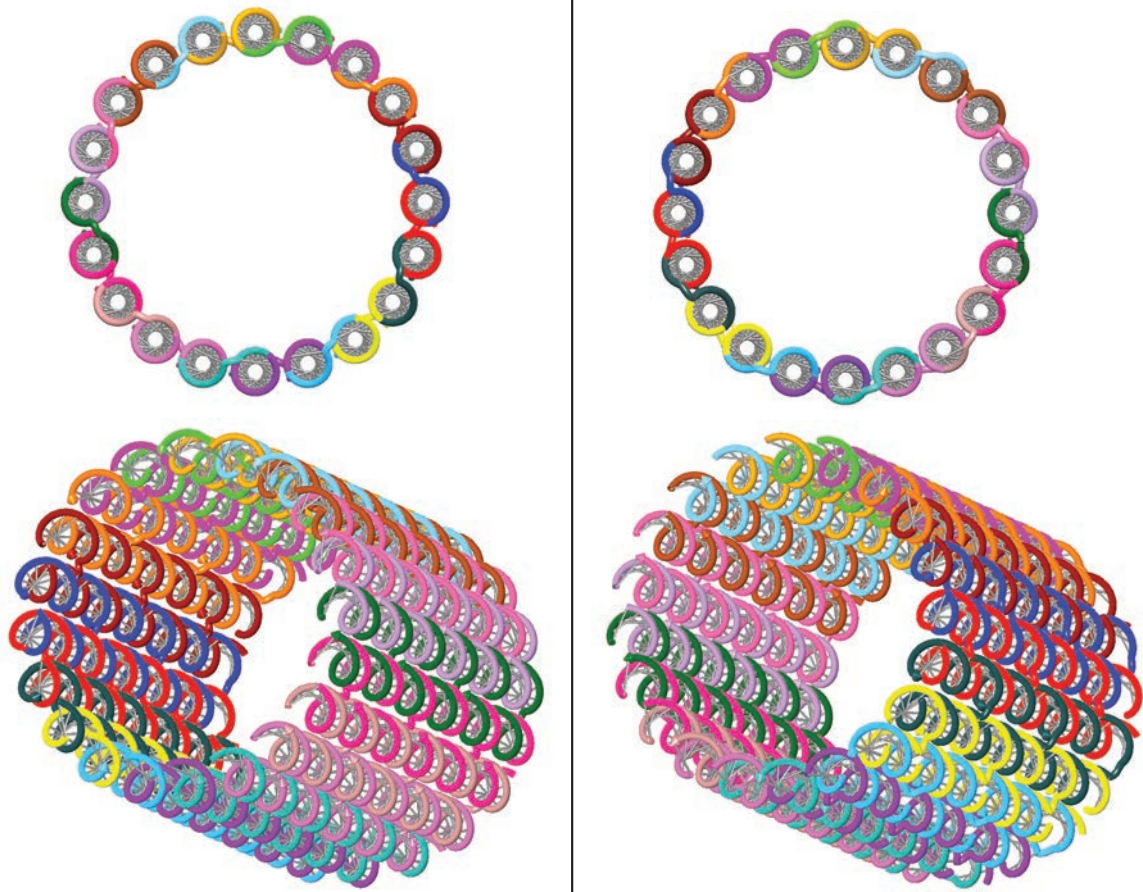


Figure A.10.: Continued.

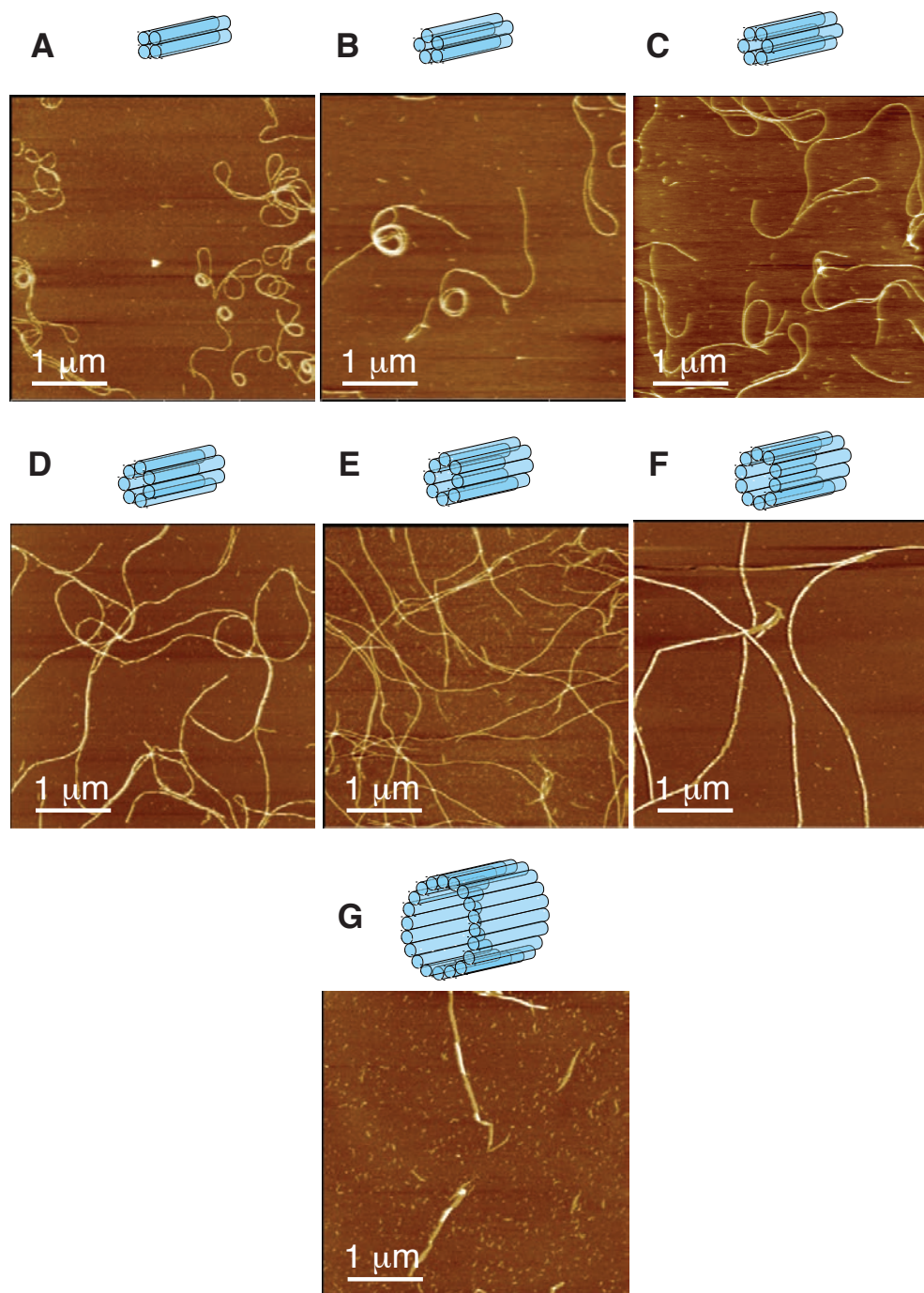


Figure A.11.: Panels **A-G** are respectively AFM images of 4-, 5-, 6-, 7-, 8-, 10-, and 20-helix SST tubes. Note that the persistent lengths of the tubes appear to increase (as expected) with the number of the circumferential helices. Also note that the 4-helix tubes and 5-helix tubes sometimes assume spiral configurations when deposited on mica. The presence of these spiral configurations may reflect the expected relatively shorter persistent lengths of the 4-helix and 5-helix tubes and/or the possibly relatively higher mechanical strain present in these tubes. Tube aggregations are commonly observed in 20-helix tubes and occasionally in other tube systems. Further, the 20-helix tubes typically appear significantly shorter than other tubes.

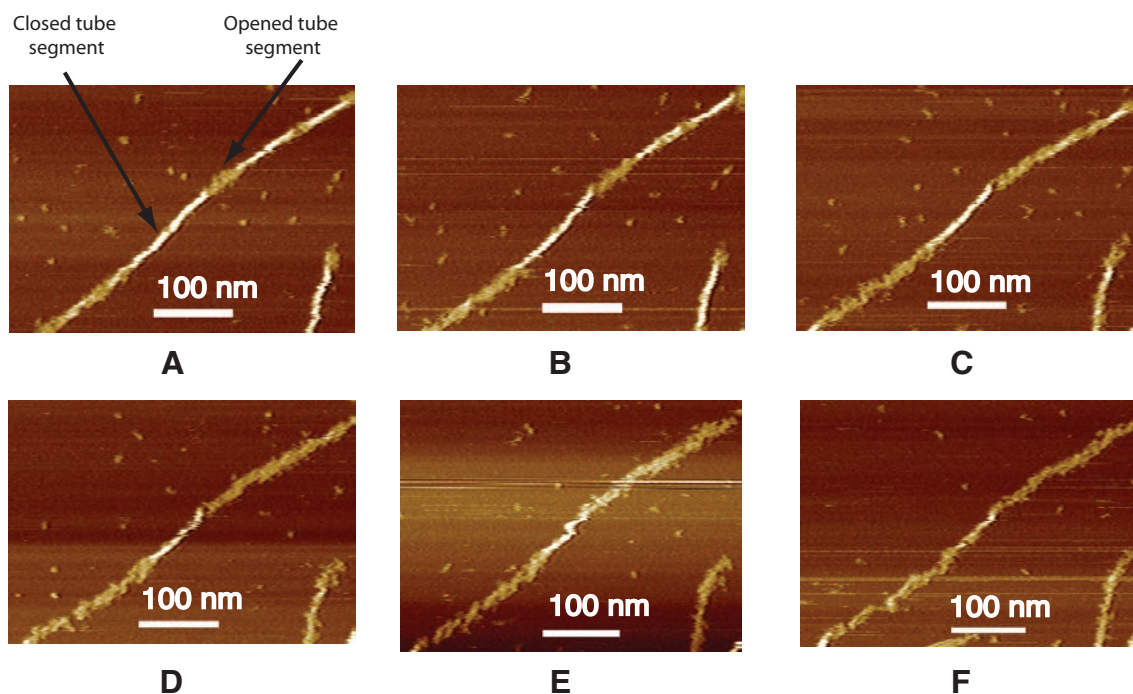


Figure A.12.: AFM images for the opening of a 6-helix tube. The panels **A-F** present sequential screenshots demonstrating the process of the opening of a 6-helix tubes by the repeated scanning of an AFM tip. The tube is opened by the mechanical force exerted by the AFM tip. The intact segments of the tube have higher height than the opened segments, and thus appear brighter. This process reveals the tubular nature of the 6-helix SST tubes.

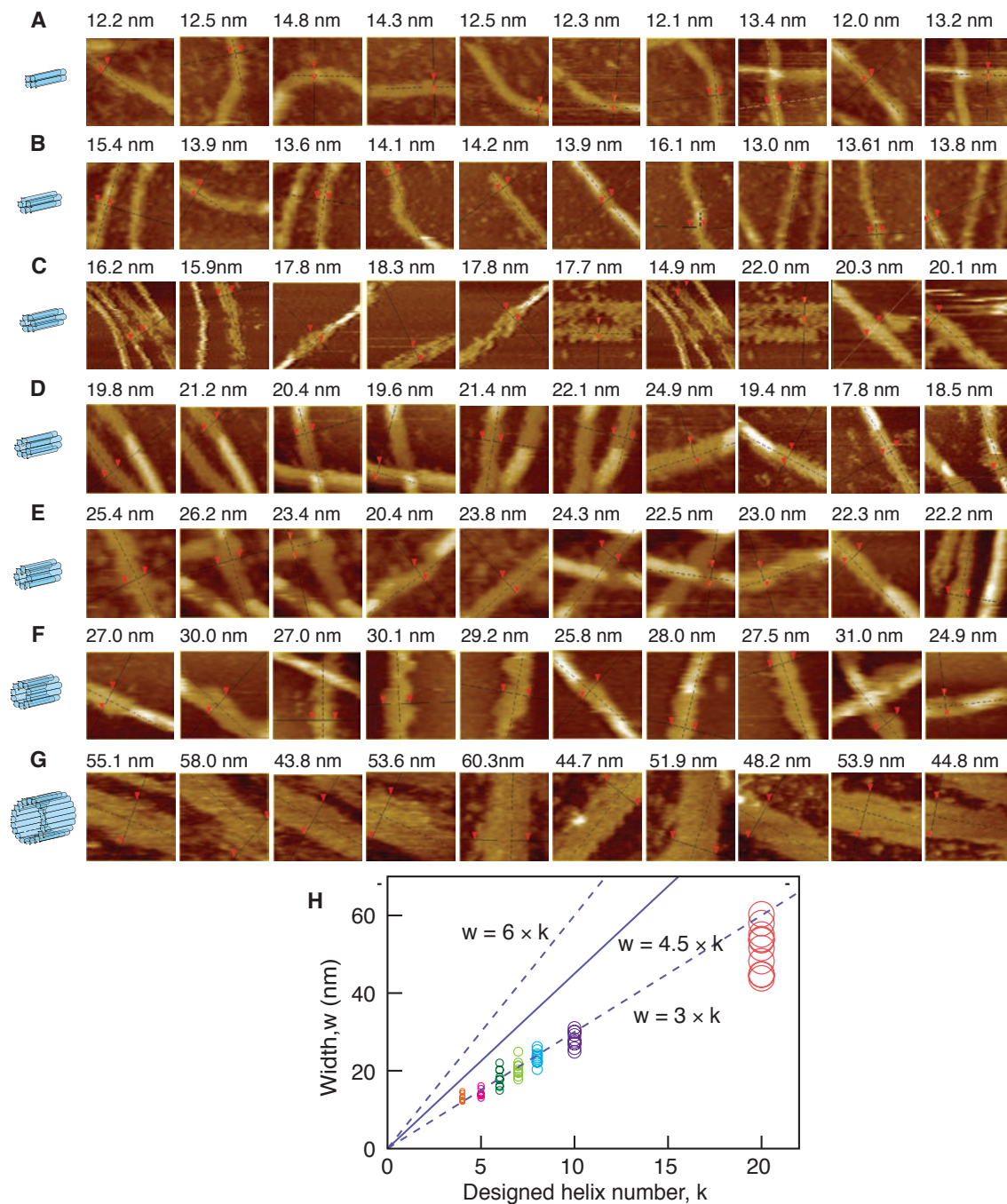


Figure A.13.: SST tube circumference measurements. (A-G) 4-, 5-, 6-, 7-, 8-, 10-, and 20-helix tubes. The AFM section file screen shots are presented along with the measured widths of the opened tubes. Image size: 100 nm \times 100 nm. (H) Width plot of opened tubes. A k -helix opened tube is expected to have a width $w \approx 3 \times k$ nm, as determined by the width measurement of the k -helix ribbons (Fig. A.6). A $2 \times k$ -helix opened tube, by contrast, is expected to have $w \approx 6 \times k$ nm. Lines corresponding to $w = 3 \times k$, $w = 4.5 \times k$, and $w = 6 \times k$ are plotted to facilitate tube circumference monodispersity determination. For each k -helix tube, 10 random, opened tubes are measured. Tube aggregations are commonly observed in 20-helix tubes and occasionally in other tube systems. Such aggregations are excluded from width measurements.

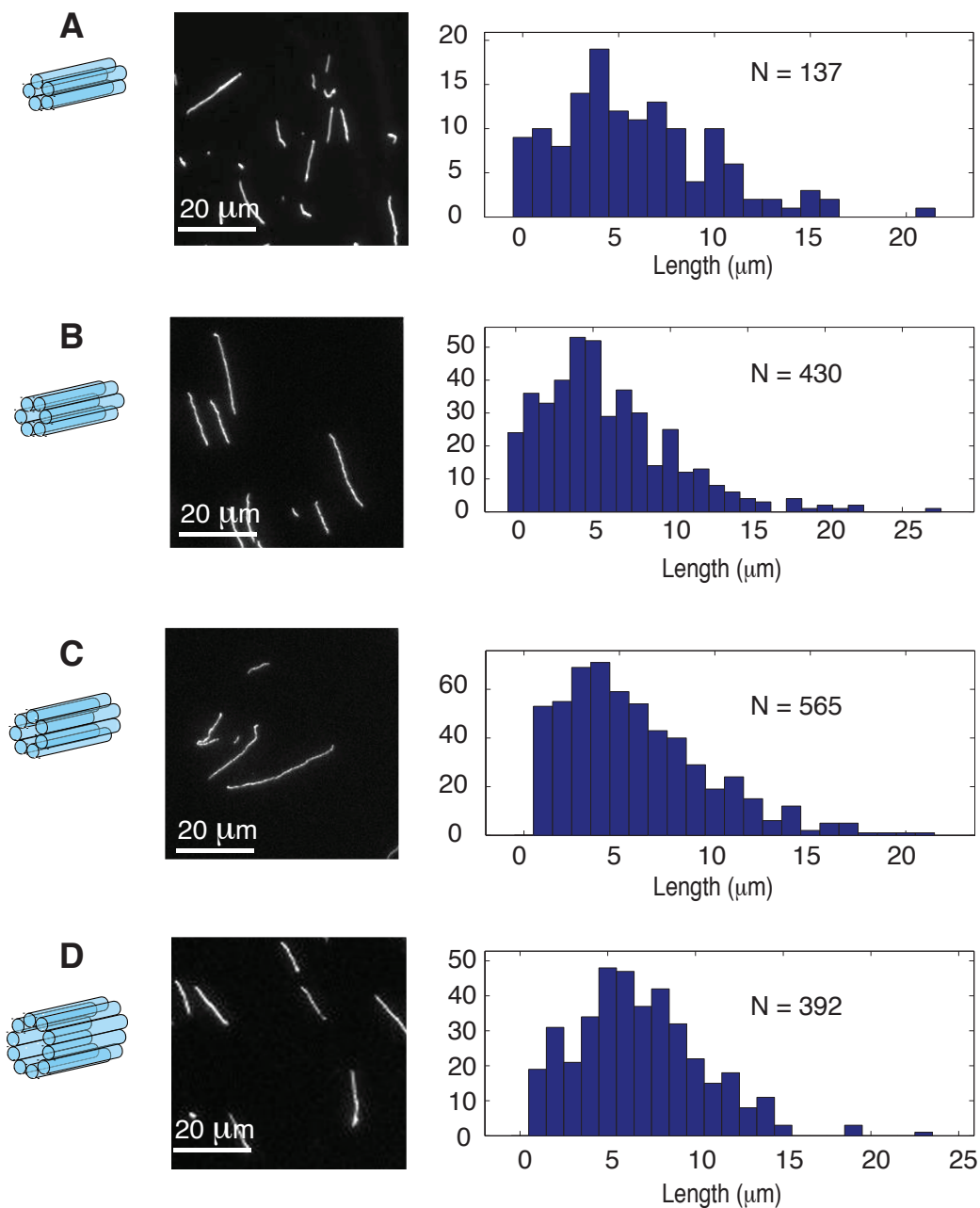


Figure A.14.: Panels (A-D) are respectively fluorescence microscopy images (left) and length profile (right) of 5-, 6-, 7-, and 10-helix tubes decorated with Cy3 fluorophores. N denotes sample size. The average lengths for 5-, 6-, 7-, and 10-helix tubes are respectively $\sim 5.9 \mu\text{m}$, $\sim 5.9 \mu\text{m}$, $\sim 5.8 \mu\text{m}$, and $\sim 6.8 \mu\text{m}$.

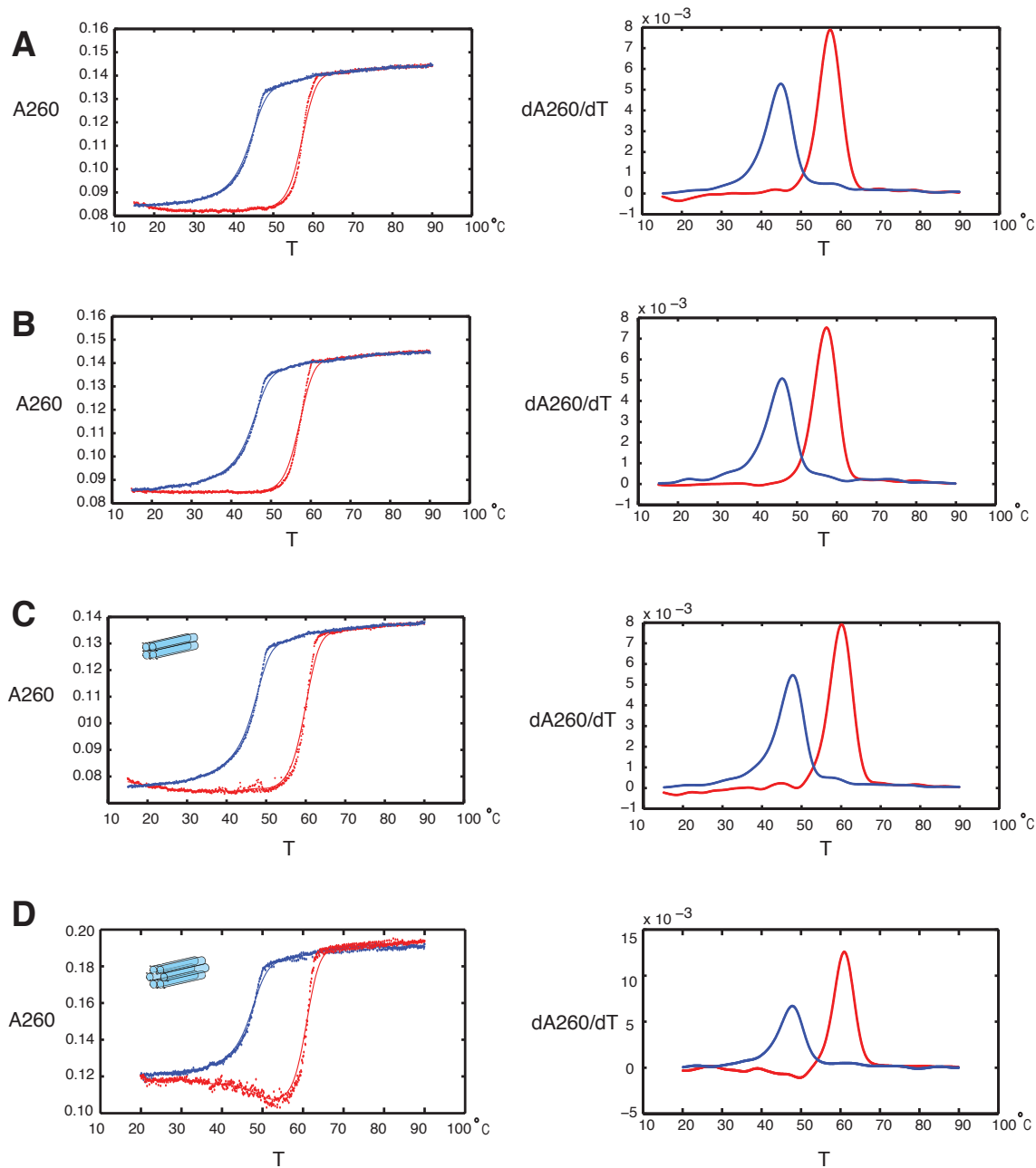


Figure A.15.: Melting (red) and annealing (blue) curves for (A) 3-helix ribbons, (B) 4-helix ribbons, (C) 4-helix tubes, and (D) 6-helix tubes. The transition temperatures for melting/annealing (measured as the peaks of the derivatives) are (A) 57°C and 45°C, (B) 58°C and 47°C, (C) 60°C and 48°C, and (D) 61°C and 48°C. Each constituent DNA strand at 100 nM. Cooling/heating rate at 0.15°C per minute for A-C and 0.115°C per minute for D. When repeating the experiment in D at a slower cooling/heating rate of 0.023°C per minute, the transition temperatures for melting/annealing become 60°C and 49°C (data not shown).

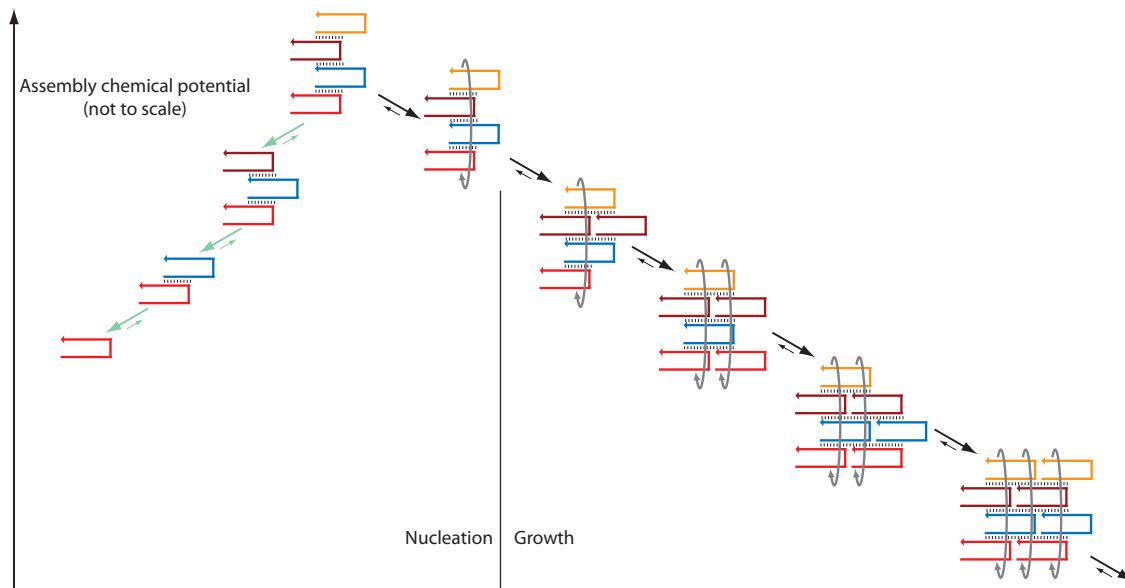


Figure A.16.: Energetics of a conjectured assembly sequence for 4-helix SST tubes. To speculate about possible kinetic assembly pathways, we adapt a nucleation-elongation model in [SW07]. The figure describes the hypothetical pathway for assembling 4-helix SST tubes under slightly super saturated conditions, where the attachment of one SST to the lattice with two sticky ends (i.e. domains) is favorable but with one sticky end is unfavorable. The rate-limiting nucleation step (left) that involves unfavorable events leads to the formation of a presumed critical nucleus, followed by growth (right) composed of only favorable events. Note that the downhill growth steps involve the formation of twice as many base pairs as the uphill nucleation steps. Large black arrows, forward-biased reaction steps. Small green arrows, unfavorable steps. The schematic is adapted from the depiction of the “standard sequence model” in [SW07].

A.7. DNA sequences

The DNA sequences for the systems described in the paper are presented both as secondary structure schematics and as text sequences annotated with domain names. The domain names are consistent with those in the secondary structure schematics figures.

Name	Sequence
U1: a1*-b1*-a2-b2	5'-GGCGATTAGG-ACGCTAAGCCA-CCTTTAGATCC-TGTATCTGGT-3'
U1-Cy3:	5'-/5Cy3/TT-GGCGATTAGG-ACGCTAAGCCA-CCTTTAGATCC-TGTATCTGGT-3'
U2: a2*-b2*-a3-b3	5'-GGATCTAAAGG-ACCAGATACA-CCACTCTTCC-TGACATCTTGT-3'
U3: a3*-b3*-a4-b4	5'-GGAAGAGTGG-ACAAGATGTCA-CCGTGAGAACC-TGCAATGCGT-3'
U4: a4*-b4*-a5-b5	5'-GGTCTCACGG-ACGCATTGCA-CCGCACGACC-TGTTTCGACAGT-3'
U5: a5*-b5*-a6-b6	5'-GGTCGTGCGG-ACTGTCGAACA-CCAACGATGCC-TGATAGAAGT-3'
L1: a1-b1	5'-CCTAATCGCC-TGGCTTAGCGT-3'
L3: a3*-b3*	5'-GGAAGAGTGG-ACAAGATGTCA-3'
L4: a4*-b4*	5'-GGTCTCACGG-ACGCATTGCA-3'
L5: a5*-b5*	5'-GGTCGTGCGG-ACTGTCGAACA-3'
L6: a6*-b6*	5'-GGCATCGTTGG-ACTTCTATCA-3'

Table A.1.: DNA sequences: 3-, 4-, 5-, 6-helix ribbons

Name	Sequence
U1: a1*-b1*-a2-b2	5'-GGCGATTAGG-ACGCTAAGCCA-CCTTTAGATCC-TGTATCTGGT-3'
V1: a1*-b1*-a2-b2	5'-GGCGATTAGG-ACGCTAAGCCA-CCTTTAGATC-CTGTATCTGGT-3'
V2: a2*-b2*-a3-b3	5'-GATCTAAAGG-ACCAGATACAG-CCACTCTTCC-TGACATCTTGT-3'
V3: a3*-b3*-a4-b4	5'-GGAAGAGTGG-ACAAGATGTCA-CCGTGAGAACC-TGCAATGCGT-3'
V4: a4*-b4*-a5-b5	5'-GTTCTCACGG-ACGCATTGCA-CCGCACGACC-TGTTTCGACAGT-3'
V5: a5*-b5*-a6-b6	5'-GGTCGTGCGG-ACTGTCGAACA-CCAACGATGC-CTGATAGAAGT-3'
V6: a6*-b6*-a7-b7	5'-GCATCGTTGG-ACTTCTATCAG-ATGCACCTCC-AGCTTTGAATG-3'
V7: a7*-b7*-a8-b8	5'-GGAGGTGCAT-CATTCAAAGCT-AACGGTAACT-ATGACTTGGGA-3'
V8: a8*-b8*-a9-b9	5'-AGTTACCGTT-TCCCAAGTCAT-AACACTAGAC-ACATGCTCCTA-3'
V9: a9*-b9*-a10-b10	5'-GTCTAGTGTT-TAGGAGCATGT-CGAGACTACA-CCCTTGCCACC-3'
V10: a10*-b10*-a11-b11	5'-TGTAAGTCTCG-GGTGGCAAGGG-TACTACCGCT-CCATTAAGAAT-3'
V11: a11*-b11*-a12-b12	5'-AGCGGTAGTA-ATTCTTAATGG-ATCCGTCTAT-CTACACTATCA-3'
V12: a12*-b12*-a13-b13	5'-ATAGACGGAT-TGATAGTGTAG-AGACGAAATC-AGCAGAATAA-3'
V13: a13*-b13*-a14-b14	5'-GATTCGTCT-TTAGTCTGCT-CTGCGAAGTA-ATCAGCCGAGC-3'
V14: a14*-b14*-a15-b15	5'-TACTTCGCAG-GCTCGGCTGAT-GAACTCGCTC-CAGAATCGACG-3'
V15: a15*-b15*-a16-b16	5'-GAGCGAGTTC-CGTCGATTCTG-AACTTCAAT-ATCATATCGTA-3'
V16: a16*-b16*-a17-b17	5'-ATTGAAAGTT-TACGATATGAT-CCGTAGCAGT-ATAAGCGATCT-3'
V17: a17*-b17*-a18-b18	5'-ACTGCTACGG-AGATCGCTTAT-CGCTAGCCAC-CAAGATCAAGC-3'
V18: a18*-b18*-a19-b19	5'-GTGGCTAGCG-GTTGATCTTG-CAATCGGACC-TGCCTTATCCT-3'
V19: a19*-b19*-a20-b20	5'-GGTCCGATTG-AGGATAAGCA-GACACGGCAC-CACTTACTCAT-3'
L20: a20*-b20*	5'-GTGCCGTGTC-ATGAGTAAGTG-3'

Table A.2.: DNA sequences: 20-helix ribbons. Note that strands V1 and U1 have identical sequences, but different domain partitions. The same is true for V3 and U3, and V5 and U5. L1 is the same as in Table A.1.

Name	Sequence
U6: a6*-b6*-a7-b7	5'-GGCATCGTTGG-ACTTCTATCA-ATGCACCTCC-AGCTTTGAATG-3'
U7: a7*-b7*-a8-b8	5'-GGAGGTGCAT-CATTCAAAGCT-AACGGTAACTA-TGACTTGGGA-3'
U8: a8*-b8*-a9-b9	5'-TAGTTACCGTT-TCCCAAGTCA-AACACTAGAC-ACATGCTCCTA-3'
U9: a9*-b9*-a10-b10	5'-GTCTAGTGTT-TAGGAGCATGT-CGAGACTACAC-CCTTGCCACC-3'
T4: a4*-b4*-a1-b1	5'-GGTTCTCACGG-ACGCATTGCA-CCTAATCGCC-TGGCTTAGCGT-3'
T5: a5*-b5*-a1-b1	5'-GGTCGTGCGG-ACTGTGGAACA-CCTAATCGCC-TGGCTTAGCGT-3'
T6: a6*-b6*-a1-b1	5'-GGCATCGTTGG-ACTTCTATCA-CCTAATCGCC-TGGCTTAGCGT-3'
T7: a7*-b7*-a1-b1	5'-GGAGGTGCAT-CATTCAAAGCT-CCTAATCGCC-TGGCTTAGCGT-3'
T8: a8*-b8*-a1-b1	5'-TAGTTACCGTT-TCCCAAGTCA-CCTAATCGCC-TGGCTTAGCGT-3'
T10: a10*-b10*-a1-b1	5'-GTGTAGTCTCG-GGTGGCAAGG-CCTAATCGCC-TGGCTTAGCGT-3'

Table A.3.: DNA sequences: 4-, 5-, 6-, 7-, 8-, 10-helix tubes. Note that strand U7 and V7 have identical sequences, but different domain partitions. The same is true for U9 and V9, and U11 and V11.

Name	Sequence
T20: a20*-b20*-a1-b1	5'-GTGCCGTGTC-ATGAGTAAGTG-CCTAATCGCC-TGGCTTAGCGT-3'

Table A.4.: DNA sequences: 20-helix tubes: The sequences for strands V1 to V19 are listed in Table A.2.

B

Supplementary materials for Chapter 3: Elongational-flow-induced scission of DNA nanotubes

B.1. Underlying scission theory

Here we present the hydrodynamic model used for comparison with our experiment. First, we derive an expression for the tension produced at the midpoint of a long cylinder. Then, an expression for the maximum elongation rate $\dot{\epsilon}$ for the microfluidic device is obtained.

In the approach taken to determine the tension produced at the midpoint of a long cylinder, the exact solution for fluid flow in the presence of a cylinder of infinite length is approximately matched with an exact solution for axially symmetric elongational flow in the absence of the rod.

For the case of low Reynolds number flow in an incompressible fluid, the continuity equation and Navier-Stokes equations are reduced to

$$\nabla \cdot \mathbf{u} = 0 \tag{B.1}$$

$$\nabla P = \mu \nabla^2 \mathbf{u}, \tag{B.2}$$

where \mathbf{u} is the velocity field, P is the pressure, and μ is the viscosity. From these two

equations, it follows that $\nabla^2 P = 0$. One can verify by direct substitution that

$$u_r = \frac{C}{2\mu} \left[r \ln \left(\frac{r}{R} \right) - \frac{r}{2} + \frac{R^2}{2r} \right] \quad (\text{B.3})$$

and

$$u_z = -\frac{C}{\mu} \ln \left(\frac{r}{R} \right) z, \quad (\text{B.4})$$

is an exact solution of Eqs. (B.1) and (B.2) where C and R are integration constants. The solution represents a fluid flow around a cylinder of radius R of infinite extent for no-slip boundary conditions that is evident from the fact that the fluid velocity vanishes at $r = R$.

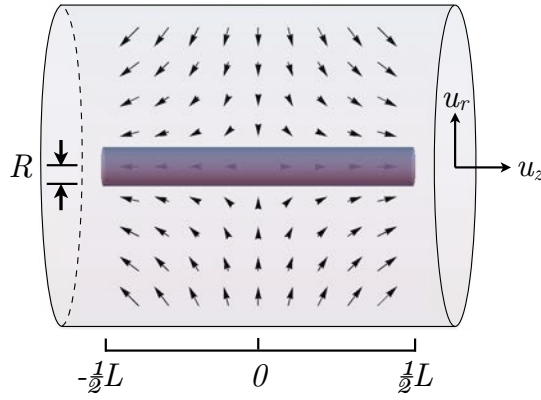


Figure B.1.: (Color) A rigid rod in an axially symmetric elongational flow

The fluid velocity field without the rod representing axially symmetric fluid flow with an elongational rate of $\dot{\epsilon}$ along the z -axis is given by

$$u_r = -\frac{\dot{\epsilon}}{2} r \quad (\text{B.5})$$

$$u_z = \dot{\epsilon} z, \quad (\text{B.6})$$

as can be verified by direct substitution into Eqs. (B.1) and (B.2). Since the first term of Eq. (B.3) dominates when r is large, a good approximate match between the solution given by Eqs. (B.3) and (B.4) and that of Eqs. (B.5) and (B.6) at the characteristic crossover

distance $r = L/2$ is obtained by setting

$$C = -\frac{\mu\dot{\epsilon}}{\ln(L/2R)}, \quad (\text{B.7})$$

where R and L are the radius and the length of n -helix DNA nanotube, respectively. Equation (B.4) then becomes

$$u_z = \dot{\epsilon} \frac{\ln(r/R)}{\ln(L/2R)} z. \quad (\text{B.8})$$

The flow induced stress in the z direction on the cylinder's surface is given by

$$\sigma_{rz} \equiv \mu \left. \frac{\partial u_z}{\partial r} \right|_{r=R} = \frac{\mu\dot{\epsilon}z}{R\ln(L/2R)}. \quad (\text{B.9})$$

The line tension at the center of the cylinder is thus given by

$$T = 4\pi R \int_0^{L/2} \sigma_{rz} dz = \frac{\pi\mu\dot{\epsilon}L^2}{4\ln(L/2R)}. \quad (\text{B.10})$$

This expression is similar to the recently published expression of the elongational-flow-induced drag force in reference [VCS06]. In our work (Eq. B.10), we provide a derivation of the $O(1)$ geometric constant for our device.

The scission occurs when the midpoint tension T is larger than the critical tension required to break all DNA helices simultaneously across the nanotubes. This critical tension is expected to be given by

$$T_{crit} = n \times f_c, \quad (\text{B.11})$$

where n is the nanotube circumference and f_c is the tension required to break a single DNA helix. In the DNA nanotubes, the DNA helices are aligned along the axis of the tube. Tension is thus exerted along the length of the binding domains of the participating DNA strands. One expects these binding domains to fail when the tension along the binding domains is greater than required to overstretch a DNA helix [SCB96]; that is, one expects f_c to be close to 65 pN.

In our device geometry, the flow into the narrow channel is approximately radial. We

take the mean flow velocity (averaged over height) \bar{u} to be given by

$$\bar{u}(\rho) = -\frac{\overline{u_w w}}{\pi\rho}, \quad (\text{B.12})$$

where ρ is the radial distance to the channel entrance and $\overline{u_w}$ is the mean flow velocity across the orifice.

The elongational flow (averaged over height) $\bar{\epsilon}$ is defined as

$$\bar{\epsilon} \equiv \frac{\partial \bar{u}}{\partial \rho} = \frac{\overline{u_w w}}{\pi\rho^2}. \quad (\text{B.13})$$

The elongational flow $\dot{\epsilon}$ is maximum near the orifice where $\pi\rho = w$

$$\bar{\epsilon}_{max} \equiv \left. \frac{\partial \bar{u}}{\partial \rho} \right|_{\rho=\frac{w}{\pi}} = \frac{\pi\overline{u_w w}}{w} = \frac{\pi\dot{V}}{w^2 h}, \quad (\text{B.14})$$

where \dot{V} is the volumetric flow rate of our syringe pump and is equal to $\overline{u_w}$ multiplied by the orifice cross-sectional area.

In Fig. 3.4, the theoretical prediction of L_{crit} for scission experiment of n -helix nanotube over a range of \dot{V} is obtained by setting $L = L_{crit}$, $T = T_{crit}$, $\dot{\epsilon} = \dot{\epsilon}_{max}$ and substituting Eqs. (B.11) and (B.14) to Eq. (B.10) that yields the equation below:

$$T_{crit} = \frac{\pi\mu\dot{\epsilon}_{max}L_{crit}^2}{4\ln(L_{crit}/2R)}, \quad (\text{B.15})$$

where T_{crit} is given by Eq. (B.11) and $\dot{\epsilon}_{max}$ is elongational flow at the center of the channel and at a distance of $\rho = w/\pi$ from the orifice where the maximum elongation flow is expected to occur.

Note that the radial flow approximation in Eq. (B.12) is only valid for a point far away from the constriction. Our scission model calculates the location of all scission events in all of our experiments to be at a distance $\rho > w/\pi$ from the orifice in order to produce the observed mean fragment length from the initial DNA nanotube distribution. This calculation is consistent with the expected position of $\bar{\epsilon}_{max}$ in Eq. (B.14) and the calculated $\bar{\epsilon}$ profiles in similar constriction devices reported in [KCdlT96,NK90]. Therefore, the radial flow approximation in Eq. (B.12) is justified.

B.2. Bayesian inference and stochastic scission simulation

In our data analysis, we utilized a Bayesian inference method to extract L_{crit} out of the fragment length histogram data \mathcal{H} by calculating the *a posteriori* probability $Pr(L_{crit}|\mathcal{H}) = Pr(\mathcal{H}|L_{crit}) \times Pr(L_{crit})/Pr(\mathcal{H})$, where the *a priori* $Pr(L_{crit})$ is taken to be uniform over $0 \leq L_{crit} \leq 10 \mu m$ and zero otherwise. The upper bound is approximately twice the average nanotube length in the control experiment. $Pr(\mathcal{H})$ is treated as a normalization constant and is set by constraining $\sum Pr(L_{crit}|\mathcal{H}) = 1$. $Pr(\mathcal{H}|L_{crit})$ was calculated by assuming the measured fragment length histograms $\{W_i(\mathcal{H})\}_{i=1}^N$, where N is the number of bins and W_i is the number of nanotubes in bin i , were generated by independent, identically-distributed fragment samples from length distribution predicted by the model $\{W_i(L_{crit_i})\}_{i=1}^N$. Then, $Pr(\mathcal{H}|L_{crit})$ can be conveniently calculated as likelihood: $\ln Pr(\mathcal{H}|L_{crit}) = D + \sum_i [W_i(\mathcal{H}) \cdot \ln W_i(L_{crit})]$, where D is a constant independent of L_{crit} and absorbed during normalization.

The fragment length distribution predicted by the scission model was computed from stochastic scission simulation of a large number of nanotubes ($> 40,000$) having the experimentally measured length distribution of the DNA nanotubes before passage through the microfluidic device. These DNA nanotubes were subjected to the following stochastic scission rules.

First, we note that the number of DNA nanotubes that crosses the orifice at position (x, y) is proportional to the flow rate at the orifice $u_w(x, y)$. By solving the Navier-Stokes equation for incompressible flow in a rectangular channel, one can obtain an expression for the flow profile involving an infinite series:

$$u_w(x, y) = E \left\{ \left[x^2 - \left(\frac{w}{2} \right)^2 \right] + \sum_{n=0}^{n=\infty} \frac{8}{a} \frac{(-1)^n}{\alpha_n^3} \frac{\cosh(\alpha_n y)}{\cosh(\alpha_n h/2)} \cos(\alpha_n x) \right\}, \quad (\text{B.16})$$

where $\alpha_n = (2n+1)\frac{\pi}{w}$ and E is a constant obtained by setting $u_w(0, 0)$ to be the maximum flow rate u_w^{max} . In this coordinate system, $(x = 0, y = 0)$ is chosen to be the center of the channel where the maximum flow occurs and the range of width and height of the flow channel are $[-w/2, w/2]$ and $[-h/2, h/2]$, respectively. In our simulation, we use the normalized $u_w(x_i, y_i)$ as the probability distribution for stochastically assigning (x_i, y_i) to nanotube i . Second, the fragment size produced by scission of nanotube i depends on (x_i, y_i) . Using the same reasoning as employed in the position-dependent flux and

Eqs. (B.10) and (B.12), one obtains the following expression for the critical length at (x_i, y_i) : $\sqrt{u_w^{max}/\ln[L_{crit_i}(x_i, y_i)/(2R)]}L_{crit_i}(x_i, y_i) = \sqrt{u_w(x_i, y_i)/\ln[L_{crit}/(2R)]}L_{crit}$.

In our model, an initial nanotube i of length L_i will experience a total of m_i mid-point scission rounds, where m_i is the largest non-negative integer that satisfies

$$L_{crit}(x_i, y_i) \geq \frac{L_i}{2^{m_i}}. \quad (\text{B.17})$$

From the equation above, m_i will be given by $m_i = \lfloor \ln[L_i/L_{crit_i}(x_i, y_i)]/\ln(2) \rfloor$, where the floor notation $\lfloor \cdot \rfloor$ denotes rounding down to the nearest integer. In our simulation, initial tube i of length L_i yields 2^{m_i} output fragments that have identical length of $L_i/(2^{m_i})$. The simulation generated fragments were then tabulated to construct the fragment length distribution predicted by the scission model $\{W_i(L_{crit_i})\}_{i=1}^N$ for computing $Pr(L_{crit}|\mathcal{H})$.

B.3. Best L_{crit} fit by Bayesian inference

Fragment length distributions for 6-, 8-, and 10-helix nanotubes for volumetric flow rates with values given by $\sqrt{2}^n$ mL/hr where n is an integer in the range $-2 \leq n \leq 4$ are shown in Fig. B.2. In each analysis, the fragment length measurement was stopped when the fragment counts reached ≈ 250 fragments. Bayesian inference of 250 simulated fragments with a chosen L_{crit} shows robust results within $\pm 12\%$ from the chosen L_{crit} , for L_{crit} smaller than the mean of initial nanotube distribution. The blue dot with blue error bars represents the average fragment length for each run. The Bayesian analysis was performed by comparing our measurement with simulation using one adjustable parameter, namely critical length L_{crit} , as described in the main text. The best simulated distribution by Bayesian *a posteriori* probability (orange line) fits our data fairly well. The orange circle denotes the most probable L_{crit} in each experiment. The orange error bar spans the range where $Pr(L_{crit}|\mathcal{H})$ is over 90% based on our model.

B.4. Best L_{crit} fit by Bayesian inference with truncated Gaussian noise

Best L_{crit} fit for the scission model with the addition of truncated Gaussian noise, summarized in Fig. B.3, shows that adding noise to account for unmodeled physical source of randomness does not significantly improve the Bayesian fit. With the addition of noise,

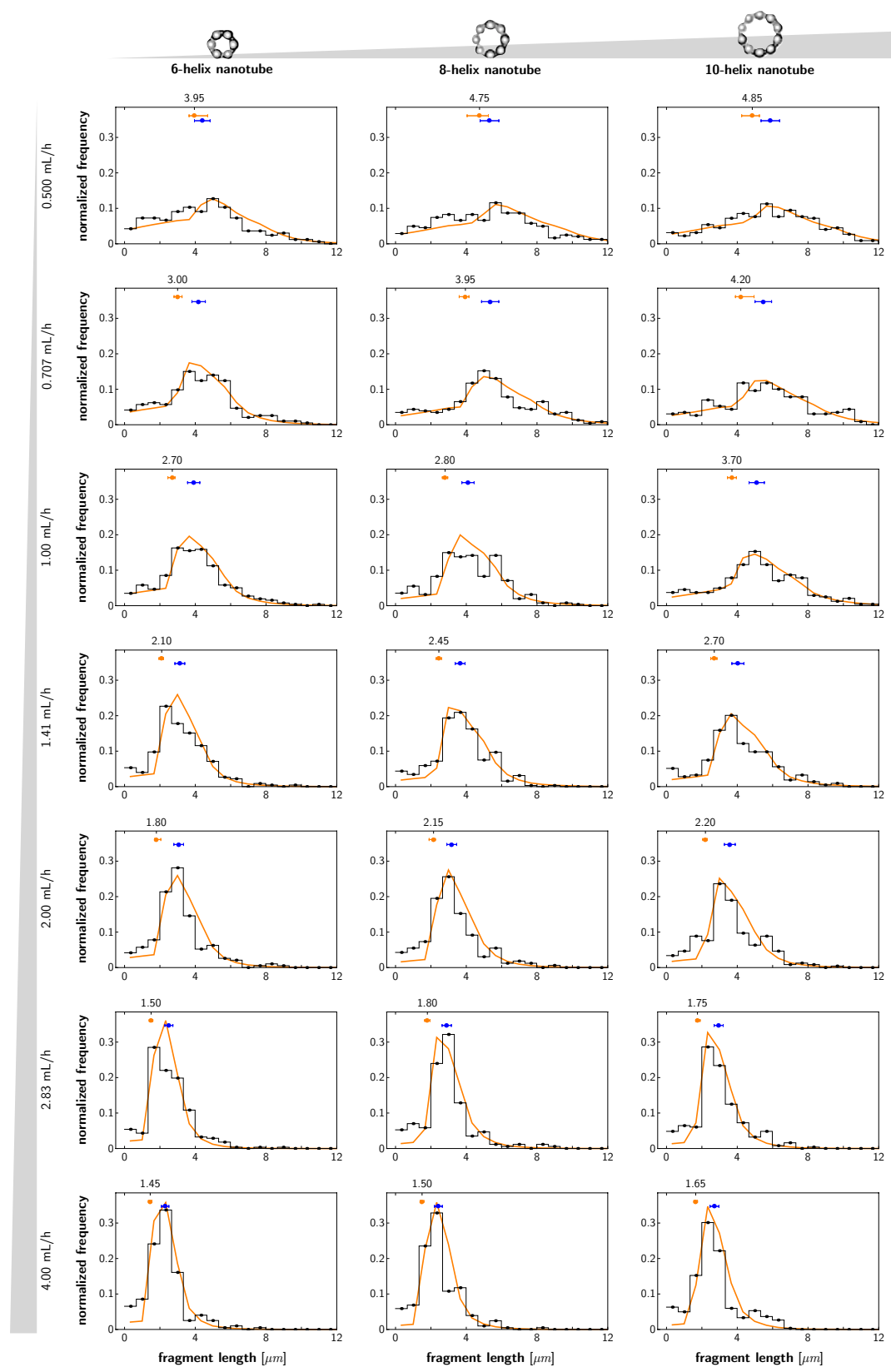


Figure B.2.: (Color) Best L_{crit} fit by Bayesian inference (see Appendix B.3 for details).

each scission event produces two not exactly equal fragment lengths. For nanotube i , the standard deviation of the truncated Gaussian noise σ_i was chosen to be proportional to tube length L_i , reflecting the results of the induced drag force calculation for which the region where the tension reaches plateau becomes narrower as the nanotube tube gets shorter. We truncated the Gaussian noise at 0 and L_i fragment sizes to eliminate unphysical fragment outputs in our simulation, namely fragments with negative lengths and fragmented nanotubes longer than initial fragment length L_i . The Bayesian fit was performed over a wide range of model parameters ($0.02L_i < \sigma_i < 0.50L_i$, $0.05 < L_{crit} < 10.00$). The upper bound of the σ_i corresponds to substantially large noise, such that for a nanotube length L_i , where $L_i > 2L_{crit}$, the probability of scission at any point along the fragment, including no scission at all, is approximately equal. Note also that the distribution of the truncated Gaussian with the upper bound of σ_i is close to uniform distribution between 0 and L_i . The orange and red circles with error bars represent the best L_{crit} fit by Bayesian inference for polymer scission without and with noise, respectively. Similarly, the orange and red lines are the best distribution fit to our normalized fragment length histogram based on simulation without and with noise, respectively.

The Bayesian histogram fits of the model with (red lines) and without noise (orange lines) show similar shapes (Fig. B.3) and further support our simple scission model presented in the main text. The extracted L_{crit} from the Bayesian inference with noise are consistent within 15% of the fit in the absence of noise. The agreement is within 5%, if we exclude the slowest volumetric flow rate data where the inference have the widest 90% confidence bands. The maximum value of the most probable σ_i overall fits is $0.20L_i$. This value of σ_i still represents truncated Gaussian noise distribution whose width is substantially smaller than the tube length L_i .

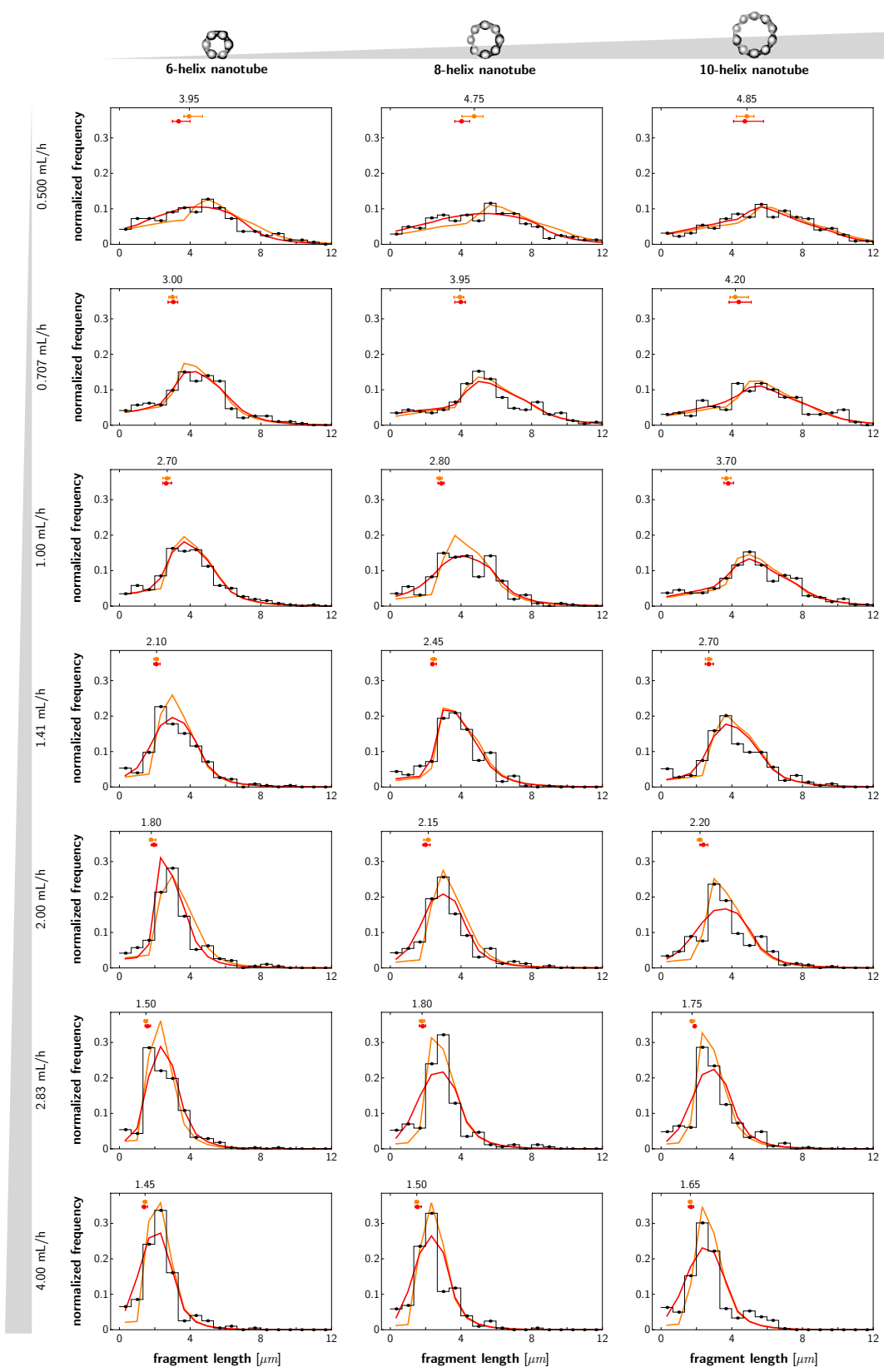


Figure B.3.: (Color) Best L_{crit} fit by Bayesian inference with truncated Gaussian noise (see Appendix B.4 for details). The red lines are the Bayesian fits with noise.

C

Supplementary materials for Chapter 6: Single molecule analysis of DNA nanotube polymerization

In English, if you say "I see", it
means that you understand
something

*(Sir John Pendry,
KNI Colloquium at Caltech,
05-14-2007)*

C.1. Movie of anomalous diffusion and side-to-side joining

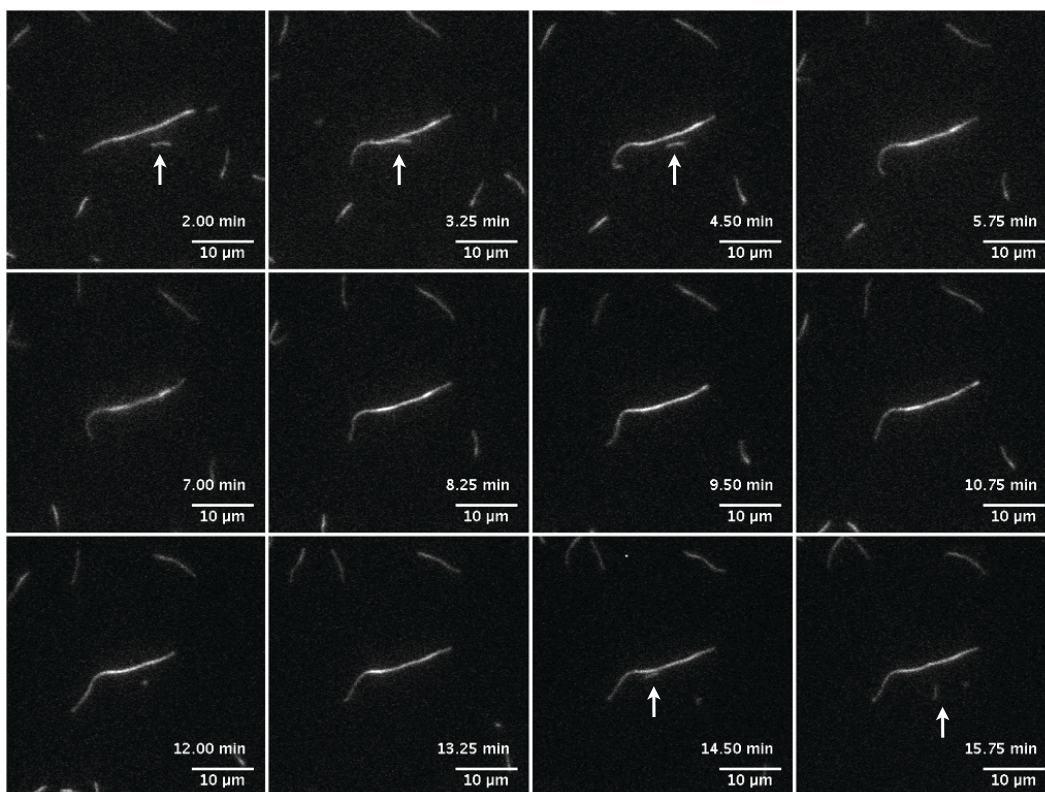


Figure C.1.: TIRF images of mobile DNA nanotubes close the glass surface at 36.7 °C and 0 nM initial monomer concentration in $1\times$ TAE/Mg⁺⁺ and 0.3% (w/v) methylcellulose. In the presence of the crowding agent, the entropy of the system is maximized when the nanotubes were confined close to a surface, such as the capillary walls. The same entropic force also drives side-to-side joining or “bundling”, such as between the short nanotubes and the long nanotubes at the center of this movie. After joining, the DNA nanotubes remained mobile relative to each other (length-wide sliding occurred) while they depolymerized from both ends as a physical response to low free monomer concentration. At the end of the movie, the short nanotubes dissociate from the long one, possibly because the entropic gain of the side-to-side joining of short nanotubes is less favorable compared to longer ones.

C.2. Movie of depolymerization experiment

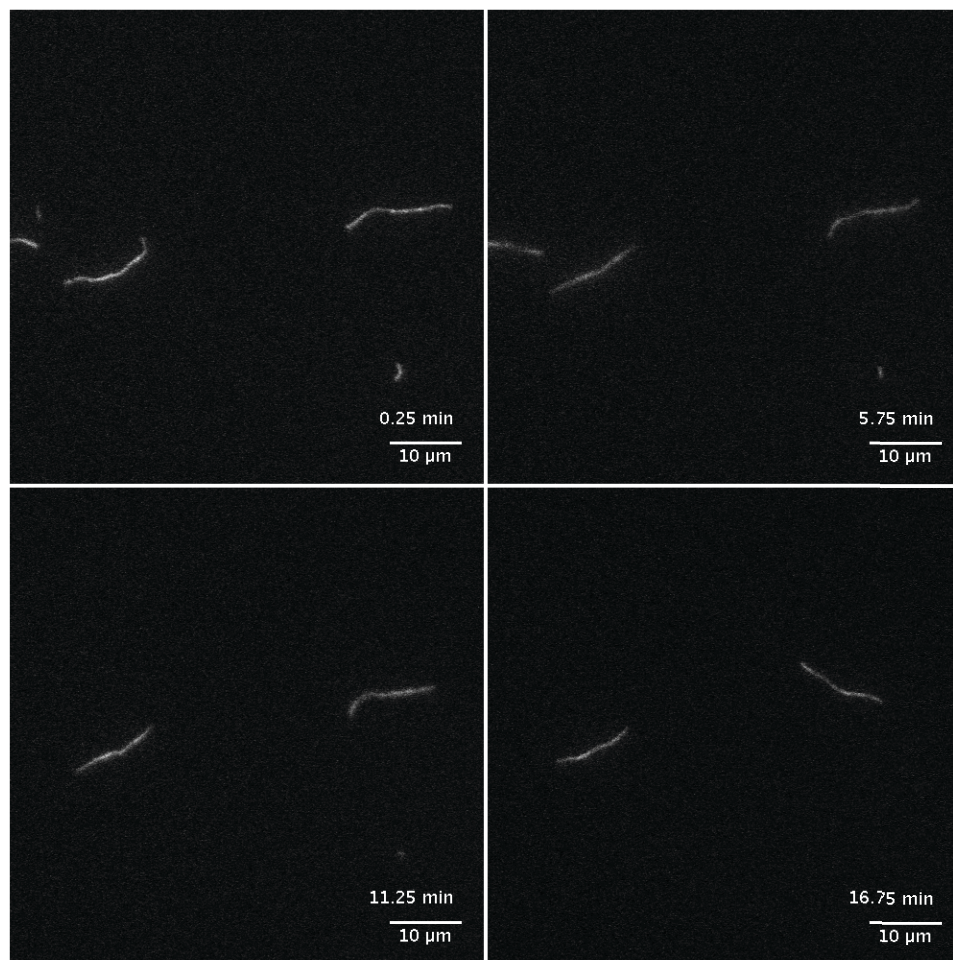


Figure C.2.: DNA nanotubes shrink at 38.3 °C with zero initial monomer concentration and 7 nM initial nuclei concentration, as shown in Fig. 6.3 of the main text.

C.3. Movie of DNA nanotube growth

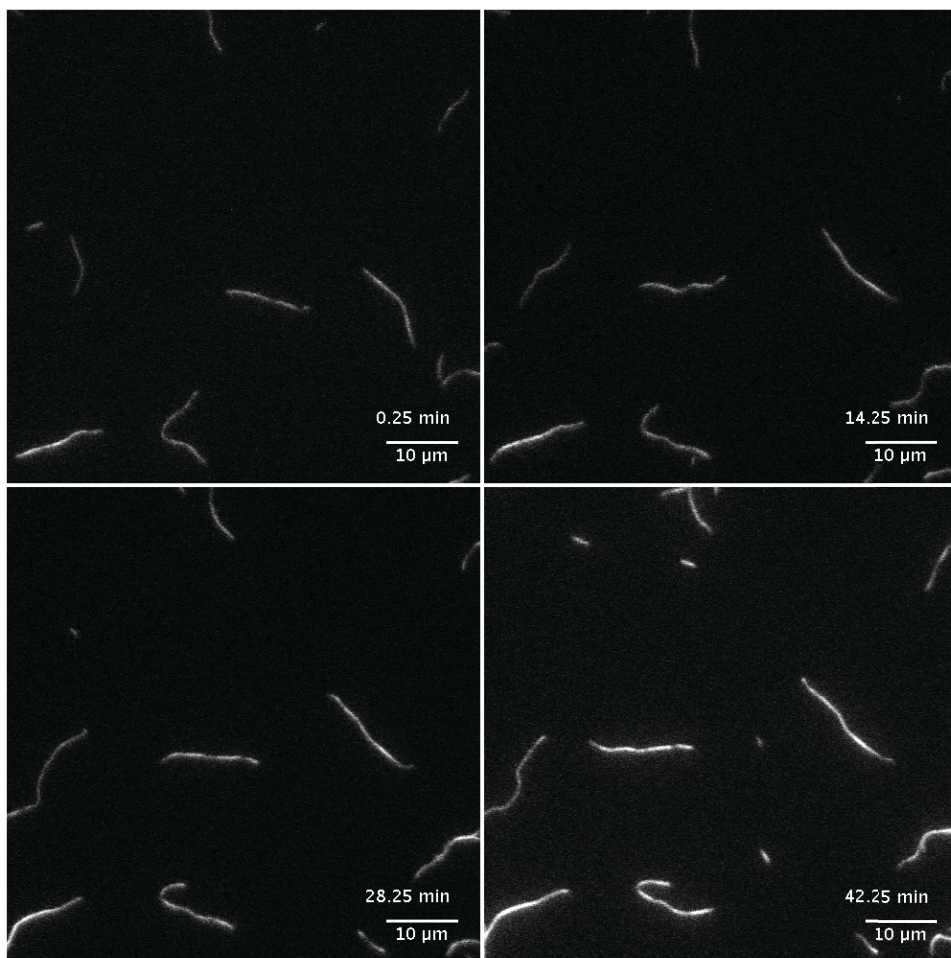


Figure C.3.: DNA nanotubes elongated at 38.3 °C with 400 nM initial monomer concentration and 7 nM initial nuclei concentration, as shown in Fig. 6.4 of the main text.

C.4. Movie of complete depolymerization of DNA nanotubes followed by annealing of newly released free DNA tiles

The annealing of free monomers at high concentration nucleates a significant number of new nuclei which immediately elongated and underwent side-to-side joining with other newly-formed nuclei. The total tile concentration was 500 nM and the reaction buffer contains $1\times$ TAE/Mg⁺⁺ and 7.5 mg/mL casein. We used casein to passivate the glass surface and to confine long DNA nanotubes close to the surface. The movie was acquired while the whole microscope room and the sample were initially at an elevated room temperature (37.4 °C). The sample was then melted by increasing the prism temperature to 70 °C. We did not measure the temperature profile of the sample during the spontaneous cooling. The annealing was achieved by simply turning off the prism heater and allowing the sample to spontaneously cool down to 37.4 °C, the elevated room temperature. During this time, the average intensity of DNA nanotube nuclei increased over time, which is the signature of side-to-side joining. Experimentally, the side-to-side joining obscures the elongation of individual DNA nanotube and makes single molecule polymerization measurements unattainable.

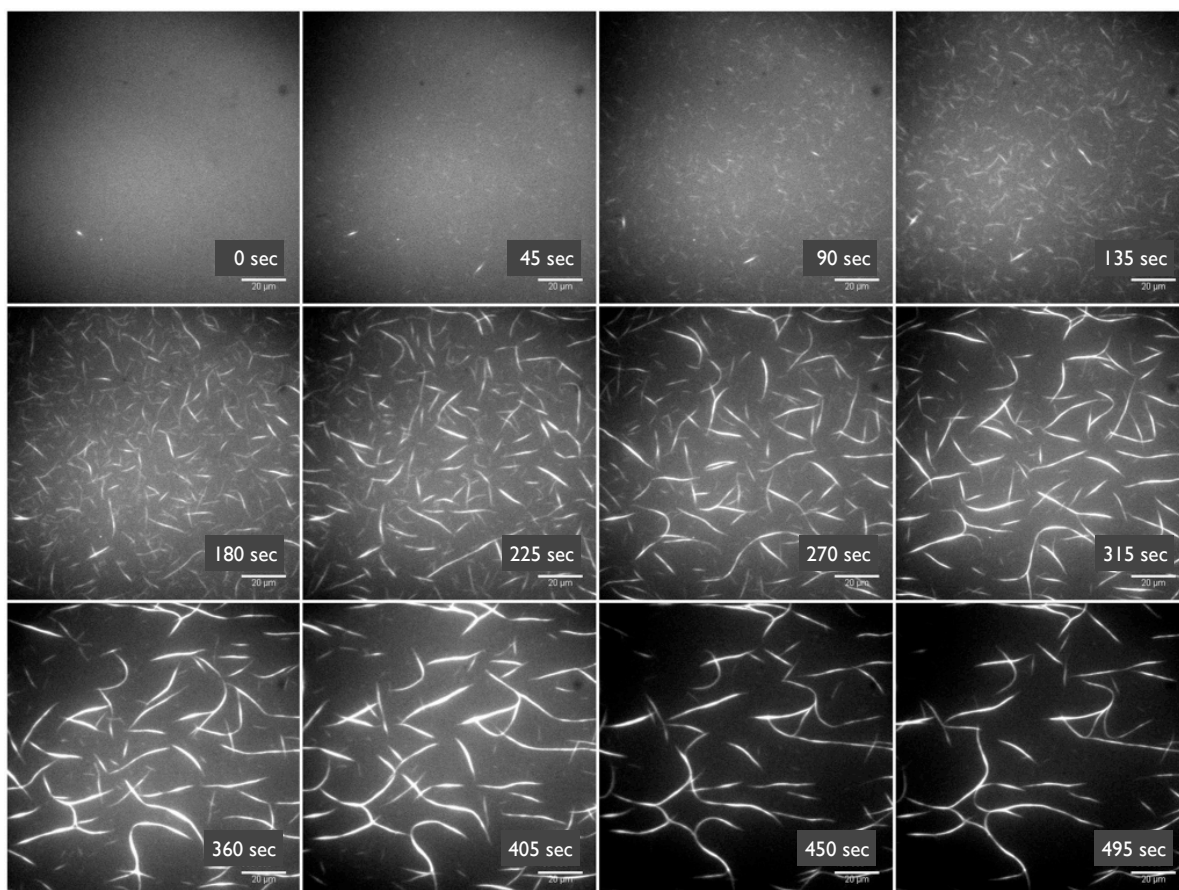


Figure C.4.: In the presence of crowding agent, complete melting of a high concentration of DNA tiles (500 nM) followed by fast annealing produces DNA nanotube “bundles”. After the spontaneous nucleation of short nuclei, the newly formed nanotubes “side-to-side” join with each other to maximize the entropy of the crowded environment. Scale bar is 20 μm.

C.5. AFM images of opened DNA nanotubes

AFM images were acquired with a tapping mode AFM on a Nanoscope IIIa controller (Veeco Instruments) equipped with nanoAnalytics Q-control III (Asylum Research) under $1\times$ TAE/Mg⁺⁺ (40 mM trisacetate and 1 mM ethylenediaminetetraacetic acid (EDTA) with 12.5 mM Mg-acetate.4H₂O, pH 8.3) buffer and 110 μm , 0.38 N/m spring constant SNL silicon nitride cantilever (Veeco Instruments). The DNA nanotubes were annealed at 1.0 μM tile concentration. Following annealing, the samples were diluted to 100 nM with $1\times$ TAE/Mg⁺⁺. 10 μL of the diluted sample and 20 μL of $1\times$ TAE/Mg⁺⁺ were deposited on a freshly cleaved piece of mica surface (Ted Pella), approximately 1 cm \times 1 cm in size, affixed to a 15 mm diameter magnetic stainless steel puck (Ted Pella) using a hot glue gun. DNA nanotubes spontaneously open on the mica surface, possibly due to the energy gain from the formation of salt bridges between DNA and the mica surface [RENP⁺04]. Under the Mg⁺⁺ buffer, DNA tiles are not completely immobilized and can still attach to or detach from an immobilized opened DNA nanotube. The DNA tile–DNA nanotube interaction effects the validity of circumference measurements of opened DNA nanotubes. To avoid such effect, after 5 minutes, to completely quenched the reaction, 20 μL of 9 mM Ni⁺⁺ in $1\times$ TAE/Mg⁺⁺ was added to the mica puck. The nickel buffer facilitates stronger binding between DNA and mica than the Mg⁺⁺ buffer [HL96].

We imaged one sample of a pre-formed nuclei stock solution at 1 μm \times 1 μm at multiple random coordinates. We used custom-written MATLAB code to flatten the images by subtracting a fitted first order polynomial from each scan line and match intensity histograms between scan lines. The circumference was measured by counting the number of DNA tiles at 5 random points along the longitudinal-axis of each DNA nanotube. The average value was then used as the circumference of that particular DNA nanotube. Hence, the tabulated DNA nanotube circumference is not restricted to positive integer numbers. A histogram (Fig. 6.9) was then constructed by binning the data from 1 μm to 15 μm within bin width = 1 μm .

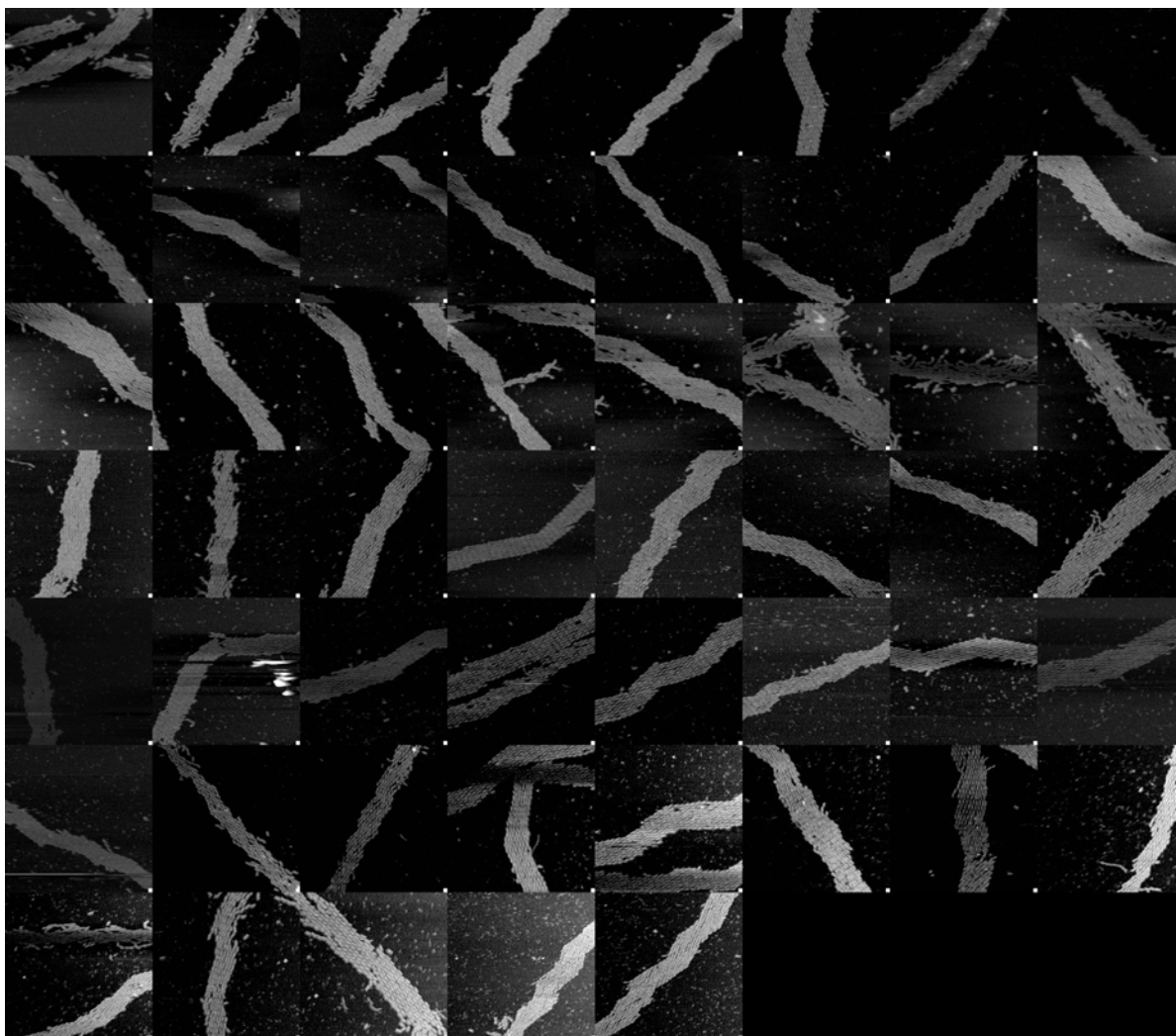


Figure C.5.: AFM images of 53 randomly chosen opened DNA nanotubes reveal the circumference heterogeneity of the nuclei. The strong interaction between negatively-charged mica surface, multivalent Ni^{++} ions, and DNA nanotubes leads to the spontaneous DNA nanotube opening. The circumference histogram of DNA nanotube diameter is shown in Fig. 6.9

C.6. UV absorbance of DNA nanotube

We chose the reaction temperature range based on the annealing curve for 200 nM Cy3-labeled DNA tiles. The UV absorbance measurement were performed using an AVIV 14DS spectrophotometer (AVIV Biomedical, Lakewood, NJ) equipped with a computer-controlled sample temperature. We informally defined the formation temperature as the temperature at which the slope of the annealing curve suddenly changed due to the formation of DNA nanotube nuclei and elongation of the stable nuclei. Because nucleation is a kinetic phenomena, the measured formation temperature depends on the speed of annealing. In Fig. C.6, the formation temperature was measured to be roughly 35 °C. Indeed, we did not observe DNA nanotube nucleation in all 200 nM polymerization experiments at temperatures above 35 °C resulting in valid rate measurements. In contrast, all polymerization data that were taken at 200 nM free monomer concentration at temperature below 35 °C suffers from spontaneous nucleation, consistent with the bulk UV measurement.

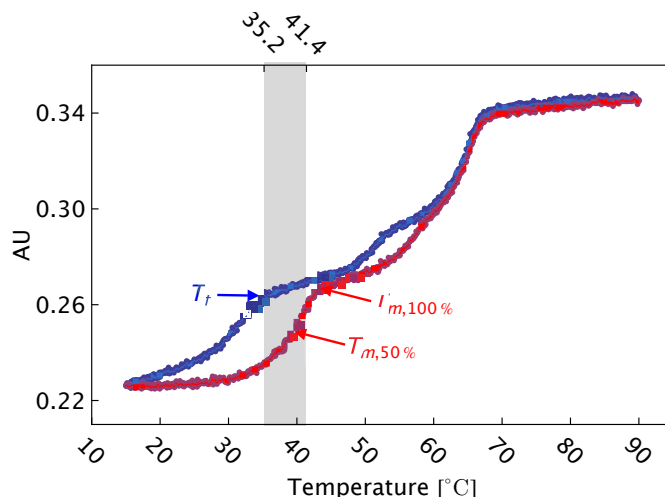


Figure C.6.: The annealing and melting curves of Cy3-labeled DNA nanotubes at 200 nM tile concentration guided the reaction temperature range of this work. The shaded region denotes the temperature range where the collected valid measurements of DNA nanotube polymerization at a 200 nM concentration of free tiles. At that tile concentration, DNA nanotube nucleation becomes noticeable at ≈ 35 °C. In the bottom left plot of Fig. 6.7, we were able to acquire valid polymerization rate measurements at this tile concentration down to 35.2 °C (the lower bound of the gray-shaded region).

The maximum temperature of our assay was set by the safe operation temperature of our objective heater, and not by any insight from the melt experiment or other assay. It is

wise to not heat the objective above 50 °C. In this work, we had to heat the objective at 47 °C to achieve a 41.4 °C sample temperature. However, as the DNA nanotube melting temperature is only slightly above 42 °C, in this case, experiments at higher temperatures would not have been interesting.

D

Supplementary materials for Chapter 7: Toward *de novo* recapitulation of cytoskeleton dynamics with DNA nanotubes

D.1. The spacing between neighboring DNA tiles in DNA lattice.

In this model, ionic strength effect is incorporated into the two-dimensional DNA crystal model. Each charge on the phosphate backbone is effectively reduced by the condensed counterions, lowering the contribution of the Coulombic interaction to the lattice energy. The current model is in fair agreement with the experimental measurement of the spacing between neighboring subunits. The spacing of the DNA lattice is also predicted in various salt concentrations and using different DNA molecule designs, which is easily tested by trivial AFM imaging.

DNA double-helix

We begin by modeling the DNA double-helix as a rigid, charged cylindrical beam with radius $r_0 \approx 1$ nm and persistence length $\xi_p \approx 50$ nm. In this coarse model, the negative charges along DNA backbones is replaced by a continuous linear charge in the center of the cylindrical beam and its density with charge density $\lambda \approx 2e_o/3.38$ Å. The line charge density corresponds to one negative charge per phosphate group. The Manning parameter or dimensionless linear polyanion charge is $\xi \approx \lambda l_B/e_o = 4.1$, where l_B is the Bjerrum

length defined as the distance where the electrostatic energy is equal to the thermal energy $l_B := e_o^2/4\pi\epsilon k_B T$. For water and dilute solution at room temperature $l_B = 7.14 \text{ \AA}$.

Double-crossover (DX) molecule and two-dimensional DNA lattice

To provide a quantitative model of the lattice, we constructed a simple parameterized double-crossover (DX) molecule, with only one free parameter, namely bending radius R_{bend} . Later in this calculation, we will minimize the lattice energy with respect to the bending radius R_{bend} . The structural approximation of a DX molecule consists of six cylindrical segments, and each has the same mechanical and electrostatic property of DNA double strands. The middle two segments (A and B) are joined due to the presence of the two crossover points, where the four strands cross-linked. The outer four segments (C-F) are bendable with identical curvatures, and each is assumed to be an arc of a circle. Furthermore, the bending of each bendable segment is constrained such that it keeps the overall structure as a two-dimensional geometrical object. Note that the model construction reduces the dimensionality of the system from three-dimensional geometry to a two-dimensional system, which reduces the complexity of the calculation while still capturing the important physics of the system.

Free energy calculation of the two-dimensional lattice

A mathematical description of the energetics of lattice packing must reflect the two competing factors, namely the electrostatic and bending energy, plus other terms that do not depend on the bending radius. The basic idea of our approach is to minimize the total energy with respect to bending radius. As a consequence, we do not need to calculate energy terms that are assumed to be independent with the lattice structure in order to find the R_{bend} where the energy is minimum.

Electrostatic free energy

The interaction energy between segment i and j is calculated as double integrations

$$G_{int} = \int ds_i \int ds_j \underbrace{(1 - Z\theta)^2}_{= r^2} \lambda^2 \underbrace{\frac{k_B T l_B}{|\vec{s}_i - \vec{s}_j|} e^{-\kappa |\vec{s}_i - \vec{s}_j|}}_{= V_{DH}}, \quad (\text{D.1})$$

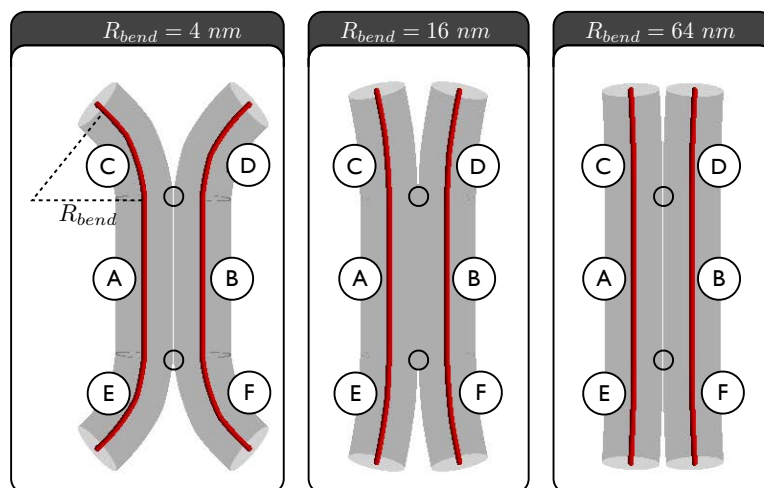


Figure D.1.: The model of a DNA double-crossover tile employed in this calculation. The part of the tile between the two crossover points is modeled as fixed beams (segments A and B). The segments C - F are bendable with persistence length $\xi_p = 50$ nm. In our calculation, the elastic and electrostatic energy of the DNA crystal are functions of one free parameter, namely the bending radius R_{bend} of the arm segments (C - F). Larger bending radius corresponds to larger crystal spacing, larger elastic penalty, and smaller Coulombic repulsion. The three models of DNA tile in this figure were constructed with the bending radius $R_{bend} = 4$ nm (left), 16 nm (middle), and 64 nm (right). For scale, the diameter of each helix is 2 nm.

where s_i parameterizes the center of the cylindrical segment i and V_{DH} is the Debye-Hückel potential. The $(1 - Z\theta)$ factor is the renormalization (r) to the counterion condensation per unit charge (θ) and valence (Z). The magnitude of r is solved by using the Manning parameter, and the result is given by

$$Z\theta \simeq 1 - \frac{1}{Z\xi} \quad (\text{D.2})$$

The κ^{-1} is the Debye screening length defined via

$$\kappa^2 = 4\pi l_B \sum_i Z_i^2 c_i, \quad (\text{D.3})$$

where Z_i and c_i are the valence and concentration of the salt species i , respectively.

Bending energy

In the generic language of beam theory, the energy cost to bend four identical bendable segments in a DX molecule scales with the bending radius R_{bend} and is given by

$$G_{bend} = k_B T \frac{2\Gamma\xi_p}{R_{bend}^2}, \quad (\text{D.4})$$

where Γ is the length of the bendable segments and ξ_p is the persistence length that depends on the temperature and Debye screening length of the form.

$$\xi_p = \xi_{int} + \xi_{el} = \xi_{int} + \frac{1}{4\kappa^2 l_B}. \quad (\text{D.5})$$

Spacing between neighboring DNA tiles

Spacing is defined as the distance between two neighboring DX molecules as shown by the cartoon in Fig D.1. In order to compare the result of our energy minimization calculation with the experimental data, we convert the bending radius into spacing s .

$$s = \left\{ r_o + R_{bend} \left[1 - \cos \left(\frac{\Gamma}{R_{bend}} \right) \right] \right\} \quad (\text{D.6})$$

Note that the conversion above gives the a priori range of spacing to be within 4 nm to 14 nm, which corresponds to the close packed structure and fully stretched lattice, respectively, as shown in Fig. D.1.

The equilibrium lattice spacing in the AFM images

Fig. D.2 shows the result of the bending calculation and the numerical integration of the electrostatic interaction energy at our standard buffer condition for AFM imaging, with Debye screening length $\kappa^{-1}=0.84$ nm. Both energy terms contain the product $k_B T$ as a factor, which makes it convenient to regard $k_B T$ as our unit energy. The contributions from the electrostatics and mechanical bending of the lattice are minimal at ~ 5 nm calculated spacing and are in fair agreement with the 6.6 nm spacing measured from AFM images, considering our rough representation of the DNA helix. This agreement demonstrates the promise of the beam theory to explain the two-dimensional DNA crystal structure.

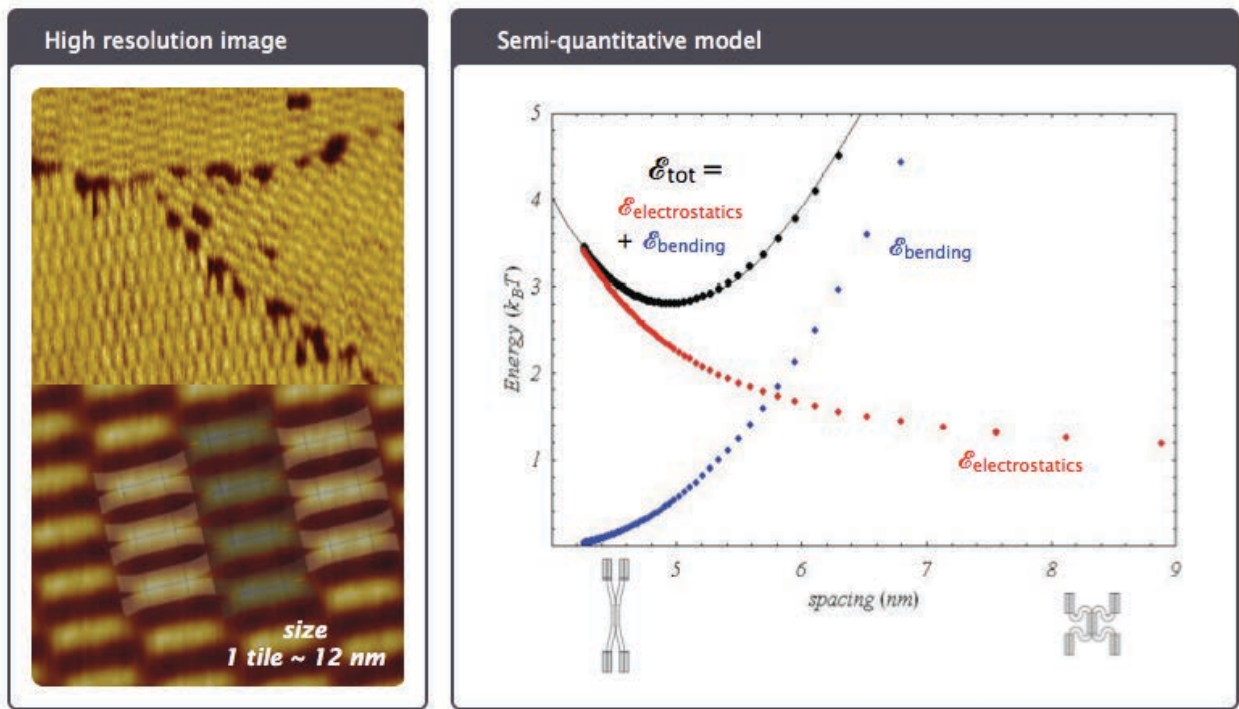


Figure D.2.: Our calculation (right) is in qualitative agreement with the observed spacing between DNA tiles in the AFM image (left). Here, the lattice spacing is defined as the distance between two neighboring tiles at perpendicular orientation with respect to the DNA axis. DNA lattice with zero empty space between the neighboring tiles has a 4 nm spacing. The simple energy argument predicts ~ 5 nm lattice spacing, instead of 4 nm. This predicted spacing provides an access for EcoRI to perform the nicking reaction on the bendable arms of the DNA tile inside a lattice.

Bibliography

- [ACP07] Phaedon Avouris, Zhihong Chen, and Vasili Perebeinos. Carbon-based electronics. *Nature Nanotechnology*, 2(10):605–615, 2007.
- [ADN⁺09] Ebbe S. Andersen, Mingdong Dong, Morten M. Nielsen, Kasper Jahn, Ramesh Subramani, Wael Mamdouh, Monika M. Golas, Bjoern Sander, Holger Stark, Cristiano L. P. Oliveira, Jan Skov Pedersen, Victoria Birkedal, Flemming Besenbacher, Kurt V Gothelf, and Jorgen Kjems. Self-assembly of a nanoscale DNA box with a controllable lid. *Nature*, 459(7243):73–76, 2009.
- [AKN⁺10] Rachel C. Angers, Hae-Eun Kang, Dana Napier, Shawn Browning, Tanya Seward, Candace Mathiason, Aru Balachandran, Debbie McKenzie, Joaquín Castilla, Claudio Soto, Jean Jewell, Catherine Graham, Edward A. Hoover, and Glenn C. Telling. Prion strain mutation determined by prion protein conformational compatibility and primary structure. *Science*, 328(5982):1154–1158, 2010.
- [Alb03] Bruce Alberts. DNA replication and recombination. *Nature*, 421(6921):431–435, 2003.
- [AP01] Kurt Amann and Thomas Pollard. Direct real-time observation of actin filament branching mediated by Arp2/3 complex using total internal reflection fluorescence microscopy. *Proceedings of the National Academy of Sciences of the United States of America*, 98(26):15009–15013, 2001.
- [APS08] Faisal A. Aldaye, Alison L. Palmer, and Hanadi F. Sleiman. Assembling materials with DNA as the guide. *Science*, 321(5897):1795–1799, 2008.
- [BBS02] Tamer Bagatur, Ahmet Baylar, and Nusret Sekerdag. The effect of nozzle type on air entrainment by plunging water jets. *Water Quality Research Journal of Canada*, 37(3):599–612, 2002.

- [BC98] T. Brattberg and H. Chanson. Air entrapment and air bubble dispersion at two-dimensional plunging water jets. *Chemical Engineering Science*, 53(24):4113 – 4127, 1998.
- [BCTH00] Victor A. Bloomfield, Donald M. Crothers, Ignacio Tinoco, and John E. Hearst. *Nucleic acids: structures, properties, and functions*. University Science Books, 2000.
- [BD72] Ray D. Bowman and Norman Davidson. Hydrodynamic shear breakage of DNA. *Biopolymers*, 11(12):2601–2624, 1972.
- [BdRCS10] James C. Bird, Rielle de Rüiter, Laurent Courbin, and Howard A. Stone. Daughter bubble cascades produced by folding of ruptured thin films. *Nature*, 465(7299):759–762, 2010.
- [BHKQ03] Ido Braslavsky, Benedict Hebert, Emil Kartalov, and Stephen R. Quake. Sequence information can be obtained from single DNA molecules. *Proceedings of the National Academy of Sciences of the United States of America*, 100(7):3960–3964, 2003.
- [BJ93] F. Bonetto and R. T. Lahey Jr. An experimental study on air carry under due to a plunging liquid jet. *International Journal of Multiphase Flow*, 19(2): 281 – 294, 1993.
- [BLS⁺07] Peter Bieling, Liedewij Laan, Henry Schek, E. Laura Munteanu, Linda Sandblad, Marileen Dogterom, Damian Brunner, and Thomas Surrey. Reconstitution of a microtubule plus-end tracking system *in vitro*. *Nature*, 450(7172):1100–1105, 2007.
- [Bow92] P. A. Bowyer. The rise of bubbles in a glass tube and the spectrum of bubbles produced by a splash. *Journal of Marine Research*, 50(4):521–543, 1992.
- [BPB77] Edward Baylor, Virginia Peters, and Martha Baylor. Water-to-air transfer of virus. *Science*, 197(4305):763–764, 1977.
- [BR09] Yuriy Brun and Dustin Reishus. Path finding in the tile assembly model. *Theoretical Computer Science*, 410(15):1461–1472, 2009.

- [BRW05] Robert D. Barish, Paul W. K. Rothmund, and Erik Winfree. Two computational primitives for algorithmic self-assembly: Copying and counting. *Nano Letters*, 5(12):2586–2592, 2005.
- [BS70] Duncan Blanchard and Lawrence Syzdek. Mechanism for the water-to-air transfer and concentration of bacteria. *Science*, 170(3958):626–628, 1970.
- [BS95] Jeremy Boulton-Stone. The effect of surfactant on bursting gas bubbles. *Journal of Fluid Mechanics*, 302 IS -:231–257, 1995.
- [BS10] Itay Budin and Jack W. Szostak. Expanding roles for diverse physical phenomena during the origin of life. *Annual Review of Biophysics*, 39(1):245–263, 2010.
- [BSB93] J. M. Boulton-Stone and J. R. Blake. Gas bubbles bursting at a free surface. *Journal of Fluid Mechanics*, 254:437–466, 1993.
- [BSLS00] Carlos Bustamante, Steven B. Smith, Jan Liphardt, and Doug Smith. Single-molecule studies of DNA mechanics. *Current Opinion in Structural Biology*, 10(3):279–285, 2000.
- [BSRW09] Robert D. Barish, Rebecca Schulman, Paul W. K. Rothmund, and Erik Winfree. An information-bearing seed for nucleating algorithmic self-assembly. *Proceedings of the National Academy of Sciences of the United States of America*, 106(15):6054–6059, 2009.
- [BT07] Jonathan Bath and Andrew J. Turberfield. DNA nanomachines. *Nature Nanotechnology*, 2(5):275–284, 2007.
- [BZK⁺04] Brett A. Buchholz, Jacob M. Zahn, Martin Kenward, Gary W. Slater, and Annelise E. Barron. Flow-induced chain scission as a physical route to narrowly distributed, high molar mass polymers. *Polymer*, 45(4):1223–1234, 2004.
- [CAH04] H. Chanson, S. Aoki, and A. Hoque. Physical modelling and similitude of air bubble entrainment at vertical circular plunging jets. *Chemical Engineering Science*, 59(4):747–758, 2004.

- [CB81] Richard H. Cote and Gary G. Borisy. Head-to-tail polymerization of microtubules *in vitro*. *Journal of Molecular Biology*, 150(4):577–599, 1981.
- [CC07] John Collinge and Anthony R. Clarke. A general model of prion strains and their pathogenicity. *Science*, 318(5852):930–936, 2007.
- [CDVW04] Sean R. Collins, Adam Douglass, Ronald D. Vale, and Jonathan S. Weissman. Mechanism of prion propagation: amyloid growth occurs by monomer addition. *PLoS Biology*, 2(10):e321, 2004.
- [CFK95] Denis Chrétien, Stephen David Fuller, and Eric Karsenti. Structure of growing microtubule ends: two-dimensional sheets close into tubes at variable rates. *Journal of Cell Biology*, 129(5):1311, 1995.
- [CH92] Robert Cherry and Carl Hulle. Cell death in the thin films of bursting bubbles. *Biotechnology Progress*, 8(1):11–18, 1992.
- [CLS96] John K. Chika, Uno Lindberg, and Clarence E. Schutt. The structure of an open state of β -actin at 265 Å resolution. *Journal of Molecular Biology*, 263:607–623, 1996.
- [CLZ82] Michael Caplow, George M. Langford, and Barry Zeeberg. Concerning the efficiency of the treadmilling phenomenon with microtubules. *Journal of Biological Chemistry*, 257(24):15012–15021, 1982.
- [CRS94] M. Caplow, R. L. Ruhlen, and J. Shanks. The free energy for hydrolysis of a microtubule-bound nucleotide triphosphate is near zero: all of the free energy for hydrolysis is stored in the microtubule lattice. *The Journal of Cell Biology*, 127(3):779–788, 1994.
- [CS66] A. G. Cairns-Smith. The origin of life and the nature of the primitive gene. *Journal of Theoretical Biology*, 10(1):53–88, 1966.
- [CS08] A. Graham Cairns-Smith. Chemistry and the missing era of evolution. *Chemistry – A European Journal*, 14(13):3830–3839, 2008.
- [CSGW07] Ho-Lin Chen, Rebecca Schulman, Ashish Goel, and Erik Winfree. Reducing facet nucleation during algorithmic self-assembly. *Nano Letters*, 7(9):2913–2919, 2007.

- [Cul60] F. E. C. Culick. Comments on a ruptured soap film. *Journal of Applied Physics*, 3:1128–1129, 1960.
- [CW91] Denis Chrétien and Richard H. Wade. New data on the microtubule surface lattice. *Biol Cell*, 71(1-2):161–174, 1991.
- [CW10] Kenneth Campellone and Matthew Welch. A nucleator arms race: cellular control of actin assembly. *Nature Reviews Molecular Cell Biology*, 11(4):237–251, 2010.
- [Dan78] Barry M. Dancis. Shear breakage of DNA. *Biophysical Journal*, 24(2):489–503, 1978.
- [DCS07] Shawn M. Douglas, James J. Chou, and William M. Shih. DNA-nanotube-induced alignment of membrane proteins for NMR structure determination. *Proceedings of the National Academy of Sciences of the United States of America*, 104(16):6644–6648, 2007.
- [DdGBW98] G. Debrégeas, P.-G de Gennes, and F. Brochard-Wyart. The life and death of “bare” viscous bubbles. *Science*, 279(5357):1704–1707, 1998.
- [DDL⁺09] Shawn M. Douglas, Hendrik Dietz, Tim Liedl, Bjorn Hogberg, Franziska Graf, and William M. Shih. Self-assembly of DNA into nanoscale three-dimensional shapes. *Nature*, 459(7245):414–418, 2009.
- [DDS09] Hendrik Dietz, Shawn M. Douglas, and William M. Shih. Folding DNA into twisted and curved nanoscale shapes. *Science*, 325(5941):725, 2009.
- [dGM08] Tom F. A. de Greef and E. W. Meijer. Materials science: Supramolecular polymers. *Nature*, 453(7192):171–173, 2008.
- [DKRLJ05] Marileen Dogterom, Jacob W. J. Kerssemakers, Guillaume Romet-Lemonne, and Marcel E Janson. Force generation by dynamic microtubules. *Current Opinion in Cell Biology*, 17(1):67–74, 2005.
- [DM97] Arshad Desai and Timothy J. Mitchison. Microtubule polymerization dynamics. *Annual Review of Cell and Developmental Biology*, 13:83–117, 1997.

- [DMBW95] G. Debrégeas, P. Martin, and F. Brochard-Wyart. Viscous bursting of suspended films. *Physical Review Letters*, 75(21):3886, 1995.
- [DMSW98] David C. Duffy, J. Cooper McDonald, Olivier J. A. Schueller, and George M. Whitesides. Rapid prototyping of microfluidic systems in poly(dimethylsiloxane). *Analytical Chemistry*, 70(23):4974–4984, 1998.
- [EHW12] Constantine G. Evans, Rizal F. Hariadi, and Erik Winfree. Direct Atomic Force Microscopy Observation of DNA Tile Crystal Growth at the Single-Molecule Level. *Journal of the American Chemical Society*, 134(25):10485–10492, 2012.
- [ENAF04] Axel Ekani-Nkodo, Kumar Ashish, and Deborah Kuchnir Fygenon. Joining and scission in the self-assembly of nanotubes from DNA tiles. *Physical Review Letters*, 93(26):268301, 2004.
- [ESF97] L. J. Evers, S. Yu. Shulepov, and G. Frens. Bursting dynamics of thin free liquid films from newtonian and viscoelastic solutions. *Physical Review Letters*, 79(24):4850–4853, 1997.
- [ESK⁺10] Masayuki Endo, Tsutomu Sugita, Yousuke Katsuda, Kumi Hidaka, and Hiroshi Sugiyama. Programmed-assembly system using DNA jigsaw pieces. *Chemistry – A European Journal*, 9999(9999):NA, 2010.
- [FBK⁺06] Marcin Fialkowski, Kyle J. M. Bishop, Rafal Klajn, Stoyan K. Smoukov, Christopher J. Campbell, and Bartosz A. Grzybowski. Principles and implementations of dissipative (dynamic) self-assembly. *Journal of Physical Chemistry B*, 110(6):2482–2496, 2006.
- [FGM⁺84] Christin Frederick, John Grable, Michele Melia, Cleopas Samudzi, Linda Jen-Jacobson, Bi-Cheng Wang, Patricia Greene, Herbert Boyer, and John Rosenberg. Kinked DNA in crystalline complex with EcoRI endonuclease. *Nature*, 309(5966):327–331, 1984.
- [FHL94] Henrik Flyvbjerg, Timothy E. Holy, and Stanisla Leibler. Stochastic dynamics of microtubules: a model for caps and catastrophes. *Physical Review Letters*, 73(17):2372–2375, 1994.

- [FHL96] Henrik Flyvbjerg, Timothy E. Holy, and Stanislas Leibler. Microtubule dynamics: Caps, catastrophes, and coupled hydrolysis. *Physical Review E*, 54(5):5538–5560, 1996.
- [FHP⁺08] Kenichi Fujibayashi, Rizal F. Hariadi, Sung Ha Park, Erik Winfree, and Satoshi Murata. Toward reliable algorithmic self-assembly of DNA tiles: A fixed-width cellular automaton pattern. *Nano Letters*, 8(7):1791–1797, 2008.
- [FM09] Kenichi Fujibayashi and Satoshi Murata. Precise simulation model for DNA tile self-assembly. *IEEE Transactions on Nanotechnology*, 8(3):361–368, 2009.
- [FN06] Udo Feldkamp and Christof Niemeyer. Rational design of DNA nanoarchitectures. *Angewandte Chemie International Edition*, 45(12):1856–1876, 2006.
- [FS93] Tsu Fu and Nadrian Seeman. DNA double-crossover molecules. *Biochemistry*, 32(13):3211–3220, 1993.
- [FTT⁺02] Ikuko Fujiwara, Shin Takahashi, Hisashi Tadakuma, Takashi Funatsu, and Shin'ichi Ishiwata. Microscopic analysis of polymerization dynamics with individual actin filaments. *Nature Cell Biology*, 4(9):666–673, 2002.
- [GBT08] S. J. Green, J. Bath, and A. J. Turberfield. Coordinated chemomechanical cycles: A mechanism for autonomous molecular motion. *Physical Review Letters*, 101(23):238101–4, 2008.
- [GCK⁺10] J. Glaser, D. Chakraborty, K. Kroy, I. Lauter, M. Degawa, N. Kirchgeßner, B. Hoffmann, R. Merkel, and M. Giesen. Tube width fluctuations in F-actin solutions. *Physical Review Letters*, 105(3):037801, 2010.
- [GCL⁺10] Elton Graugnard, Amber Cox, Jeunghoon Lee, Cheryl Jorcyk, Bernard Yurke, and William L. Hughes. Kinetics of DNA and RNA hybridization in serum and serum-SDS. *IEEE Transactions on Nanotechnology*, 9(5):603–609, 2010.
- [GCM04] Ethan C. Garner, Christopher S. Campbell, and R. Dyrche Mullins. Dynamic instability in a DNA-segregating prokaryotic actin homolog. *Science*, 306(5698):1021–1025, 2004.

- [GCWM07] Ethan C. Garner, Christopher S. Campbell, Douglas B. Weibel, and R. Dyche Mullins. Reconstitution of DNA segregation driven by assembly of a prokaryotic actin homolog. *Science*, 315(5816):1270–1274, 2007.
- [GHD⁺08] Russell P. Goodman, Mike Heilemann, Soren Doose, Christoph M. Erben, Achillefs N. Kapanidis, and Andrew J. Turberfield. Reconfigurable, braced, three-dimensional DNA nanostructures. *Nature Nanotechnology*, 3:93–96, 2008.
- [GMNH93] Frederick Gittes, Brian Mickey, Jilda Nettleton, and Jonathon Howard. Flexural rigidity of microtubules and actin filaments measured from thermal fluctuations in shape. *The Journal of Cell Biology*, 120(4):923, 1993.
- [GSW00] Bartosz A. Grzybowski, Howard A. Stone, and George M. Whitesides. Dynamic self-assembly of magnetized, millimetre-sized objects rotating at a liquid–air interface. *Nature*, 405(6790):1033–1036, 2000.
- [GT81] Cal Green and Clark Tibbetts. Reassociation rate limited displacement of DNA strands by branch migration. *Nucleic Acids Research*, 9(8):1905–1918, 1981.
- [HAD02] M. El Hammoumi, J. L. Achard, and L. Davoust. Measurements of air entrainment by vertical plunging liquid jets. *Experiments in Fluids*, 32(6):624–638, 2002.
- [HH86] Tetsuya Horio and Hirokazu Hotani. Visualization of the dynamic instability of individual microtubules by dark-field microscopy. *Nature*, 321:605–607, 1986.
- [HH03] Joe Howard and Anthony A. Hyman. Dynamics and mechanics of the microtubule plus end. *Nature*, 422:753–758, 2003.
- [HL96] H. G. Hansma and D. E. Laney. DNA binding to mica correlates with cationic radius: assay by atomic force microscopy. *Biophysical Journal*, 70(4):1933–1939, 1996.
- [HL10] Yu He and David R. Liu. Autonomous multistep organic synthesis in a single isothermal solution mediated by a DNA walker. *Nature Nanotechnology*, 5:778–782, 2010.

- [HM84] A. F. Horn and E. W. Merrill. Midpoint scission of macromolecules in dilute solution in turbulent flow. *Nature*, 312(5990):140–141, 1984.
- [HO10] Mark Hedglin and Patrick J O’Brien. Hopping enables a DNA repair glycosylase to search both strands and bypass a bound protein. *ACS Chemical Biology*, 5(4):427–436, 2010.
- [HSD⁺92] Anthony A. Hyman, S. Salser, D. N. Drechsel, N. Unwin, and Timothy J. Mitchison. Role of GTP hydrolysis in microtubule dynamics: information from a slowly hydrolyzable analogue, GMPCPP. *Molecular Biology of the Cell*, 3(10):1155, 1992.
- [HW04] Rizal F. Hariadi and Erik Winfree. Atomic force microscopy movies and measurements of DNA crystals. *Foundations of Nanoscience (Poster)*, 1, 2004.
- [HY] Rizal F. Hariadi and Bernard Yurke. Elongational rates in bursting bubbles measured using DNA nanotubes, *in preparation*.
- [H97] Timothy E. Holy. Physical aspects of the assembly and function of microtubules, 1997.
- [HY10] Rizal F. Hariadi and Bernard Yurke. Elongational-flow-induced scission of DNA nanotubes in laminar flow. *Physical Review E*, 82(4):046307, 2010.
- [IGC02] Ilia Ichetovkin, Wayne Grant, and John Condeelis. Cofilin produces newly polymerized actin filaments that are preferred for dendritic nucleation by the Arp2/3 complex. *Current Biology*, 12(1):79–84, 2002.
- [Jac75] M Jacobs. Part IX. nucleotide-tubulin interactions: Tubulin nucleotide reactions and their role in microtubule assembly and dissociation. *Annals of the New York Academy of Sciences*, 253:562–572, 1975.
- [KCdIT96] K. D. Knudsen, J. G. Hernández Cifre, and J. García de la Torre. Conformation and fracture of polystyrene chains in extensional flow studied by numerical simulation. *Macromolecules*, 29(10):3603–3610, 1996.

- [KDE⁺98] A. Krishnan, E. Dujardin, T. W. Ebbesen, P. N. Yianilos, and M. M. J. Treacy. Young's modulus of single-walled nanotubes. *Physical Review B*, 58(20):14013–14019, 1998.
- [KEW⁺04] Michael Kurpiewski, Lisa Engler, Lucyna Wozniak, Anna Kobylanska, Maria Koziolkiewicz, Wojciech Stec, and Linda Jen-Jacobson. Mechanisms of coupling between DNA recognition specificity and catalysis in EcoRI endonuclease. *Structure*, 12(10):1775–1788, 2004.
- [KGL⁺90] Young Chang Kim, John C. Grable, Robert Love, Patricia J. Greene, and John M. Rosenberg. Refinement of EcoRI endonuclease crystal structure: a revised protein chain tracing. *Science*, 249(4974):1307–1309, 1990.
- [KLZY06] Yonggang Ke, Yan Liu, Junping Zhang, and Hao Yan. A study of DNA tube formation mechanisms using 4-, 8-, and 12-helix DNA nanostructures. *Journal of the American Chemical Society*, 128(13):4414–4421, 2006.
- [KNT⁺08] Stoyan Karakashev, Phong Nguyen, Roumen Tsekov, Marc Hampton, and Anh Nguyen. Anomalous ion effects on rupture and lifetime of aqueous foam films formed from monovalent salt solutions up to saturation concentration. *Langmuir*, 24(20):11587–11591, 2008.
- [KNYO90] Daisuke Kusabiraki, Hidefumi Niki, Kazuaki Yamagiwa, and Akira Ohkawa. Gas entrainment rate and flow pattern of vertical plunging liquid jets. *The Canadian Journal of Chemical Engineering*, 68(6):893–903, 1990.
- [KP05] Jeffrey R. Kuhn and Thomas D. Pollard. Real-time measurements of actin filament polymerization by total internal reflection fluorescence microscopy. *Biophysical Journal*, 88(2):1387–1402, 2005.
- [KP07] Jeffrey R. Kuhn and Thomas D. Pollard. Single molecule kinetic analysis of actin filament capping: Polyphosphoinositides do not dissociate capping proteins. *Journal of Biological Chemistry*, 282(38):28014–28024, 2007.
- [KWSS07] Kinori Kuzuya, Risheng Wang, Ruojie Sha, and Nadrian C. Seeman. Six-helix and eight-helix DNA nanotubes assembled from half-tubes. *Nano Letters*, 7(6):1757–1763, 2007.

- [LC04] Clive Lloyd and Jordi Chan. Microtubules and the shape of plants to come. *Nature Reviews Molecular Cell Biology*, 5(1):13–23, 2004.
- [LCC96] N. Y. Liang, C. K. Chan, and H. J. Choi. Dynamics of the formation of an aureole in the bursting of soap films. *Physical Review E*, 54(4):R3117–R3120, 1996.
- [LCH⁺06] Haipeng Liu, Yi Chen, Yu He, Alexander E. Ribbe, and Chengde Mao. Approaching the limit: Can one DNA oligonucleotide assemble into large nanostructures? *Angewandte Chemie International Edition*, 45(12):1942–1945, 2006.
- [LF09] Allen Liu and Daniel Fletcher. Biology under construction: *in vitro* reconstitution of cellular function. *Nature Reviews Molecular Cell Biology*, 10(9):644–650, 2009.
- [LG08] Rong Li and Gregg G. Gundersen. Beyond polymer polarity: how the cytoskeleton builds a polarized cell. *Nature Reviews Molecular Cell Biology*, 9(11):860–873, 2008.
- [LLRY06] Chenxiang Lin, Yan Liu, Sherri Rinker, and Hao Yan. DNA tile based self assembly: Building complex nanoarchitectures. *ChemPhysChem*, 7(8):1641–1647, 2006.
- [LMD⁺10] Kyle Lund, Anthony Manzo, Nadine Dabby, Nicole Michelotti, Alexander Johnson-Buck, Jeanette Nangreave, Steven Taylor, Renjun Pei, Milan Stojanovic, Nils Walter, Erik Winfree, and Hao Yan. Molecular robots guided by prescriptive landscapes. *Nature*, 465(7295):206–210, 2010.
- [LMFM⁺10] Kara Lavender Law, S. Moret-Ferguson, Nikolai A. Maximenko, Giora Proskurowski, Emily E. Peacock, Jan Hafner, and Christopher M. Reddy. Plastic accumulation in the north atlantic subtropical gyre. *Science*, 329(5996):1185–1188, 2010.
- [LPH93] Michael Lorenz, David Popp, and Kenneth C. Holmes. Refinement of the F-actin model against X-ray fiber diffraction data by the use of a directed mutation algorithm. *Journal of Molecular Biology*, 234(3):826–836, 1993.

- [LPRL04] Dage Liu, Sung Ha Park, John H. Reif, and Thomas H. LaBean. DNA nanotubes self-assembled from triple-crossover tiles as templates for conductive nanowires. *Proceedings of the National Academy of Sciences of the United States of America*, 101(3):717–722, 2004.
- [LPSC97] R. G. Larson, T. T. Perkins, D. E. Smith, and S. Chu. Hydrodynamics of a DNA molecule in a flow field. *Physical Review E*, 55(2):1794–1797, 1997.
- [LR95] J. C. Lin and D. Rockwell. Evolution of a quasi-steady breaking wave. *Journal of Fluid Mechanics*, 302:29–44, 1995.
- [LS04] Shiping Liao and Nadrian C. Seeman. Translation of DNA signals into polymer assembly instructions. *Science*, 306(5704):2072–2074, 2004.
- [LYL05] D. C. Lin, Bernard Yurke, and N. A. Langrana. Inducing reversible stiffness changes in DNA-crosslinked gels. *Journal of Materials Research*, 20(6):1456–1464, 2005.
- [LYZ⁺06] Jonathan W. Larson, Gregory R. Yantz, Qun Zhong, Rebecca Charnas, Christina M. D’Antoni, Michael V. Gallo, Kimberly A. Gillis, Lori A. Neely, Kevin M. Phillips, Gordon G. Wong, Steven R. Gullans, and Rudolf Gilman-shin. Single DNA molecule stretching in sudden mixed shear and elongational microflows. *Lab on a Chip*, 6:1187–1199, 2006.
- [LZWS10] Wenyan Liu, Hong Zhong, Risheng Wang, and Nadrian Seeman. Crystalline two-dimensional DNA-origami arrays. *Angewandte Chemie International Edition*, 50(1):264–267, 2010.
- [Man08] Stephen Mann. Life as a nanoscale phenomenon. *Angewandte Chemie International Edition*, 47:5306–5320, 2008.
- [Mar38] Douglas A. Marsland. The effects of high hydrostatic pressure upon cell division in *Arbacia* eggs. *Journal of Cellular and Comparative Physiology*, 12(1):57–70, 1938.
- [MBBW94] P. Martin, A. Buguin, and F. Brochard-Wyart. Bursting of a liquid film on a liquid substrate. *Europhysics Letters*, 28(6):421–426, 1994.

- [MD52] Daniel Mazia and Katsuma Dan. The isolation and biochemical characterization of the mitotic apparatus of dividing cells. *Proceedings of the National Academy of Sciences of the United States of America*, 38(9):826–838, 1952.
- [MFZ⁺97] R. Scott Muir, Humberto Flores, Norton D. Zinder, Peter Model, Xavier Soberon, and Joseph Heitman. Temperature-sensitive mutants of the EcoRI endonuclease. *Journal of Molecular Biology*, 274(5):722–737, 1997.
- [MH95] B. Mickey and J. Howard. Rigidity of microtubules is increased by stabilizing agents. *The Journal of Cell Biology*, 130(4):909–917, 1995.
- [MHM⁺04] James C. Mitchell, J. Robin Harris, Jonathan Malo, Jonathan Bath, and Andrew J. Turberfield. Self-assembly of chiral DNA nanotubes. *Journal of the American Chemical Society*, 126(50):16342–16343, 2004.
- [MK84a] Timothy J. Mitchison and Marc Kirschner. Dynamic instability of microtubule growth. *Nature*, 312:237–242, 1984.
- [MK84b] Timothy J. Mitchison and Marc Kirschner. Microtubule assembly nucleated by isolated centrosomes. *Nature*, 312:232–237, 1984.
- [MKB⁺07] Julia Morfill, Ferdinand Kuhner, Kerstin Blank, Robert A. Lugmaier, Julia Sedlmair, and Hermann E Gaub. B-S transition in short oligonucleotides. *Biophysical Journal*, 93(7):2400–2409, 2007.
- [ML08] Pieta K. Mattila and Pekka Lappalainen. Filopodia: molecular architecture and cellular functions. *Nature Reviews Molecular Cell Biology*, 9(6):446–454, 2008.
- [MLK⁺05] Frederick Mathieu, Shiping Liao, Jens Kopatsch, Tong Wang, Chengde Mao, and Nadrian C. Seeman. Six-helix bundles designed from DNA. *Nano Letters*, 5(4):661–665, 2005.
- [MKS07] Frank Müller, Iler, Ulrike Kornek, and Ralf Stannarius. Experimental study of the bursting of inviscid bubbles. *Physical Review E*, 75(6):065302, 2007.
- [MMM91] Eva-Maria Mandelkow, Eckhard Mandelkow, and Ronald A. Milligan. Microtubule dynamics and microtubule caps: a time-resolved cryo-electron microscopy study. *The Journal of Cell Biology*, 114(5):977–991, 1991.

- [MS93] Larry E. Morrison and Lucy M. Stols. Sensitive fluorescence-based thermodynamic and kinetic measurements of DNA hybridization in solution. *Biochemistry*, 32(12):3095–3104, 1993.
- [MW78] Robert L. Margolis and Leslie Wilson. Opposite end assembly and disassembly of microtubules at steady state *in vitro*. *Cell*, 13(1):1–8, 1978.
- [NK90] Tuan Q. Nguyen and Henning H. Kausch. Effects of solvent viscosity on polystyrene degradation in transient elongational flow. *Macromolecules*, 23(24):5137–5145, 1990.
- [NK92] Tuan Q. Nguyen and Henning H. Kausch. Chain extension and degradation in convergent flow. *Polymer*, 33(12):2611–2621, 1992.
- [NN09] Phong Nguyen and Anh Nguyen. Drainage, rupture, and lifetime of deionized water films: Effect of dissolved gases? *Langmuir*, 26(5):3356–3363, 2009.
- [NSML97] F. J. Ndlec, T. Surrey, A. C. Maggs, and Stanislas Leibler. Self-organization of microtubules and motors. *Nature*, 389(6648):305–308, 1997.
- [NYL09] Jeanette Nangreave, Hao Yan, and Yan Liu. Studies of thermal stability of multivalent DNA hybridization in a nanostructured system. *Biophysical Journal*, 97(2):563–571, 2009.
- [Ogu98] Hasan N. Oguz. The role of surface disturbances in the entrainment of bubbles by a liquid jet. *Journal of Fluid Mechanics*, 372:189–212, 1998.
- [OHSC⁺96] P. J. Oefner, S. P. Hunicke-Smith, L. Chiang, F. Dietrich, J. Mulligan, and R. W. Davis. Efficient random subcloning of DNA sheared in a recirculating point- sink flow system. *Nucleic Acid Research*, 24(20):3879–3886, 1996.
- [OK62] F. Oosawa and M. Kasai. A theory of linear and helical aggregations of macromolecules. *Journal of Molecular Biology*, 4:10–21, 1962.
- [OK86] J. A. Odell and A. Keller. Flow-induced chain fracture of isolated linear macromolecules in solution. *Journal of Polymer Science Part B: Polymer Physics*, 24(9):1889–1916, 1986.
- [Opa52] A. I. Oparin. *The origin of life*. Dover, 1952.

- [ORKF06] Patrick O’Neill, Paul W. K. Rothemund, Ashish Kumar, and D. K. Fygenson. Sturdier DNA nanotubes via ligation. *Nano Letters*, 6(7):1379–1383, 2006.
- [OT94] J. A. Odell and M. A. Taylor. Dynamics and thermomechanical stability of DNA in solution. *Biopolymers*, 34(11):1483–1493, 1994.
- [PBL⁺05] Sung Ha Park, Robert D. Barish, Hanying Li, John H. Reif, Gleb Finkelstein, Hao Yan, and Thomas H. LaBean. Three-helix bundle DNA tiles self-assemble into 2D lattice or 1D templates for silver nanowires. *Nano Letters*, 5(4):693–696, 2005.
- [PF08] Francesco Pampaloni and Ernst-Ludwig Florin. Microtubule architecture: inspiration for novel carbon nanotube-based biomimetic materials. *Trends in Biotechnology*, 26(6):302–310, 2008.
- [PH94] I. G. Panyutin and P. Hsieh. The kinetics of spontaneous DNA branch migration. *Proceedings of the National Academy of Sciences of the United States of America*, 91(6):2021–2025, 1994.
- [PKTG09] Rob Phillips, Jane Kondev, Julie Theriot, and Hernan Garcia. *Physical biology of the cell*. Garland Science, 2009.
- [PTS⁺06] Renjun Pei, Steven K. Taylor, Darko Stefanovic, Sergei Rudchenko, Tiffany E. Mitchell, and Milan N. Stojanovic. Behavior of polycatalytic assemblies in a substrate-displaying matrix. *Journal of the American Chemical Society*, 128(39):12693–12699, 2006.
- [Qua03] M. Quail. *Encyclopedia of the Human Genome*. Nature Publishing, London, 2003.
- [QW89] Robin Quartin and James Wetmur. Effect of ionic strength on the hybridization of oligodeoxynucleotides with reduced charge due to methylphosphonate linkages to unmodified oligodeoxynucleotides containing the complementary sequence. *Biochemistry*, 28(3):1040–1047, 1989.
- [RBHW77] C. M. Radding, K. L. Beattie, W. K. Holloman, and R. C. Wiegand. Uptake of homologous single-stranded fragments by superhelical DNA IV: Branch migration. *Journal of Molecular Biology*, 116(4):825–839, 1977.

- [RENP⁺04] Paul W. K. Rothemund, Axel Ekani-Nkodo, Nick Papadakis, Ashish Kumar, Deborah Kuchnir Fygenon, and Erik Winfree. Design and characterization of programmable DNA nanotubes. *Journal of the American Chemical Society*, 126(50):16344–16352, 2004.
- [RHF⁺10] Lynn M. Russell, Lelia N. Hawkins, Amanda A. Frossard, Patricia K. Quinn, and Tim S. Bates. Carbohydrate-like composition of submicron atmospheric particles and their production from ocean bubble bursting. *Proceedings of the National Academy of Sciences of the United States of America*, 107(15):6652–6657, 2010.
- [Rot06] Paul W. K. Rothemund. Folding DNA to create nanoscale shapes and patterns. *Nature*, 440(7082):297–302, 2006.
- [RPW04] Paul W. K. Rothemund, Nick Papadakis, and Erik Winfree. Algorithmic self-assembly of DNA Sierpinski triangles. *PLoS Biology*, 2(12), 2004.
- [RQ06] É. Reyssat and D. Quéré. Bursting of a fluid film in a viscous environment. *Europhysics Letters*, 76(2):236, 2006.
- [RS10] Donald Rau and Nina Sidorova. Diffusion of the restriction nuclease EcoRI along DNA. *Journal of Molecular Biology*, 395(2):408–416, 2010.
- [RSB⁺05] Dustin Reishus, Bilal Shaw, Yuriy Brun, Nickolas Chelyapov, and Leonard Adleman. Self-assembly of DNA double-double crossover complexes into high-density, doubly connected, planar structures. *Journal of the American Chemical Society*, 127(50):17590–17591, 2005.
- [SB99] G. J. Storr and M. Behnia. Experiments with large diameter gravity driven impacting liquid jets. *Experiments in Fluids*, 27(1):60–69, 1999.
- [SBL01] Jack W. Szostak, David P. Bartel, and P. Luigi Luisi. Synthesizing life. *Nature*, 409(6818):387–390, 2001.
- [SCB96] Steven B. Smith, Yujia Cui, and Carlos Bustamante. Overstretching B-DNA: The elastic response of individual double-stranded and single-stranded DNA molecules. *Science*, 271(5250):795–799, 1996.

- [Sch07] Rebecca Schulman. *The Self-Replication and Evolution of DNA Crystals*. PhD thesis, California Institute of Technology, May 2007.
- [SCK⁺00] Tricia R. Serio, Anil G. Cashikar, Anthony S. Kowal, George J. Sawicki, Jahan J. Moslehi, Louise Serpell, Morton F. Arnsdorf, and Susan L. Lindquist. Nucleated conformational conversion and the replication of conformational information by a prion determinant. *Science*, 289(5483):1317–1321, 2000.
- [SCM00] Rava Silveira, Sahraoui Chaïeb, and L. Mahadevan. Rippling instability of a collapsing bubble. *Science*, 287(5457):1468–1471, 2000.
- [SCW08] David Soloveichik, Matthew Cook, and Erik Winfree. Combining self-healing and proofreading in self-assembly. *Natural Computing*, 7(2):203–218, 2008.
- [See82] Nadrian C. Seeman. Nucleic acid junctions and lattices. *Journal of Theoretical Biology*, 99(2):237 – 247, 1982.
- [See90] Nadrian C. Seeman. *De novo* design of sequences for nucleic acid structural engineering. *Journal of Biomolecular Structure & Dynamics*, 8(3):573–581, 1990.
- [See03] Nadrian C. Seeman. DNA in a material world. *Nature*, 421(6921):427–431, 2003.
- [See07] Nadrian C. Seeman. An overview of structural DNA nanotechnology. *Molecular biotechnology*, 37(3):246–257, 2007.
- [SKOS01] Masahito Sano, Ayumi Kamino, Junko Okamura, and Seiji Shinkai. Ring closure of carbon nanotubes. *Science*, 293(5533):1299–1301, 2001.
- [SL06] James Shorter and Susan Lindquist. Destruction or potentiation of different prions catalyzed by similar hsp104 remodeling activities. *Molecular Cell*, 23(3):425–438, 2006.
- [SP04] Jong-Shik Shin and Niles A. Pierce. A synthetic DNA walker for molecular transport. *Journal of American Chemical Society*, 126(35):10834–10835, 2004.

- [SS76] E. Van De Sande and John M. Smith. Jet break-up and air entrainment by low velocity turbulent water jets. *Chemical Engineering Science*, 31(3):219–224, 1976.
- [SS02] Andrew P. Somlyo and Avril V. Somlyo. Signal transduction and regulation in smooth muscle. *Nature*, 372:231–236, 2002.
- [SS04] William B. Sherman and Nadrian C. Seeman. A precisely controlled DNA biped walking device. *Nano Letters*, 4(7):1203–1207, 2004.
- [SS06] William B Sherman and Nadrian C Seeman. Design of Minimally Strained Nucleic Acid Nanotubes. *Biophysical Journal*, 90(12):4546–4557, 2006.
- [SSW10] David Soloveichik, Georg Seelig, and Erik Winfree. DNA as a universal substrate for chemical kinetics. *Proceedings of the National Academy of Sciences of the United States of America*, 107(12):5393, 2010.
- [SSZW06] Georg Seelig, David Soloveichik, David Yu Zhang, and Erik Winfree. Enzyme-free nucleic acid logic circuits. *Science*, 314(5805):1585–1588, 2006.
- [ST68] Michael L. Shelanski and Edwin W. Taylor. Properties of the protein subunit of central-pair and outer-doublet microtubules of sea urchin flagella. *The Journal of Cell Biology*, 38(2):304–315, 1968.
- [Str99] John William Strutt. *Scientific Papers*, volume 1. Cambridge University Press, Cambridge, 1899.
- [Str02] John William Strutt. *Scientific Papers*, volume 3. Cambridge University Press, Cambridge, 1902.
- [SW03] Manfred Schliwa and Günther Woehlke. Molecular motors. *Nature*, 422(6933):759–765, 2003.
- [SW05] Rebecca Schulman and Erik Winfree. Self-replication and evolution of DNA crystals. *Advances in Artificial Life*, pages 734–743, 2005.
- [SW07] Rebecca Schulman and Erik Winfree. Synthesis of crystals with a programmable kinetic barrier to nucleation. *Proceedings of the National Academy of Sciences of the United States of America*, 104(39):15236–15241, 2007.

- [SW11] Rebecca Schulman and Erik Winfree. Simple evolution of complex crystal species. *Lecture Notes in Computer Science*, 6518:147–161, 2011.
- [SWY⁺98] Nadrian C. Seeman, Hui Wang, Xiaoping Yang, Furong Liu, Chengde Mao, Weiqiong Sun, Lisa A. Wenzler, Zhiyong Shen, Ruojie Sha, Hao Yan, Man Hoi Wong, Phiset Sa-Ardyen, Bing Liu, Hangxia Qiu, Xiaojun Li, Jing Qi, Shou Ming Du, Yuwen Zhang, John E. Mueller, Tsu-Ju Fu, Yinli Wang, and Junghuei Chen. New motifs in DNA nanotechnology. *Nanotechnology*, 9(3):257–273, 1998.
- [SY10] Rebecca Schulman and Bernard Yurke. A molecular algorithm for path self-assembly in 3 dimensions. *In Proceedings of Robotics: Science and Systems*, 2010.
- [Tay59] Geoffrey Taylor. The dynamics of thin sheets of fluid. III. disintegration of fluid sheets. *Proceedings of the Royal Society of London. Series A, Mathematical and Physical Sciences*, 253(1274):313–321, 1959.
- [The00] Julie A. Theriot. The polymerization motor. *Traffic*, 1:19–28, 2000.
- [THSOD98] Yvonne Thorstenson, Scott Hunicke-Smith, Peter Oefner, and Ronald Davis. An automated hydrodynamic process for controlled, unbiased DNA shearing. *Genome Research*, 8(8):848–855, 1998.
- [TPSW97] Bernard Tinland, Alain Pluen, Jean Sturm, and Gilbert Weill. Persistence length of single-stranded DNA. *Macromolecules*, 30(19):5763–5765, 1997.
- [TW78] D. L. Taylor and Y. L. Wang. Molecular cytochemistry: incorporation of fluorescently labeled actin into living cells. *Proceedings of the National Academy of Sciences of the United States of America*, 75(2):857, 1978.
- [TW80] D. L. Taylor and Y. L. Wang. Fluorescently labelled molecules as probes of the structure and function of living cells. *Nature*, 284(5755):405, 1980.
- [UCT⁺00] Marc A. Unger, Hou-Pu Chou, Todd Thorsen, Axel Scherer, and Stephen R. Quake. Monolithic microfabricated valves and pumps by multilayer soft lithography. *Science*, 288(5463):113–116, 2000.

- [VCS06] Siva A. Vanapalli, Steven L. Ceccio, and Michael J. Solomon. Universal scaling for polymer chain scission in turbulence. *Proceedings of the National Academy of Sciences of the United States of America*, 103(45):16660–16665, 2006.
- [VDR⁺07] Suvir Venkataraman, Robert M. Dirks, Paul W. K. Rothmund, Erik Winfree, and Niles A. Pierce. An autonomous polymerization motor powered by DNA hybridization. *Nature Nanotechnology*, 2(8):490–494, 2007.
- [WC53] James D. Watson and Francis H. C. Crick. A structure for deoxyribose nucleic acid. *Nature*, 171:737–738, 1953.
- [WC93] Richard H. Wade and Denis Chrétien. Cryoelectron microscopy of microtubules. *Journal of Structural Biology*, 110(1):1–27, 1993.
- [WCJ90] Richard H. Wade, Denis Chrétien, and D. Job. Characterization of microtubule protofilament numbers. How does the surface lattice accommodate? *Journal of Molecular Biology*, 212(4):775–786, 1990.
- [Weg76] Albrecht Wegner. Head to tail polymerization of actin. *Journal of Molecular Biology*, 108(1):139–50, 1976.
- [Wei72] Richard C. Weisenberg. Microtubule formation *in vitro* in solutions containing low calcium concentrations. *Science*, 177(54):1104, 1972.
- [WF91] James Wetmur and Jacques Fresco. DNA probes: Applications of the principles of nucleic acid hybridization. *Critical Reviews in Biochemistry and Molecular Biology*, 26(3-4):227–259, 1991.
- [WG02] George M. Whitesides and Bartosz Grzybowski. Self-assembly at all scales. *Science*, 295(5564):2418–2421, 2002.
- [WGA⁺10] Bo Wang, Juan Guan, Stephen Anthony, Sung Bae, Kenneth Schweizer, and Steve Granick. Confining potential when a biopolymer filament reptates. *Physical Review Letters*, 104(11):118301, 2010.
- [Win98] Erik Winfree. Simulations of computing by self-assembly. *Caltech CS Tech Report*, 22, 1998.

- [Win06] Erik Winfree. Self-healing tile sets. *Nanotechnology: science and computation*, pages 55–78, 2006.
- [WJM99] David Wright, William Jack, and Paul Modrich. The kinetic mechanism of EcoRI endonuclease. *Journal of Biological Chemistry*, 274(45):31896–31902, 1999.
- [WLWS98] Erik Winfree, Furong Liu, Lisa A. Wenzler, and Nadrian C Seeman. Design and self-assembly of two-dimensional DNA crystals. *Nature*, 394(6693):539–544, 1998.
- [WM05] Bryant Wei and Yongli Mi. A new triple crossover triangle (TXT) motif for DNA self-assembly. *Biomacromolecules*, 6(5):2528–2532, 2005.
- [WOP⁺88] R. A. Walker, E. T. O’Brien, N. K. Pryer, M. F. Soboeiro, W. A. Voter, H. P. Erickson, and E. D. Salmon. Dynamic instability of individual microtubules analyzed by video light microscopy: rate constants and transition frequencies. *The Journal of Cell Biology*, 107(4):1437, 1988.
- [Wu81] Jin Wu. Evidence of sea spray produced by bursting bubbles. *Science*, 212(4492):324–326, 1981.
- [WWAS⁺06] Stefan Westermann, Hong-Wei Wang, Agustin Avila-Sakar, David G. Drubin, Eva Nogales, and Georjana Barnes. The Dam1 kinetochore ring complex moves processively on depolymerizing microtubule ends. *Nature*, 440(7083):565–569, 2006.
- [YCCP08] Peng Yin, Harry M. T. Choi, Colby R. Calvert, and Niles A. Pierce. Programming biomolecular self-assembly pathways. *Nature*, 451(7176):318–322, 2008.
- [YGB⁺04] Peng Yin, Bu Guo, Christina Belmore, Will Palmeri, Erik Winfree, Thomas H. LaBean, and John H. Reif. TileSoft: Sequence optimization software for designing DNA secondary structures, 2004. *TR-CS-2004-09, Duke* 2004.
- [YHS⁺08] Peng Yin, Rizal F. Hariadi, Sudheer Sahu, Harry M. T. Choi, Sung Ha Park, Thomas H. LaBean, and John H Reif. Programming DNA tube circumferences. *Science*, 321(5890):824–826, 2008.

- [YO10] Nina Yao and Mike O'Donnell. Snapshot: The replisome. *Cell*, 141(6), 2010.
- [YPF⁺03] Hao Yan, Sung Ha Park, Gleb Finkelstein, John H. Reif, and Thomas H. LaBean. DNA-templated self-assembly of protein arrays and highly conductive nanowires. *Science*, 301(5641):1882–1884, 2003.
- [YTM⁺00] Bernard Yurke, Andrew J. Turberfield, Allen P. Mills, Friedrich C. Simmel, and Jennifer L Neumann. A DNA-fuelled molecular machine made of DNA. *Nature*, 406(6796):605–608, 2000.
- [ZBC⁺09] Jianping Zheng, Jens J. Birktoft, Yi Chen, Tong Wang, Ruojie Sha, Pamela E. Constantinou, Stephan L. Ginell, Chengde Mao, and Nadrian C. Seeman. From molecular to macroscopic via the rational design of a self-assembled 3D DNA crystal. *Nature*, 461(7260):74–77, 2009.
- [ZHCW13] David Yu Zhang, Rizal F. Hariadi, Harry M. T. Choi, and Erik Winfree. Integrating DNA strand-displacement circuitry with DNA tile self-assembly. *Nature Communications*, 4:1965, 2013.
- [ZS09] Ting F. Zhu and Jack W. Szostak. Coupled growth and division of model protocell membranes. *Journal of the American Chemical Society*, 131(15):5705–5713, 2009.
- [ZS11] David Yu Zhang and Georg Seelig. Dynamic DNA nanotechnology using strand-displacement reactions. *Nature Chemistry*, 3(2):103–113, 2011.
- [ZW09] David Yu Zhang and Erik Winfree. Control of DNA strand displacement kinetics using toehold exchange. *Journal of the American Chemical Society*, 131(47):17303–17314, 2009.
- [ZWAM95] Yixian Zheng, Mei Lie Wong, Bruce Alberts, and Timothy J. Mitchison. Nucleation of microtubule assembly by a γ -tubulin-containing ring complex. *Nature*, 378(6557):578, 1995.